UNIVERSITY OF SOUTHAMPTON

In Situ Observations of Magnetic Reconnection within the Magnetotails of Saturn and Mercury

by

Andrew Smith

A thesis submitted in partial fulfillment for the
degree of Doctor of Philosophy

in the
Faculty of Physical Sciences and Engineering
Department of Physics and Astronomy

October 2018

UNIVERSITY OF SOUTHAMPTON

Abstract

Faculty of Physical Sciences and Engineering
Department of Physics and Astronomy

Doctor of Philosophy

by Andrew Smith

This thesis concerns magnetotail reconnection at the planets Saturn and Mercury. Magnetotail reconnection generates large magnetic structures that may pass over orbiting spacecraft, creating identifiable signatures in *in situ* magnetic field and plasma data. At Saturn, a comprehensive survey of Cassini magnetometer data was performed; the distribution, recurrence and properties of the identified reconnection related events were investigated. The identifications were most frequently observed post-midnight, while the reconnection site was inferred to lie between $\sim 20 - 30\,R_S$ from the planet. Mass loss through magnetotail reconnection was found to be insufficient to balance the addition from sources such as the moon Enceladus. Dipolarization fronts were further investigated with regard to their plasma properties. The energized populations behind the fronts were found to be $\sim 4 - 12$ times hotter and $\sim 3 - 10$ times less dense than the local ambient plasma sheet. The plasma properties of the dipolarizations were found to be more variable in the post-midnight events, perhaps suggesting a more variable x-line location. Two case studies were presented, the first evidenced short duration flows (~ 10 minutes), indicating bursty or azimuthally limited reconnection. The second displayed a series of dipolarizations carrying increasingly hot and tenuous plasma, suggesting that the reconnection site was retreating tailward.

For Mercury's magnetotail, a method was presented by which encounters with quasi-force-free flux ropes can be automatically identified in magnetic field data. The method combined new techniques such as wavelet transforms, while automating the analysis of properties that are commonly used to identify flux ropes. The technique was applied to 319 intervals in which MESSENGER was within the Hermean plasma sheet, locating a total of 248 flux ropes. The identifications exhibited a small dawnward preference. Identifications were more likely if the preceding lobe magnetic field was enhanced. Two Monte Carlo based techniques were presented to investigate the effects of spacecraft sampling and selection criteria. The Hermean magnetotail reconnection site was found to be most consistent with an offset $\sim 0.4\,R_M$ dawnward of midnight, with a reconnection width of $\sim$ half the model magnetotail. Dissipation mechanisms planetward of the reconnection site were required to explain the observed distributions. Two sets of selection criteria were compared and found to preferentially select different subsets of the intrinsic population. The method allowed the quantification of these effects, firstly allowing distributions of properties to be corrected (e.g. flux rope radii), and secondly allowing the rate of identifications to be corrected for the fraction of the population that is undetected.

Declarations

This thesis is based upon the following papers:

1. **Smith, A. W.**, Jackman, C. M., & Thomsen, M. F. (2016). Magnetic reconnection in Saturns magnetotail: A comprehensive magnetic field survey. Journal of Geophysical Research A: Space Physics, 121(4), 2984-3005. http://doi.org/10.1002/2015JA022005

2. **Smith, A. W.**, Slavin, J. A., Jackman, C. M., Fear, R. C., Poh, G. K., DiBraccio, G. A., Trenchi, L. (2017). Automated force-free flux rope identification. Journal of Geophysical Research: Space Physics, 122(1), 780-791. http://doi.org/10.1002/2016JA022994

3. **Smith, A. W.**, Slavin, J. A., Jackman, C. M., Poh, G. K., & Fear, R. C. (2017). Flux ropes in the Hermean magnetotail: Distribution, properties, and formation. Journal of Geophysical Research: Space Physics, 122(8), 8136-8153. http://doi.org/10.1002/2017JA024295

4. **Smith, A. W.**, Jackman, C. M., Thomsen, M. F., Sergis, N., Mitchell, D. G., & Roussos, E. (2018), Dipolarization Fronts with Associated Energized Electrons in Saturn's Magnetotail, Journal of Geophysical Research: Space Physics, 123(4), 2714-2735, http://doi.org/10.1002/2017JA024904.

5. **Smith, A. W.**, Jackman, C. M., Thomsen, M. F., Lamy, L., Sergis, N. (2018), Multi-instrument Investigation of the Location of Saturn's Magnetotail X-Line, Journal of Geophysical Research: Space Physics, 123, http://doi.org/10.1029/2018JA025532.

6. **Smith, A. W.**, C. M. Jackman, C. Frohmaier, J. C. Coxon, J. A. Slavin, and R. C. Fear (2018, Under Review), Evaluating Single Spacecraft Observations of Planetary Magnetotails with Simple Monte Carlo Simulations: 1. Spatial Distributions, J. Geophys. Res. Space Physics [Under Review]

7. **Smith, A. W.**, C. M. Jackman, C. Frohmaier, R. C. Fear , J. A. Slavin, and J. C. Coxon (2018, Under Review), Evaluating Single Spacecraft Observations of Planetary Magnetotails with Simple Monte Carlo Simulations: 2. Selection Effects, J. Geophys. Res. Space Physics [Under Review]

The following papers are not included in this thesis:

1. Jackman, C. M., Thomsen, M. F., Mitchell, D. G., Sergis, N., Arridge, C. S., Felici, M., Badman, S. V., Paranicas, C., Jia, X., Hospodarksy, G. B., Andriopoulou, M.,

Khurana, K. K., **Smith, A. W.**, and Dougherty, M. K. (2015). Field dipolarization in Saturns magnetotail with planetward ion flows and energetic particle flow bursts: Evidence of quasi-steady reconnection. Journal of Geophysical Research: Space Physics, 120(5), 36033617. http://doi.org/10.1002/2015JA020995

2. Poh, G., Slavin, J. A., Jia, X., Raines, J. M., Imber, S. M., Sun, W. J., Gershman, D. J., DiBraccio, G. A., Genestreti, K. J. **Smith, A. W.** (2017). Mercurys cross-tail current sheet: Structure, X-line location and stress balance. Geophysical Research Letters, 44(2), 678686. http://doi.org/10.1002/2016GL071612

3. Poh, G., Slavin, J. A., Jia, X., Raines, J. M., Imber, S. M., Sun, W. J., Gershman, D. J., DiBraccio, G. A., Genestreti, K. J., **Smith, A. W.** (2017). Coupling between Mercury and its nightside magnetosphere: Cross-tail current sheet asymmetry and substorm current wedge formation. Journal of Geophysical Research: Space Physics, 122(8), 84198433. http://doi.org/10.1002/2017JA024266

4. Bradley, T., Cowley, C., Bunce, E., **Smith, A. W.**, Jackman, C. M., Provan, G., (2018, Under Review). Planetary Period Modulation of Reconnection Bursts in Saturn's Magnetotail, Journal of Geophysical Research: Space Physics [Under Review]

"To err is human, but to really foul things up you need a computer."

Paul R. Ehrlich

Contents

List of Figures

List of Tables

Abbreviations

CAPS	**CA**ssini **P**lasma **S**pectrometer
CHEMS	**C**harge **E**nergy **M**ass **S**pectrometer
CIR	**C**orotating **I**nteraction **R**egion
CME	**C**oronal **M**ass **E**jection
CWT	**C**ontinuous **W**avelet **T**ransform
DSN	**D**eep **S**pace **N**etwork
ECPC	**E**xpanding-**C**ontracting **P**olar **C**ap
ELS	**EL**ectron **S**pectrometer
FGM	**F**lux**G**ate **M**agnetometer
FOV	**F**ield **O**f **V**iew
FTE	**F**lux **T**ransfer **E**vent
HCS	**H**eliospheric **C**urrent **S**heet
HST	**H**ubble **S**pace **Telescope**
IMF	**I**nterplanetary **M**agnetic **F**ield
IMS	**I**on **M**ass **S**pectrometer
INCA	**I**on and **N**eutral **CA**mera
KRTP	**K**ronocentric **R**adial **T**heta **P**hi
KSM	**K**ronocentric **S**olar **M**agnetospheric
LEMMS	**L**ow-**E**nergy **M**agnetospheric **M**easurement **S**ystem
LFE	**L**ow **F**requency **E**xtension
LLBL	**L**ow **L**atitude **B**oundary **L**ayer
MESSENGER	**ME**rcury **S**urface, **S**pace **EN**vironment, **GE**ochemistry, and **R**anging
MHD	**M**agneto-**H**ydro **D**ynamics
MIMI	**M**agnetospheric **IM**aging **I**nstrument
MSM	**M**ercury **S**olar **M**agnetospheric

MSO	**M**ercury **S**olar **O**rbital
MVA	**M**inimum **V**ariance **A**nalysis
NMNL	**N**ear **M**ercury **N**eutral **L**ine
PPPS	**P**ost **P**lasmoid **P**lasma **S**heet
PHA	**P**ulse **H**eight **A**nalysis
QQ Plot	**Q**uantile-**Q**uantile Plot
RMS	**R**oot **M**ean **S**quare
RPWS	**R**adio and **P**lasma **W**ave **S**cience instrument
SCAS	**S**cience **C**alibration and **A**lignment **S**ubsystem
SEA	**S**uperposed **E**poch **A**nalysis
SKR	**S**aturn **K**ilometric **R**adiation
SOI	**S**aturn **O**rbit **I**nsertion
TCR	**T**ravelling **C**ompression **R**egion
VHM	**V**ector and **H**elium **M**agnetometer

Declaration of Authorship

I, Andrew Smith, declare that this thesis titled, 'In Situ Observations of Magnetic Reconnection within the Magnetotails of Saturn and Mercury' and the work presented in it are my own. I confirm that:

- This work was done wholly or mainly while in candidature for a research degree at this University.
- Where any part of this thesis has previously been submitted for a degree or any other qualification at this University or any other institution, this has been clearly stated.
- Where I have consulted the published work of others, this is always clearly attributed.
- Where I have quoted from the work of others, the source is always given. With the exception of such quotations, this thesis is entirely my own work.
- I have acknowledged all main sources of help.
- Where the thesis is based on work done by myself jointly with others, I have made clear exactly what was done by others and what I have contributed myself.

Signed:

Date:

Acknowledgements

Firstly, I would like to thank my supervisor, Caitriona Jackman, without whom none of this would have been possible. I am eternally grateful for her guidance, support and understanding through the last four years. I'd like to take the opportunity to apologise for the many grammatical crimes she has had to correct!

Thank you to the SEP group, you've made these four years a pleasure. I couldn't have asked for a greater community to work within; Jade, Steve, John and David I've enjoyed working with you and attending the post-work pub! It has also been great to be a part of the larger astronomy group, particularly for the early morning football! Thank you to all the astronomers, both past and present. James, Aarran, Sam, Rob and CFro, thanks for all the great times and Trago quizzes. Boon and Aarran, thanks for introducing me to the Highfield cricket team, it's been a fun few years!

Thank you to Jim Slavin and the Michigan group for hosting me on two occasions. The trips were great experiences and really helped me to develop through my PhD.

Joe. You've been the best mate I could've asked for. Thank you for putting up with me, in the office, the flat and at conferences! Your spot on the sofa(/floor) is always there if you want it.

Mum and Dad, thanks for always being there if I needed a chat. Apologies for not visiting home often enough, but thank you for always making me feel welcome when I did.

Logan and Dexter, it is always a pleasure to come home to you two. My phone is full of the pictures of your antics, you never fail to cheer me up.

Amy. You are incredible. I could not have done this without you and your support. Thank you for always being there, putting up with me and keeping me on track. Let's see what the future holds! Love you so much.

Chapter 1

Introduction

1.1 Overview

This thesis concerns single spacecraft observations of the products of magnetic reconnection in the magnetospheres of Saturn and Mercury.

The first chapter will present the fundamental physics governing the behaviour of space plasmas, including the frozen in approximation, the heliosphere, planetary magnetospheres and magnetic reconnection. Chapter 2 will then expand upon these concepts with the specifics of the magnetospheres of Mercury and Saturn, with a particular focus on their properties and dynamics. Chapter 3 will describe the spacecraft and instrumentation used in this thesis. Chapters 4 - 9 then present the scientific investigations completed for the submission of this thesis. The science chapters are presented in the chronological order in which the associated papers were published, with Chapters 4, 7 and 8 regarding Saturn's magnetotail while Chapters 5, 6 and 9 investigate the Hermean magnetotail. Chapter 10 will then conclude with a summary and a discussion of potential future avenues of investigation.

1.2 Plasma Physics

Plasma is one of the four fundamental states of matter; it describes a quasi-neutral gas, where many of the constituent atoms have dissociated into their positive and negative components.

There are several methods by which it is possible to generate a plasma. The first method is by heating a gas until the average kinetic energy of the particles is greater than its

ionization energy: the energy required to remove an electron. Another method is photo-ionization, where high energy photons can provide sufficient energy to ionise the gas.

There are three criteria that are used to define a plasma. The first criterion concerns the distance over which charge separation can occur, known as the Debye length:

$$\lambda_D = \sqrt{\frac{\epsilon_0 k_B T_e}{n_e e^2}} \tag{1.1}$$

where ϵ_0 is the permittivity of free space, k_B is Boltzmann's constant, T_e and n_e are the electron temperature and density, while e is the charge on an electron. The Debye length represents the distance at which there is a balance between the thermal energy (that would act to separate charges) and the electrostatic potential (that would act to restore charge neutrality). For quasi-neutrality to remain in effect the physical size of the system must be sufficiently large ($L >> \lambda_D$).

The second criterion describes the conditions necessary for Debye (or collective) shielding to be effective. Each ion will be surrounded by a region of slightly higher electron number density due to its electrostatic attraction. The electrons in this region will shield the electric field of the ion. The second criterion requires that there are sufficient electrons within the 'Debye' sphere to shield the ion's electric field, or:

$$N_D = \frac{4\pi}{3} n_e \lambda_D^3 \tag{1.2}$$

must be $>> 1$. Finally, a plasma will generally not be fully ionised, there will be some fraction of neutrals that remain, collisions with which will disturb the motion of the plasma. To evaluate this effect, the electron plasma frequency (ω_{pe}), describing the oscillation of electrons about ions, should be considered:

$$\omega_{pe} = \sqrt{\frac{n_e e^2}{m_e \epsilon_0}} \tag{1.3}$$

where m_e is the mass of an electron. In order to behave like a plasma, the time between electron-neutral collisions (τ_n) must be much greater than the period of the plasma oscillations, or:

$$\omega_{pn} \tau_n >> 1 \tag{1.4}$$

represents the third plasma criterion. An ideal plasma is generally assumed to be collisionless. Notably, this assumption breaks down close to planetary atmospheres, where the increased density of neutral species violates the third plasma criterion. Elsewhere in the solar system, the plasma can often be approximated as collisionless, for example in the stream of plasma continuously ejected from the Sun: the solar wind (discussed further in Section 1.3).

As plasmas are predominantly formed of charged particles, electric (**E**) and magnetic (**B**) fields play a fundamental role in governing their motion. In turn, the behaviour of the fields can be described by Maxwell's equations:

$$\nabla \cdot \mathbf{E} = \frac{\rho_q}{\epsilon_0} \tag{1.5}$$

$$\nabla \cdot \mathbf{B} = 0 \tag{1.6}$$

$$\nabla \times \mathbf{E} = -\frac{\partial \mathbf{B}}{\partial t} \tag{1.7}$$

$$\nabla \times \mathbf{B} = \mu_0(\mathbf{j} + \epsilon_0 \frac{\partial \mathbf{E}}{\partial t}) \tag{1.8}$$

where ρ_q is the charge density, $\mathbf{j}$ is the current density, and ϵ_0 and μ_0 are the permittivity and permeability of free space respectively. Gauss' laws of electric and magnetic fields are represented in Equations 1.5 and 1.6 respectively. Faraday's law is shown in Equation 1.7 while the Ampère-Maxwell law is displayed in Equation 1.8.

1.2.1 Single Particle Motion

To begin, we will consider the simplest description of a plasma, ignoring collective motion and focusing on the motion of individual particles under the influence of electric and magnetic fields. The equation of motion for a particle of mass m, with charge q and velocity $\mathbf{v}$ experiencing electric and magnetic fields ($\mathbf{E}$ and $\mathbf{B}$ respectively) is given by the Lorentz equation:

$$m\frac{d\mathbf{v}}{dt} = q(\mathbf{E} + \mathbf{v} \times \mathbf{B}) \tag{1.9}$$

It is often useful to break a particle's velocity ($\mathbf{v}$) into two components; those parallel ($v_{\parallel}$) and perpendicular to the magnetic field ($v_{\perp}$) such that:

$$\mathbf{v} = \mathbf{v}_{\parallel} + \mathbf{v}_{\perp} \tag{1.10}$$

The angle between the magnetic field and the particles velocity is known as the pitch angle (α):

$$\alpha = \tan^{-1}\left(\frac{\mathbf{v}_{\perp}}{\mathbf{v}_{\parallel}}\right) \tag{1.11}$$

For example, a pitch angle of 0 or 180° corresponds to the particle's velocity being entirely field aligned (and parallel/anti-parallel to the field respectively).

1.2.1.1 In the Absence of an Electric Field

For the case where $\mathbf{E} = 0$ and the magnetic field is uniform it can be shown that the magnitude of the velocity ($|\mathbf{v}|$) of the particle will remain constant. Equation 1.9 reduces to:

$$\frac{d\mathbf{v}}{dt} = \frac{q}{m}(\mathbf{v} \times \mathbf{B}) \tag{1.12}$$

Taking the dot product of both sides with $\mathbf{v}$, produces:

$$\mathbf{v} \cdot \frac{d\mathbf{v}}{dt} = \frac{q}{m}\mathbf{v} \cdot (\mathbf{v} \times \mathbf{B}) \tag{1.13}$$

where $\mathbf{v} \cdot (\mathbf{v} \times \mathbf{B}) = 0$, therefore:

$$\mathbf{v} \cdot \frac{d\mathbf{v}}{dt} = \frac{d}{dt}\left(\frac{1}{2}m\mathbf{v}^2\right) = 0 \tag{1.14}$$

showing that the kinetic energy of the particle, and therefore the magnitude of its velocity, must be constant. In addition, when the particle's velocity ($\mathbf{v}$) has been decomposed into the components parallel ($\mathbf{v}_{\parallel}$) and perpendicular ($\mathbf{v}_{\perp}$) to the field ($\mathbf{B}$) (using Equation 1.10), the perpendicular part of Equation 1.9 can be rewritten as:

$$\frac{d\mathbf{v}_{\perp}}{dt} = \frac{q}{m}(\mathbf{v}_{\perp} \times \mathbf{B}) \tag{1.15}$$

The time derivative of the parallel component equation is equal to zero (as $\mathbf{v}_{\parallel} \times \mathbf{B} = 0$). Therefore, the parallel velocity ($\mathbf{v}_{\parallel}$) is constant with time, while the perpendicular component experiences an acceleration that is perpendicular to both the current $\mathbf{v}_{\perp}$ and $\mathbf{B}$. As the kinetic energy of the particle is constant (Equation 1.14), the particle gyrates around a guiding centre, tracing a spiral. This motion is illustrated by Figure 1.1. The shape of the spiral will depend on the relative magnitudes of $\mathbf{v}_{\parallel}$ and $\mathbf{v}_{\perp}$ (i.e. the pitch angle: α).

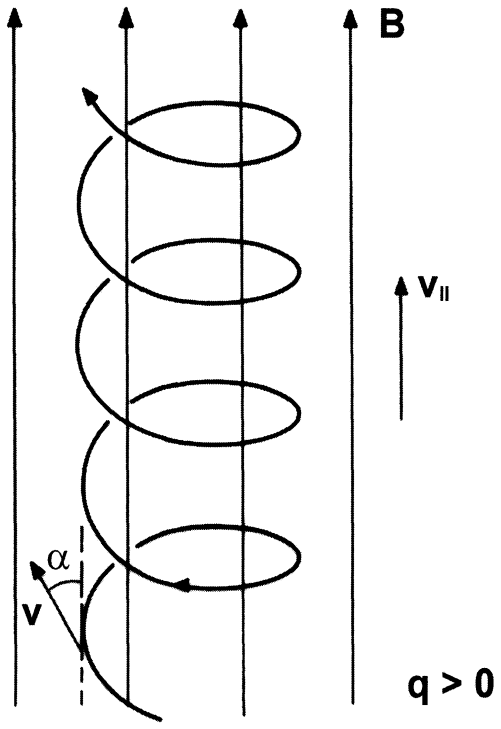

FIGURE 1.1: Schematic illustrating the gyration of a positive particle around the magnetic field. The pitch angle (α) is also shown [*Bittencourt*, 2004].

The angular frequency of the gyration will be given by:

$$\omega_g = \frac{|q|B}{m} \tag{1.16}$$

where ω_g is known as the gyrofrequency (or cyclotron/Larmor frequency). Due to the presence of the charge (q) in Equation 1.15, the direction of the gyration is dependent upon the sign of the particle's charge. The radius of gyration/Larmor radius (r_g) can also be calculated:

$$r_g = \frac{v_{\perp}}{\omega_g} = \frac{mv_{\perp}}{qB} \tag{1.17}$$

1.2.1.2 Adiabatic Invariants

Above, it was proven that the kinetic energy of the particle is constant (Equation 1.14), provided there are no electric fields present and the magnetic field changes slowly (such that $\mathbf{v} \cdot (\mathbf{v} \times \mathbf{B}) = 0$). Following this, the magnetic moment (μ), given by:

$$\mu = \frac{mv_{\perp}^2}{2B} = \frac{W_{\perp}}{B} \tag{1.18}$$

where $W_{\perp}$ is the kinetic energy of the perpendicular motion, must be conserved. When it is said that the magnetic field must change slowly for this to hold, it is meant that any change in magnetic field encountered over the course of a gyration must be small (i.e. any changes in B must be small within the timescale provided by the gyrofrequency). The magnetic moment (μ) is known as the first adiabatic invariant.

Consider a particle that moves (slowly compared to the gyrofrequency) from a region of low magnetic field strength (B_1) to a region where the field strength is greater (B_2), i.e. $B_1 < B_2$. As B increases, the perpendicular velocity ($v_{\perp}$) must increase in order to conserve μ. However, the total kinetic energy of the particle must remain constant ($W = W_{\perp} + W_{\parallel}$). Therefore, the parallel velocity of the particle must decrease. If B were to continually (and gradually) increase, then the parallel velocity of the particle will eventually drop to zero (and conversely $\mathbf{v} = \mathbf{v}_{\perp}$: $\alpha = 90°$). At this point the particle is reflected, 'mirrored', reversing direction along the field.

Using the conservation of the magnetic moment (Equation 1.18) it is possible to show that the field strength at which a particle (starting at field strength B_0 with a pitch angle of α) will reflect (B_M) is given by:

$$B_M = \frac{B_0}{sin^2\alpha} \tag{1.19}$$

Therefore, the mirror point is only dependent upon the pitch angle of the particle and the initial field strength (B_0), and not on the magnitude of the kinetic energy or charge of the particle. Magnetic mirroring is particularly important if the total field strength changes along the direction of the field, e.g. for a planetary dipole field. Such a system is shown in Figure 1.2, where the adjacent current carrying coils increase the magnetic field at either end of the system. This arrangement effectively traps particles between $-z_m$ and z_m, oscillating back and forth.

However, from Equation 1.19 it can be seen that as the pitch angle (α) decreases, the particle will only mirror at larger field strengths (i.e. B_M must be larger). For a given

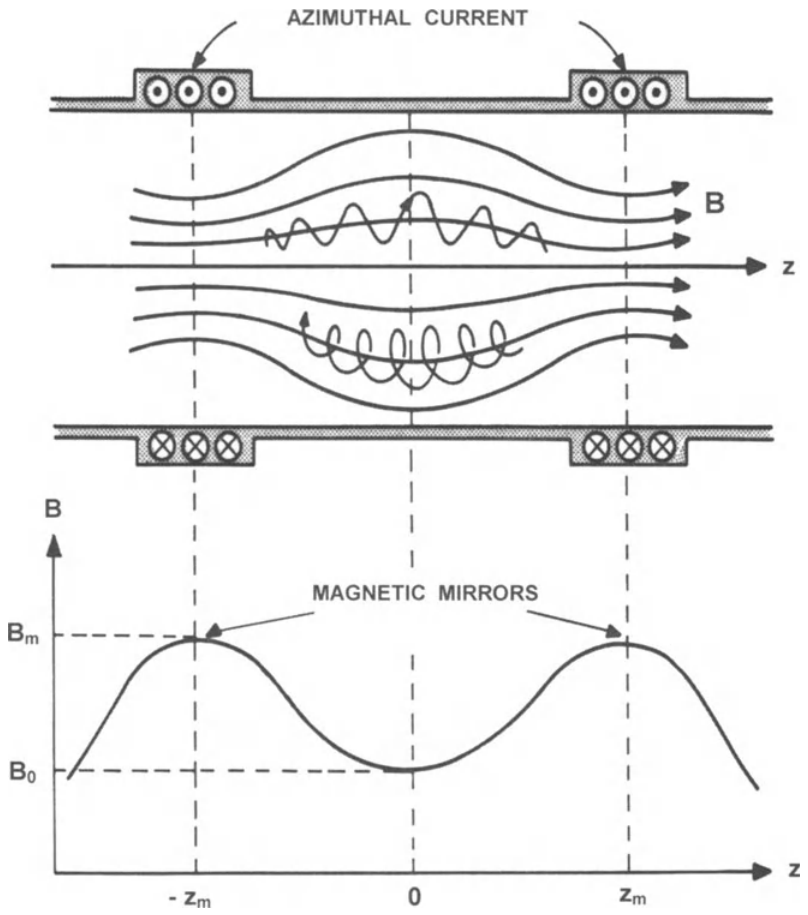

FIGURE 1.2: Schematic showing a magnetic bottle, with two adjacent coils forming magnetic mirrors [*Bittencourt*, 2004].

system, with a starting field B_0 and maximum field strength B_{max}, it is possible to calculate the minimum pitch angle that will reflect (α_{min}):

$$\alpha_{min} = sin^{-1}\left(\sqrt{\frac{B_0}{B_{max}}}\right) \tag{1.20}$$

The range of pitch angles given by $\alpha < \alpha_{min}$ are known as the loss cone, as particles with these pitch angles will not be reflected. In a planetary dipole the total field strength increases closer to the planet. Particles with large pitch angles will oscillate back and forth along the field lines and are trapped. At lower pitch angles the particles will mirror closer to the planet (where the field is stronger). If a particle's pitch angle is sufficiently small, and its mirror point is consequently close to the planet, then it will enter the atmosphere where it can collide with atmospheric particles (causing aurora) and be lost to the system.

In addition to magnetic mirroring, conservation of the first adiabatic invariant (the magnetic moment) can result in particle acceleration. If the magnetic field experienced by a particle varies with time, an increase in the field strength will result in a corresponding increase in the perpendicular velocity of the particle (and therefore energy). This is known as betatron acceleration, and it represents an important mechanism in magnetotail dynamics. Its occurrence and consequences in planetary magnetotails will be discussed in Section 1.4.3, as well as Chapters 7 and 8.

The second adiabatic invariant, **J**, is known as the longitudinal invariant and applies to particles trapped between two mirror points:

$$\mathbf{J} = m \oint v_{\parallel} ds \tag{1.21}$$

where ds is an element of the path followed by the particle, and the integral is over the full oscillation of the particle between the mirror points. For **J** to be conserved the timescales of any changes in the field must be long compared to the bounce period of the particle between the two mirror points. A direct consequence of the conservation of the second adiabatic invariant is a phenomenon known as Fermi acceleration. If the distance between the mirror points decreases, $\mathbf{v}_{\parallel}$ must increase to compensate. As with betatron acceleration, the process will be further discussed in the context of Saturn's dynamics in Section 1.4.3 and Chapters 7 and 8.

Finally, the third adiabatic invariant, Φ, is known as the drift invariant:

$$\Phi = \frac{2\pi m \mu}{q^2} \tag{1.22}$$

Physically, Φ corresponds to the conservation of magnetic flux enclosed by a particle performing a periodic orbit in an axisymmetric field (e.g. a planetary dipole field). In the case of a planetary dipole field there is a gradient in field strength perpendicular to the field, such that as a particle gyrates it periodically encounters a region of stronger field. The invariant is conserved if the field varies slowly relative to the drift motion of the particle (e.g. in an drift orbit around a planet).

In general, all three adiabatic invariants are conserved so long as the field variations experienced by the particle are much slower than the relevant oscillation: the gyration time, the bounce period, or the drift period respectively. It is also worth noting that sharp spatial gradients in the magnetic field are also capable of causing the invariants to be violated e.g. large changes within the gyroradius of a particle. The three types of

particle motion relevant for consideration of the adiabatic invariants are illustrated in Figure 1.3.

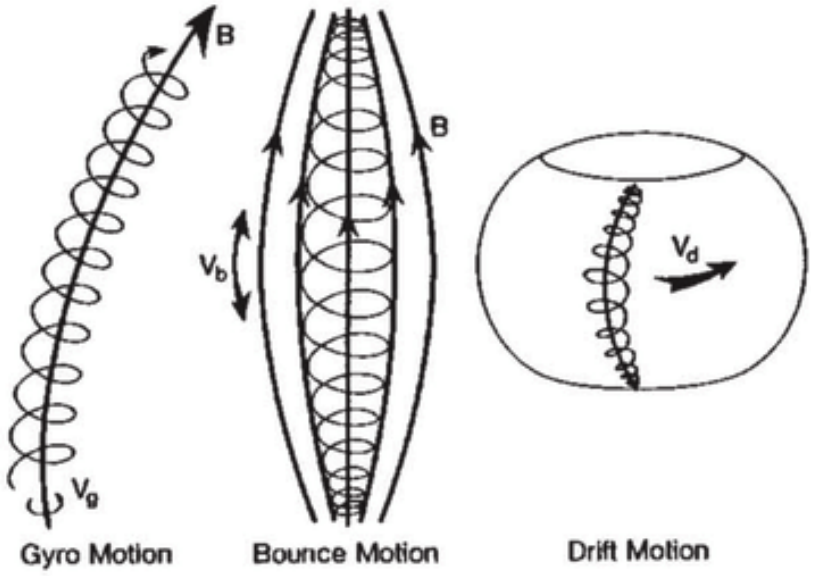

FIGURE 1.3: Schematic showing types of particle motion in a magnetic field. Adapted from *Kivelson and Russell* [1995].

1.2.1.3 Introducing Electric Fields

We now consider the application of an external electric field. If there is a non-zero component of the electric field in the direction of the magnetic field, i.e. such that $\mathbf{E} \cdot \hat{\mathbf{B}} \neq 0$, then the parallel component of Equation 1.9 can be rewritten as:

$$\frac{d\mathbf{v}_{\parallel}}{dt} = \frac{q}{m}\mathbf{E} \tag{1.23}$$

and so, there is now a non-zero acceleration in the field aligned direction. The direction of this acceleration is dependent upon the sign of the charge of the particle (q). Therefore, the application of the electric field will result in charge separation. This charge separation will induce an electric field which can build to the point at which it will completely negate the external electric field, resulting in no further parallel acceleration.

In the direction perpendicular to the field, the situation is more complicated. In this plane the electrons and positively charged ions will gyrate in opposing directions. A perpendicular electric field (i.e. $\mathbf{E} \times \hat{\mathbf{B}} \neq 0$) will accelerate the electrons and ions during a part of their respective gyration, and decelerate them during the other part. During the accelerating portion of their gyration the radius of curvature will increase, while it will be reduced during the deceleration phase: the result is a distorted orbit during

which the guiding centre will move: there will be a net displacement. This is illustrated by Figure 1.4. This drift is known as the $\mathbf{E} \times \mathbf{B}$ drift, and can be calculated using:

$$\mathbf{V}_D = \frac{\mathbf{E} \times \mathbf{B}}{B^2} \tag{1.24}$$

It should be noted that the drift velocity ($\mathbf{V}_D$) is independent of both the charge and mass of the particles (q and m), and therefore electrons and ions will drift in the same direction, with the same speed ($\mathbf{V}_D$ or $\mathbf{u}$ in Figure 1.4).

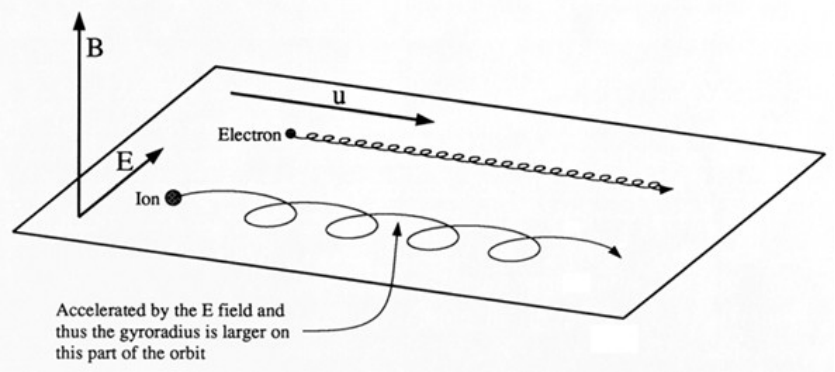

FIGURE 1.4: Schematic illustrating the drift motions of ions and electrons in the presence of perpendicular electric ($\mathbf{E}$) and magnetic ($\mathbf{B}$) fields [*Kivelson and Russell*, 1995].

1.2.2 Magnetohydrodynamics

The physics above, while sufficient for the consideration of a single particle does not account for the collective motion of a plasma, or fields that are time variable. To more fully describe the collective motion we can consider the plasma as a charged (conducting) fluid using Magnetohydrodynamics (MHD). As a fluid the plasma is governed by the conservation laws for mass, momentum and energy. These conservation laws lead to the general equation of motion of an element of a quasi-neutral plasma:

$$\rho \frac{d\mathbf{V}}{dt} = \rho \mathbf{g} - \nabla P + \mathbf{j} \times \mathbf{B} \tag{1.25}$$

where ρ is the mass density in the element of plasma, $\mathbf{V}$ is the mass-weighted average velocity of ions and electrons, $\mathbf{g}$ is the acceleration due to gravity, P is the pressure, and $\mathbf{j}$ and $\mathbf{B}$ are the current density and magnetic field. The force due to the magnetic field can be seen to be provided by the $\mathbf{j} \times \mathbf{B}$ term on the right hand side. Applying Ampere's law (Equation 1.8) in low frequency situations allows the derivation:

$$\mathbf{j} \times \mathbf{B} = \frac{1}{\mu_0}(\nabla \times \mathbf{B}) \times \mathbf{B} = -\frac{\nabla \mathbf{B}^2}{2\mu_0} + \frac{(\mathbf{B} \cdot \nabla)\mathbf{B}}{\mu_0} \tag{1.26}$$

The negative gradient present in the first term can be interpreted as the magnetic pressure:

$$P_B = \frac{B^2}{2\mu_0} \tag{1.27}$$

Meanwhile, the second term acts to reduce the curvature of magnetic field lines, and is often known as the magnetic tension force. This force acts towards the centre of curvature of a field line (of radius R_c):

$$F_T = -\frac{B^2}{\mu_0}\frac{\hat{\mathbf{R}}_\mathbf{c}}{R_c} \tag{1.28}$$

In effect, the magnetic field acts like a rubber band, attempting to straighten under the action of the tension force.

1.2.3 The Frozen-In Approximation

In addition to the equation of motion shown above, it is possible to derive a generalised form of Ohm's law:

$$\mathbf{j} = \sigma(\mathbf{E} + \mathbf{v} \times \mathbf{B}) \tag{1.29}$$

where σ represents the conductivity of the plasma, in turn given by:

$$\sigma = \frac{n_e e^2}{m_e v_c} \tag{1.30}$$

where v_c is the collision frequency (between ions and electrons). Combining this with Equations 1.7 and 1.8 (neglecting the contribution of the displacement current: $\frac{\partial \mathbf{E}}{\partial t} = 0$) allows the derivation of the induction equation:

$$\frac{\partial \mathbf{B}}{\partial t} = \nabla \times (\mathbf{v} \times \mathbf{B}) + \frac{1}{\mu_0 \sigma}\nabla^2 \mathbf{B} \tag{1.31}$$

which describes how the magnetic field ($\mathbf{B}$) varies with time. The first term on the right hand side is called the convective (or transport) term, while the second term is known

as the diffusive term. It can be useful to consider which of the terms in Equation 1.31 is dominant, i.e. whether the evolution of the field is predominantly convective or diffusive. This can be evaluated using the ratio of one term to the other, a quantity known as the Reynolds number:

$$R_m = \frac{|\nabla \times (\mathbf{v} \times \mathbf{B})|}{|\nabla^2 \mathbf{B}/_{\mu_0 \sigma}|} = \frac{{}^{vB}/_{L}}{{}^{B}/_{\mu_0 \sigma L^2}} = \mu_0 \sigma v L \tag{1.32}$$

where v is the characteristic velocity of the plasma and L is the length scale of variations. If the Reynolds number is $>> 1$ then the transport (or convective) term dominates. If this is the case, then the plasma and the magnetic field are *frozen-in*: the magnetic field is tied to the motion of the plasma, and vice versa. This is known as the convective limit. The solar wind, associated with very large length scales, is a good example of the convective regime with a Reynolds number of $\sim 10^{16}$ [*Baumjohann and Treumann*, 2012].

Alternatively, if the plasma is at rest then $\mathbf{v} = 0$, and the first term of Equation 1.31 would disappear. This would leave a diffusion equation, and the Reynolds number would be zero. In general, the Reynolds number is low (and the plasma diffusive) if the conductivity is low or if there are very small spatial scales present.

For the most part space plasmas are characterized by very high conductivities (due to very low v_c) and very large length scales: therefore the Reynolds number is large, and the plasma and field are *frozen-in*. This approximation notably breaks down in some situations, which can lead to a process called magnetic reconnection (discussion of which will follow in Section 1.2.3).

Finally, while the *frozen-in* approximation is valid, it is often important to know whether the magnetic field is following the motion of the plasma (or vice versa). For this purpose the ratio of thermal and magnetic pressures (known as the plasma beta) can be used:

$$\beta = \frac{P_{th}}{P_B} = \frac{n k_b T}{{}^{B^2}/_{2\mu_0}} \tag{1.33}$$

where P_{th} and P_B are the thermal and magnetic pressure (from Equation 1.27) respectively and n is the number density of the plasma. If the thermal pressure is large (e.g. n and T are very high), then $\beta >> 1$, and the field will follow the motion of the plasma. On the other hand if the magnetic field is very strong, then $\beta << 1$ and the plasma will follow the motion of the field.

1.2.4 Magnetic Reconnection

Magnetic reconnection is a fundamental physical process in space plasma physics; it describes the explosive reconfiguration of the magnetic field [*Parker*, 1957; *Sweet*, 1958; *Petschek*, 1964]. It is also notably a process during which the *frozen-in* approximation breaks down. Below, we will consider a simplified two-dimensional picture of reconnection.

Consider a current sheet that separates two distinct magnetic regimes, such as shown by Figure 1.5a, where the current is directed into the plane of the page. Magnetic and plasma pressure will compress the current sheet (represented by the shaded region). As the length scale of the current sheet decreases, so will the Reynolds number (Equation 1.32), and so the diffusive term of Equation 1.31 will dominate. This dominance breaks the *frozen-in* conditions, and means that the **B** field will diffuse from high to low field strength regions, i.e. towards the centre of the current sheet (as shown in Figure 1.5b). The region within which the *frozen-in* approximation is broken is known as the diffusion region. A minimum in the magnetic field is located at the centre of the X-type configuration, known as a magnetic neutral point or x-line (when extended to three dimensions). The X-shape that passes through the neutral point is called the separatrix.

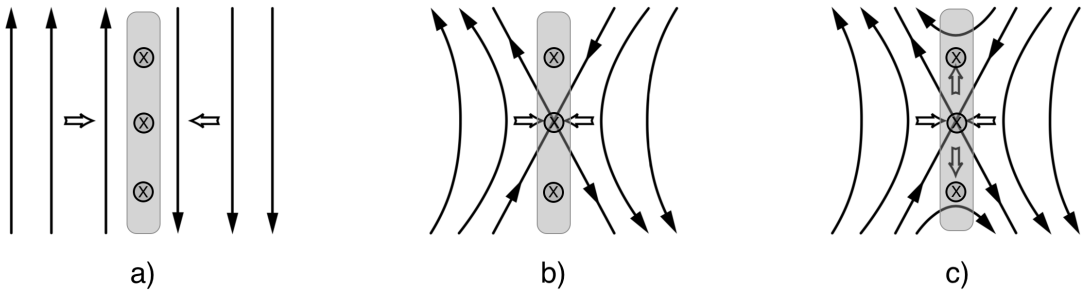

FIGURE 1.5: Schematic showing the reconnection process acting to rearrange the magnetic field from two magnetic regimes. The shaded grey region shows a current sheet within which the current flows into the page. The thick black lines indicate the magnetic field while the hollow arrows indicate the motion of the field and associated plasma. Adapted from *Baumjohann and Treumann* [2012]

The field lines within the diffusion region can reconfigure, before being ejected from the diffusion region under the effects of magnetic tension (as shown in Figure 1.5c). The reconnection site is often termed the 'x-line' due to the shape of the field lines that are undergoing the process. If a spacecraft is located either side of the reconnection site it may encounter the outflowing plasma or newly reconfigured magnetic field. This concept is fundamental for this thesis, and will be discussed in more detail in Section 1.4, and in the context of Mercury and Saturn in Sections 2.2.4 and 2.2.5 respectively.

Overall, reconnection allows the interconnection of two distinct magnetic regimes, and can allow the mixing of plasma. It also transfers energy from the magnetic field to the local plasma. Reconnection is a very small scale process, and as such the diffusion region is rarely directly observed by spacecraft [e.g. *Øieroset et al.*, 2001; *Eastwood et al.*, 2010], however it generates much larger products and flows that may be more commonly observed. These observations and products will be discussed in detail in Section 1.4.3.

1.3 The Sun and Heliosphere

The heliosphere is the region of space that is dominated by the influence of the Sun's magnetic field. The Sun is a main sequence star and is mainly composed of Hydrogen and Helium, with traces of heavier elements. The Sun's large mass ($1.99 \times 10^{30}\,kg$) causes huge gravitational pressures on its core, resulting in the fusion of Hydrogen and the release of huge quantities of energy, which heats the core to $15 \times 10^{6}\,K$. This heat is transported outwards towards the surface of the Sun, first through radiation and then through convection. The temperature of the Sun drops towards its visible surface, known as the photosphere, which is at a temperature of around $6000\,K$. Lying above the photosphere is the atmosphere of the Sun, called the corona. For reasons that are as yet unclear, the corona is many times hotter than the photosphere at over $1 \times 10^{6}\,K$.

1.3.1 The Solar Wind

The high temperature of the corona results in a gas pressure of $\sim 10^{-5}\,Pa$, orders of magnitude greater than the pressure of interstellar space ($\sim 10^{-13}\,Pa$). This pressure difference drives the coronal plasma outward from the surface, forming a continuous radial stream known as the solar wind [*Parker*, 1958]. The solar wind accelerates within the first few solar radii of travel to $\sim 400 - 800\,kms^{-1}$. After this point, as it expands through the solar system its velocity remains relatively constant, while its density drops as a consequence of its expanding volume ($n \propto {}^{1}/_{r^2}$).

Large scale convective motions within the Sun act as a dynamo to generate (to a first approximation) a dipolar magnetic field. The polarity of this field is observed to reverse every 11 years, forming the 22 year periodic solar cycle. The activity of the Sun varies over the course of this cycle, with its dynamics in particular varying significantly from solar maximum to solar minimum. For example, Sun spots are regions of intense magnetic field located on the photosphere. The number and location of sunspots varies over the course of the solar cycle; at the beginning of the cycle the sunspots are relatively rare, and start to appear in belts of activity at the mid-latitudes ($\pm \sim 30°$). As the

cycle progresses towards solar maximum sunspots appear in increasing numbers while the belts drift towards the equator as the magnetic field of the Sun becomes more disordered. In the declining phase of the cycle sunspots are mainly confined to the equatorial regions as their numbers decline. This pattern is shown in Figure 1.6.

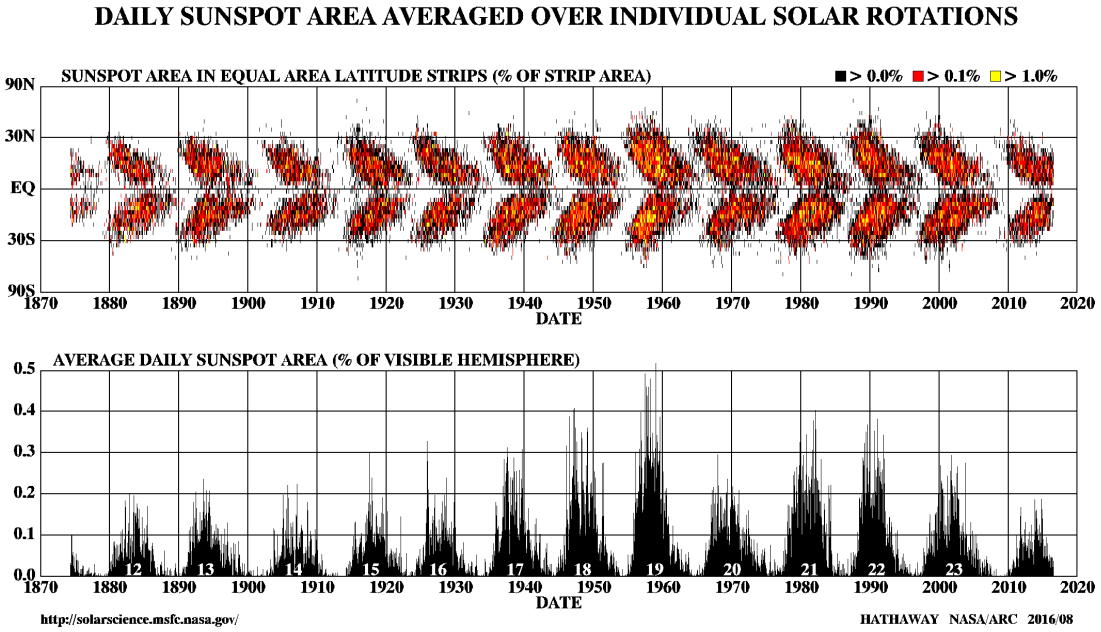

FIGURE 1.6: The latitudinal location of sunspots (top panel) and their total area (bottom panel) as a function of date [Courtesy of David Hathaway, NASA/MSFC].

Sunspots are particularly important as they are often linked with other transient solar phenomena, e.g. solar flares and Coronal Mass Ejections (CMEs). Solar flares are violent explosions on the surface of the Sun, generating huge amounts of radiation and accelerating electrons and protons into the solar system. CMEs meanwhile, are much larger phenomena: huge loops of plasma and magnetic field (that rival the size of the Sun) that are hurled into interplanetary space. As with sunspots, solar flares and CMEs are more common during solar maximum.

The high conductivity and large length scales ($\sim 10^9 m$) associated with the solar wind mean that the *frozen-in* theorem is satisfied (Equation 1.32), and as a direct result the radial outflow of the solar wind drags with it the magnetic field of the Sun. Once beyond the Sun the magnetic field becomes known as the Interplanetary Magnetic Field (or IMF), first observed by Pioneer V [*Coleman et al.*, 1960]. For typical solar wind conditions the plasma beta (Equation 1.33) is < 1, which would suggest that the plasma should follow the motion of the field. However, the plasma beta does not take into account the bulk motion of the solar wind, which in this case is sufficient to drag the magnetic field away from the Sun.

The motion of the solar wind can be generally approximated as radial, however as a parcel of plasma and field is ejected the Sun continues to rotate (with a period of $\sim$ 27 days at the equator) carrying with it the associated magnetic foot point. A magnetically linked parcel of plasma, released sometime after the first, will be slightly closer to the Sun and displaced longitudinally according to the solar rotation. This causes the magnetic field on a large scale to form a spiral, known as the 'Parker spiral' [*Parker*, 1958], shown by Figure 1.7. Close to the Sun the field will be almost radial, however as the plasma travels further through the solar system the field becomes more tightly coiled. For instance, by the orbit of Jupiter the angle between the field and the radial vector outward from the Sun is $\sim 80°$ [*Forsyth et al.*, 1996], while by Saturn's orbit the angle is $\sim 87°$ [*Jackman et al.*, 2008a]. It should be noted that the field will carry the opposite polarity in the northern and southern hemispheres. This necessitates, due to Ampere's law (Equation 1.8), an azimuthally extended current sheet around the heliospheric equator known as the Heliospheric Current Sheet (HCS).

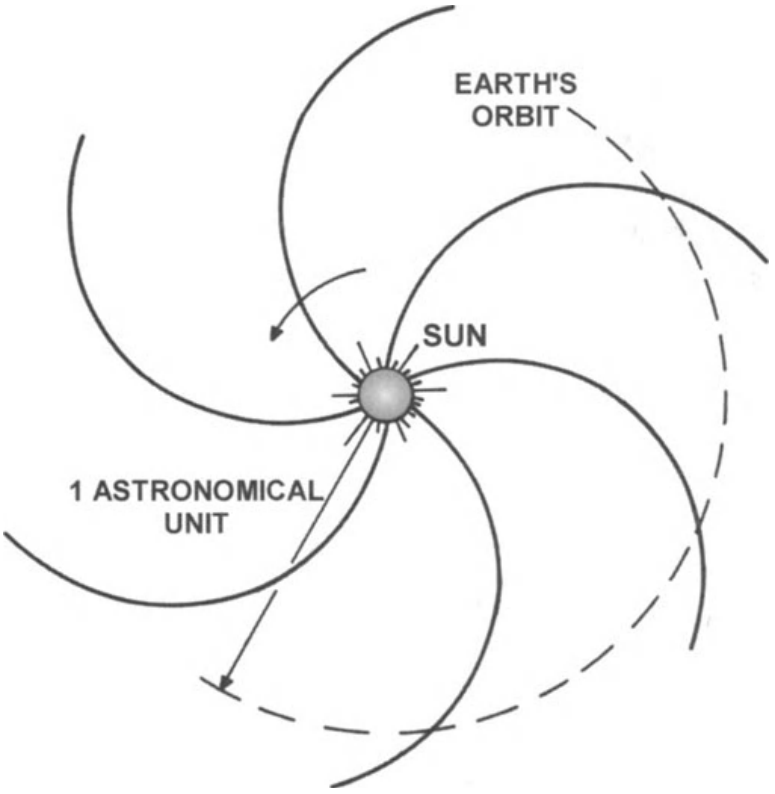

FIGURE 1.7: Schematic showing the Archimedean spiral of the IMF formed by the radial solar wind outflow and solar rotation [*Bittencourt*, 2004]

In general, the velocity of the solar wind can be described by a bimodal distribution. The slow solar wind ($\sim 400 km\, s^{-1}$) is denser and originates from the closed field, equatorial regions, while the fast solar wind ($\sim 800 km\, s^{-1}$) comes from open field regions (coronal holes), often located at higher solar latitudes. Fast solar wind can catch up to and

interact with slow solar wind, forming a large scale structure known as a Corotating Interaction Region (CIR) [e.g. *Gosling and Pizzo*, 1999; *Bothmer et al.*, 1999]. The structure will be preceded by a region of ambient, slow solar wind. This may be followed by a forward shock (if the fast solar wind speed is greater than the local sound speed), before compressed solar wind is encountered. This will then be followed by the high speed solar wind steam, which may be bounded by a reverse shock before a region of rarefaction is observed. A schematic of this configuration is shown in Figure 1.8.

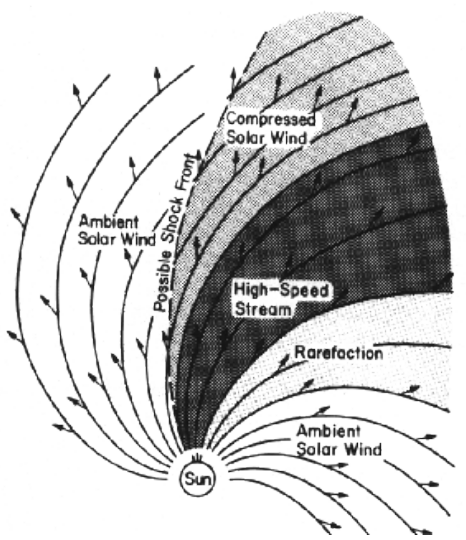

FIGURE 1.8: Schematic of the interaction between fast and slow solar wind, forming a corotating interaction region [*Hundhausen*, 1972].

1.4 Planetary Magnetospheres

Planets can be protected from the direct impact of the solar wind by their internally generated magnetic fields. As a direct consequence of the *frozen-in* theorem, and to a first approximation, the internal magnetic field and plasma of the planet and the IMF and solar wind plasma cannot mix. Therefore, the magnetic field of the planet produces a bubble, known as a magnetosphere.

1.4.1 Magnetospheric Structure

In the absence of any external factors this bubble would take the shape of a magnetic dipole, with field lines forming loops between the northern and southern magnetic poles (i.e. closed field). However, the impact of the solar wind has the effect of distorting the dipole magnetic field of the planet, compressing it on the dayside of the planet, while on the nightside it can stretch for large distances forming what is known as the magnetotail [*Wolfe et al.*, 1967].

The supersonic nature of the solar wind necessitates the presence of a shock between itself and any obstacle (i.e. a planetary magnetosphere). The bow shock forms upstream of the planet, separating the supersonic solar wind from the heated, subsonic magnetosheath plasma. The magnetopause boundary then separates the magnetosheath plasma from the magnetospheric plasma (or equivalently the IMF from the planetary magnetic field). A schematic of this configuration is shown in Figure 1.9.

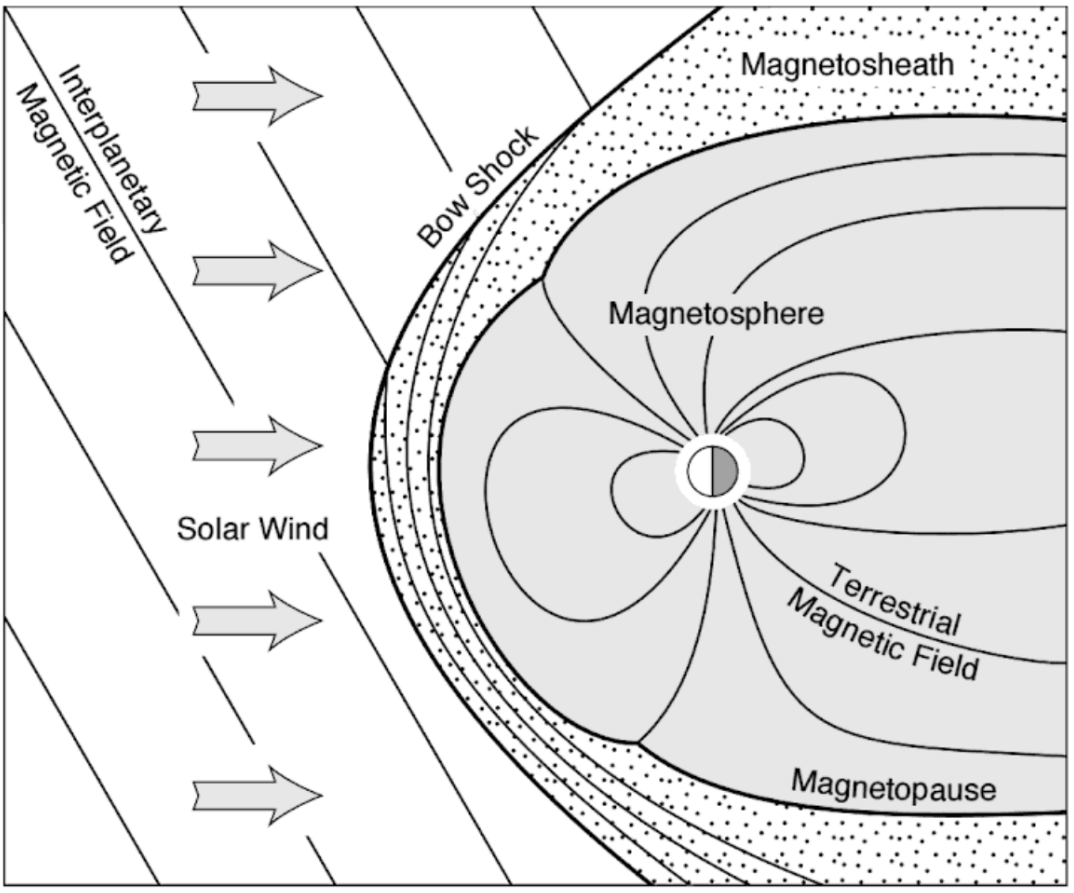

FIGURE 1.9: Schematic showing a cut through of the noon-midnight meridian of the Earth's magnetosphere. The Sun is off to the left, where it emits the solar wind and associated interplanetary magnetic field (IMF) [*Baumjohann and Treumann*, 2012].

The magnetopause boundary was first postulated by *Chapman and Ferraro* [1931], and the currents that flow along the magnetopause surface are named accordingly (Chapman-Ferraro currents). The currents are generated by the deflection of the incident solar wind plasma as it encounters the stronger planetary magnetic field, this decreases the gyroradii of the particles and deflects positive and negative particles in opposing directions.

At low latitudes a transient magnetopause boundary layer can form, containing a mixture of plasma from the magnetosheath and magnetosphere [*Eastman et al.*, 1976]. The processes that have been suggested to form the low latitude boundary layer (LLBL) include reconnection between the solar wind and magnetospheric field, and instabilities on

the magnetopause surface (e.g. Kelvin-Helmholtz vortices). A spacecraft encountering the LLBL may experience a change in plasma character and rotation of the magnetic field.

1.4.2 Magnetospheric Size

The general size of the magnetosphere is determined by the local pressure balance between the external (solar wind) and internal (magnetospheric) plasma and magnetic field pressures. The pressure balance can be described as:

$$P_{SW} + \frac{B_{SW}^2}{2\mu_0} = P_M + \frac{B_M^2}{2\mu_0} \tag{1.34}$$

where P_{SW} and P_M are the solar wind dynamic pressure and magnetospheric plasma pressure respectively, B_{SW} is the magnitude of the IMF and B_M is the magnetospheric field strength. The solar wind dynamic pressure (perpendicular to the subsolar point) can also be written as:

$$P_{SW} = 2\rho_{SW} v_{SW}^2 \tag{1.35}$$

where ρ_{SW} and v_{SW} are the density and velocity of the solar wind. The magnetic pressure in the solar wind is much lower than the dynamic pressure, and can therefore be neglected in the pressure balance equation leading to:

$$P_{SW} = P_M + \frac{B_M^2}{2\mu_0} \tag{1.36}$$

The magnetospheric field strength just inside of the magnetopause is enhanced by the presence of the Chapman-Ferraro currents, and can be approximated by:

$$B_M \sim 2B_{Dipole} \sim 2B_{Eq}\left(\frac{R_P}{R_M}\right)^3 \tag{1.37}$$

where B_{Dipole} is the dipole field strength at the location of the magnetopause, B_{Eq} is the equatorial magnetic field strength at the surface of the planet, and R_P and R_M are the radius of the planet and the magnetopause standoff distance respectively. Substituting into Equation 1.36 and rearranging results allows the formation of the magnetopause standoff distance (in units of planetary radii):

$$\frac{R_M}{R_P} = \left(\frac{B_{Eq}^2}{\mu_0(\rho_{SW} v_{SW}^2 - P_M)} \right)^{1/6} \tag{1.38}$$

In general, Equation 1.38 shows that the magnetopause standoff distance (R_M) will increase with a stronger internal field (B_{Eq}) or increased internal plasma pressure (P_M), and decrease with a faster (v_{SW}), or denser (ρ_{SW}) solar wind. For the Earth and Mercury, the internal plasma pressure (P_M) can be neglected, while at Saturn and Jupiter it is necessary to obtain an accurate estimation of the standoff distance. The magnetopause standoff distance will be discussed in more detail for Mercury and Saturn in Sections 2.2.2 and 2.3.2 respectively.

The dynamic pressure of the solar wind can vary on relatively short timescales ($\sim$ hours to days) due to transient events such as those discussed in Section 1.3 (e.g. CIRs and CMEs). It also varies with radial distance from the Sun due to the decreasing density of the solar wind, meaning its typical range is different for each of the solar system planets. Each planet also has a different strength dipole magnetic field, and may have significant sources of internal plasma pressure (e.g. Io at Jupiter and Enceladus at Saturn) which will contribute to Equation 1.38. The internal plasma pressure (P_M) has been found to have contributions from several sources at Saturn: from suprathermal water group ions [*Sergis et al.*, 2009], thermal electrons and from cold plasma [*Pilkington et al.*, 2015]. The relative sizes of four planetary magnetospheres are shown in Figure 1.10. The magnetospheres of Mercury and Saturn will be specifically discussed in Sections 2.2 and 2.3 respectively.

1.4.3 Magnetospheric Reconnection and Dynamics

Reconnection is a small-scale process, and the region within which it occurs, the diffusion region, is only rarely observed by *in situ* spacecraft. However, reconnection can significantly influence the global dynamics of the magnetosphere and also produce large magnetic structures, as will be discussed below.

Magnetic reconnection can occur both in the dayside magnetopause current layer and also within the magnetotail. At the subsolar dayside magnetopause, reconnection between the IMF and closed planetary magnetic field will have the effect of opening magnetospheric flux. This is where the magnetic field will now have one end connected to the planet and the other to the Sun. At the Earth, the polar caps are defined as the ionospheric regions threaded by open magnetic flux around the northern and southern magnetic poles. Newly opened magnetic flux will be carried across the polar caps of the

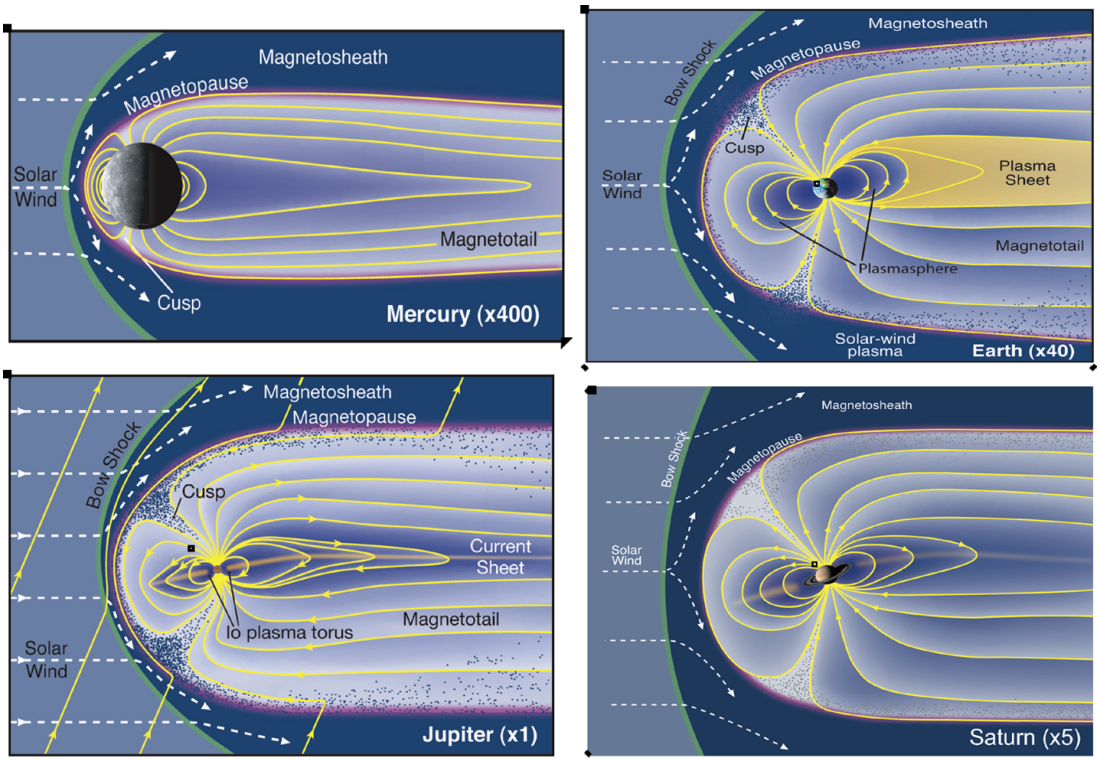

FIGURE 1.10: Schematic comparison of the magnetospheres of Mercury, Earth, Jupiter and Saturn. The Sun is off the left of the panels, with the solar wind therefore moving from left to right [Credit: Fran Bagenal and Steve Bartlett].

planet onto the nightside, where it forms the magnetotail lobes [*Ness*, 1965]. The magnetic fields of the northern and southern tail lobes are oppositely directed, necessitating the presence of a current sheet between the two. The current sheet is surrounded by a region known as the plasma sheet, which is typified by a much higher plasma β than the magnetotail lobes. The Hermean and Kronian plasma sheets are further discussed in Section 2.2 and 2.3 respectively.

The size of the polar cap (the region of open magnetic flux) is determined by the open flux content, and therefore the balance between dayside reconnection (of previously closed field), which acts to expand its area [*Milan et al.*, 2012], and nightside lobe reconnection, which shrinks the area of the polar cap [*Lockwood and Cowley*, 1992; *Milan et al.*, 2003, 2007]. This is known as the expanding-contracting polar cap paradigm (ECPC) [*Siscoe and Huang*, 1985; *Cowley and Lockwood*, 1992]. Studies have been performed to link the conditions in the solar wind (i.e. velocity and the clock angle and transverse component of the IMF) to the dayside reconnection rate, using the area [*Newell et al.*, 2007] and time derivative of the area of the polar cap [*Milan et al.*, 2012]. Similarly, the dayside reconnection rate has been parametrized as a function of the solar wind properties for Jupiter [*Nichols et al.*, 2006] and Saturn [*Jackman et al.*, 2004].

The rate of reconnection on the dayside magnetopause is dependent upon the variable conditions in the adjacent magnetosheath (and therefore the solar wind). At the Earth, high magnetic shear angles (between the IMF and planetary field) have been found to be favourable for the occurrence of reconnection [*Paschmann et al.*, 1979]. However, a high shear angle is not a sufficient condition to predict reconnection [e.g. *Paschmann et al.*, 1986]; high values of the magnetosheath plasma β ($\gtrsim 2$) will inhibit magnetopause reconnection [*Sonnerup*, 1974; *Scurry et al.*, 1994]. Later, *Swisdak et al.* [2003] linked these factors to the diamagnetic suppression of reconnection. The implications of this will be discussed in Sections 2.2 and 2.3 with respect to the interaction between the solar wind and the Hermean and Kronian magnetospheres.

On the nightside of the planet reconnection can occur in the magnetotail current sheet. In principle the reconnection can involve closed or open (i.e. lobe) magnetic field. An important process in the onset of magnetotail reconnection is the thinning of the current sheet. From terrestrial observations and simulations, a thickness of $\sim$ one ion inertial length (or smaller) is required to trigger significant reconnection [e.g. *Sergeev et al.*, 1993; *Birn and Schindler*, 2002; *Baumjohann et al.*, 2007; *Snekvik et al.*, 2012]. The thin current sheet is thought to be susceptible to tearing mode [e.g. *Schindler*, 1974] or other smaller scale kinetic instabilities [*Baumjohann et al.*, 2007]. The instabilities are suppressed by the normal component of the magnetic field, and so this must also reduce to initiate reconnection [*Birn and Schindler*, 2002; *Milan et al.*, 2009]. Therefore, a potential cause of magnetotail reconnection is the presence of an internal mechanism that can act to stretch the magnetic field; this is particularly important in the magnetotail of Saturn, and will be discussed in detail in below. The nature of the flux involved in magnetotail reconnection (i.e. open or closed) is an important question at Saturn, and will be discussed in more detail in Section 2.3.4 and further in science chapters 4, 7 and 8.

At the Earth, an increase in lobe magnetic flux (as a result of low latitude dayside reconnection) causes the magnetotail to flare outwards. This increases the cross-sectional area of the magnetotail as seen by the incident solar wind, resulting in a higher lobe magnetic pressure. The increased lobe pressure is exerted on the magnetotail current sheet, which eventually results in reconnection acting to close the open flux. How long the open flux can be stored in the lobes, and the nature of the reconnection trigger is a contested topic [e.g. *Henderson et al.*, 1996; *Lyons et al.*, 1997; *Cheng*, 2004, and references therein]. Perhaps up to half of terrestrial reconnection events can be explained by sudden changes in the solar wind [*Lyons et al.*, 1997; *Milan et al.*, 2007; *Hsu and McPherron*, 2004], though statistical studies have since suggested that the link with sudden changes in the IMF orientation may not be as significant as first thought [*Freeman and Morley*, 2009; *Newell and Liou*, 2011]. Nevertheless, solar wind shocks

have been unambiguously linked with individual instances of magnetotail reconnection [*Boudouridis et al.*, 2004; *Milan et al.*, 2004; *Hubert et al.*, 2006]. Solar wind driving will be discussed for the Hermean and Kronian magnetospheres in Section 2.2 and 2.3 respectively. Solar wind loading at Mercury will also be discussed in Chapter 6.

1.4.3.1 Global Convection Cycles

Reconnection on the magnetopause and in the magnetotail can form a global cycle of field and plasma convection, first proposed by (and named for) *Dungey* [1961]. Figure 1.11 shows a schematic describing the Dungey cycle for the case of the Earth. The incident IMF (1) opens magnetospheric field and then convects over the polar cap (2-4), forming the magnetotail lobes (5). The stretched lobe field can then reconnect at the magnetotail current sheet (6), allowing the closed field to shrink back towards the planet (7). The recently closed field (8) then convects around the flanks of the magnetosphere back to the dayside (9). In this cycle, magnetospheric flux is opened and later closed, while mass can be introduced to the magnetosphere from the solar wind and then subsequently lost down the magnetotail. This cycle is particularly significant at the Earth and Mercury, where it is the dominant driver of magnetospheric dynamics. The Dungey cycle will be discussed with regard to Mercury and Saturn in Sections 2.2 and 2.3.

This cycle can also be considered in terms of energy. Energy is added to the magnetosphere through interactions with the solar wind on the dayside of the planet. The energy builds and is stored in the magnetotail lobes until it is released at a reconnection site or neutral line within the magnetotail. This is often referred to as the near earth-neutral line model [e.g. *Baker et al.*, 1996], where the neutral line lies relatively close to the planet, much closer than the distant tail neutral line, which is classically found beyond the last closed field line.

The convection due to the solar wind interaction (i.e. the Dungey cycle) will depend strongly on the solar wind conditions (and rate of magnetopause reconnection). In the magnetotail the returning Dungey cycle plasma flows ($\mathbf{V}_{Conv}$) are directed planetward, and can equivalently be considered as a cross-tail electric field:

$$\mathbf{E}_{Conv} = -\mathbf{V}_{Conv} \times \mathbf{B} \tag{1.39}$$

where $\mathbf{B}$ is the local magnetic field. At Earth, the cross tail electric field ($|\mathbf{E}_{Conv}|$) has been found to be $\sim 10 - 20\%$ of the electric field found in the incident solar wind. In other words, magnetopause reconnection consumes $\sim 10 - 20\%$ of the incident magnetic energy in the solar wind. The local magnetic field ($\mathbf{B}$) depends upon the radial distance

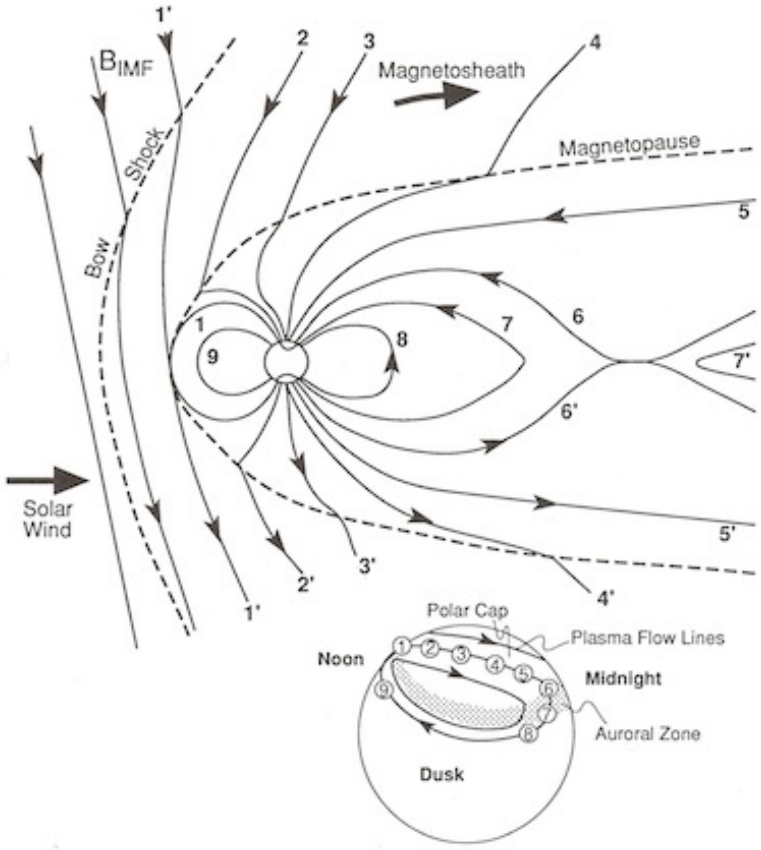

FIGURE 1.11: A schematic showing the stages of the Dungey cycle [*Kivelson and Russell*, 1995].

from the planet and, approximating the field as a dipole, the convection velocity can be rewritten as:

$$|\mathbf{V}_{Conv}| = \frac{|\mathbf{E}_{Conv}|}{\mathbf{B_{Eq}}} \left(\frac{r}{R_P}\right)^3 \tag{1.40}$$

where $|\mathbf{B_{Eq}}|$ is the magnitude of the planet's magnetic field at the equator of the planet. $\mathbf{V}_{Conv}$ therefore becomes much more significant at larger radial distances (scaling with r^3), but will also be dependent upon the electric field within the solar wind (and magnetopause reconnection).

Another source of magnetospheric convection is the rotation of the planet. For the solar system planets with a conducting ionosphere, collisions between the (rotating) neutral atmosphere and the plasma of the lower ionosphere will transfer a torque to the magnetic field. This torque is then communicated to the magnetospheric plasma through field aligned currents. In order to rotate with the planet, the strict corotational velocity ($\mathbf{V}_{Corot}$) of the plasma will increase with radial distance (r) from the planet:

$$|\mathbf{V}_{Corot}| = r\omega_P \tag{1.41}$$

where ω_P is the angular velocity of the planet. Close to the planet, it may be expected that corotational convection will dominate, provided ω_P is sufficiently large, due to strength of the local field. At larger radial distances however, solar wind induced convection will dominate. For each planet there will be a distance at which the two convection systems cancel: this is known as the stagnation point. Figure 1.12 illustrates the expected flow patterns and stagnation points for Mercury, Earth, Jupiter and Saturn. These depend on the average solar wind conditions at the heliocentric distance of the planet, and the internal field and rotation rates of the planets.

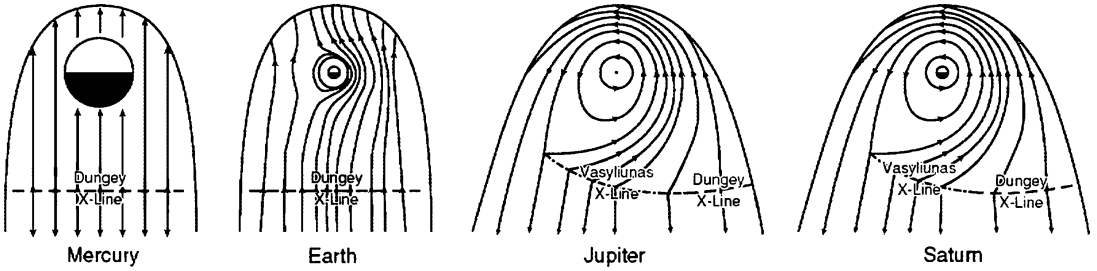

FIGURE 1.12: Magnetospheric flow schematics for Mercury, Earth, Jupiter and Saturn [*Jackman et al.*, 2014a].

Mercury is located relatively close to the Sun and possesses a very slow rotation rate, and thus in Figure 1.12 the convection can be dominated by by the Dungey cycle. At the Earth, with average solar wind conditions, the stagnation point is located $\sim 4\,R_E$ from the planet (well within an average magnetopause standoff distance of $\sim 9\,R_E$). The size of this region will expand and contract with the changing solar wind conditions.

From Equations 1.40 and 1.41, it can be seen that if a planet possesses both a large internal field (i.e. large B_{Eq}) and a fast rotation rate (high ω_P) then corotation convection will be relatively dominant. This is the case at Jupiter and Saturn, where the calculated values of the stagnation points generally exceed the average magnetopause standoff distance.

Both Jupiter and Saturn rotate relatively quickly and also possess significant mass sources within their inner magnetospheres: the moons Io and Enceladus respectively. These factors combine to result in the Vasyliunas cycle [*Vasyliunas*, 1983], sketched in Figure 1.13. As the mass-loaded flux tubes rotate around the dusk flank they are no longer supported by the magnetopause and so begin to stretch down the magnetotail (1-2). Eventually the current sheet has thinned such that reconnection can occur (3), allowing the closed field to return towards the planet and releasing mass down the magnetotail. The Vasyliunas cycle involves the reconnection of closed field, and as such

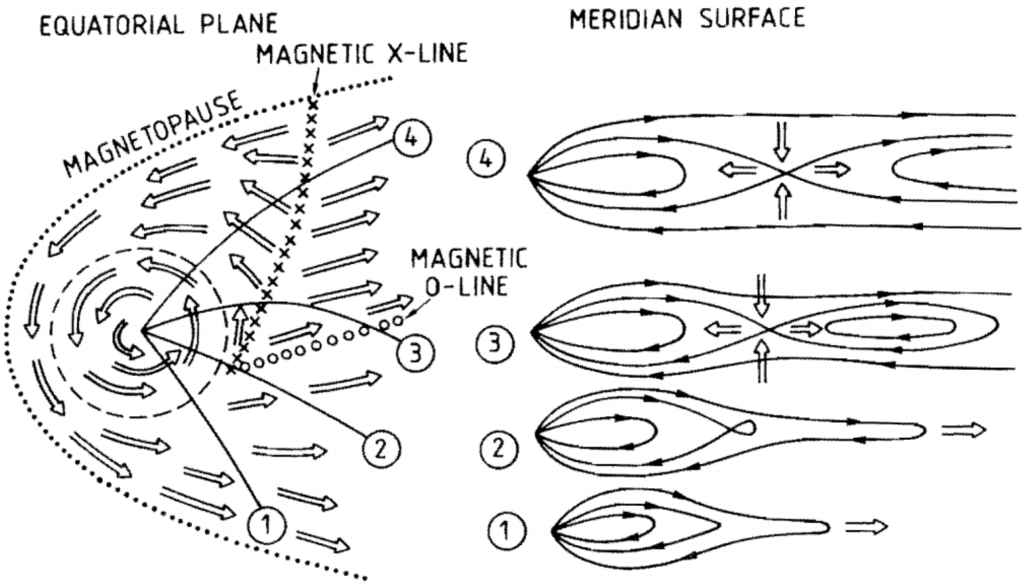

FIGURE 1.13: A qualitative sketch of the convection associated with the Vasyliunas cycle in the equatorial plane (left) and the noon-midnight meridian (right) [*Vasyliunas*, 1983].

does not change the flux contained within the magnetosphere. This signatures and consequences of Vasyliunas style reconnection will be discussed in Section 2.3.

1.4.3.2 Reconnection Products

As detailed above, the small-scale process of reconnection is fundamentally important for magnetospheric dynamics. Though direct observations by spacecraft are rare, reconnection generates large scale magnetic products that may be encountered by spacecraft. These will be discussed below.

1.4.3.3 Magnetopause Reconnection Products

Globally, magnetopause reconnection can result in the generation of open magnetic field. Flux transfer events (FTEs) are a non-local signature of this process occurring [e.g. *Russell and Elphic*, 1978]. FTEs are helical magnetic structures that display a strong core field and a clear field rotation as they pass over a spacecraft. The structures are either thought to be generated as a result of a narrow tube of reconnected flux [*Russell and Elphic*, 1978], patchy reconnection on the magnetopause surface [*Southwood et al.*, 1988; *Scholer*, 1988] or between multiple adjacent x-lines [*Lee and Fu*, 1985]. FTEs are not studied within this thesis, however this brief introduction has been included for the purposes of later comparison with magnetic structures observed within the magnetotail.

It is also possible that reconnection can occur, for certain IMF clock angles, between the IMF and the open lobe magnetic flux (tailward of the cusp) [*Dungey*, 1963; *Russell*, 1972; *Gosling et al.*, 1991; *Kessel et al.*, 1996; *Milan et al.*, 2000]. In this scenario no new magnetic flux has been opened, but the topology of the field has been changed.

1.4.3.4 Magnetotail Reconnection Products

Reconnection on the nightside of a planet will result in planetward and tailward moving jets of plasma and magnetic structures. This reconnection can form part of a larger cycle, involving open lobe field [e.g. *Dungey*, 1961] or closed magnetospheric flux [e.g. *Vasyliunas*, 1983].

Planetward of a reconnection site the newly reconnected field will contract towards the planet under the influence of magnetic tension forces. At Earth, the inflowing plasma population is often termed a bursty bulk flow [*Baumjohann et al.*, 1990; *Angelopoulos et al.*, 1992, 1994]. A sharp rotation of the magnetic field in the north-south direction can also be observed in conjunction with the inflow, and in the terrestrial environment this is known as a dipolarization front [e.g. *Nakamura et al.*, 2002; *Ohtani et al.*, 2004]. These signatures have also been observed at Mercury [e.g. *Sundberg et al.*, 2012a; *Sun et al.*, 2016], Jupiter [e.g. *Vogt et al.*, 2010; *Kasahara et al.*, 2011] and Saturn [e.g. *Bunce et al.*, 2005; *Jackman et al.*, 2015].

The dipolarization front, defined by the sharp field rotation, is approximately the thickness of the ion gyroradius [*Runov et al.*, 2009; *Deng et al.*, 2010; *Hwang et al.*, 2011], and often separates the ambient plasma sheet preceding the front from a hotter, more tenuous plasma population [*Runov et al.*, 2015]. The heated population is generated either by processes local to the reconnection site [*Ohtani et al.*, 2004; *Fu et al.*, 2017], or those active during the planetward propagation of the plasma. During the motion of the front adiabatic Fermi and betatron acceleration mechanisms (related to the conservation of the first and second adiabatic invariants: Section 1.2.1.2) will heat portions of the pitch angle distribution [*Ashour-Abdalla et al.*, 2011; *Birn et al.*, 2014; *Pan et al.*, 2014a,b; *Gabrielse et al.*, 2017]. Additional non-adiabatic wave-particle interactions will also heat the plasma [*Deng et al.*, 2010; *Huang et al.*, 2012, 2015; *Grigorenko et al.*, 2017]. This heating will be further explored in Chapters 7 and 8.

In two dimensions, the reconnection of oppositely directed fields at two or more points in a current sheet will result in the generation of magnetic islands (or loops) between the x-lines. The centre of each island is sometimes termed an 'o-line' (on account of their elongated structure). This physical scenario is illustrated in Figure 1.14, where the 'x-' and 'o-lines' can be thought of as extending into and out of the plane of the page. The

magnetic islands can be subsequently ejected by the dominant x-line. If one of these loop-like structures were to pass over a spacecraft, the magnetometer would record a smooth rotation of the field in the north-south component of the field (corresponding to the change in field orientation between the leading and trailing hemispheres). The orientation of the field deflection will depend on the direction of propagation of the structure, and therefore allows the inference of the location of the dominant x-line relative to the spacecraft. The spacecraft will also record a minimum in the magnetic field strength in the centre of the structure (the magnetic o-line).

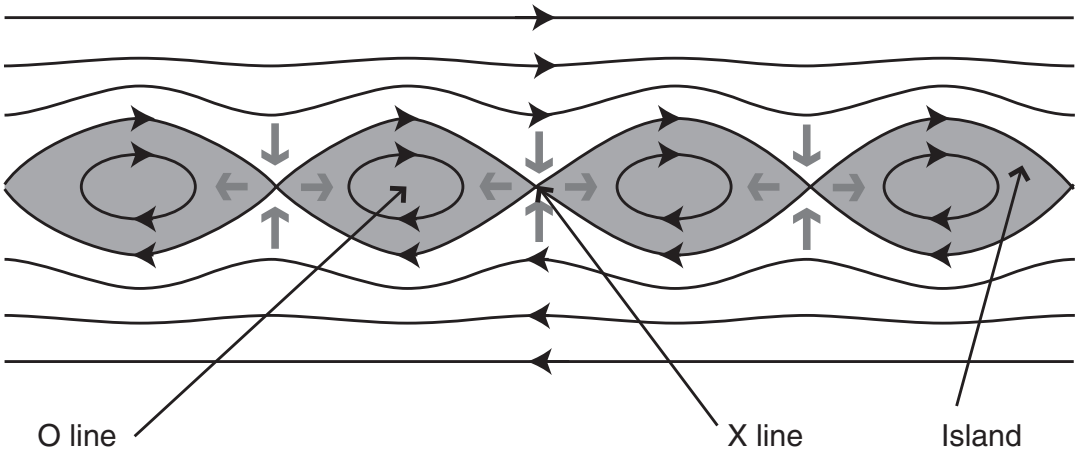

FIGURE 1.14: Schematic showing the result of a current sheet reconnecting at multiple locations, forming a series of magnetic islands. Adapted from *Eastwood and Kiehas* [2015].

In three dimensions, the presence of a magnetic shear will break the symmetry between the field above and below the current sheet: a field line above the sheet will not map to a field line beneath. In the extended x-line geometry this results in a more complex reconnection process and the generation of a three-dimensional, helical field structure known as a flux rope. A hypothetical spacecraft in the path of one of these structures will record a similar rotation of the north-south component of the magnetic field, however instead of a local minimum of the field strength at the centre, the spacecraft will observe a local maximum corresponding to the presence of a strong axially aligned field (into/out of the page in Figure 1.14).

The force free model is commonly used to evaluate the magnetic structure of flux ropes. It represents a relatively stable configuration where no pressure gradients are assumed to be present ($\nabla P = 0$). In this model the magnetic pressure ($^{B^2}/_{2\mu_0}$) from the strong axial field is balanced by the magnetic tension force ($^{B^2}/_{2\mu_0 R_c}$), where μ_0 is the magnetic permeability of free space and R_c is the radius of curvature of the helical field. This corresponds to the lowest energy state of helical magnetic fields, and is therefore perhaps the end point of the evolution of the flux rope morphology [*Priest*, 1990]. Under these

conditions *Lepping et al.* [1990] showed that, using the *Lundquist* [1950] solutions, the field inside the flux rope can be written in cylindrical coordinates as:

$$B_{axial} = B_0 J_0(\alpha r') \tag{1.42}$$

$$B_{azimuthal} = B_0 H J_1(\alpha r') \tag{1.43}$$

$$B_r = 0 \tag{1.44}$$

where B_0 is the peak axial field strength, $J_0(\alpha r')$ and $J_1(\alpha r')$ are the zeroth and first-order Bessel functions and H is the helicity or handedness of the flux rope ($H = \pm 1$). The Bessel functions depend on the radial distance from the axis of the flux rope (r') and α. With α set to 2.4048 [*Burlaga*, 1988], and setting the impact parameter: $r' = r/R_0$ (with R_0 being the radius of the flux rope) the model represents a flux rope with a completely axial field at the centre ($B_{azimuthal}(r = 0) = 0$) and an entirely azimuthal field at the edge ($B_{axial}(r = R_0) = 0$). This formulation represents a cylindrically symmetric, linear (constant-α) force free flux rope. The model has been successfully applied to interplanetary magnetic clouds [*Lepping et al.*, 1990], FTEs at the magnetopause of Earth [*Eastwood et al.*, 2012a], Saturn [*Jasinski et al.*, 2016] and Mercury [*Imber et al.*, 2014] as well as flux ropes in the magnetotails of Earth [*Lepping et al.*, 1995, 1996; *Slavin et al.*, 2003a,b], Mars [*Eastwood et al.*, 2012b] and Mercury [*DiBraccio et al.*, 2015].

Finally, as these magnetic structures travel through the plasma sheet they create a local bulge. This bulge compresses the adjacent lobe magnetic field, creating a detectable compression and rotation of the field termed a Travelling Compression Region (or TCR). The spacecraft will record a similar field rotation to that of the loops and flux ropes described above, however it will be accompanied by a modest but smooth increase in field magnitude (of between 1 and 10% at the Earth [*Slavin et al.*, 1984, 1993, 2005]).

These three distinct scenarios, and the resulting magnetic field signatures in a planetary magnetotail (with the north-south field component and total field magnitude) are displayed in Figure 1.15. It should be noted that the term plasmoid was originally reserved for the magnetic island formed between the most distant tail x-line and the near-Earth x-line [e.g. *Hones*, 1977; *Baker et al.*, 1996] i.e., the region of plasma sheet pinched off by tail reconnection. However, the term plasmoid is often used to encompass both structures containing a core field (i.e. flux ropes) [e.g. *Moldwin and Hughes*, 1991] and those with a loop-like structure [e.g. *Ieda et al.*, 1998].

The magnetic field signature recorded by an *in situ* spacecraft does not solely depend upon the type of structure incident (e.g. flux rope or loop-like structure), but also upon

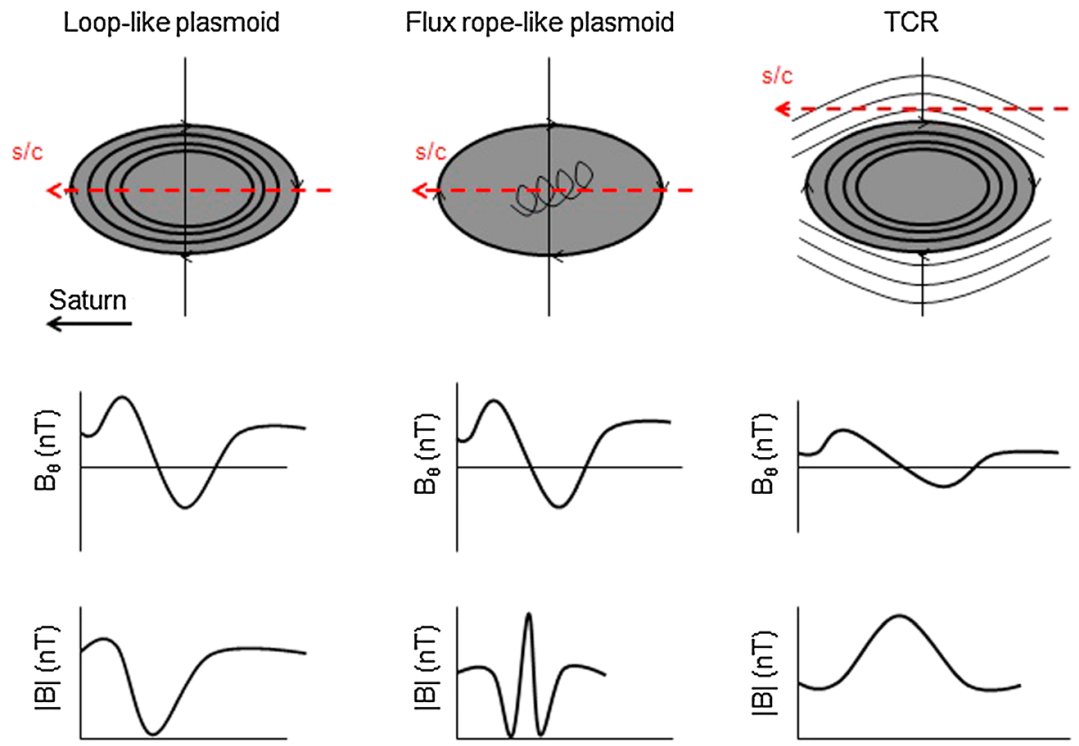

FIGURE 1.15: Schematic sketch of loop-like plasmoids, flux ropes and travelling compression regions (TCRs). Below, the signatures recorded by a spacecraft in the north-south meridional field component and total field magnitude are displayed [*Jackman et al.*, 2014b].

the relative trajectory of the spacecraft. This is shown for five different trajectories through flux ropes in Figure 1.16.

Historically, surveys of plasmoids and flux ropes in Earths magnetotail have been performed by visual inspection of spacecraft data [e.g. *Scholer et al.*, 1984; *Richardson et al.*, 1987; *Moldwin and Hughes*, 1992; *Ieda et al.*, 1998; *Slavin et al.*, 2003a]. Criteria based on the magnetic field and local plasma environment were developed and applied by eye to create self-consistent catalogues. Similarly, studies of plasmoids and flux ropes in the magnetotails of Mercury [*Slavin et al.*, 2009, 2012a; *DiBraccio et al.*, 2015; *Sun et al.*, 2016], Jupiter [*Vogt et al.*, 2010, 2014] and Saturn [*Jackman et al.*, 2011, 2014b] have been performed. Unlike at the Earth, where high-resolution plasma data are generally available, these studies have relied more heavily on the magnetometer data to identify these structures. Again, selection criteria were applied manually and each event processed individually. This has worked very well, however, it is hugely time consuming and difficult to keep the selection process completely consistent. Moreover, by eye selection has inherent biases as separate authors may well select different subsets of events.

Some studies have begun to introduce some degree of automation to the process of plasmoid identification, e.g., for locating periods when the north-south component of the

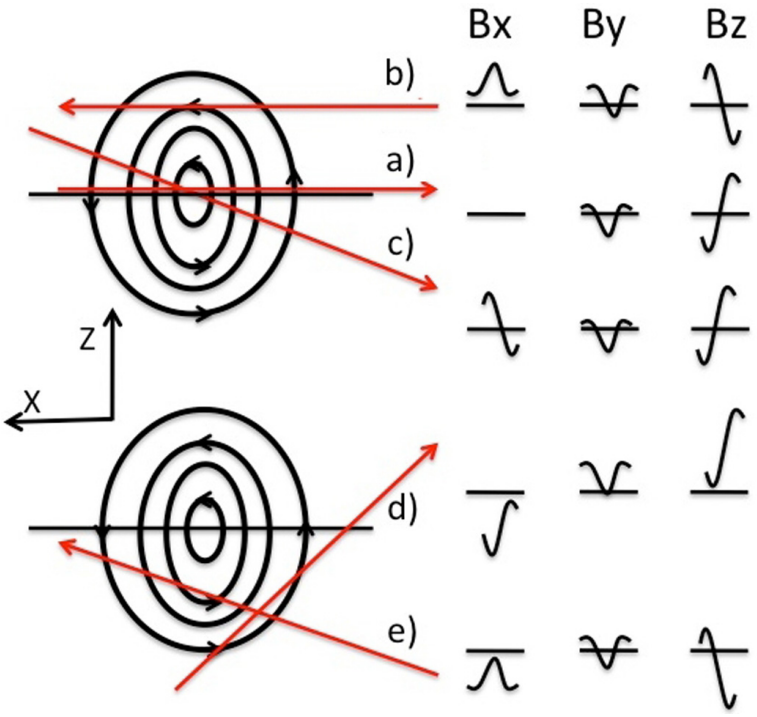

FIGURE 1.16: Schematic showing the magnetometer signatures (right) recorded by various spacecraft trajectories (red) through magnetic flux ropes (left and black). The core field of the flux ropes is directed into the plane of the page (opposing the Y coordinate which completes the right handed set shown) [*Borg et al.*, 2012].

magnetic field is enhanced above background levels at Jupiter and Saturn [*Vogt et al.*, 2010; *Jackman et al.*, 2014b]. Automated techniques have also been used to identify magnetopause flux transfer events (FTEs) via bipolar field deflections [*Kawano et al.*, 1992], albeit still requiring manual confirmation. *Karimabadi et al.* [2007] introduced a data mining technique (MineTool) and later applied it to locate FTEs [*Karimabadi et al.*, 2009], using a combination of magnetic field and plasma data. Recently, *Malaspina and Gosling* [2012] refined a technique to identify rotational discontinuities in the STEREO solar wind data using the gradient of the magnetic field (the method was initially developed by *Vasquez et al.* [2007]). These techniques are well designed to pick out large scale rotations of a single field component. Flux rope signatures, however, are complex and show coordinated changes in multiple field components. In this thesis new automated methods are designed to locate the products of tail reconnection in the magnetospheres of Mercury (Chapter 5) and Saturn (Chapters 4 and 7).

1.5 Summary

This chapter has concerned the necessary plasma physics, and heliospheric and magnetospheric background required for this thesis. Chapter two will now summarise the spacecraft observations made at Mercury and Saturn, and apply the physical concepts described above to the specifics of those systems.

Chapter 2

The Magnetospheres of Mercury and Saturn

2.1 Introduction

Chapter 1 has introduced the basic space plasma and magnetospheric physics required by this thesis. This section will now build upon that with details of the Hermean and Kronian magnetospheres, including their structure, properties and dynamics.

2.2 The Hermean Magnetosphere

Mercury is the closest planet to the Sun, with an average heliocentric distance of $\sim 0.38\,AU$ ($1\,AU = 1.49 \times 10^8\,km$); a Hermean year is correspondingly short at only $\sim$ 88 Earth days. Mercury is a small rocky planet, with a radius of $2440\,km$, and is characterized by an almost complete lack of an atmosphere (or ionosphere). Mercury's eccentric orbit and close proximity to the Sun results in strong tidal forces and a 3 : 2 spin-orbit resonance. Therefore, a single solar day lasts $\sim$ 176 Earth days, while a sidereal day (the rotation period) is $\sim$ 59 Earth days.

Despite its small size Mercury possesses an internal magnetic field with a moment of $195 \pm 10\,nT\,R_M^3$ [*Anderson et al.*, 2012] ($\sim 1\%$ of the Earth's field). The polarity of the dipole field is the same as the Earth, such that the field is directed northward at the equator. The dipole is approximately aligned with its spin axis but offset north from the planetary centre by approximately $0.2\,R_M$ [*Alexeev et al.*, 2008, 2010; *Anderson et al.*, 2008, 2010, 2011; *Johnson et al.*, 2012].

2.2.1 Spacecraft Observations

The first spacecraft to visit Mercury was NASA's Mariner 10 mission, which performed three flybys in 1974 and 1975. These flybys first demonstrated the presence of an internal magnetic field [*Ness et al.*, 1974, 1976]. More recently, the MESSENGER (MErcury Surface, Space ENvironment, GEochemistry, and Ranging) spacecraft [*Solomon et al.*, 2007] performed three flybys before successfully orbiting Mercury between March 2011 and April 2015. MESSENGER's orbit was eccentric and highly inclined ($\sim 80°$ to the equatorial plane) with an initial period of 12 hours (later in the mission this was reduced to 8 hours). A schematic of the orbit is shown in Figure 2.1. The orbit was not sun-synchronous, but took tens of days to rotate fully around the planet (in a clockwise fashion).

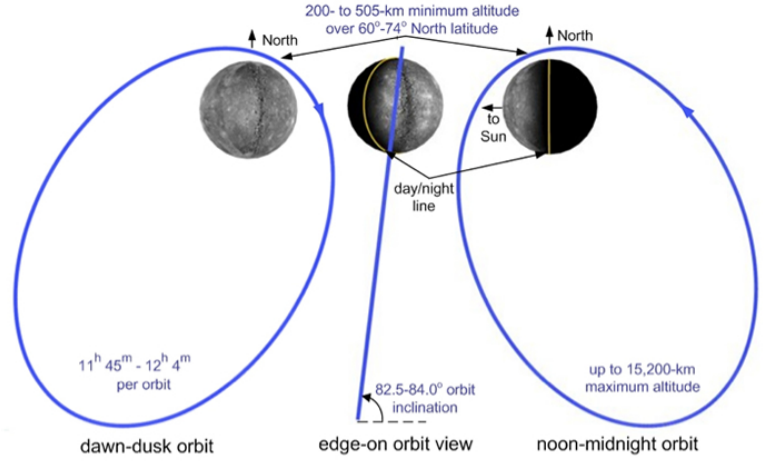

FIGURE 2.1: Schematic of MESSENGER's initial orbit around Mercury shown for three intervals and perspectives [*McNutt et al.*, 2014].

2.2.2 Interaction with the solar wind

At the orbit of Mercury, by conservation of mass and magnetic flux, the solar wind is found to be $\sim 5 - 10$ times denser and coupled with an interplanetary magnetic field (IMF) $\sim 3 - 6$ times stronger than is observed at Earth [*Burlaga*, 2001]. The combination of its relatively weak internal field and proximity to the Sun results in a very compact magnetosphere, with an average magnetopause standoff distance of only $\sim 1.45\,R_M$ [*Ness et al.*, 1976; *Winslow et al.*, 2013; *Zhong et al.*, 2015]. Furthermore, during extreme solar wind dynamic events the magnetopause standoff distance has been observed to decrease to $1.03 - 1.12\,R_M$, only just above the planetary surface [*Slavin et al.*, 2014].

The incident solar wind can interact with Mercury's magnetosphere through several mechanisms. The first, as introduced in Section 1.4, is through reconnection with the dayside magnetopause [*DiBraccio et al.*, 2013; *Jasinski et al.*, 2017], the observable effects of which include FTEs [e.g. *Slavin et al.*, 2009, 2012b; *Imber et al.*, 2014] and cusp filaments [e.g. *Poh et al.*, 2016]. It is also important to consider the viscous-like interaction with the solar wind along the magnetopause (proposed for the Earth by *Axford and Hines* [1961]), which may take the form of Kelvin-Helmholtz vortices [*Sundberg et al.*, 2012b; *Korth et al.*, 2014; *Gershman et al.*, 2015], driven by the flow shear at the boundary. It should be noted that these viscous-driven instabilities may also result in magnetic reconnection [e.g. *Hasegawa et al.*, 2004; *Nykyri et al.*, 2006; *Ma et al.*, 2017].

2.2.3 Plasma Sources and Cycles

Lacking a significant atmosphere, moons, or rings, the largest plasma source for Mercury's magnetosphere is the solar wind. Such material gains access to the magnetosphere through both dayside reconnection and viscous-like interactions, as described above. Correspondingly, the dominant constituent of Mercury's magnetospheric plasma has been found to be H^+, of solar wind origin [*Gershman et al.*, 2014]. However, bombardment of the planetary surface by energetic particles and solar photons also provides a source of heavier ions (e.g. O^+, Na^+, K^+, Mg^+) [*Zurbuchen et al.*, 2008, 2011; *Raines et al.*, 2011, 2013].

Poh et al. [2017a] determined that, though less numerous, the presence of the heavier ions is required to maintain stress balance in the Hermean plasma sheet. Recent studies have also shown that there is a significant dawn-dusk asymmetry in the observed Na^+ density [*Raines et al.*, 2013; *Gershman et al.*, 2014], with higher densities observed pre-midnight. These observations are consistent with modelling efforts that suggest that heavy planetary ions are preferentially injected into the duskside plasma sheet [*Delcourt*, 2013]. At Earth, the presence of heavy ions has been postulated to inhibit the initiation of reconnection [*Shay and Swisdak*, 2004], though the opposite effect has also been suggested [*Baker et al.*, 1982]. Mercury provides another laboratory within which to test these hypotheses.

2.2.3.1 Global Convection

Mercury's slow orbital rotation and high rate of magnetopause reconnection leads to a magnetospheric convection pattern that is completely dominated by the Dungey cycle (as shown in Figure 1.12). At Earth, the time-scale for the Dungey cycle, the time

between the field lines being opened on the dayside and their subsequent closure on the nightside, is of the order of $1 - 3$ hours [*Cowley*, 1981; *Fear and Milan*, 2012; *Browett et al.*, 2017]. In contrast, the time-scale at Mercury is thought to be as little as ~ 2 minutes [*Siscoe et al.*, 1975; *Christon*, 1987; *Slavin et al.*, 2009, 2010, 2012a] due to the character of the solar wind at $\sim 0.38\,AU$ and the small scale of the magnetosphere.

2.2.4 Magnetotail Reconnection

Evidence for reconnection-driven magnetotail dynamics at Mercury was first identified in the energetic particle data obtained during the Mariner 10 flybys [*Baker et al.*, 1986; *Eraker and Simpson*, 1986]. More recently, analysis of the MESSENGER magnetometer data has revealed many *in situ* encounters with dipolarizations [*Sundberg et al.*, 2012a; *Sun et al.*, 2016] and flux ropes [*Slavin et al.*, 2009, 2012a; *DiBraccio et al.*, 2015; *Sun et al.*, 2016] within the Hermean magnetotail. Figure 2.2 shows a schematic of the Hermean magnetosphere where a flyby of MESSENGER observed numerous dynamic structures associated with reconnection including FTEs, plasmoids and TCRs.

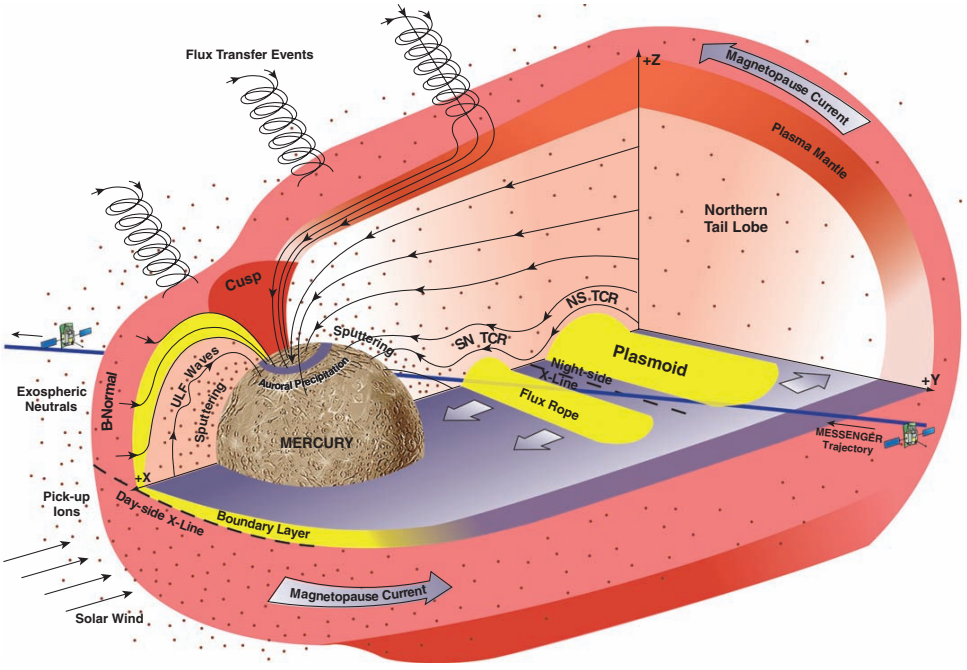

FIGURE 2.2: Schematic of Mercury's magnetosphere under IMF conditions conducive to magnetopause reconnection during a MESSENGER flyby on 6 October 2008 [*Slavin et al.*, 2009].

The dominant direction of motion of flux ropes in the magnetotail is determined by the location of the near-Mercury neutral line (NMNL) relative to the flux rope. From energetic particle data collected during the Mariner 10 flyby, *Baker et al.* [1986] concluded that the NMNL was located between 3 and $6\,R_M$ down the Hermean tail. Following

this, evidence from the MESSENGER M2 and M3 flybys determined the location of the neutral line (during those flybys) to be $2.8\,R_M$ and $1.8\,R_M$ from the planet, respectively [*Slavin et al.*, 2012a]. The vicinity of the NMNL ($\sim 1-3\,R_M$) was later well sampled by the MESSENGER mission's orbital phase; a survey of flux ropes during this phase agreed the location of the NMNL to be approximately $2-3\,R_M$ downtail [*DiBraccio et al.*, 2015]. Most recently, *Poh et al.* [2017a] performed a statistical analysis, using the sign of the B_Z (north-south) component of the magnetic field to infer the relative location of MESSENGER and concluded that the NMNL is statistically located $\sim 3\,R_M$ down the Hermean tail.

In their flux rope survey, *DiBraccio et al.* [2015] only considered orbits close to the centre of the Hermean magnetotail ($\pm 0.5\,R_M$) in order to reduce the likelihood of dynamic events on the magnetopause contaminating the sample. Within this region a relatively even distribution was observed, with no clear asymmetries. Later, *Sun et al.* [2016] expanded the survey region and consequently observed many more flux ropes dawnward of midnight. Complementary studies of the statistical field [*Poh et al.*, 2017b], dipolarization fronts [*Dewey et al.*, 2017] and surface X-ray emission caused by electron precipitation [*Lindsay et al.*, 2015] have also observed preferential occurrence in the dawn region of the magnetotail. The cause of this asymmetry is likely to be related to the relative abundances of heavy planetary ions [e.g. *Raines et al.*, 2013; *Gershman et al.*, 2014].

As to the frequency of magnetotail reconnection, *Sun et al.* [2016] found that the average rate of flux rope observations was $22 \times 10^{-3}\,min^{-1}$, a value almost 30 times the rate observed at the Earth [*Imber et al.*, 2011]. In the same study, the average rate of dipolarization fronts was found to be $44 \times 10^{-3}\,min^{-1}$, an order of magnitude greater than the rate observed at the Earth [*Liu et al.*, 2013]. From this it has been concluded that Mercury's magnetotail is a highly dynamic system.

This thesis will look to perform the most detailed surveys of the Hermean magnetotail to date (Chapters 5, 6 and 9). This will allow the evaluation of previously observed magnetotail asymmetries, and enable the investigation of their cause: are they due to the limited sample size of previous surveys? Or are they potentially due to properties of the Hermean magnetotail (e.g. asymmetric ion abundances)?

2.3 The Kronian Magnetosphere

Saturn is the second largest planet in the solar system, orbiting the Sun at an average distance of $\sim 9.5\,AU$. Saturn rotates quickly relative to Earth, with a rotation period

of $\sim$ 10.7 hours. The large size and fast rotation leads to a large degree of polar flattening: where the equatorial radius is $\sim 10\%$ greater than its polar radius [*Anderson and Schubert*, 2007]. For the remains of this thesis the radius of Saturn will be taken as its equatorial 1 bar radius: $60268\,km$.

A layer of liquid metallic hydrogen in Saturn's outer core acts as a dynamo, generating a large magnetic field with a dipole moment of $4.6 \times 10^{18} T\,m^2$ (over two orders of magnitude greater than Earth) [*Burton et al.*, 2009]. The polarity of the field is the opposite of that found at the Earth, with the northern magnetic pole being located in Saturn's northern hemisphere. Saturn's magnetic field is almost perfectly aligned with Saturn's spin axis (to within 0.06°), while the magnetic equator is offset marginally ($\sim 0.036\,R_S$) northward of the geographic centre [*Dougherty et al.*, 2005a; *Cao et al.*, 2011].

Saturn has more than 60 moons, the majority of which are smaller than a few km in size. There are two in particular that are deserving of mention: Titan is the largest moon (larger even than the planet Mercury) and is the only solar system moon to have a dense atmosphere. Enceladus on the other hand, is a much smaller moon whose icy crust is thought to cover a subsurface ocean [*Thomas et al.*, 2016]. The moons will be discussed in more detail in Section 2.3.3 in the context of plasma sources.

2.3.1 Spacecraft Observations

The first spacecraft to visit Saturn was Pioneer 11, which performed a flyby in 1979. Pioneer data enabled the first estimation of the internal magnetic field structure and suggested that the magnetic field was closely aligned with the spin axis of the planet [*Smith et al.*, 1980; *Acuña and Ness*, 1980]. Later, in 1980 and 1981 Voyager 1 and 2 (respectively) performed flybys, further confirming the lack of dipole offset [*Ness et al.*, 1981]. The three flybys were later used together to create the first global model of Saturn's intrinsic field [*Davis and Smith*, 1990].

Most recently, the Cassini spacecraft orbited Saturn between July 2004 and September 2017, the trajectory of Cassini during the mission is shown in Figure 2.3. Thus Cassini provides an unprecedented 13 year data set with which to study the Kronian system. Cassini's orbit was adjusted continually throughout the mission, often using flybys of the moons (e.g. Titan) to change orbit. The deepest tail orbits were performed in 2006, when Cassini travelled up to $68\,R_S$ down the Kronian magnetotail. These orbits have provided the most heavily studied data in terms of magnetotail reconnection [e.g. *Jackman et al.*, 2007; *Hill et al.*, 2008]. Cassini data from 2006, 2009 and 2010 will be

used in Chapters 4, 7 and 8 (corresponding to parts of the green, orange and purple orbits in Figure 2.3).

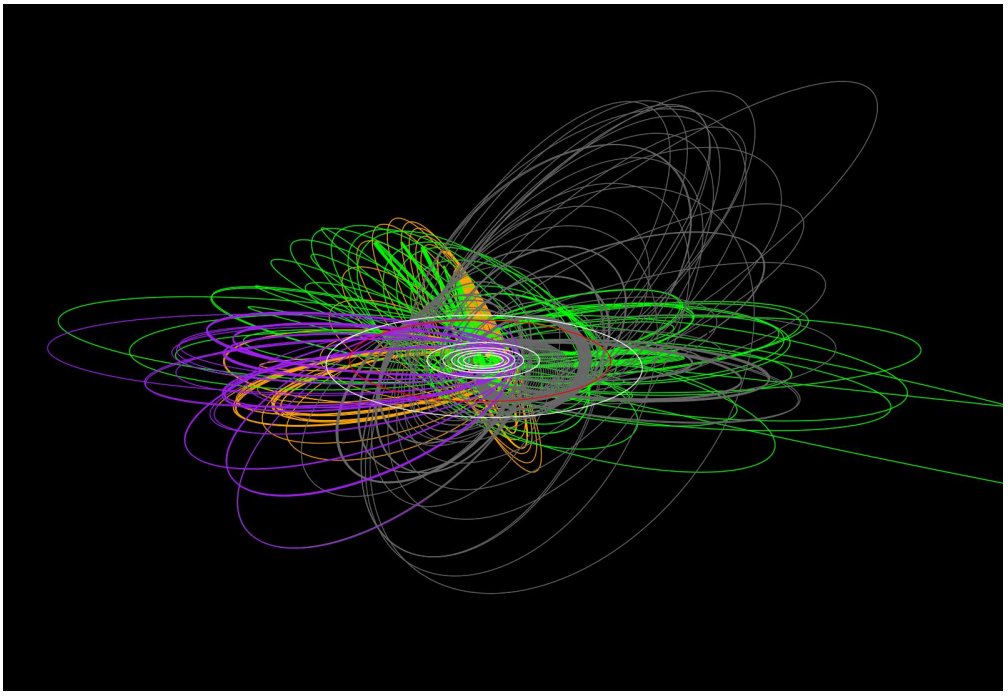

FIGURE 2.3: Cassini's orbit around Saturn. Saturn is in the centre, while the orbits of Titan and the other six inner moons are shown in red and white respectively. The prime mission (up to 2008) is shown in green, while the equinox mission (up to 2010) is in orange. The solstice mission up to March 2012 is in purple while the final orbits are in dark grey. Credit: NASA/JPL-Caltech.

2.3.2 Interaction with the Solar Wind

As discussed in Section 1, the average dynamic pressure exerted by the solar wind drops off as the distance from the Sun increases. By the time the solar wind reaches Saturn the average dynamic pressure is $\sim 0.01\,nPa$ [*Jackman and Arridge*, 2011a], approximately 200 times smaller than that observed at the Earth. The magnetopause standoff distance at Saturn has been found to be bimodal, with the subsolar point most commonly located at either ~ 20.7 or $27.1\,R_S$ [*Achilleos et al.*, 2008; *Pilkington et al.*, 2015].

The bimodality was originally attributed to the dominant compression-rarefaction pattern in the solar wind at Saturn's orbit [e.g. *Jackman et al.*, 2004]. However, dynamic pressure changes alone are unable to explain the variability of the magnetopause distance. Voyager 1 and 2 measurements first indicated the presence of significant internal energetic plasma in the Kronian magnetosphere [*Krimigis et al.*, 1982, 1983]. Cassini observations later suggested that the plasma sheet extends to the dayside magnetopause, and that the pressure associated with the suprathermal plasma is often of the same order as the magnetic pressure at the magnetopause, inflating the magnetosphere [*Sergis et al.*,

2007, 2009]. Additionally, the pressures associated with the lower energy plasma population must be taken into account [*Thomsen et al.*, 2010; *Sergis et al.*, 2010]. Therefore, plasma production and loss processes will have a significant effect on the magnetopause location [*Achilleos et al.*, 2008; *Pilkington et al.*, 2015].

The impact of the solar wind on Saturn's magnetospheric dynamics is a large area of current research. Saturn's magnetosheath contains high beta plasma and strong low-latitude shear flows, which are thought to inhibit reconnection for all but large magnetic shear regions [*Desroche et al.*, 2013; *Masters et al.*, 2012; *Masters*, 2015]. Despite these constraints, *in situ* evidence for occasional magnetopause reconnection has been observed [e.g. *McAndrews et al.*, 2008; *Lai et al.*, 2012; *Badman et al.*, 2013; *Fuselier et al.*, 2014; *Jasinski et al.*, 2014, 2016].

Saturn also experiences seasonal effects due to the changing latitude of the Sun. Saturn's current sheet stretches away on the nightside of the planet, and after a certain distance (R_H) hinges up out of the plane of the dipole equator, forming a bowl-like shape [*Arridge et al.*, 2008]. This is shown schematically in Figure 2.4. This hinging is caused by the relative attack angle of the solar wind (or equivalently the solar latitude), and thus changes over time. Cassini arrived during Saturn's southern hemisphere summer, during which time the current sheet was hinged upwards $\sim 5°$. The hinging distance was modelled to be $\sim 25\,R_S$ at this time, but was observed to be sensitive to the current solar wind conditions [*Arridge et al.*, 2008]. The position of the current sheet has an important effect on spacecraft observations, and will be discussed in Section 4.

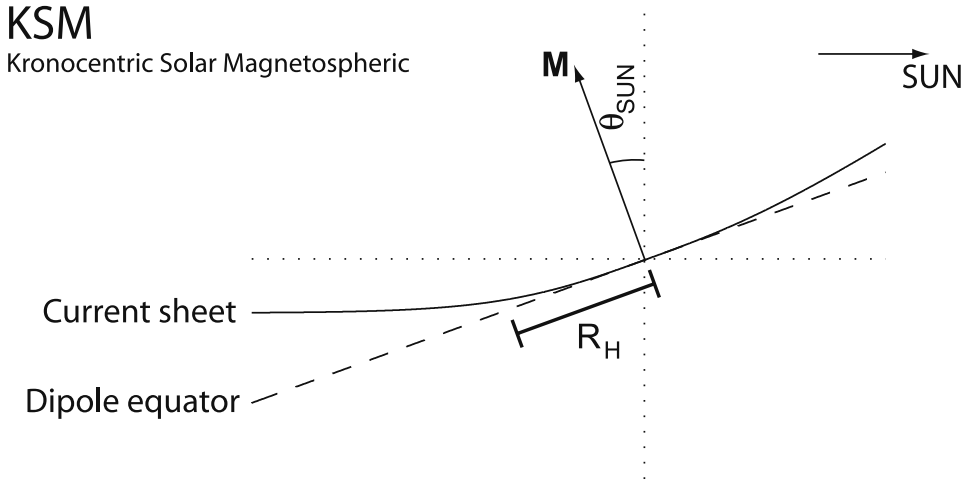

FIGURE 2.4: Schematic illustrating Saturn's bowl shaped current sheet model. θ_{SUN} represents the latitude of the Sun, while R_H represents the hinging distance. Adapted from *Arridge et al.* [2008].

In addition to the bowl-like deformation of the current sheet, it is also observed to flap vertically. The period of this flapping motion is similar to the planetary rotation

[*Arridge et al.*, 2011a; *Provan et al.*, 2012]. The close alignment of Saturn's dipole and rotation axes [*Cao et al.*, 2011] rules this out as a potential source of the flapping motion. Other potential drivers include rotating magnetic perturbations [e.g. *Andrews et al.*, 2010; *Jia and Kivelson*, 2012] and magnetotail reconnection [e.g. *Jackman et al.*, 2007]. Care must be taken to distinguish encounters with the flapping current sheet from magnetotail reconnection related transients [*Jackman et al.*, 2009a].

Saturn's aurora generally forms a main oval around the poles [*Broadfoot et al.*, 1979; *Clarke et al.*, 2005]. These auroral emissions are thought to be generated by upward field aligned currents driven by shear flows near the boundary between open and closed magnetic field lines [*Cowley et al.*, 2004a; *Badman et al.*, 2006; *Bunce et al.*, 2008]. Therefore, much like at Earth, low-latitude dayside and nightside lobe reconnection will change the size of the polar cap. Hubble Space Telescope (HST) images of the dark polar cap have been used to estimate the open flux contained within Saturn's magnetosphere and infer magnetopause and tail lobe reconnection [e.g. *Badman et al.*, 2005; *Belenkaya et al.*, 2007; *Badman et al.*, 2012, 2014; *Nichols et al.*, 2014].

Viscous-like interactions with the solar wind are also important [e.g. *Delamere et al.*, 2015a]; vortices driven by the Kelvin-Helmholtz instability can cause small scale reconnection on the magnetopause [*Ma et al.*, 2014]. Instability driven reconnection can act to transport mass, magnetic flux and momentum across the magnetopause [e.g. *Burkholder et al.*, 2017; *Ma et al.*, 2017].

2.3.3 Plasma Sources and Cycles

The potential sources of plasma in Saturn's magnetosphere are the solar wind, the atmosphere/ionosphere of the planet, and the moons and rings [*Blanc et al.*, 2015]. Somewhat unexpectedly, Cassini has found that the largest source of neutrals in the Kronian magnetosphere is the moon Enceladus: geysers on the icy surface spew copious amounts of neutral water group atoms into the magnetosphere [*Dougherty et al.*, 2006; *Hansen et al.*, 2006; *Porco et al.*, 2006]. An image of the jets, taken by Cassini, is shown in Figure 2.5. The vents are likely supplied by a subsurface liquid ocean, and caused by tidal heating resulting from Enceladus' orbital resonance with the moon Dione [*Spencer et al.*, 2009; *Iess et al.*, 2014]. Enceladus' neutral cloud is later ionized [*Jurac and Richardson*, 2005; *Fleshman et al.*, 2010], producing $\sim 12-250\,kgs^{-1}$ of plasma [*Bagenal and Delamere*, 2011; *Blanc et al.*, 2015]. In this thesis, water group ions will often be referred to as W^+ and includes species such as O^+, OH^+, H_2O^+ and H_3O^+. Titan, originally proposed to be the main magnetospheric plasma source (prior to Cassini), has been found to be a relatively small source of H_2, N_2 and CH_4 [*Smith et al.*, 2007, 2008;

De La Haye et al., 2007]. By virtue of its atmospheric composition, the ionosphere of Saturn is a source of H^+, while the rings of Saturn are known to produce small amounts of O_2 and H_2 [*Tseng et al.*, 2011].

Overall, the presence of W^+ group ions is a good indicator that the plasma is of internal origin. In contrast, He^{++} is abundant in the solar wind but has no known magnetospheric source; therefore its presence could indicate that at least some fraction of the observed population originated within the solar wind. Light ion species (e.g. H^+) are generally not good indicators of the origin of the plasma as they have both internal and external sources [e.g. *Glocer et al.*, 2007; *Felici et al.*, 2016].

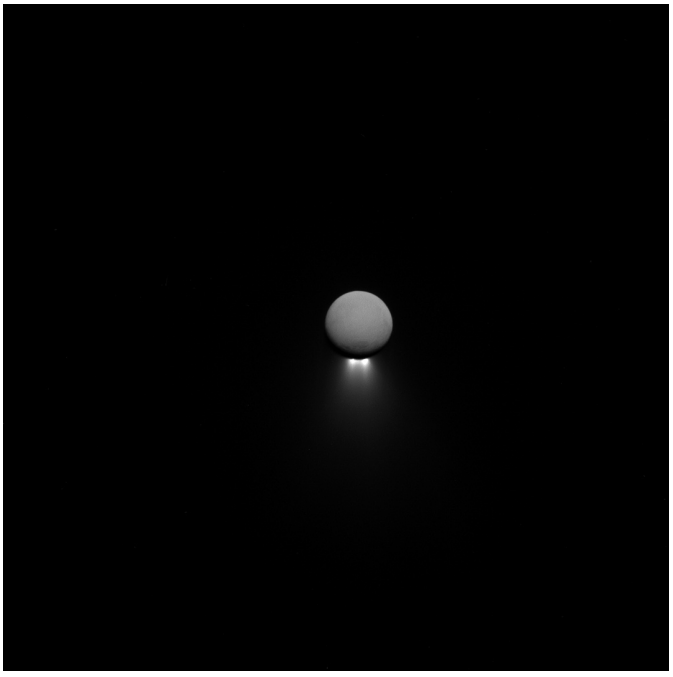

FIGURE 2.5: The jets on Enceladus illuminated by sunlight, taken from Cassini in April 2017. Credit: NASA/JPL-Caltech/Space Science Institute.

Solar wind origin material can enter Saturn's magnetosphere either directly via magnetopause reconnection, or as a result of Kelvin-Helmholtz instability-related vortices [*Masters et al.*, 2009, 2010; *Delamere et al.*, 2011, 2013; *Delamere and Bagenal*, 2013]. The ability of solar wind material to penetrate the Kronian magnetosphere is unknown, although the relative abundance of He^{++} is generally low. At its peak He^{++} has been found to constitute a fractional abundance of up to 5% in the midnight, dawn and noon regions of the magnetosphere (at relatively large radial distances) [*Allen et al.*, 2018]. In general though, the fractional abundance of He^{++} has been found to be very low in the plasma sheet [e.g. *Kmigis et al.*, 2005].

2.3.3.1 Global Convection

Once ionized, the plasma of internal origin is picked up by the magnetic field. The plasma is then accelerated up to corotational velocities by a torque generated by field aligned currents, coupling the magnetosphere and ionosphere. Plasma from the Enceladus torus at a radial distance of $\sim 4\,R_S$ must eventually move outward; initially this is accomplished through flux tube interchange, a process that is driven by the fast planetary rotation. Interchange is analogous to the gravitationally driven Rayleigh-Taylor instability, with centrifugal forces taking the place of gravity. In this interchange process, flux tubes filled with cold, Enceladus-origin plasma move outward and are replaced with flux tubes containing relatively hot, more tenuous plasma. This process has been observed in simulations [*Liu et al.*, 2010] (shown in Figure 2.6), and also *in situ* by Cassini [e.g. *Burch et al.*, 2005; *Hill et al.*, 2005; *Thomsen et al.*, 2016; *Azari et al.*, 2018].

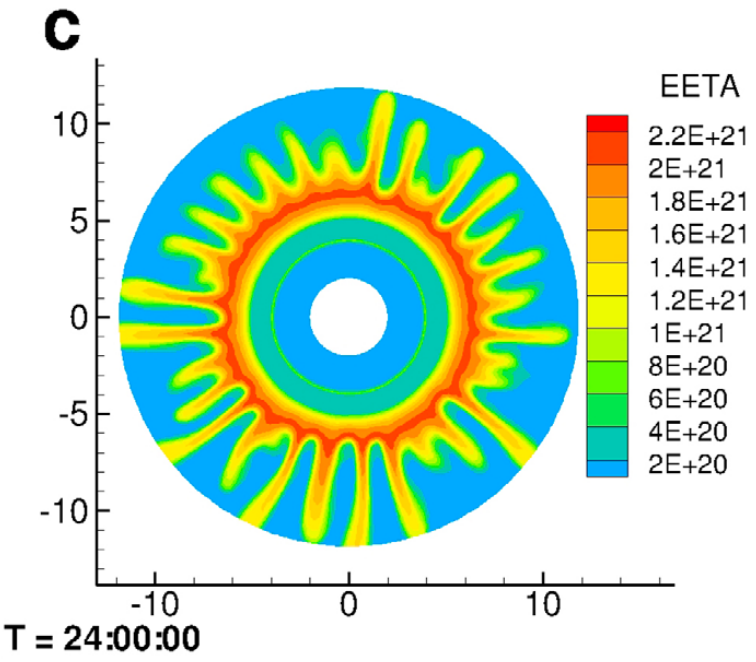

FIGURE 2.6: Simulation results showing the flux rope interchange process. Adapted from *Liu et al.* [2010].

Flux tube interchange effectively transports the plasma from ~ 5 to $\sim 12\,R_S$ [*Chen and Hill*, 2008; *Chen et al.*, 2010], beyond which the plasma flow is characterized by sub-corotational motion. At $\sim 12 - 15\,R_S$ the ionosphere can no longer provide a sufficient torque to accelerate the outward moving plasma up to full corotational velocities ($V_{Corot} = \omega r$), a mechanism first discussed in terms of Jupiter's magnetosphere [*Hill*, 1979] and to explain the generation of Jupiter's auroral oval [*Cowley and Bunce*, 2001]. The resulting field aligned current system at Saturn is shown by the sketch in Figure

2.7. The subcorotational lagging field configuration has been studied with both Voyager [*Bunce et al.*, 2003; *Cowley and Bunce*, 2003] and Cassini data [*Pontius and Hill*, 2009; *Delamere et al.*, 2015b].

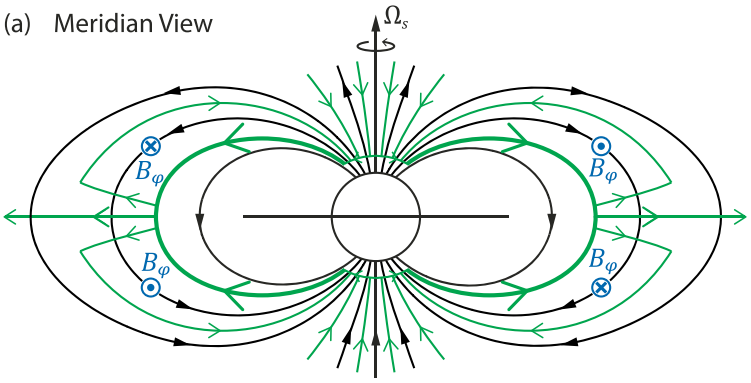

FIGURE 2.7: A meridional cut through sketch showing the current systems associated with plasma subcorotation in Saturn's magnetosphere. Black lines represent the planetary field, green indicate the current system and blue dots and crosses represent the magnetic field component perpendicular to the plane of the page. Adapted from *Hunt et al.* [2014].

Over the years various different theoretical models have been proposed for the convection of the more distant regions ($> 15\,R_S$) of the Kronian magnetosphere [e.g. *Cowley et al.*, 2004a; *Kivelson and Southwood*, 2005; *Kane et al.*, 2014; *Delamere et al.*, 2015b]. Though different in some respects, all models suggest differences between the dawn and dusk flanks of the magnetotail, differences that have been observed by Cassini in both plasma and magnetic field data [*Arridge et al.*, 2015a, and references therein]. For example, evidence suggests that the flows are predominantly corotational throughout most of the magnetotail inside $\sim 50\,R_S$, with outflow more common from dusk to $\sim 0200 - 0300$ local time and some inflow seen at local times beyond 0200 [*McAndrews et al.*, 2009; *Kane et al.*, 2014; *Thomsen et al.*, 2013, 2014a]. Asymmetries are also present in some global MHD [*Jia et al.*, 2012] and multifluid models [*Kidder et al.*, 2012]. Asymmetries in the observed reconnection products will be investigated in Chapters 4 and 7.

Given the large internal mass source and fast rotation, it may be expected that the Vasyliunas cycle will dominate dynamics at Saturn. However, in principle, and given specific solar wind conditions, the Dungey cycle could also play a role: the degree to which it does so is an active area of research. The Vasyliunas cycle voltage has been estimated to be several hundred kV, while the voltage related to Dungey cycle has been estimated to range between $\sim 25\,kV$ during solar wind rarefactions and $\sim 150\,kV$ during compressions [*Badman and Cowley*, 2007], with an average of $\sim 40\,kV$ [*Masters*, 2015]. Therefore, in general magnetotail reconnection can be expected to be predominantly Vasyliunas cycle related. However, while the Kronian magnetosphere

is strongly compressed the Dungey cycle could contribute significantly to magnetotail dynamics [e.g. *Thomsen et al.*, 2015]. The nature of the observed magnetotail dynamics and their relation to the Vasyliunas and/or Dungey cycles will be probed in Chapters 4, 7 and 8.

2.3.4 Magnetotail Reconnection

A key driver of Saturn's magnetotail dynamics is magnetic reconnection within the magnetotail current sheet, resulting in accelerated flows and plasma heating. Planetward of the magnetotail neutral line, a dipolarization may be expected to pass over the spacecraft. Such a structure was first observed during the outbound pass of Cassini's SOI (Saturn Orbit Insertion) manoeuvre [*Bunce et al.*, 2005]. In this event the Cassini spacecraft observed the sudden arrival of a hot tenuous plasma population accompanying a sharp rotation of the magnetic field. More recent Kronian studies have located dipolarization fronts either from their southward rotation of the magnetic field [*Russell et al.*, 2008; *Jackman et al.*, 2013, 2015; *Yao et al.*, 2017a] or from the presence of an inflowing [*Thomsen et al.*, 2013] or heated plasma population [*Thomsen et al.*, 2015].

Tailward of the neutral line a plasmoid would be expected to form, removing mass (and potentially flux) from the magnetosphere. *Jackman et al.* [2007, 2008b] and *Hill et al.* [2008] first reported several observations of encounters with plasmoids and dipolarizations during the deep tail orbits performed during 2006. These structures were identified both from the magnetic field and plasma signatures. The catalogue of magnetotail reconnection related events was later expanded by *Jackman et al.* [2011] to include 34 newly identified *in situ* plasmoid encounters. This work also began to consider the impact of these events on the open flux contained in the magnetotail lobes, by examining the statistical post plasmoid plasma sheet (PPPS), a region where flux is closed following plasmoid release [*Richardson et al.*, 1987]. A schematic of this scenario is shown in the lower panel of Figure 2.8. From their observed PPPS events, *Jackman et al.* [2011] estimated that on average $\sim 3\,GWb$ of open flux is closed (with a maximum of $\sim 6\,GWb$); a significant fraction of the mean $\sim 40\,GWb$ contained within the polar cap [*Badman et al.*, 2005]. Later, *Badman et al.* [2014] used HST images of the polar cap to investigate changes in open magnetic flux content due to tail reconnection, recovering values similar to those inferred from the *in situ* observations.

Recently, the 2006 magnetotail orbits were surveyed in detail by *Jackman et al.* [2014b] who reported a total of 69 plasmoids, 17 TCRs, and 13 planetward moving structures. Chapter 4 will look to further expand this catalogue, using automated techniques to survey a large volume of data, including additional orbits to probe the dusk flank.

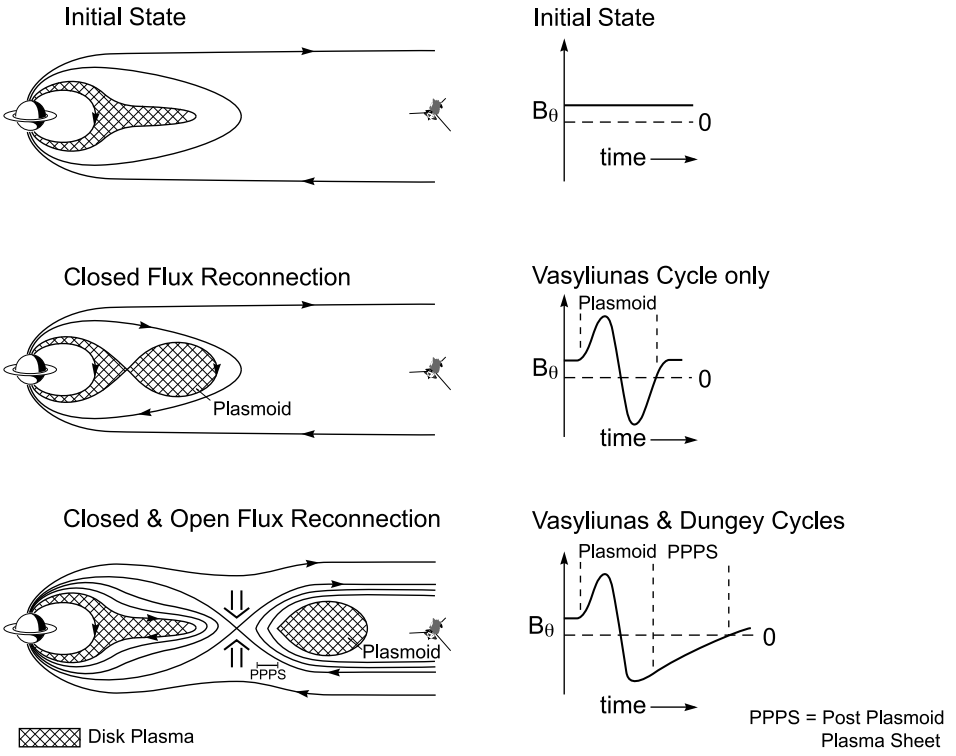

FIGURE 2.8: Schematic of three states of the Kronian magnetotail, the lower two showing the expected magnetometer signature for the reconnection of closed and open flux [*Jackman et al.*, 2011].

It is worth noting that flows in the corotational direction (though below full corotational speed) are observed to dominate Kronian nightside convection [e.g. *McAndrews et al.*, 2009; *Thomsen et al.*, 2014a], with only transient departures observed. If a plasmoid is completely magnetically disconnected from the planet it would be expected to move tailward, and plasma outflow be observed. However, if the plasmoid is still trapped by closed field lines (that have yet to reconnect) then it will continue to be entrained with the ambient corotating plasma [*Thomsen et al.*, 2013]. Additionally, if the reconnection process does not expel the plasmoid such that its radial velocity is much greater than its azimuthal motion, then the flow will still have considerable momentum in the corotational direction. In a similar manner, the corotational velocity may form a significant component of any inflow associated with a dipolarization. With this in mind, pure radial in/out-flow is perhaps not expected at Saturn. As an example, Figure 2.9 shows a theoretical model of equatorial plasma flows.

As discussed above, from a magnetometer perspective, the closure of open flux (i.e. Dungey-type reconnection) can be inferred from the presence of a PPPS following a plasmoid [*Richardson et al.*, 1987; *Jackman et al.*, 2011]. However, the composition of the plasma will also provide evidence that lobe magnetic field has been closed. For example, the majority of Kronian dipolarizations reported to date show strong signatures of water

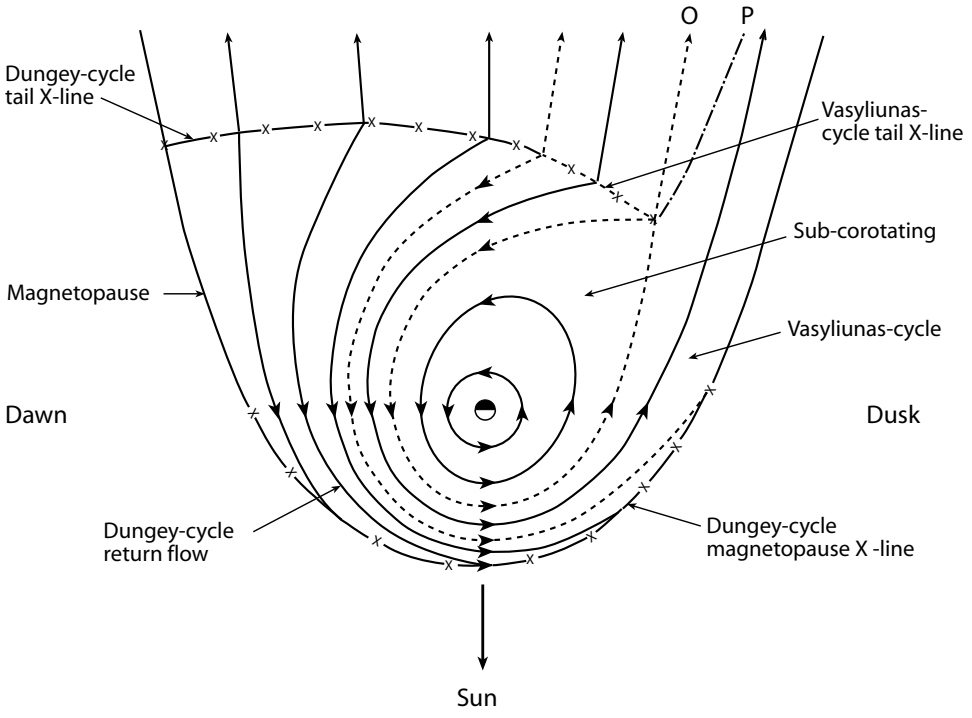

FIGURE 2.9: Theoretical schematic of plasma flow in Saturn's equatorial plane. The Sun is at the bottom, dusk to the right and dawn on the left. The solid lines represent plasma streamlines, while the dashed lines also indicate streamlines but separate distinct flow regimes. The reconnection sites associated with the Dungey and Vasyliunas cycles are indicated by lines with crosses [*Cowley et al.*, 2004a].

group ions (i.e. W^+ originating from Enceladus), suggesting they are Vasyliunas cycle related [e.g. *Mitchell et al.*, 2005; *Masters et al.*, 2011; *Thomsen et al.*, 2013; *Jackman et al.*, 2015]. However, *Thomsen et al.* [2015] reported a long duration W^+ depleted inflow, suggested to be the result of Dungey-type reconnection following a solar wind-driven magnetospheric compression. At Saturn therefore, there exists a balance between the two systems, one that will be explored further in this thesis, particularly in Chapters 4 and 7.

With the use of some assumptions regarding the plasmoid geometry and extent it is possible to calculate the mass lost in plasmoids down the magnetotail. However, recent studies have found that this figure is insufficient, by almost an order of magnitude, to account for the mass entering the system from Enceladus (and other sources) [e.g. *Bagenal and Delamere*, 2011; *Jackman et al.*, 2014b]. Solutions put forward to solve this problem include unobserved loss down the flanks of the magnetosphere, discussed for the Jovian magnetosphere by *Kivelson and Southwood* [2005], or the loss of mass through small-scale mechanisms, such as cross-field diffusion [*Bagenal and Delamere*, 2011]. Most recently, *Cowley et al.* [2015] developed a theoretical argument suggesting that the event duration, as defined in recent studies, only represents a small portion of

the plasmoid structure. This imbalance will be further explored in Chapter 4, using the most detailed current survey of plasmoids in Saturn's magnetotail.

2.4 Summary

This chapter has covered the current understanding of the magnetospheres of Mercury and Saturn, with a particular emphasis on the magnetotail dynamics, building on the concepts introduced in Chapter 1. The next chapter will discuss the instrumentation that will be used to explore some of the questions and topics highlighted so far.

Chapter 3

Data and Instrumentation

3.1 Introduction

The investigations described within this thesis use several spacecraft and instruments. This chapter will provide a brief overview of the instrumentation and data of relevance to the thesis.

3.2 MESSENGER at Mercury

NASA's MESSENGER spacecraft was the first to orbit Mercury, following three flybys by the Mariner 10 spacecraft almost 40 years previously. The close proximity of Mercury to the Sun heavily influenced the design of MESSENGER, the most obvious example of which is the very large sun shield, shown in green in Figure 3.1.

As described in Chapter 2, following the Mariner 10 flybys Mercury was known to be a highly dynamic magnetosphere. The main science objective of relevance to this thesis was to characterize the geometry and time variability of the magnetospheric field. Additional science objectives include the investigation of:

1. Wave-particle interactions
2. Magnetotail dynamics
3. Magnetopause structure and dynamics
4. Field aligned currents

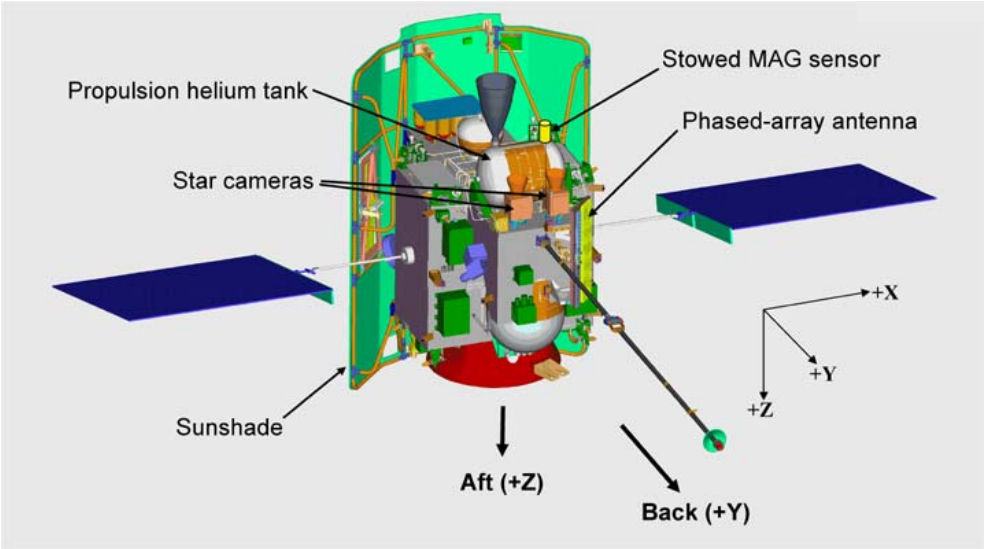

FIGURE 3.1: The MESSENGER spacecraft showing the spacecraft coordinates, with the magnetometer boom shown deployed in the $+Y$ direction. The large sun shield is shown in green (in the $-Y$ direction) [*Anderson et al.*, 2007].

The investigations described within this thesis fall mainly within the purview of science objective #2.

3.2.1 Fluxgate Magnetometer

To achieve the science objectives outlined above, an instrument was required to measure the magnetic field with a high accuracy (to within $\sim 0.1\,nT$) and fast cadence (a few Hz or greater). Therefore, MESSENGER employed a low noise fluxgate magnetometer on a $3.6\,m$ deployable boom, seen in the lower right of Figure 3.1. A picture of the instrument is shown in Figure 3.2.

Fluxgate magnetometers were originally invented by *Aschenbrenner and Goubau* [1936], and later developed during the second world war. In each sensor a drive coil is wrapped around a high permeability core. The drive coil cyclically saturates the core with a large amplitude signal wave. While saturated the core has a very low permeability, and thus the core is cycled between high and low permeabilities at the frequency of the drive signal. This cycle modulates the ambient magnetic flux, resulting in a asymmetric signal that is detected with an outer sensing coil (at twice the drive signal frequency). The amplitude of the signal in the sensing coil is proportional to the magnitude of the ambient field projected along the axis of the core and coils. Three orthogonally mounted fluxgate sensors can provide a full three-dimensional description of the ambient magnetic field. The three axis fluxgate magnetometer has considerable heritage, having been used on more than 50 space missions [*Acuña*, 2002, and references therein]

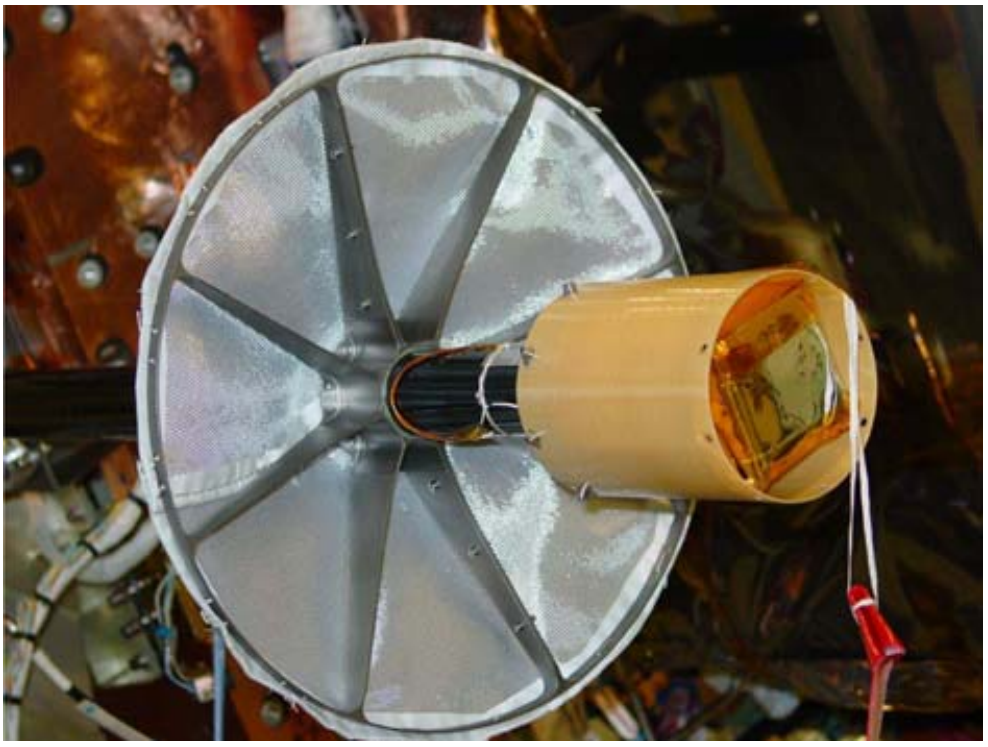

FIGURE 3.2: The MESSENGER Magnetometer sensor and sunshade [*Anderson et al.*, 2007].

MESSENGER's three axis fluxgate magnetometer is located at the end of a $3.6\,m$ deployable boom, in order to reduce the impact of magnetic noise generated by the spacecraft. Tests before and after the deployment of the boom confirmed that the fixed spacecraft contribution is of the order of a few nT, while the variable field from the spacecraft amounts to less than $0.05\,nT$. There are 11 output rates, ranging between $0.01\,s^{-1}$ and $20\,s^{-1}$, allowing a wide variety of data rates. The measurement capability of the magnetometer allows for fields as large as $\pm 51300\,nT$ to be recorded in the coarse sensor range, and a resolution of $0.047\,nT$ when set to its fine range.

MESSENGER magnetometer data are principally used in Chapters 5 and 6 to identify magnetic structures associated with magnetotail reconnection.

3.3 Cassini-Huygens at Saturn

Cassini-Huygens was a two part joint NASA-ESA mission to Saturn. It consists of the NASA Cassini orbiter and the ESA Huygens probe. The orbiter was named for French/Italian astronomer Giovanni Domenico Cassini, discoverer of several of the Kronian moons and the first to identify several prominent features of the rings (e.g. the Cassini division). Meanwhile, the Dutch astronomer Christiaan Huygens, discoverer of

Titan, lends his name to the probe that successfully descended to the surface of Titan in 2005.

Figure 3.3 shows a schematic of the Cassini spacecraft, detailing the scientific payload and the location of the various instruments. The instruments used by this thesis will be discussed below. It is important to note that Cassini is a three axis stabilized spacecraft, which means that particle instruments afixed to Cassini will not see the full $4\pi\, sr$ of the sky at any one time, unless the spacecraft happens to be rolling in that interval. This will be discussed further below, particularly in relation to the CAPS (CAssini Plasma Spectrometer) suite of instruments.

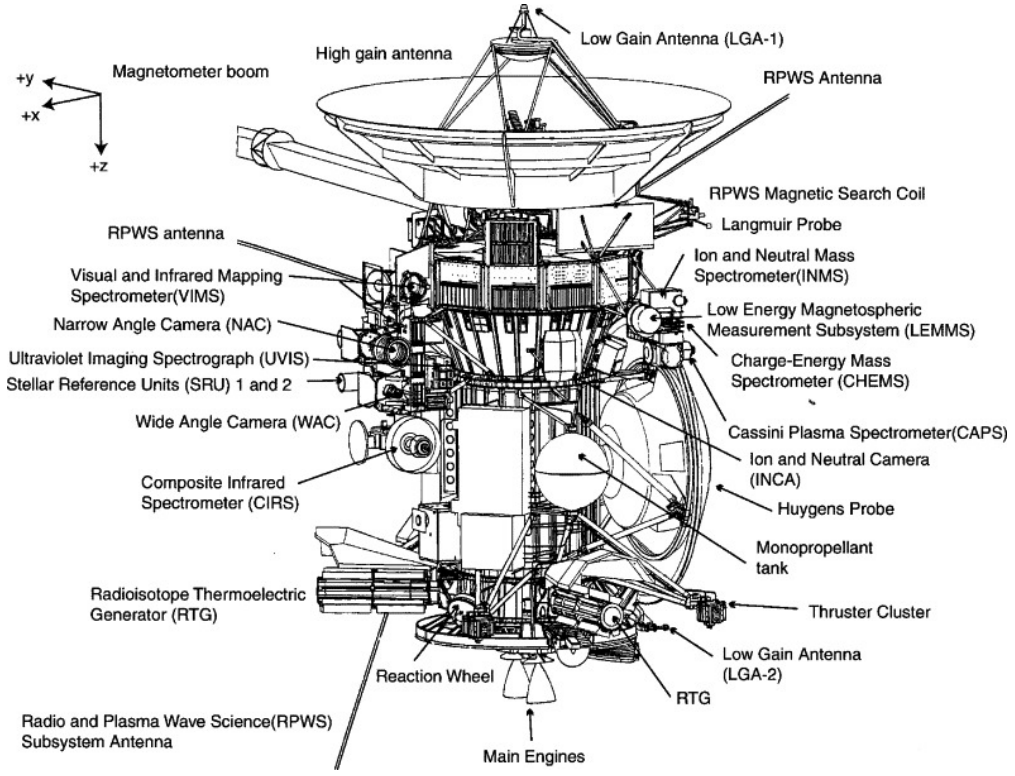

FIGURE 3.3: Schematic of the Cassini spacecraft illustrating the presence and location of the various instruments that comprise the scientific payload [*Burton et al.*, 2001].

3.3.1 Science Objectives

The flybys of the Pioneer and Voyager spacecraft in the 1970s highlighted some interesting science questions, particularly regarding the magnetosphere of Saturn. Overall, Cassini's science objectives can be broadly summarized as regarding the topics of: the planet and its formation, the rings and satellites, and the magnetosphere. Some of the science goals of the magnetometer instrument include the exploration of:

1. The origin and details of the internal planetary magnetic field.

2. Satellite magnetospheric and plasma interactions.

3. Magnetospheric instabilities.

4. The magnetotail structure and dynamic processes.

Figure 3.4 shows a schematic of the Kronian magnetosphere along with some of the magnetometer science goals. The work contained within Chapters 4, 7 and 8, falls mainly within the investigation of bullet points 3 and 4.

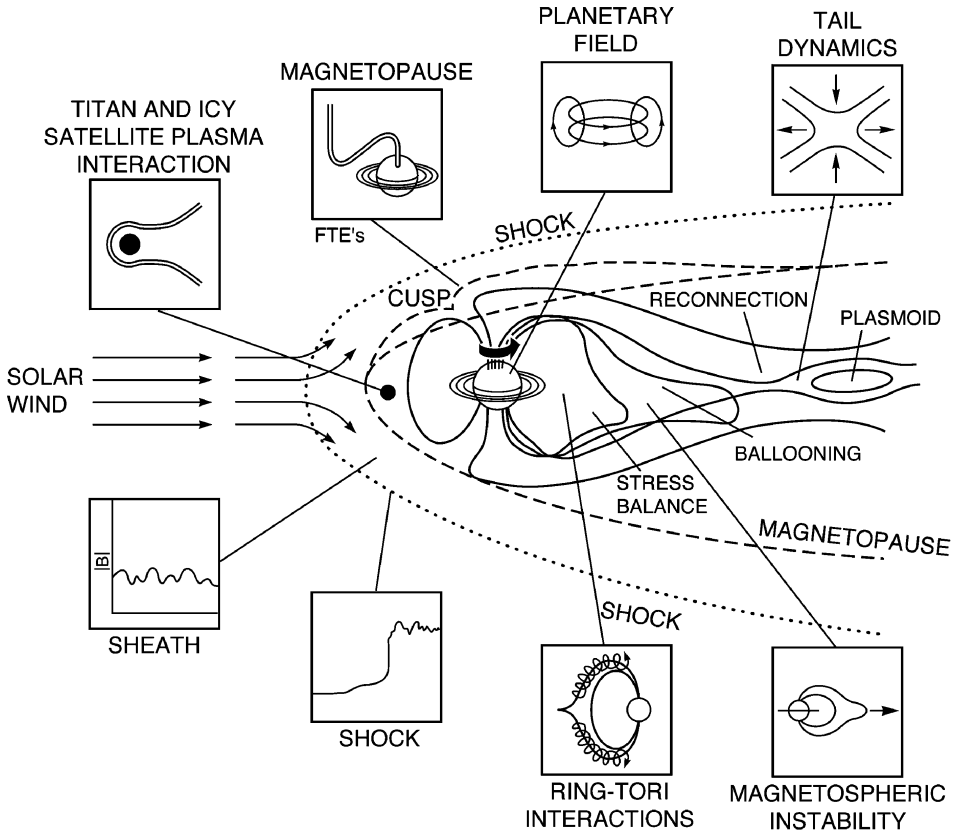

FIGURE 3.4: Schematic of the Kronian magnetosphere, with the Cassini magnetometer science objectives highlighted [*Dougherty et al.*, 2004].

3.3.2 Magnetometers

There are two magnetometers on board the Cassini spacecraft: a Fluxgate magnetometer (FGM) and a Vector Helium magnetometer (VHM) [*Dougherty et al.*, 2004]. Both are mounted on Cassini's magnetometer boom (which can be seen in Figure 3.3). The magnetometers are mounted at different distances along the boom to allow the spacecraft's intrinsic field to be better characterized and removed from the data.

3.3.2.1 Fluxgate Magnetometer

The first magnetometer on-board Cassini is a fluxgate magnetometer (FGM), which is mounted halfway along the magnetometer boom. The general method by which FGMs operate has been covered in Section 3.2.1, and so will not be repeated here. The instrument itself is similar to the that flown on the Ulyssess mission [*Balogh et al.*, 1992] among others [*Acuña*, 2002]. The sensor can be operated in four different scales, the smallest of which allows the measurement of fields up to $\pm 40\,nT$, while the largest of which allows a range of $\pm 44000\,nT$. Switching between the different scales is performed automatically by the on-board electronics.

The data from the FGM are generally downlinked at a resolution of 32 vectors per second, it can then be post-processed to other common cadences (e.g. $1\,Hz$ or 1 minute resolution). Due to practical limits on the use of the Deep Space Network (DSN), the data are stored on board until it can be beamed back to Earth.

3.3.2.2 Vector Helium Magnetometer

The second component of Cassini's magnetometer package is a Vector Helium Magnetometer (VHM). VHMs have a large history at the outer planets; for example they formed part of the payloads of Pioneers 10 and 11 [*Smith et al.*, 1974, 1975]. The VHM is placed at the end of the $11\,m$ long magnetometer boom to remove it as much as possible from the influence of spacecraft magnetic fields. The operation of VHMs is based upon magnetic field dependent light absorption (i.e. the Zeeman effect) and optical pumping. Helium is contained within an absorption cell and excited using a radio frequency discharge, creating a population of metastable He atoms. Infrared radiation is generated by a helium lamp (also by radio frequency discharge) and passed through a circular polariser before traversing through the He absorption cell. The absorption that takes place within the cell is dependent upon the ambient magnetic field direction. To be more precise, the pumping efficiency of the cell is proportional to $cos^2(\theta)$, where θ is the angle between the magnetic field and the optical axis. In vector mode the directional dependence is used by applying sweep fields (generated using a set of Helmholtz coils) that rotate around the cell (at low frequencies). This allows the determination of three orthogonal field components. Cassini's VHM has two dynamic ranges, the smallest of which is $\pm 32\,nT$, while the largest is $\pm 256\,nT$. In general, the data are recorded from the VHM at a cadence of $2\,Hz$.

Approximately a year after Saturn orbit insertion (SOI) the VHM stopped operating due to a malfunction. As a result of this, the still operational FGM required more

complex calibration procedures. For example, in order to calibrate the FGM Cassini needed to roll around two orthogonal axes while the spacecraft is located in a region of quiet ambient field (the magnetotail lobe for example).

Cassini magnetometer data (FGM) are used in Chapters 4, 7 and 8 as the primary means of identifying transient structures related to magnetotail reconnection.

3.3.3 Cassini Plasma Spectrometer

The Cassini Plasma Spectrometer (CAPS) samples the low energy plasma ($\sim 1\,eV \leq E \leq 26\,keV$) plasma environment of Cassini [*Young et al.*, 1998]. CAPS is constructed of three sensors: the Electron Spectrometer (ELS), Ion Beam Spectrometer (IBS) and the Ion Mass Spectrometer (IMS). The layout of the instrument is shown in Figure 3.5. All three instruments function using approximately the same principles. Electrostatic fields are used to guide and separate the charged particles that enter the apertures of the instrument (i.e. are in the field of view). The particles are guided onto micro-channel plates (MCPs in Figure 3.5) where they are recorded. As mentioned above, Cassini is a three-axis stabilised spacecraft, meaning that an instrument affixed to the side of the spacecraft will not see the full $4\pi\,sr$ of the sky. Therefore, CAPS is mounted upon an actuating platform that rotates through $\sim 180°$. The motion of this platform allows the CAPS instruments to view $\sim 2\pi\,sr$ of the sky every three minutes. If the spacecraft is rolling during an interval then it is possible to obtain more complete all-sky information.

Due to the presence of an electrical short, CAPS was turned off in mid-2012 for the remainder of the Cassini mission. However, within this thesis data are used from the orbital period preceding the deactivation.

Data from the ELS and IMS instruments are used in this thesis and will be further discussed below.

3.3.3.1 Electron Spectrometer

The Electron Spectrometer (ELS) is a hemispherical top-hat electrostatic analyser that samples the local thermal electron population between energies of $0.6\,eV$ and $28.25\,keV$. The 74 energy bins in this range are spaced logarithmically and are scanned over a period of $2\,s$. The instantaneous field of view of the instrument is 5.2° in azimuth by 160° in elevation. This field of view combined with the eight anodes (MCPs) give an angular resolution of $\sim 20°$ in elevation.

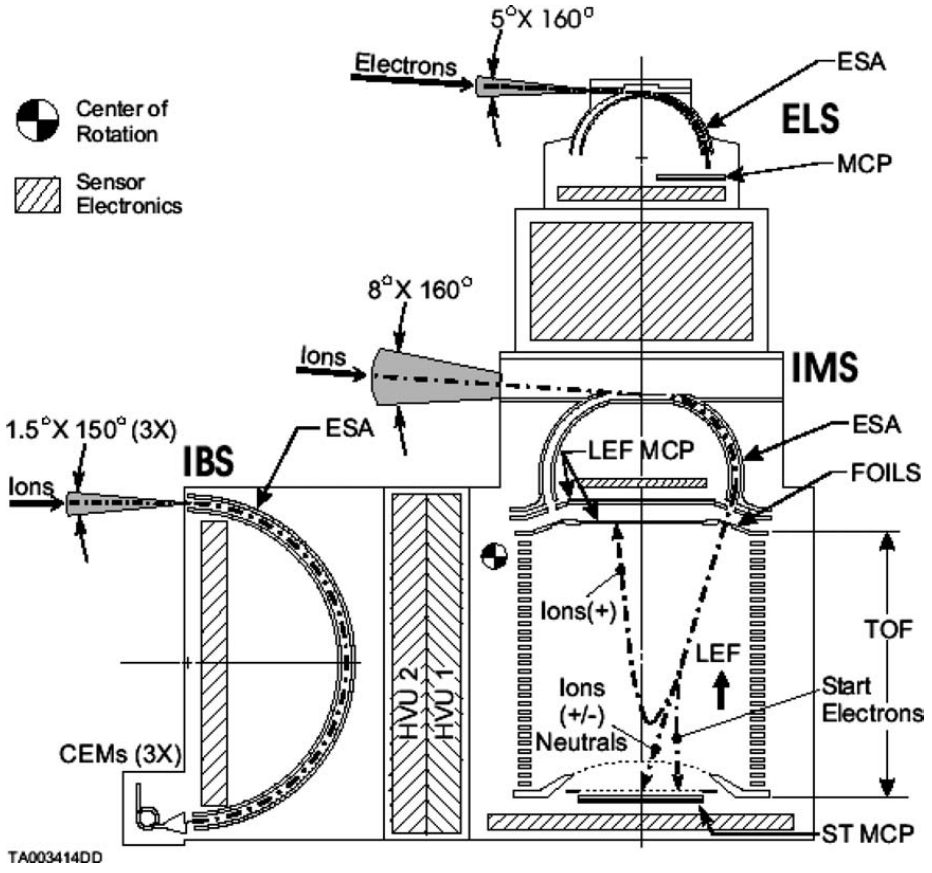

FIGURE 3.5: Schematic of the CAPS Instrument onboard Cassini. The fields of view of the instruments are represented by the grey cones, and example particle trajectories by the dot-dash lines [*Young et al.*, 1998].

ELS data are used in Chapter 4 for magnetospheric environment classification (to derive magnetic field criteria), and in Chapters 7 and 8 to investigate the changes in the electron population encountered by Cassini.

3.3.3.2 Ion Mass Spectrometer

The Ion Mass Spectrometer measures the distributions of ions between 1 eV and 50.28 keV. It combines a top hat electrostatic analyser (for $^{E}/_{q}$ determination) followed by a time of flight (TOF) analyser (for determination of the ion velocity). The 63 logarithmically spaced energy bins are swept every 4 s. The instantaneous field of view of the sensor is 8° in azimuth by 160° in elevation, once more combined with the eight anodes (MCPs) this gives an angular resolution of 20°.

IMS data are used in Chapters 7 and 8 to investigate the magnitude and orientation of the local plasma velocity.

3.3.4 Magnetospheric Imaging Instrument

The Magnetospheric Imaging Instrument (MIMI) provides information on Cassini's *in situ* energetic particle environment. It is composed of three instruments: the Charge Energy Mass Spectrometer (CHEMS), the Low-Energy Magnetospheric Measurement System (LEMMS) and the Ion and Neutral Camera (INCA) [*Krimigis et al.*, 2004]. The individual sensors will be discussed below.

3.3.4.1 Charge Energy Mass Spectrometer

The Charge Energy Mass Spectrometer (CHEMS) measures the mass and mass-per-charge of incident ions with energies between 3 and 236 keV for H^+ and between 8 and 236 keV for O^+. Figure 3.6 shows a schematic of the CHEMS instrument.

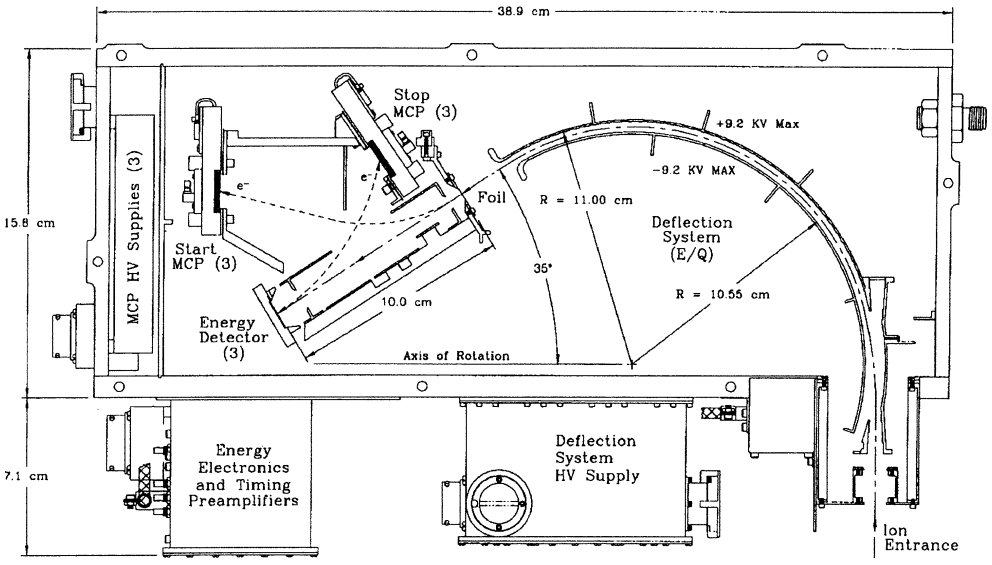

FIGURE 3.6: Schematic of CHEMS [*Krimigis et al.*, 2004].

Upon entering the instrument the electrostatic deflection analyzer acts as an energy per charge filter, centred on the value of the applied deflection voltage. The time of flight system measures the velocity of the particle using the time between the particle encountering the 'start' and 'stop' detectors. The residual energy is then measured using a solid state detector. The field of view of the CHEMS instrument is 160° in latitude and 4° in azimuth.

CHEMS can return pulse-height analysis (PHA) data, containing the complete information set recorded from the incident ions. This information can be plotted as mass per charge vs. mass, an example of which is shown in Figure 3.7. In such a figure it is possible to define regions in mass per charge vs. mass space which correspond to species

common in Saturn's magnetosphere. This is particularly useful to distinguish species such as He^{++} and H_2^+ that have the same mass per charge, but different masses and originate from distinct sources (the solar wind and magnetosphere respectively).

Data from CHEMS are used in Chapters 7 and 8 to evaluate the suprathermal plasma composition.

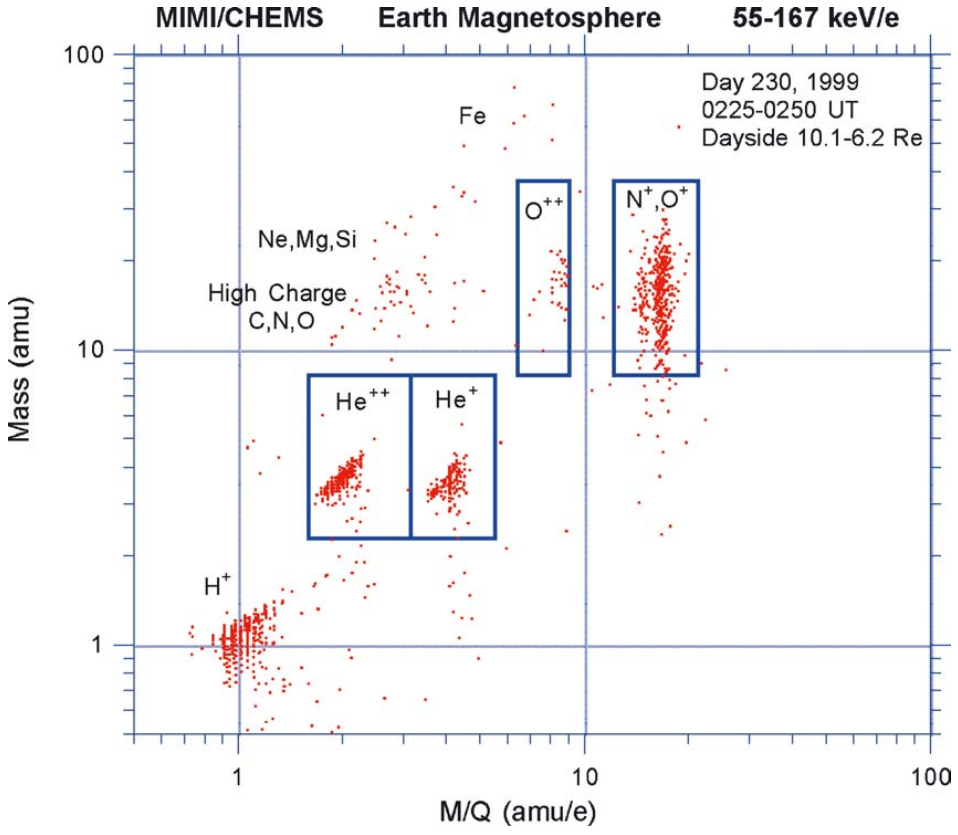

FIGURE 3.7: Example CHEMS PHA data taken during a flyby of the Earth's magnetosphere [*Krimigis et al.*, 2004].

3.3.4.2 Low-Energy Magnetospheric Measurement System

The Low-Energy Magnetospheric Measurement System (LEMMS) is a two ended telescope that measures high energy electrons and ions: a schematic is shown in Figure 3.8. In the forward direction LEMMS measures ions between 0.03 and 18 MeV and electrons between 15 keV and 0.88 MeV. In the reverse direction it measures ions between 1.6 and 160 MeV and electrons between 0.1 and 5 MeV. In the low energy end, particles are deflected by an inhomogeneous magnetic field, and the particles' energy determines which of the detectors is impacted. The high energy end contains a stack of five detectors which are covered with a layer of foil to block incoming light and low energy ions. The LEMMS instrument has oppositely directed conical fields of view, with angular sizes of

15° and 30° for the forward and reverse directions respectively. However, it is mounted on a rotating platform to allow the instrument to observe a larger swathe of the sky.

Data from LEMMS is used in Chapter 7 to investigate the high energy electron environment. Unfortunately, during the interval of data considered in Chapter 7 the platform on which LEMMS is mounted did not rotate, limiting the fraction of sky (and pitch angles) observed.

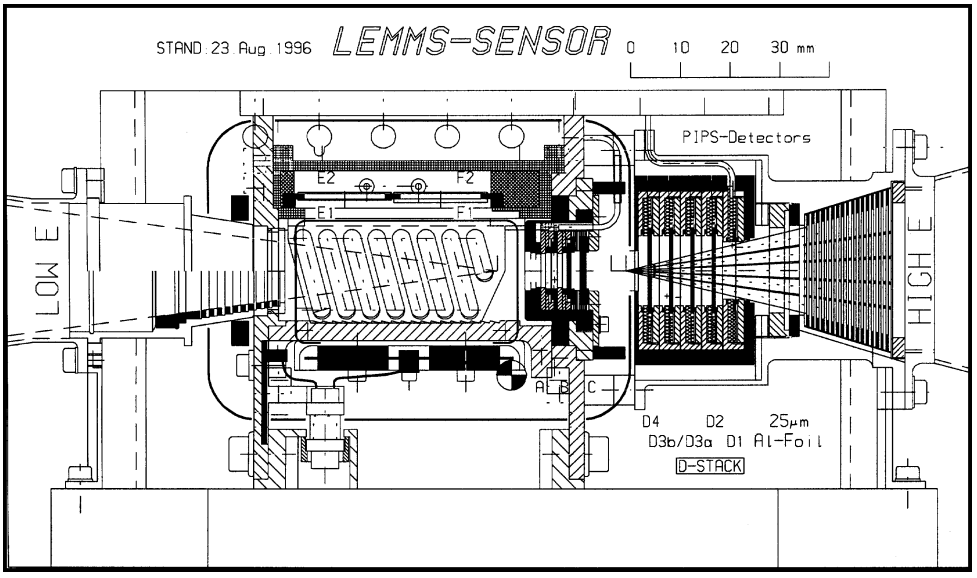

FIGURE 3.8: A schematic showing the configuration of the LEMMS detector [*Krimigis et al.*, 2004].

3.3.4.3 Ion and Neutral Camera

The Ion and Neutral Camera (INCA) is a large geometry factor ($G \sim 2.4\,cm^2sr$) foil time of flight camera, a schematic of which is shown in Figure 3.9. INCA can make two different types of measurements; the first of which is remote images of the global distribution of energetic neutral atoms (ENAs), recording the composition and energy spectra for each pixel. The second type of measurement is the directional distribution, energy spectra and approximate composition of magnetospheric ions between $\sim 7\,keV$ and $3\,MeV$. INCA has a very large field of view of 120° by 90°, making its directional information very useful even when the spacecraft is not rolling (as it observes a large range of magnetic pitch angles).

Data from the INCA sensor are used in Chapter 7 to measure the spatial distributions of energetic particles, particularly with respect to the magnetic pitch angle.

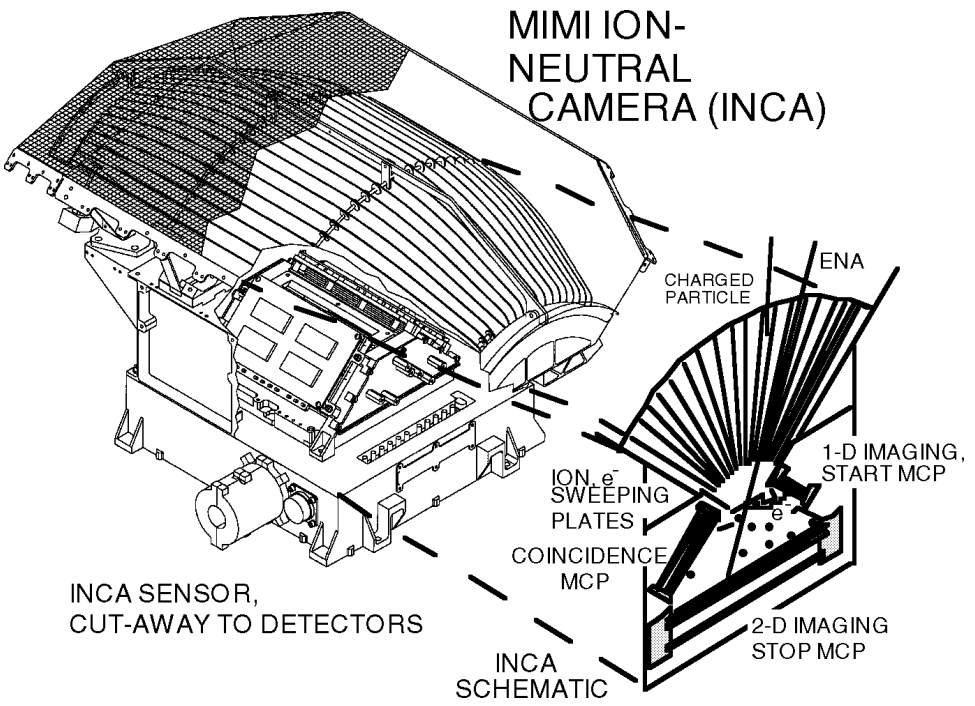

FIGURE 3.9: Perspective sketch of the INCA head. A series of serrated collimator plates cover the aperture [*Krimigis et al.*, 2004].

3.3.5 Radio and Plasma Wave Spectrometer

Cassini's Radio and Plasma Wave Spectrometer (RPWS) instrument is designed to study radio emissions, plasma waves, thermal plasma and dust [*Gurnett et al.*, 2004]. The RPWS instrument follows the radio and plasma wave instruments onboard the Voyager 1 and 2 spacecraft, dramatically improving on their sensitivity, dynamic range and ability to determine the direction of wave-normals. It also allows both active and passive measurements of plasma resonances.

The RPWS instrument is composed of three perpendicular electric antennas, three perpendicular magnetic antennas and a Langmuir probe. The orthogonal electric antennas detect electric fields between $1\,Hz$ and $16\,MHz$, while the tri-axial coil magnetic antennas enable the detection of magnetic fields (e.g. the transverse components of electromagnetic waves) from $1\,Hz$ to $12\,kHz$. In addition, the Langmuir probe allows measurement of the local electron density and temperature. Both the electric antennas and the Langmuir probe are sensitive to dust impacts. Five receiver systems process the signals from the electric and magnetic antennas, each receiver covering a different range of frequencies. Overall, each receiver determines the power per Hz in each frequency band (the total power divided by the filter width), which can then be plotted on spectrograms. A sound transmitter is also present, that can be used to stimulate plasma resonances between $3.6\,kHz$ and $115.2\,kHz$.

Cassini RPWS data are used in Chapter 8 to measure the Saturn Kilometric Radiation (SKR), a radio emission that provides information on auroral field aligned currents in Saturn's magnetosphere.

3.4 Summary

This chapter has summarised the instrumentation used by the investigations in this thesis, their methods of operation and ranges of detection. The specific details of the data used in each study will be described individually in each chapter, for example the cadence or coordinate systems of the data.

Chapter 4

Magnetic Reconnection in Saturn's Magnetotail: A Comprehensive Magnetic Field Survey

4.1 Introduction

This chapter discusses an investigation into the recurrence, distribution and properties of reconnection related structures (e.g. plasmoids, dipolarizations and TCRs) in Saturn's magnetotail.

The aim of this Chapter is to expand upon previous reconnection surveys, developing and using a new automated technique to identify reconnection events from Cassini magnetometer data. The survey incorporates new data from the dusk orbits of 2009 and 2010, in addition to the midnight-dawn orbits of 2006 (previously surveyed by *Jackman et al.* [2014b]) to gain more complete local time coverage of the magnetotail. This selection of data also allows the examination of reconnection both pre- and post-Kronian equinox. The new technique enables more consistent and unbiased event identification, and includes smaller scale events missed by previous studies. The inclusion of data surveying different regions of the magnetosphere enables more reliable conclusions to be drawn regarding the location and recurrence of reconnection in the Kronian magnetotail. In particular, expanding the catalogue of known reconnection related events enables the mass budget and the relative dominance of internal/external driving of the Kronian magnetosphere to be re-examined (discussed in Section 4.6).

Section 4.2 below introduces the data set, field deflections, and definitions. This is followed in the next section by a detailed discussion of the algorithm developed to find the reconnection related events. Section 4.4 then explores the catalogue of detections and some of the broad statistical properties. The occurrence frequency, location and signatures are then discussed in Section 4.5, before Section 4.6 looks into a global interpretation of the results.

4.2 Data Set and Observations

The data primarily used in this study come from the Cassini magnetometer [*Dougherty et al.*, 2004], in orbit around Saturn since July 2004. The coordinate system selected for this study is the Kronocentric radial theta phi (KRTP) system. In this spherical polar system the radial component (B_r) is positive outward from Saturn, the meridional component (B_θ) is positive southward (at the equator) and the azimuthal component (B_ϕ) is positive in the direction of corotation (prograde). This coordinate system was evaluated by *Jackman et al.* [2009a] and shown to be useful in distinguishing reconnection related events from those caused by waves in the hinged current sheet. One minute resolution data were selected as appropriate for this work; previous studies have shown the average duration of a reconnection related event in the Kronian magnetotail to be around 18 minutes [*Jackman et al.*, 2014b].

4.2.1 Data Location

Figure 4.1 shows the Cassini orbits examined in this study. They are displayed in the KSM (Kronocentric Solar Magnetospheric) coordinate system where the x axis points towards the sun, the x-z plane contains the planetary dipole axis and the y component completes the right handed set. Reconnection is thought to occur at the center of the hinged current sheet, a key consideration when selecting appropriate data. Data from 2006 have been heavily relied on in the past for reconnection studies; during 2006 Cassini performed its deepest tail orbits around midnight and dawn. Cassini began 2006 with equatorial orbits around the dawn flank (shown by the red orbits in Figure 4.1), moving to slightly inclined orbits around midnight later in the year beyond day 200 (the orange orbits in Figure 4.1). To complement this, data is used from orbits in late 2009 (day 280 onwards, shown by the blue orbits in Figure 4.1) and 2010, giving equatorial coverage on the dusk flank (the green orbits in Figure 4.1). During early 2009 Cassini performed high latitude passes of the dusk flank, and it was not until later in that year that the orbit became more equatorial and suitable for this study. These low latitude relevant dusk orbits continued throughout 2010. The 2009-2010 orbits sample the majority of the

dusk flank, but the orientation of the orbits only allows exploration of distances up to 20 R_S down the magnetotail. These newly included orbits sample local time magnetotail regions between 18:00 and 22:00; filling the region of the magnetotail unexplored during 2006.

4.2.2 Event Field Deflections

Jackman and Arridge [2011b] used magnetic field data in the KRTP system to show that the average north-south component of field in the Kronian magnetotail was small and southward during the deep, relatively low latitude orbits of 2006. Any deviation from this southward steady state may be caused by reconnection at some location in the magnetotail. At Saturn, tailward moving events are expected to display a characteristic south to north deflection of the field. Figure 4.2 shows examples of the possible field deflections caused by such structures. It is important to note that although the south to north deflection of the field has been related to tailward (radially outward) moving events there could be a considerable azimuthal/corotational component to their motion following release (discussed in Chapter 2.3). This is seen consistently in both statistical plasma flow maps and magnetic field studies [*McAndrews et al.*, 2009, 2014; *Kane et al.*, 2014; *Thomsen et al.*, 2014a; *Jackman et al.*, 2014b], where the vast majority of plasma flow is in the direction of corotation. However, for the purpose of this chapter the term tailward (planetward) moving should be understood as events inferred to be tailward (planetward) of the reconnection site, from the orientation of the B_θ deflection.

As discussed in Chapter 1, the field structure of plasmoids can, broadly speaking, take one of two morphologies; closed loops or helical fields (flux ropes) [*Slavin et al.* [2003a]; *Keiling et al.* [2015] and references therein]. These categories can be principally identified from inspection of the B_ϕ and $|B|$ components of the field; loop like plasmoids show a strong reduction of the field at the center of the structure while flux rope type plasmoids show a strong intensification of both the B_ϕ and $|B|$ components of the field at the core of the helical fields. These field changes are distinct from TCRs, which display a smooth increase in the total field corresponding to the compression of the field due to the plasmoid's passage downtail. Planetward moving events meanwhile are expected to show the opposite bipolar field signature, a north to south deflection, associated with the snapping back of recently broken field lines to a more dipole-like configuration. Though dipolarizations exhibit a dip in the north-south field component at the leading edge of the event the field does not always fully reverse (turn northward, or negative in the KRTP system, at Saturn) [*Ohtani et al.*, 2004; *Shiokawa et al.*, 2005; *Nakamura et al.*, 2009; *Pan et al.*, 2015].

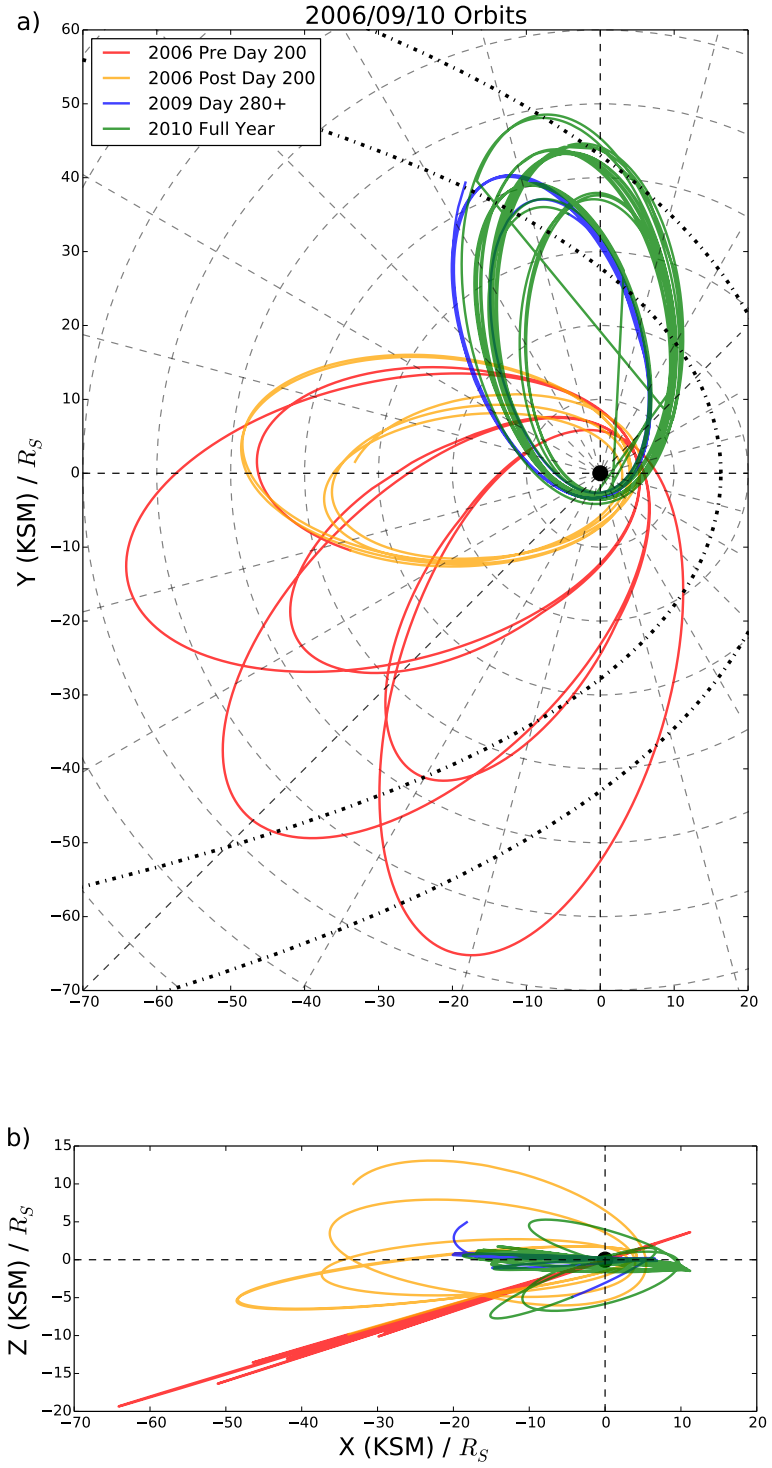

FIGURE 4.1: Cassini trajectory during 2006, 2009 and 2010 in the KSM (Kronocentric Solar Magnetospheric) coordinate system; the x axis traces the sunward direction, the x-z plane contains the planetary dipole axis, and the y axis is positive towards dusk. Panel (a) shows the X-Y view while panel (b) shows the X-Z projection. The dashed concentric circles on (a) are marked every 10 R_S, while the radial dashed lines identify the local time hours. The orbital trajectory is marked in red for orbits before day 200 in 2006, orange for orbits after day 200 in 2006, blue for orbits after day 280 in 2009 and green for orbits during 2010. The black dot-dashed lines marked on (a) show the *Kanani et al.* [2010] model magnetopause for solar wind dynamic pressures of 0.1 and 0.01 nPa.

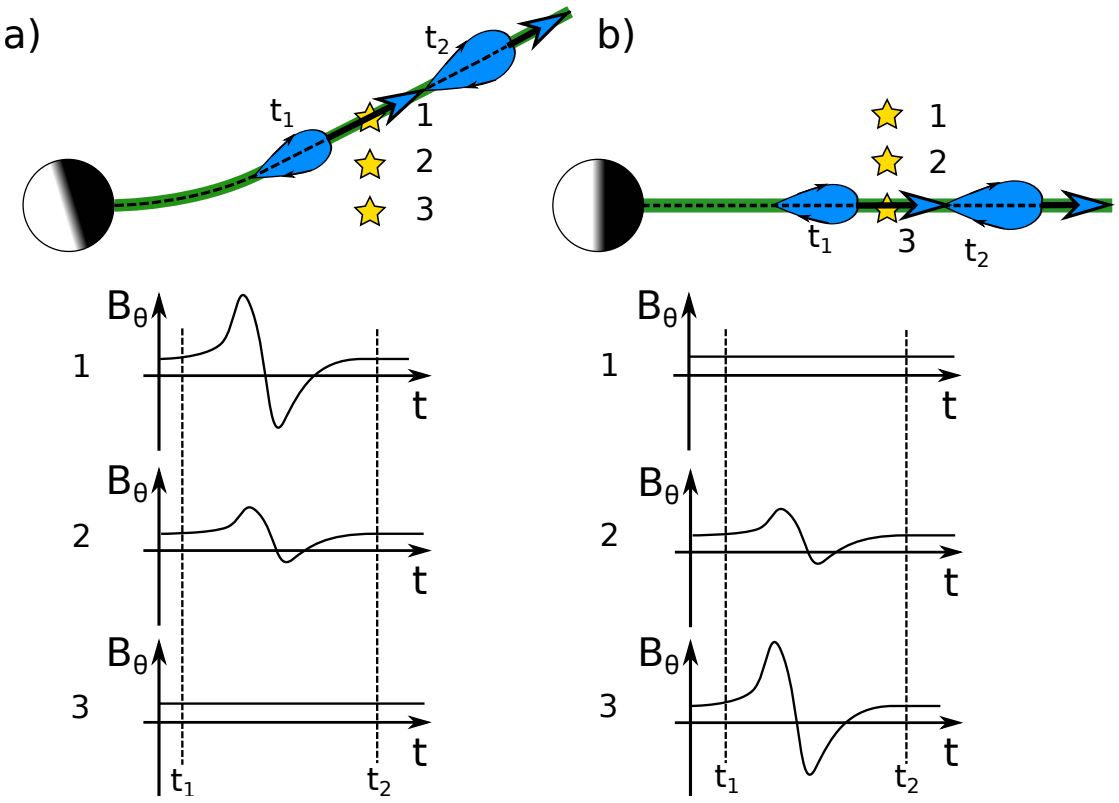

FIGURE 4.2: Schematic showing model magnetometer deflections associated with plasmoid release downtail. The magnetometer sketches are shown for spacecraft at three different latitudes, the spacecraft positions are represented by stars. The current sheet is indicated with a dashed black line, while the green region indicates the extent of the plasma sheet. Panel a) (left) shows the case when the current sheet is hinged up out of the equatorial plane, while panel b) (right) shows the plasma sheet in the equatorial plane. The (blue) plasmoid is shown propagating down the current sheet at two times, t_1 and t_2, with the direction of travel given by the large blue arrows. The small black arrows on the plasmoids indicate the magnetic field direction around the structure.

It should be noted that there are other phenomena that can cause variations in the north-south component of the field. These include: waves or flapping of the plasma sheet and passage of the spacecraft through Saturn's Low-Latitude Boundary Layer (LLBL) or magnetopause. Further discussion of these can be found in Section 4.3.

4.2.3 Viewing Region Definition

When looking at the occurrence rate or frequency of reconnection related events the spacecraft 'viewing region' must be defined. This is the area of the magnetosphere within which events can be detected *in-situ* by the spacecraft. In this study it has been defined as anywhere on the night side of Saturn, at a distance of more than 15 R_S from the planet and within the magnetosphere. It is also required that Cassini is not performing SCAS (Science Calibration and Alignment Subsystem) manoeuvres, and that the field measured by Cassini is unaffected by Titan. No latitude criteria have been enforced,

firstly because of the different seasons during which the data were collected, and secondly because this has been accounted for in the selection of the orbits used by this study. Times outside the magnetosphere (and data within 15 minutes of the crossing) were excluded using a database of magnetopause crossings, the same utilized by *Pilkington et al.* [2015].

4.2.4 Magnetospheric Environment Classification

The location of the spacecraft relative to the plasma sheet has implications for the interpretation of the occurrence rate of events, i.e. a low frequency measured in the lobe may only relate to those events large enough to trigger detections far from the current sheet center. For this purpose, and also for automatically classifying events as plasmoids or TCRs, criteria based on the magnetic field readings were developed to constrain Cassini's local plasma environment. Previous studies that have attempted similar classifications have additionally used criteria on the readings from the Cassini Electron Spectrometer (ELS) instrument, a constituent of the Cassini Plasma Spectrometer (CAPS) [*Young et al.*, 1998]. ELS measures electrons over the energy range $0.8\,eV$ to $27\,keV$, and can be useful when differentiating the high density current sheet from the very low plasma densities common in the magnetotail lobes [*Arridge et al.*, 2011a; *Jackman and Arridge*, 2011b]. However, due to pointing constraints and low counts in the lobes, no formal criteria have been applied to the ELS readings, though example periods were compared to the magnetic field conditions to determine the correct criteria. The field criteria are similar to those used in previous studies, for example those utilized by *Simon et al.* [2010] and *Jackman and Arridge* [2011b]. Equations 4.1 and 4.2 show the two criteria that must be satisfied for Cassini to be classified as within the lobe. These criteria are checked during events, and if they are satisfied for the entire event duration then the event is classed as a TCR. If either condition is violated during the event then it is deemed to be close to the plasma sheet.

$$|B_r|/_{|B|} \geq 0.6 \tag{4.1}$$

$$\sigma B_r/_{|B|} \leq 0.25 \tag{4.2}$$

where σB_r is the standard deviation of the B_r component of the field for the period 30 minutes either side of the data point. The conditions were selected as, from a magnetic field perspective, the lobe can be characterized by quiet steady field predominantly in the radial direction. During the process of selecting the limits outlined above it was noted

that some borderline events see quiet, radial field but small counts in the ELS data. The resulting TCR classifications were deemed acceptable as no significant changes in plasma character were observed during the events. The lack of a sharp boundary between lobe-like and current sheet-like field character was also noted by *Jackman and Arridge* [2011b].

Equations 4.1 and 4.2 have also been applied to the data in general to classify Cassini's local environment during all orbits. As with the event classification, if both criteria are satisfied then Cassini is said to be within the lobe; if either are violated then Cassini is classified as near to the plasma sheet.

4.2.5 Magnetospheric Environment Variation Within Data Set

It is important to consider the effect of changing Kronian season on the magnetospheric environment encountered by Cassini during the 2006, 2009 and 2010 orbits. 2006 corresponded to southern hemisphere summer, and as a result the hinged current sheet was displaced above the dipole equator, generally above a latitude of $\sim 5°$. The warping and hinging of the Kronian current sheet has been discussed in detail by *Arridge et al.* [2008]. The arrangement during southern hemisphere summer is shown schematically in Figure 4.2a, where yellow stars represent possible positions of the spacecraft (at different latitudes). Accordingly, the early 2006 low latitude ($\sim 0°$) dawn orbits found Cassini mainly within the southern lobe of the magnetotail (similar to position 3 in Figure 4.2a); Table 4.1 shows that 92% of the early part of the year was spent within the lobe. Later in 2006, around day 200, the orbit became more inclined and more similar to positions 1 and 2 in Figure 4.2a. Consequently Cassini spent more time within the plasma sheet: from Table 4.1 the lobe occupation time dropped to 74%. In comparison the 2009 and 2010 data were recorded around and beyond Kronian equinox, a time when the plasma sheet was located in a more equatorial location, similar to the position shown in Figure 4.2b. Therefore, the low latitude orbits of late 2009 and 2010 lay within the plasma sheet the majority of the time (similar to position 3 in Figure 4.2b), with Cassini spending 56% and 59% of the time near the plasma sheet respectively (from Table 4.1). As plasmoids are thought to form and propagate along the current sheet, orbits located within the lobe are likely to see only the largest events; either as they cause the plasma sheet to bulge over the spacecraft allowing direct plasmoid detection, or as the downtail motion of plasmoids warps the surrounding lobe field lines such that TCRs can be detected from locations in the lobe.

TABLE 4.1: Data Summary

	Viewing Region (days)	Lobe (days)[a]	Plasma Sheet (days)[a]
All Years	415	265 (64%)	150 (36%)
2006	208	177 (85%)	31 (15%)
2006 Pre Day 200	131	121 (92%)	10 (8%)
2006 Post Day 200	76	56 (74%)	20 (26%)
2009	50	22 (44%)	28 (56%)
2010	157	65 (41%)	92 (59%)

[a] Location inferred from criteria on the magnetometer readings outlined in Section 4.2.4

4.3 Algorithm for Event Identification

An algorithm was designed to automate the search for reconnection related events (plasmoids, dipolarizations and TCRs), creating an unbiased and consistent catalogue. The main identification criterion is a clear, unambiguous deflection of the north-south component of the field, unrelated to the periodic or long term variation observed during orbits.

At this point it is important to mention that though Figure 4.2 shows symmetric bipolar deflections of the field, they are not always observed. The classic, symmetric, bipolar signature is only seen if the spacecraft trajectory passes through both the leading and trailing portions of the plasmoid evenly. In comparison, if the spacecraft trajectory is such that the passage through a plasmoid structure misses the leading edge or occurs at a large distance from the centre then the signature is more unipolar [*Borg et al.*, 2012; *Jackman et al.*, 2014b]. Such magnetic field signatures were discussed in detail by *Cowley et al.* [2015], who suggested that the coverage of Cassini often precludes the observation of the full length of plasmoid structures.

4.3.1 Event Selection Process

Two example outputs from the algorithm are provided in Figure 4.3. The top example shows a TCR observed in 2006, while the second example shows a plasmoid observed during 2009. Neither example has been found by previous reconnection surveys.

The algorithm first takes the average of B_θ for the 30 minutes either side of each data point. This average is taken to provide a baseline about which a deflection in B_θ must be observed. Every occasion where the data crosses through the baseline is then recorded (henceforth referred to as a B_θ crossing). These provide locations at which the algorithm can check for significant deflections.

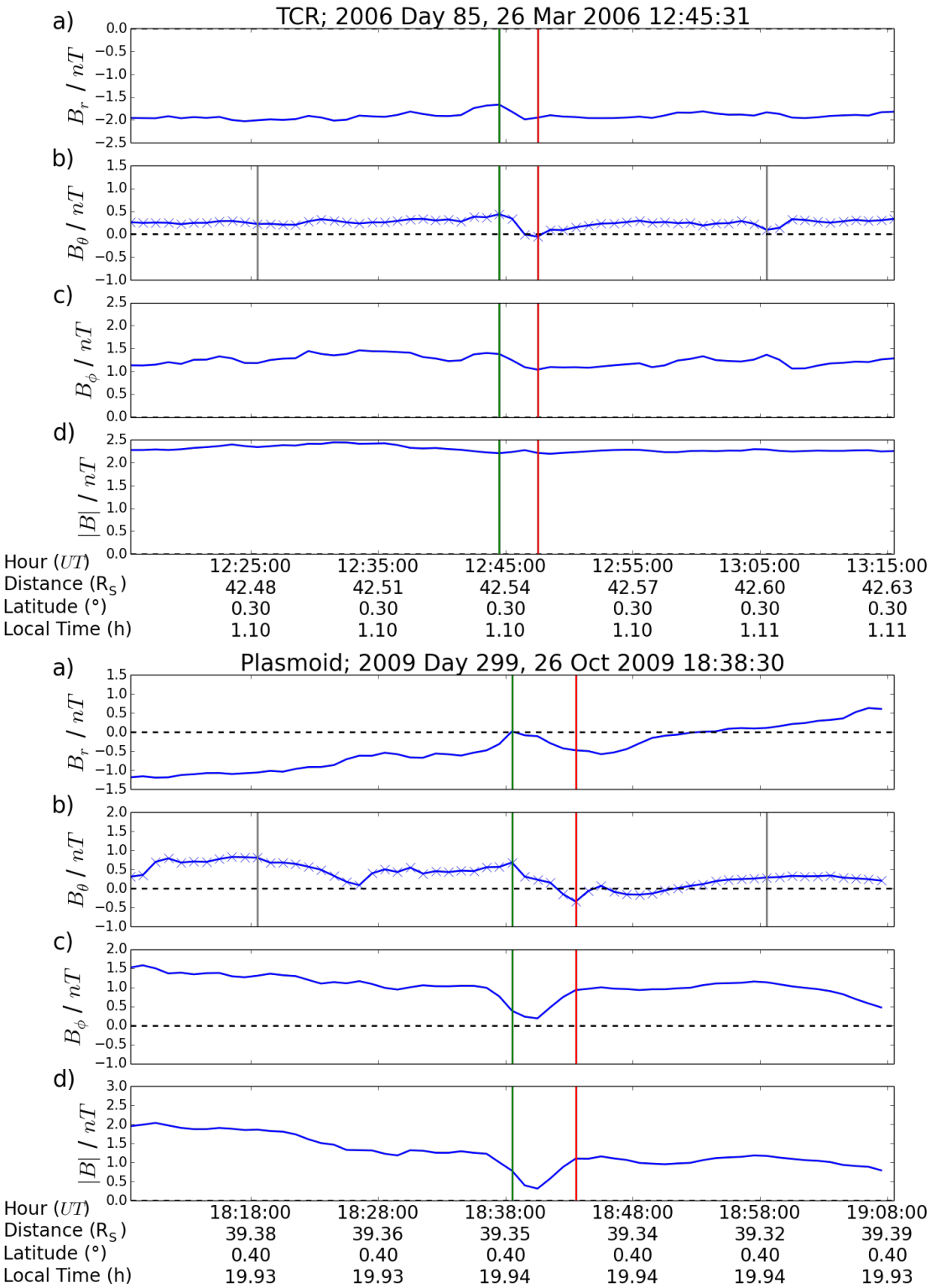

FIGURE 4.3: Algorithm outputs showing example TCR (top) and plasmoid (bottom) detections. The magnetic field is given in KRTP coordinates. The green and red lines give the algorithm's defined start and end of the events respectively. The faint grey vertical lines give the extent of the time windows (20 minutes) either side of the event that are searched for the beginning and end of the event.

The algorithm then searches for the start and end of the deflection within a 20 minute time window (either side of each B_θ crossing). The aim of this step is to select the local maxima and minima of B_θ as the start and end of the event, as in *Slavin et al.* [1993] and more recently *Jackman et al.* [2014b] and *Vogt et al.* [2014]. The 20 minute window was created to balance minimising the computational time while allowing the correct limits to be found for known events (i.e. from *Jackman et al.* [2014b]).

If the B_θ deflection is northward, i.e. the value of B_θ decreases, then local maxima of B_θ (places where the B_θ value is greater than at adjacent time points) up to 20 minutes before the B_θ crossing are selected as potential starts. On the other side of the B_θ crossing the local minima of B_θ (where the B_θ values are less than at their adjacent time points) are selected as potential ends. The opposite holds true if the deflection is southward; i.e. has increased the value of B_θ.

All pairings of potential starts and stops are then checked. A second order polynomial is least squares fitted between each pairing. The value of r^2 (the coefficient of determination) is calculated for each fit using Equation 4.3.

$$r^2 = 1 - {\sum_0^N (B_\theta^t - f_t)^2} \Big/ {\sum_0^N (B_\theta^t - \bar{B_\theta})^2} \tag{4.3}$$

Where $t = 0$ is the start and $t = N$ is the end, B_θ^t is the value of B_θ for point t, $\bar{B_\theta}$ is the average of B_θ between the start and end and f_t is the value of the fitted polynomial for point t. If the value of the r^2 calculated is less than 0.9 (the quality of the fit to the data is poor) then the start/end pair is rejected. For all pairs that have a value of $r^2 \geq 0.9$ a value of ΔB_θ is calculated (the 'size' of the event), using Equation 4.4.

$$\Delta B_\theta = y_N - y_0 \tag{4.4}$$

The start/end pair with the highest absolute value of ΔB_θ is then selected. The first condition on ΔB_θ for the event to be accepted is:

$$\frac{|\Delta B_\theta|}{B_{\theta RMS}} \geq 1.5 \tag{4.5}$$

Where the RMS (Root Mean Square) of B_θ is calculated for a period extending 30 minutes either side of the B_θ crossing. This criterion was selected as it was shown to preferentially select only significant deflections. The second criterion on event acceptance is that $|\Delta B_\theta| \geq 0.25\, nT$. This lower limit was imposed after inspection of a selection of false positive detections. The time window for which the RMS is calculated is the full

time plotted on Figure 4.3. The vertical grey bars show the maximum possible length of the event.

This method produces a list that often contains duplicates and pairs of events. Duplicates are cases where the events have the same orientation and overlap. 'Pairs' are, for example, a northward turning immediately followed by a southward turning. This combination can occasionally be erroneously interpreted by the algorithm as a tailward moving plasmoid followed immediately by a dipolarization, however the correct interpretation (in this example) is that of a tailward moving plasmoid followed by the return of the field to background (small and southward) levels. To deal with these a series of rules were developed. Any events that overlap, or occur with the opposite orientation within one duration (difference in time between the start and the end of the event) of the start or the end of the event are grouped together. The event with the largest ΔB_θ in the group is selected. If another in the group has a value of ΔB_θ within 10% of the largest event then they are inspected by eye to pick the correct deflection. In the vast majority ($> 95\%$) of cases the largest detection was confirmed by eye to correspond to the correct deflection.

The events that pass all of the above criteria were then inspected by eye, and the false detections removed. False detections are due to the phenomena mentioned in Section 4.2.2; mainly flapping of the plasma sheet and encounters with the magnetopause or LLBL. Observing the field over a period of several days around the identified event allowed those related to the bulk flapping motion of the current sheet to be distinguished; they are related to longer-term quasi-sinusoidal trends in the north-south component of the field [*Nakagawa and Nishida*, 1989; *Jackman et al.*, 2009a]. Magnetopause crossings on the other hand, were discarded using the method discussed in Section 4.2.3. Encounters with the LLBL can be typified by a clear change in the field regime either side of a large, rapid rotation of the field [*Masters et al.*, 2011].

During the inspections several events were found to have been detected with the opposite orientation to that which may have been chosen by eye. They were noted (and appear in Table 4.2), but do not appear in the rest of the analysis.

4.3.2 Failed Criteria

Many different criteria were tested and later discarded in favour of the conditions outlined above. For example a threshold on ΔB_θ was tested that varied with radial distance, a similar function to the way the lobe field reduces with radial distance down the tail [*Jackman and Arridge*, 2011b]. This was found to give some good results; however as it

was not dependent on the local properties of the field it missed many of the small scale events, especially TCRs, that this study targeted.

Another threshold that was tested involved a limit that was linked to the mean absolute value of B_θ. This gave reasonable results, but it showed no distinct advantages over the threshold given in Equation 4.5.

Another technique considered in place of the algorithm was a wavelet analysis/fitting method. This requires a base 'wavelet' which is manipulated to attempt to match the data and the quality of the fit is then evaluated. This method was discarded as it may have too tightly constrained the type of event that was found. For example, there are two similar, but distinct, signatures/types of B_θ deflection observed depending on whether open flux is closed in the course of the reconnection event, discussed in detail by *Jackman et al.* [2011]. Additionally, the method involves fitting the template wavelet for a range of time scales; occasionally the best fit found was not the same as the event that would be identified by eye. This result could be due to degeneracies in the wavelet fit, where one or more length scales satisfactorily fit the data and the technique simply picks the incorrect one.

Overall, the algorithm presented in Section 4.3.1 represents an efficient method to automate the search for reconnection events in a planetary magnetotail.

4.4 Catalogue

In total the algorithm made 2388 detections in the 2006, 2009 (day 280 onwards) and 2010 Cassini magnetometer data. A summary of the algorithm detections is presented in Table 4.2. Of the 2388 detections, 2094 (88 %) were confirmed by eye as likely corresponding to reconnection events. This leaves 294 events (12 %) which were rejected. Of these rejections, 72 (24% of the subset) are believed to be detections of reconnection related events, but with the incorrect orientation (and so represent the return of the field to normal levels or the run-up to an event), where the 'correct' detection was erroneously excluded by the process outlined in Section 3.1. With this in mind the false positive fraction could be said to be around 9% (222 Events). The false positive events were thought to be caused by encounters with the LLBL or flapping magnetotail current sheet. All figures and analysis from this point will focus solely on those events confirmed by eye. This large number of events provides an excellent base for statistical analysis. Importantly, the dataset covers a large range of local times, radial distances, latitudes and Kronian season, allowing the differences to be explored.

TABLE 4.2: Algorithm Results

	Tailward	Planetward	Bad Orientation	False Positives	Clusters (Isolated)
Total	1382 (58%)	712 (30%)	72 (3%)	222 (9%)	381 (220)
2006	693 (59%)	354 (30%)	21 (2%)	105 (9%)	171 (74)
2006 (Pre 200)	187 (64%)	85 (29%)	6 (2%)	13 (5%)	65 (47)
2006 (Post 200)	506 (57%)	269 (31%)	15 (2%)	92 (10%)	106 (27)
2009 (Post 280)	158 (55%)	87 (30%)	8 (3%)	35 (12%)	55 (42)
2010	531 (57%)	271 (29%)	43 (5%)	82 (9%)	155 (104)

Of the 86 events published in the previous study by *Jackman et al.* [2014b], 77 (90%) were independently re-found by the algorithm. Further inspection of the events not found revealed that several are rejected by the exclusion of data around magnetopause crossings (±15 minutes of *Pilkington et al.* [2015] magnetopause encounters).

Recently *Arridge et al.* [2015b] uncovered an encounter of the Cassini spacecraft with a reconnection diffusion region. During this encounter they identified several secondary islands, in addition to the crossing of the x-line itself. The algorithm recovers three tailward detections before the crossing of the x-line, in agreement with their identification of secondary islands. It then recovers the x-line crossing itself, along with a further secondary island some time after. A detailed search of the catalogue for further diffusion region encounters will form the basis of future work.

The final column of Table 4.2 shows the number of event 'clusters' identified. A cluster has been defined as a group (or chain) of events that occur within 180 minutes of their nearest neighbour, as in *Jackman et al.* [2014b] (scaled for the Saturn system from the value of 30 minutes used by *Slavin et al.* [1993]). It can be seen that although 2094 detections were made in total; there were 381 groups of more than one event. These clusters generally consisted of $2-6$ events. Only 220 of the events were found to occur in isolation. For example, all five detections relating to the diffusion region identified by *Arridge et al.* [2015b] are classified as one cluster. In the same manner, the chain of events highlighted by *Jackman et al.* [2014b] in their Figure 5, where they see a procession of four tailward events, is classified as one cluster. So the results of the algorithm can be thought of as relating to at least 601 'episodes' of reconnection (381 clusters + 220 isolated events).

Table 4.3 displays some of the statistical properties of the event catalogue. Of the 2094 events identified by the algorithm 66% are inferred to be tailward of the x-line, from the orientation of the field deflection. In theory, given appropriate viewing geometry, symmetric either side of a reconnection x-line, equal numbers of each orientation of event should be observed, assuming reconnection events produce both a plasmoid (tailward)

Table 4.3: Event Details

	All Events	Tailward Events	Planetward Events
Number	2094	1382 (66%)	712 (34%)
Mean Duration (min)	7.8	9.2	5.3
Mean $\|\Delta B_\theta\|$ (nT)	0.98	0.96	1.01

		Near Plasma Sheet	TCR	Near Plasma Sheet	TCR[a]
Number	2094	1011	371	484	228
Mean Duration (min)	7.8	8.6	10.7	5.6	4.6
Median Duration (min)	6.0	6.0	8.0	4.0	4.0
Durations (min)	1 - 36	1 - 35	1 - 36	1 - 31	1 - 20
Mean $\|\Delta B_\theta\|$ (nT)	0.98	1.07	0.67	1.16	0.69
Median $\|\Delta B_\theta\|$ (nT)	0.83	0.94	0.57	0.99	0.59
$\|\Delta B_\theta\|$ (nT)	0.25 - 4.71	0.25 - 4.24	0.25 - 2.22	0.26 - 4.71	0.25 - 2.81
Radial Distances (R_S)	15.0 - 68.3	15.5 - 68.2	18.5 - 68.3	15.0 - 65.0	16.6 - 68.2
Local Times (h)	18.05 - 5.12	18.02 - 5.11	18.20 - 5.11	18.02 - 4.12	18.29 - 4.49

[a] Distinctions made using the criteria on the magnetometer readings outlined in Section 2.4

and dipolarization (planetward). The imbalance between the detections could suggest that Cassini is more often tailward of the reconnection site during the orbits selected.

4.5 Occurrence, Location and Morphology

4.5.1 Event Occurrence and Location

From Table 4.3 it can be seen that events are, in general, observed at all local times and radial distances sampled by Cassini. However, any statistical dependence of events on location and season will now be explored.

4.5.1.1 Event Occurrence

Figure 4.4 shows plots of the north-south component of the field at one minute time resolution over several orbits, with the confirmed event detections marked on as vertical bars. Each panel has been selected to show different seasons, latitudes or local times. Panel a) shows the early 2006 low latitude dawn flank orbits, recorded during southern

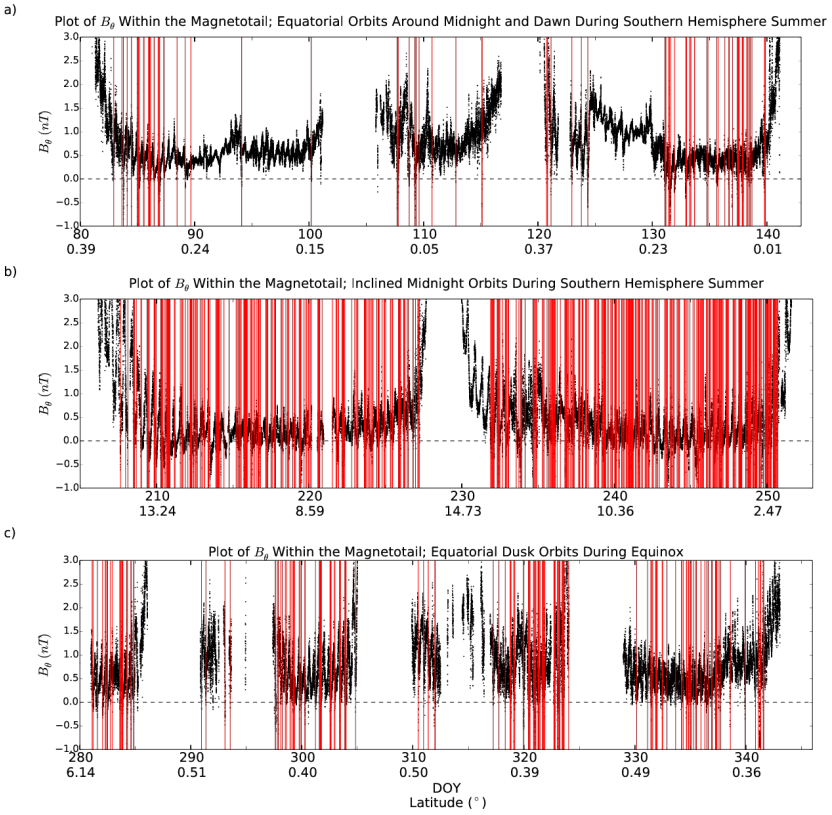

FIGURE 4.4: Plot showing the variation in the north-south component of the magnetic field (B_θ in KRTP co-ordinates) during selected orbits. Each panel of the plot shows several orbital rotations of Cassini between perikrones. Times when Cassini was outside of the magnetosphere, near Titan or performing a SCAS interval have been removed from the data. Red vertical bars represent reconnection events identified by the algorithm and then confirmed by eye. Panel a) shows equatorial orbits during southern hemisphere summer around dawn and midnight during which time Cassini was mostly within the lobe. Panel b) shows more inclined orbits during southern hemisphere summer around the midnight local time sector. Panel c) displays equatorial dawn orbits during equinox.

hemisphere summer (where Cassini was in similar locations to positions 2 and 3 of Figure 4.2a)) . Panel b) shows the orbits from later in 2006 during which time the midnight region of the magnetosphere was explored at a slightly higher latitude (similar to positions 1 and 2 in Figure 4.2a)). Finally, Panel c) shows dusk flank equatorial orbits performed in 2009, around Kronian equinox (where Cassini was found in a similar environment to position 3 in Figure 4.2b). Any data recorded when Cassini was outside of the magnetosphere, close to Titan, within 15 R_S of the planet or during a SCAS interval have been removed. Examples of intervals where data were removed on panel a) include between days 102 and 106 (where Cassini was within the magnetosheath), and between 117 and 119 (where Cassini was near peri-krone and closer than 15 R_S). Each panel of the plot shows several orbits of Cassini between the points of closest approach to Saturn.

Plotting the catalogue of events in this manner helps to highlight a few key aspects. Firstly, a regular oscillation of B_θ can be seen in all panels. This is likely related to the flapping of the hinged current sheet around and perhaps over the spacecraft, discussed in detail by *Arridge et al.* [2008, 2011a] and *Jackman et al.* [2009a]. Secondly, there is a clear change in both the number and frequency of events between the different magnetospheric environments explored by Cassini. Panel a), detailing dawn flank equatorial orbits performed during southern hemisphere summer, shows a low occurrence rate and an uneven distribution of event detections. During these orbits only around 8% of the time was spent within the plasma sheet (from Table 4.1). The low occurrence rate could be evidence of sporadic reconnection between midnight and dawn. The patchy nature of the observations could also be a result of the variable distance to the plasma sheet over this period, as the plasma sheet flaps up and down near the spacecraft. When Cassini is closer to the plasma sheet it could become more likely to observe reconnection products.

An interesting period included in this plot is around day 127, shown on right of panel a). For a few days around day 127 the field strength increases, with little reconnection observed. This buildup is then lost, accompanied by a flurry of reconnection events. *Jackman et al.* [2010] related this field signature to the build up of open flux in the tail lobes following solar wind compression induced dayside reconnection. This open flux is later closed through a cascade of reconnection events, many of which are picked up by the algorithm. Recently, a solar wind compression event has been shown to result in sustained lobe reconnection, inferred from the plasma sheet composition [*Thomsen et al.*, 2015].

Comparatively panel b) shows a much larger number and frequency of events. The orbits shown here are more inclined (with latitudes up to 15°) and centre around midnight. Due to the hinging of the current sheet at Saturn during southern hemisphere summer Cassini is more often located within the plasma sheet during these orbits (lobe residence fraction decreases from 92% to 74% compared to the orbits displayed in panel a)). Panel b) contrasts once again with panel c), which shows equatorial dusk flank observations (during equinox), again mostly within the plasma sheet, but with a lower rate of observation than panel b). The events in panel c) are also seen more consistently and appear less clustered than they are in panel a).

The difference between panels a) and b) could be explained by the different magnetospheric environments encountered, i.e. the latitude differences illustrated by positions 1 and 3 in Figure 4.2a. If this is the case then it suggests that the *in-situ* viewing conditions are highly latitude-dependent, and thanks to the hinging of the current sheet, season dependent. Comparing panels b) and c) the main difference in orbit is the local

time region explored, midnight in panel b) and dusk in panel c). The latitude difference is compensated for with the seasonal change, meaning both data sets are collected close to or within the plasma sheet. This could suggest an increased frequency of events around the midnight region of the magnetotail, with more infrequent but steady loss down the dusk flank. The dependence on distance to the plasma sheet will be explored in the next section.

As outlined in Section 4.2.3 a definition of the 'viewing region' is required when exploring the frequency of events observed. This study defines the viewing region as any location on the nightside of the planet, at a distance of more than 15 R_S from Saturn, within the magnetosphere, outside of the area of Titan's influence and not concurrent with a spacecraft SCAS manoeuvre. Discarding data not fulfilling these criteria leaves a total of 415 days worth of magnetometer observations. This equates to an average reconnection rate of 5.0 events, or 1.4 clusters/episodes of reconnection per day. However, this does not take into account the different seasons and latitudes explored during this time. For example, during southern hemisphere summer when Cassini was closer to the hinged plasma sheet (in the later half of 2006), a subset of which is seen in panel b), the reconnection rate reached 10.2 events per day.

4.5.1.2 Event Frequency Across the Magnetotail

The occurrence of reconnection related events will be further examined: Figure 4.5a shows the spatial distribution of the number of events detected including plasmoids, TCRs and dipolarizations. Figure 4.5b shows the coverage of Cassini inside the viewing region during the selected periods, and Figure 4.5c combines these to show the number of events normalized to the observing time within each sector. It is important to note that these figures are projected on the equatorial plane of the KSM system, and so the latitude of the orbits, and the magnetospheric environments encountered, are not accounted for.

It should be noted that the viewing region, as defined in Section 4.2.3 above and illustrated in Figure 4.5b, includes broad magnetotail coverage and thus incorporates both lobe and plasma sheet intervals. Figure 4.5b shows that a large proportion of the data selected for this study lie on the dusk flank, namely those orbits performed during 2009 and 2010. Meanwhile, Figure 4.5c is particularly useful when attempting to understand if a large number of event detections seen in Figure 4.5a reflects an increase in the occurrence frequency of events, or is due to the large amount of time Cassini spent sampling that region.

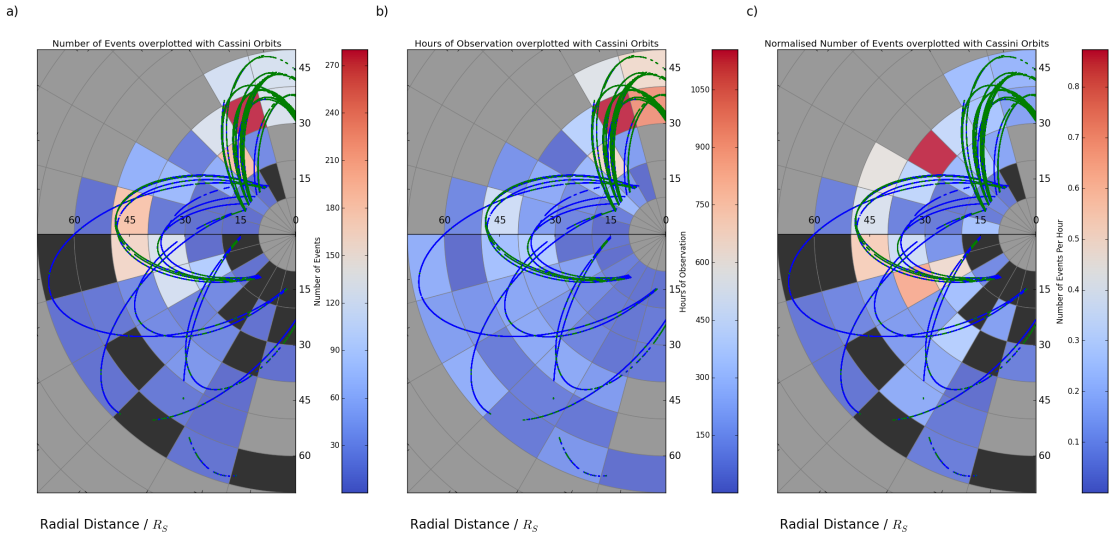

FIGURE 4.5: Colour coded maps with 10 R_S radial and 1 hour local time bins. Maps are shown projected on the equatorial plane of the KSM system, with the Sun off to the right. Superimposed on the figure are the orbital trajectories of Cassini for 2006, late 2009 and 2010; within the viewing region. The blue sections of the trajectory represent times identified as within the lobe, while the green orbits outline times when Cassini is closer to or within the plasma sheet (from the criteria in Section 4.2.4). Black regions show sectors where data were collected within the viewing region, but no events were detected. Meanwhile, grey segments show areas where no data within the viewing region were collected. (a) The number of reconnection events seen in each sector. (b) The number of hours Cassini spent inside the viewing region within that sector. (c) The number of reconnection events normalized to observation time.

Figure 4.5a displays a large number of events around dusk and midnight (during the symmetric midnight orbits near the plasma sheet), with considerably lower numbers seen on the dawn flank. The differences between the dawn and dusk regions are slightly reduced when the orbit occupation time is taken into consideration (in Figure 4.5c), where it appears that the majority of the events occur around or slightly post midnight. It is unclear from these figures whether the lower frequency of events on the dawn flank is due to inherent differences on the dawn flank, or a result of the low latitude, and lobe occupation, of these orbits (see Figure 4.4a for an example of typical orbits during these intervals). As previously recognized, the orbits around the dawn flank (recorded during the early part of 2006) were made at a lower latitude, and so were further from the position of the hinged plasma sheet during the southern hemisphere's summer. This is reflected in the large proportion of the trajectory that is coloured blue, indicating that Cassini was most likely within the lobe (from the criteria in Section 4.2.4). The trajectory of the more symmetric midnight orbits, which observed the higher frequency of reconnection related events, is mostly coloured green, indicating likely residence within or close to the plasma sheet. This would suggest that the difference in observation frequency could be, at least in part, due to the different viewing conditions found during the orbits.

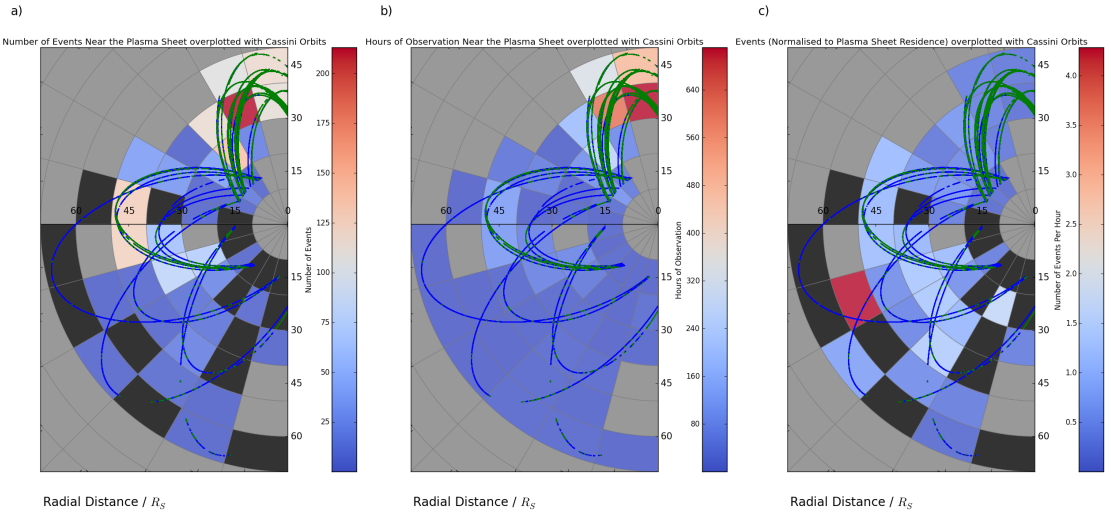

FIGURE 4.6: Colour coded maps with 10 R_S radial and 1 hour local time bins. Maps are shown projected on the equatorial plane of the KSM system, with the Sun off to the right. Superimposed on the graph are the orbital trajectories of Cassini for 2006, late 2009 and 2010; within the viewing region. The blue sections of the trajectory represent times identified as within the lobe, while the green orbits outline times when Cassini is closer to or within the plasma sheet (from the criteria in Section 4.2.4). Black regions show sectors where data were collected near or within the plasma sheet, but no events were detected. Meanwhile grey segments show areas where no data near the plasma sheet were collected. (a) The number of reconnection events near the plasma sheet seen in each sector. (b) The number of hours Cassini spent near or within the plasma sheet in that sector. (c) The number of reconnection events (near the plasma sheet) normalized to observation time near the plasma sheet.

To explore this difference in more detail Figure 4.6 looks solely at those events and parts of the orbit during which Cassini was located within or close to the plasma sheet (from the criteria in Section 4.2.4). Figure 4.6a shows that, as in Figure 4.5a, the majority of detections are made on the dusk flank or around midnight. Comparing this to Figure 4.6b it can be seen that this correlates with the areas where Cassini spent the most time surveying the plasma sheet vicinity. Looking at the normalized rate in Figure 4.6c it is clear that when this is taken into account the rate of detection peaks post midnight. The drawback to this method is that plasma sheet occupation is not always independent of the event detections. In other words, the fact that the events themselves can cause the plasma sheet to bulge over spacecraft (changing the local conditions interpreted via the criteria in Section 4.2.4) can have an effect on the observed occurrence rates. However, overall Figure 4.6 shows a steady increase in the frequency of event observations moving from dusk around to the post-midnight orbits. This could suggest that reconnection becomes more likely as the stretched flux tubes rotate through midnight. A similar interpretation was made by *Thomsen et al.* [2013] in their survey of plasma data. Similarly at Jupiter *Vogt et al.* [2014] found reconnection signatures most frequently in the dawn sector, though they note there could be other explanations for this.

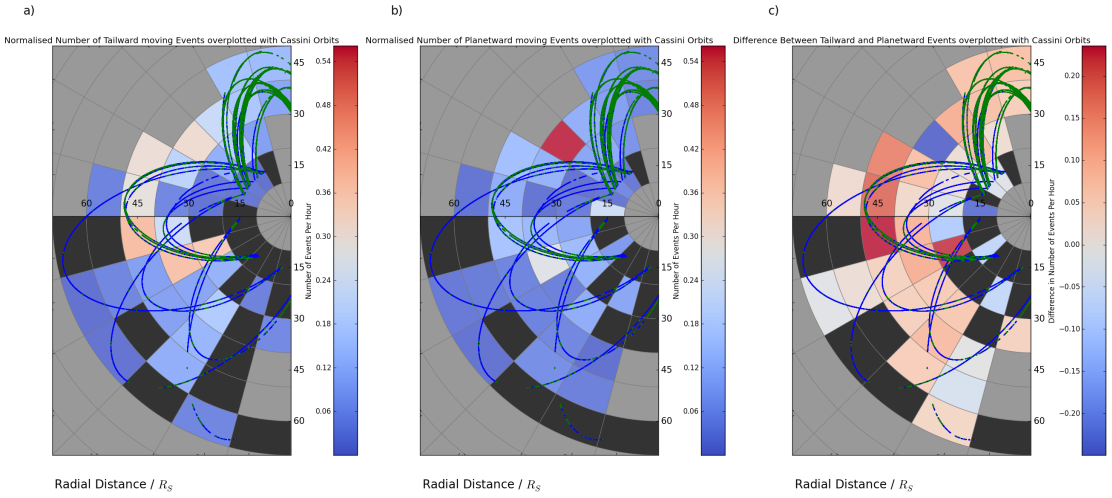

FIGURE 4.7: Maps comparing the frequency of tailward (a) and planetward (b) moving events with 10 R_S radial and 1 hour local time bins; event frequency is normalized to time spent in the viewing region within that sector. Maps are shown projected on the equatorial plane of the KSM system, with the Sun off to the right. Superimposed on the graph are the orbital trajectories of Cassini for 2006, late 2009 and 2010; within the viewing region. The blue sections of the trajectory represent time identified as within the lobe, while the green orbits outline times when Cassini is closer to or within the plasma sheet. Black regions show sectors where data was collected within the viewing region, but no events were detected. Meanwhile, grey segments show areas where no data within the viewing region was collected. Both (a) and (b) are normalized to the same color scale for ease of comparison. Panel (c) shows the map in (a) minus the map in (b); the difference between the two.

It should be noted that the trends discussed above persist if the bin sizes are adjusted.

4.5.1.3 Event Occurrence: Tailward and Planetward Events

Figures 4.7a and 4.7b show the same type of map as Figure 4.5c but for tailward and planetward moving detections respectively. If the x-line was typically located within a relatively narrow range of radial distance then this might be expected to show planetward events preferentially occurring closer to the planet, with tailward events regularly found further downtail (as has been observed at Jupiter [c.f. *Vogt et al.* [2010]]). However this is not strictly observed in the figure. Events inferred, from the sign of the B_θ deflection, to be planetward of the x-line are observed at radial distances from 18 to 68.2 R_S, while those inferred to be tailward of the x-line are observed at radial distances of 18 to 68.3 R_S. This spread of planetward and tailward detections suggests a variable x-line. The inconsistent sampling conditions encountered by this study could also result in a such a spread, and complicate the search for a statistical separatrix.

Figure 4.7c shows the difference between the maps in Figure 4.7a and Figure 4.7b. Positive (red) values show sectors where more (normalized) tailward events are observed, while negative (blue) sectors show areas where planetward events are observed more

often. The change from positive (red) to negative (blue) shows the region where the x-line is most often located lies approximately between 20 and 30 R_S (pre-midnight). If correct, this result would be approximately consistent with the modelling of *Jia et al.* [2012], which suggested a range of x-line locations between 25 and 40 R_S, and the work of *Arridge et al.* [2015b] who reported an encounter with the diffusion region associated with reconnection at approximately 29 R_S. *Mitchell et al.* [2005] also suggested that reconnection could be playing a significant role in observed ion heating between 20 and 30 R_S. Though the results are broadly consistent, the presence of planetward moving events up to 68 R_S downtail suggests there could be other factors which control the x-line location such as external solar wind changes or processes internal to the magnetosphere.

4.5.2 Event Morphology

The mean durations and B_θ deflections of the different classifications of events are shown in Table 4.3. TCR detections on both sides of the reconnection x-line are observed to have a smaller ΔB_θ deflection than their plasmoid/dipolarization counterparts within the plasma sheet. This can be explained as TCRs are an indirect detection of the main event occurring within the plasma sheet.

Tailward moving TCRs are seen to have a larger average duration than plasmoids (those detections observed within the plasma sheet), the duration being the time between the northward and southward peaks. This could be explained as TCRs represent the draping of the magnetotail lobe field over the plasmoids (or dipolarizations), so they typify a wider disturbance rather than a direct encounter.

4.5.2.1 Superposed Epoch Analyses of Events

Superposed Epoch Analyses (SEAs) of the event detections inferred to be tailward of the reconnection site can be seen in Figures 4.8a and 4.8b, which depict the results for 735 plasmoids and 296 TCRs respectively. These do not represent the full catalogue of events, but only those which cross through $B_\theta = 0$ (73% and 80% of the total detections respectively). This has been done to facilitate comparison with previous studies, which had the requirement that the event pass through zero. The events have been aligned such that the point before which the trace becomes negative is at $t = 0$. The magnetic field is presented in KRTP co-ordinates, with the second panels (showing B_θ) being double the height and range. The average traces are plotted with thick black lines, the first and third panels being the average of the absolute values of the B_r and B_ϕ components to ensure that they do not average to zero. In the B_θ panel the red shaded regions sketch the $\pm 1\sigma$ extent of the results, while the individual event traces have been

included in green to demonstrate that there is a significant spread in the signatures. The split between plasmoids and TCRs has been made using the lobe criteria detailed in Equations 4.1 and 4.2 in Section 4.2.4. As in the previous sections; any event during which the lobe criteria are violated is deemed to be a plasmoid in this classification scheme.

The first point of interest in both Figures 4.8a and 4.8b is that though the individual B_θ traces appear noisy before the event, the average (thick black line) corresponds well to the steady-state small and southward field noted by *Jackman and Arridge* [2011b] as characteristic of the background field in the magnetotail. Secondly, on average no sharp southward turn is seen at the start of events (in contrast to the idealized schematics in Figure 4.2) leaving only the northward turning. To explain this asymmetry it is possible that the events in our catalogue are those linked to reconnection at a "near-planet" x-line. Scaling the "near-planet" x-line at Earth (typically found around $\sim 30\,R_E$ [*Imber et al.*, 2011]) using the magnetopause standoff distances results in a predicted analogous "near-planet" x-line distance of $\sim 75\,R_S$ at Saturn. The terrestrial magnetosphere also contains a "distant" x-line which typically lies $\sim 100 + R_E$ downtail [*Slavin et al.*, 1985]; this scales to over $250\,R_S$ downtail at Saturn. If the picture in the Kronian magnetotail is similar to that at Earth, then the orbits performed by Cassini do not often reach far enough down-tail to reach the distant x-line (c.f. Figure 16.1 [*Keiling et al.*, 2015]). For a spacecraft trajectory which only samples the near-planet region the asymmetry in the B_θ deflection results from the trajectory of the spacecraft through the magnetic structure; the effects of which have been discussed by *Borg et al.* [2012] and *Jackman et al.* [2014b]. Furthermore, *Cowley et al.* [2015] argues that the asymmetric magnetic field signatures identified by *Jackman et al.* [2014b] only represent the spacecraft's traversal of a small planetward section of the large extended plasmoid structure.

Figure 4.8a shows that the average SEA ΔB_θ for plasmoids is just under twice the size of the average SEA ΔB_θ for TCRs in Figure 4.8b ($0.60\,nT$ compared to $0.37\,nT$), as would be expected. This relationship is also seen in the mean values calculated from the catalogue (discussed above and shown in Table 4.3).

In the average traces, as in the algorithm discussed in Section 4.3.1, the start and the end of the event have been defined as the local north-south maxima of the field. These have been indicated on Figures 4.8a and 4.8b by the blue and red vertical lines. For tailward moving plasmoids the start of the event is -8 minutes, and the end is at $+1$ minutes giving a duration of 9 minutes. The method of measuring duration is not particularly appropriate for this plot as the lack of a significant southward peak means the start is not well defined. The same is true for Figure 4.8b, detailing the tailward moving TCRs, where the duration of the average event is found to be 11 minutes (from -10 to $+1$

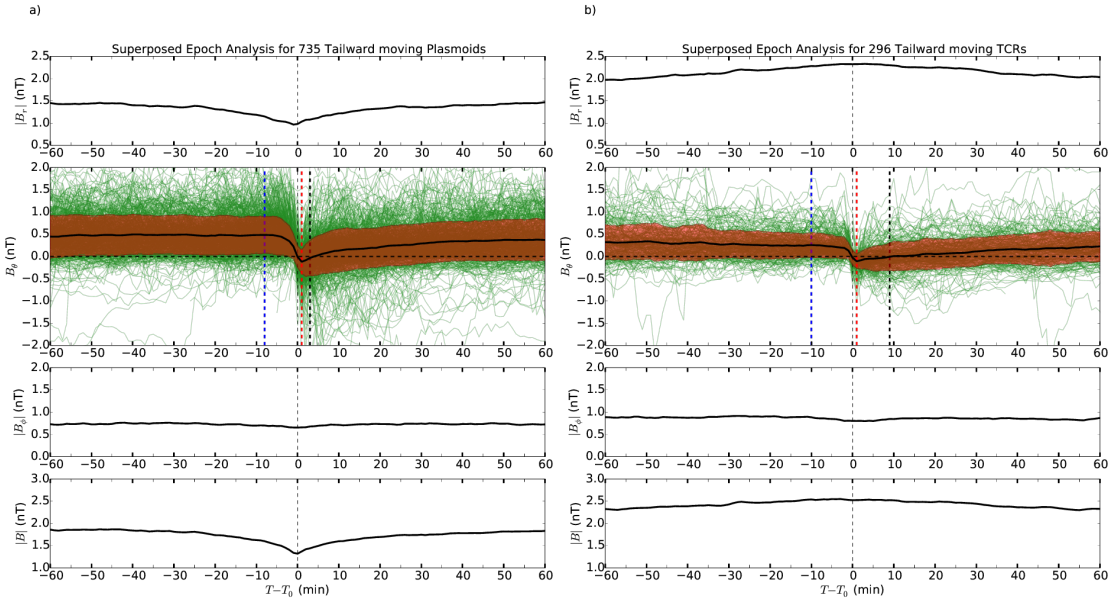

FIGURE 4.8: Superposed epoch analyses of (a) Plasmoids and (b) TCR events inferred to be tailward of the reconnection site. The magnetic field is given in the KRTP coordinate system, and the vertical scales are identical for both panels. The average traces for each component of the field are plotted with a thick black line. For the radial and azimuthal components the average absolute values are plotted as they can be positive or negative. The second panels (showing B_θ) are double the size and range for both plots to illustrate the spread of field values. Also on the second panels, the faint green lines show the individual event traces that have been averaged while the red shaded regions show the $\pm 1\sigma$ extent of the results. The blue and red vertical dashed lines indicate the start and end of the event in the averaged trace, defined in the same way as in the algorithm, i.e. the largest maxima/minima either side of the event. The black dashed line marks the point at which the trace becomes southward again; the end of the (small) PPPS in a.

minutes). In the same plot, the compression of the TCR in the $|B|$ component of the field is observed to be much longer lived, up to 80 minutes. This could indicate that plasmoid release occurs, on average, $\sim$ 20 - 30 minutes prior to the TCR event time.

The top (B_r) panels of Figures 4.8a and 4.8b both show consistent values of B_r before and after the event disturbance. This average background B_r can be seen to be around $1.4\,nT$ for plasmoids and $2.0\,nT$ for TCRs (representative of the lobe). At the centre of the current sheet $B_r = 0$; in line with previous studies $|B_r|$ can be used as a rough proxy for distance from the current sheet, assuming Harris sheet geometry [*Runov et al.*, 2006; *Arridge et al.*, 2008; *Jackman et al.*, 2011]. By this reasoning it can be confirmed that TCRs are, on average, seen at a greater distance from the centre of the current sheet, as would be expected.

The average TCR signature, shown in Figure 4.8b, shows a change in the value of $|B|$ during the event of $\sim$ 8%. This is approximately consistent with the $1 - 10\%$ typical compression ratios reported at Earth [*Slavin et al.*, 1993, 2005]. The vertical extent of

plasmoids, as inferred by their impact parameter, will be the focus of future work to examine the interior morphology of these structures.

The $|B_\phi|$ panel of Figure 4.8a shows no major deviations during the average plasmoid passage. This may be consistent with a loop-like picture of plasmoid field structure, as opposed to a flux rope-type arrangement. Additionally the $|B|$ component of the field shows a marked reduction in the field during the event, again symptomatic of loop-like structures (rather than flux rope-type).

The average trace in Figure 4.8a does not display a long period where B_θ remains northward following the designated end of the event, in contrast with previous studies. The extended northward interval has been previously observed and interpreted as a Post Plasmoid Plasma Sheet (PPPS) [*Richardson et al.*, 1987; *Jackman et al.*, 2011, 2014b]. This is an interval during which open flux in the magnetotail is closed following plasmoid passage down the magnetotail. Previously, *Jackman et al.* [2011] observed a 58 minute long northward interval following the average event, while *Jackman et al.* [2014b] reported 27 minutes more recently based on a larger catalog from the deepest tail orbits of 2006. In contrast, Figure 4.8a only shows a two minute northward excursion. If the sample of events plotted is limited to those found in 2006 (the same time period as explored by *Jackman et al.* [2014b]) then this increases to a 5 minute interval. The simplest explanation for the absence of a large statistical PPPS in this new catalogue is the inclusion of many smaller events (in terms of ΔB_θ and duration); the largest deflections of the field are easier to spot and therefore more likely to have been selected in the past. Furthermore, previous by-eye studies were perhaps more likely to pick out events with a significant PPPS, as they would stand out more.

Though there is no PPPS as such in Figure 4.8a, the gentle sloping recovery (whereby the field takes 40 to 50 minutes to return to background levels) is consistent in shape to the asymmetry reported by *Jackman et al.* [2014b].

4.6 Discussion

The combination of a larger data set encompassing a greater proportion of the Kronian magnetotail, including coverage during different seasons, and a new automated method ideal for identifying small scale reconnection related events allows insight into the global dynamics of the Kronian magnetosphere.

4.6.1 Mass Budget

The contribution of the inferred reconnection events to mass circulation at Saturn will now be examined. As discussed in Chapter 2, there are three main ways in which plasma can enter the magnetosphere: from the solar wind, from the Kronian ionosphere or from ionized neutrals originating from the moons and rings [See *Blanc et al.* [2015] for a review]. The main plasma source for the Kronian magnetosphere is the moon Enceladus, from which the majority of the water group ions originate [e.g. *Hansen* [2006]; *Sittler et al.* [2008]]. The rings also contribute a small fraction of the detected water group ions, while Titan is a (smaller) source of Nitrogen and Hydrogen ions [*Smith et al.*, 2007, 2008; *De La Haye et al.*, 2007], including a significant amount of H_2+ ions [e.g. *Thomsen et al.* [2010]]. Light ions are generally thought to originate from either Saturn's ionosphere, Enceladus, Titan or the solar wind, depending on their location within the magnetosphere [*Glocer et al.*, 2007; *Felici et al.*, 2016]. The majority of the neutrals produced from the rings or moons escape the Kronian system, but between $\sim$ 10% [*Fleshman et al.*, 2010] and 30% [*Jurac and Richardson*, 2005] are ionized, leading to a plasma mass loading rate of between 10 and 220 kgs^{-1}. In order to lose just 100 kgs^{-1} *Bagenal and Delamere* [2011] calculated that plasmoids would need to be ejected at a rate of 200 per day. This calculation was based on a plasmoid volume of $(10\,R_S)^3$ with a density of 0.01 cm^{-3} (18 amu ions).

Reliable plasma moments are not available for the majority of events in the catalogue, therefore a conservative value of 300 kms^{-1} is taken for the plasmoid velocity (based on the mean value found for 29 events in the study by *Jackman et al.* [2014b]). This velocity estimate is combined with the range of durations observed with the new catalogue, resulting in a range of plasmoid lengths between 0.30 and 10.45 R_S. For the height of the plasmoid a value of 7 R_S is used (as in *Cowley et al.* [2015]); to account for the bulging of the plasma sheet (whose quiescent thickness has been observed to be around 4 R_S [*Kellert et al.*, 2009; *Arridge et al.*, 2011a; *Sergis et al.*, 2011; *Szego et al.*, 2012]). A value of 80 R_S has been assumed as the upper limit to the azimuthal extent of a plasmoid. This represents the approximate width of the Kronian tail at $X_{KSM} = -40\,R_S$ from the model of *Pilkington et al.* [2015] (with a relatively high solar wind dynamic pressure of 0.1 nPa). Combining these values with a density of 0.1 cm^{-3} (16 amu ions) [*Thomsen et al.*, 2014a] gives a range of plasmoid masses between $9.8 \times 10^4\,kg$ and $342 \times 10^4\,kg$. These masses correspond to a required plasmoid loss rate of between 2.5 and 88 per day, in order to explain the loss of 100 kgs^{-1}.

Though an average occurrence rate of 10.2 events per day was observed during the midnight orbits, which is within the lower estimate required to balance the Enceladus input, it is highly unlikely that the bulk of events found fulfill the large azimuthal extent

incorporated into the above calculation. MHD modeling by *Zieger et al.* [2010] and *Jia et al.* [2012] suggest that large scale plasmoids may only be responsible for around 8% - 10% of the total mass loss, around $0.8\,kgs^{-1}$ to $22\,kgs^{-1}$; a total that could be explained or exceeded by the observations in this work. In this scenario the majority of the mass is lost through smaller scale mechanisms, such as cross-field diffusion [*Bagenal and Delamere*, 2011] or along the flanks [*Kivelson and Southwood*, 2005; *Jia et al.*, 2012].

At Earth various studies have estimated the azimuthal width of flux ropes (plasmoids) resulting from tail reconnection, and results range from $15\,R_E$ [*Slavin et al.*, 1993] to $40\,R_E$ [*Ieda et al.*, 1998]. In general, observations agree that they do not fill the entire width ($\sim 48\,R_E$ [*Fairfield*, 1992]) of the magnetotail [*Kiehas et al.*, 2013]. Additionally, the lack of a one-to-one correlation between substorms and flux rope observations supports the notion that flux ropes are limited in their azimuthal range [*Nagai et al.*, 1994]. Therefore the use of the approximate full tail width, $80\,R_S$, as the upper limit to the azimuthal extent will lead to an overestimation of the mass contained within the plasmoid structures. However, it is not possible to determine the true azimuthal extent with a single spacecraft, and so the numbers calculated with this must be viewed as an upper limit in this regard. The azimuthal extent of the structures also has ramifications as to the observed frequency of events; if plasmoids are tightly azimuthally confined then many will be missed by a single spacecraft. As noted by *Cowley et al.* [2015] these factors cancel, given isotropic observation and occurrence.

Another important caveat to consider in this interpretation is the uncertainty in the plasmoid length. The definition of duration used by the algorithm (the time between northward and southward extrema [*Slavin et al.*, 1993]) has been shown in the past to underestimate plasmoid size by a factor of ~ 4 to 8 [*Kivelson and Khurana*, 1995]. Additionally, the plasma signature of events observed by *Jackman et al.* [2014b] had a longer duration than the magnetic field signature. Indeed recent work, including *Arridge et al.* [2015b], *Jackman et al.* [2015] and *Thomsen et al.* [2015], has suggested that reconnection related flows can last for many hours.

The MHD simulations of *Jia et al.* [2012] produced plasmoids with an approximately circular cross-section of radius $\sim 10\,R_S$, giving a length of $\sim 20\,R_S$, also somewhat larger than our estimate. Recently, *Cowley et al.* [2015] suggested from geometrical arguments that the observed asymmetric magnetic field signatures identified by this study represent only a small proportion of the full plasmoid structure. Therefore, the method used above to calculate the plasmoid length significantly underestimates their full length. During the 4.8 hours between events, corresponding to the average occurrence rate of 5.0 per day observed by this study, and using the arguments of *Cowley et al.* [2015] it is possible to calculate that the full stretched plasmoid length could be around $30\,R_S$. This estimation

assumes that the events in the catalogue are isolated, however as discussed in Section 4.4 some of these events could be related to the same reconnection episode (e.g. the secondary island detections in the interval discussed by *Arridge et al.* [2015b]). For this reason, the true stretched length could be larger than this, and in any case significantly greater than the 0.3 to 10.45 R_S calculated from the magnetic field deflections. These length arguments could help reconcile the imbalance between the observed and required mass loss.

4.6.2 Flux Closure and Reconnection Cycles

Previous studies linking the change in size of the auroral oval to the varying magnetic flux contained in the polar cap (e.g. *Badman et al.* [2005, 2012]) have highlighted the importance of reconnection both at the magnetopause and in the magnetotail. It is possible to estimate the flux closed in a reconnection event using the duration of the northward interval, interpreted as a Post Plasmoid Plasma Sheet (PPPS). Unlike previous studies, Figure 4.8a does not show a statistical average extended northward period (discussed in Section 4.5.2.1), which could be a result of the different selection criteria and the inclusion of large numbers of new events. If many of these new events do not show a distinct PPPS they could represent the reconnection of purely closed flux; i.e. be related to the Vasyliunas cycle, and some may be detections of secondary islands which would not be expected to produce a PPPS.

Though no statistical PPPS is observed, some individual events do show considerable extended northward intervals. 25 events show a PPPS longer than 30 minutes, while six of these are longer than one hour. This could suggest that the closing of flux in tail reconnection is sporadic, and occurs primarily in fewer, large scale events.

The reconnection signatures observed in the dawn and dusk regions of the magnetosphere will now be compared. Previous theoretical studies have suggested that there may be distinct locations in the magnetotail where the Dungey and Vasyliunas cycles preferentially operate [*Cowley et al.*, 2004b; *Badman and Cowley*, 2007]. For this purpose SEAs have been produced using subsets of the observed plasmoid events. The subsets have been selected based on the local time at which the events were observed. The primary features of comparison in these plots are the lengths of the PPPS seen, and depth of northward deflections.

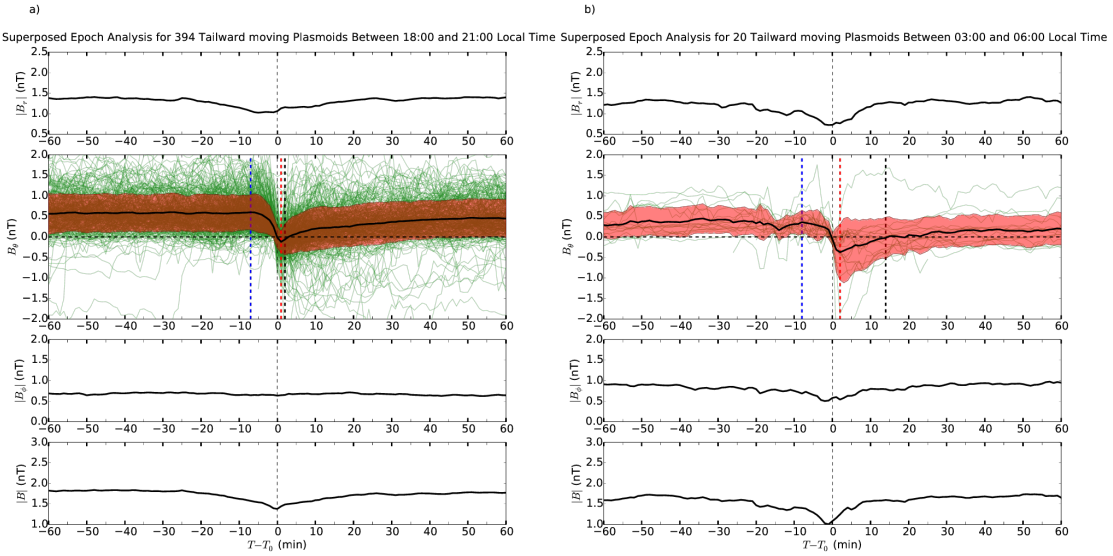

FIGURE 4.9: Superposed epoch analyses of events observed post-dusk (left) and pre-dawn (right) inferred to be tailward of the reconnection site. The format is the same as for Figure 4.8

4.6.2.1 Comparing Dawn and Dusk

The SEAs shown in Figure 4.9 only include events that were observed within 3 hours of dusk and dawn respectively. The SEAs are plotted in the same format as Figure 4.8 above. When analyzing these plots it is important to consider the differences in magnetospheric environment encountered by Cassini during these orbits. For example, the three hour window pre-dawn (03:00 to 06:00) contains orbits performed during 2006. Figure 4.1 shows that these orbits were all performed at approximately the same equatorial latitude (between 0° and 0.5°); during southern hemisphere summer this latitude was below the position of the hinged plasma sheet for the majority of the time, similar to position 3 in Figure 4.2a. In comparison, the orbits in the dusk sector (18:00 to 21:00) were mainly obtained during 2009 and 2010 (around Kronian equinox), in locations where Cassini spent over 50% of its time close to or within the plasma sheet (from Table 4.1).

The right (dawn) panel of Figure 4.9 reveals the presence of a significant (12 minute) PPPS, while the left (dusk) panel shows no such long northward interval. From this figure it could be concluded that the events around dawn are more likely to involve the closure of open field.

However, there are a few considerations to take into account. Firstly, only 20 plasmoid-like events were observed within the selected dawn local time sector, compared to 394 events in the three hours around dusk. The effect of this can be seen in the less steady average traces observed in all four panels of the dawn SEA. Secondly, as previously

mentioned, the orbits around dawn were low latitude, equatorial orbits performed during southern hemisphere summer; Cassini spent 92% of this period within the lobe (Table 4.1). Therefore, it is possible that the 20 events sampled by Cassini during this time correspond to larger events, perhaps those most likely to involve the closure of open field.

The Kolmogorov-Smirnov test can be used to compare two samples, with the null hypothesis that the samples are drawn from the same distribution. Applying the test to the distributions of PPPS duration observed results in a p-value of 0.209, with a K-S statistic of 0.236. These numbers suggest that the null hypothesis cannot be rejected, and that the two samples could be from the same distribution. Therefore the difference in PPPS lengths could be a sampling effect; a much larger sample at dawn would be required to show otherwise.

It is also worth noting that when the local time bins are expanded to cover the full width of the magnetotail (with the two local time bins being separated at midnight) the distributions of PPPS length are very similar (with a K-S statistic and p-value of 0.74 and 0.055 respectively). Additionally, when the local time distribution of the 25 events with considerably large PPPS (greater than 30 minutes) is analysed it is found that the proportion of event detections that these represent pre- and post-midnight is approximately equal ($\sim 3-4\%$).

4.7 Conclusions

A new catalogue of reconnection related events has been presented, identified using an algorithm which automatically selects deflections in the meridional (B_θ) component of the magnetic field. In order to be selected the events must fit a polynomial to a sufficient quality and the size of the deflection must be greater than $1.5\times$ the local RMS of B_θ (and be greater than $0.25\,nT$). The orientation of the change was related to the position of the spacecraft relative to the x-line. The events were also confirmed by eye. The new catalog covers data taken by the Cassini spacecraft over three years: 2006, 2009 and 2010. This combination allows, for the first time, the asymmetry between dawn (2006) and dusk (2009 and 2010) to be explored in terms of the magnetic field signatures associated with reconnection.

When normalized to observation time, reconnection is observed most frequently around and post-midnight, with more infrequent but steady loss seen on the dusk flank. The increasing occurrence frequency as the mass loaded flux tubes rotate from dusk past

midnight perhaps indicates the increase in instability as they stretch down the magnetotail. Observations on the dawn flank took place largely while the spacecraft was in the southern magnetotail lobe, which often precluded the direct observation of plasmoids and dipolarizations, but allowed for observations of TCRs. This data set shows sporadic and clustered reconnection. The observed frequency of reconnection events is seen to change dramatically depending on the latitude of the observations (relative to the position of the hinged plasma sheet). For example, the frequency is relatively low during intervals when Cassini explored the magnetotail lobes. Normalizing the occurrence to plasma sheet occupation confirms an increased frequency of observation post-midnight. The reconnection x-line position appears to be highly variable, with events inferred to be both planetward and tailward of the x-line observed at most radial distances and local times. Overall however, more planetward moving events are seen at distances closer than $30\,R_S$, suggesting the reconnection x-line is often located in this vicinity.

The average Post Plasmoid Plasma Sheet (PPPS) observed following plasmoids in previous studies is not observed with this catalogue. This could be a result of the different selection criteria and inclusion of many more events with smaller deflections (shown by the smaller average deflection size). Due to a limited sample of events near dawn it is not possible to determine conclusively whether flux is closed preferentially pre- or post-midnight, though it is likely that other factors, such as the solar wind conditions, play a role. The upper limit to the mass loss calculated from the catalogue alone is insufficient to balance the input from Enceladus. Potential solutions to this disparity include mass loss from other processes [*Kivelson and Southwood*, 2005; *Zieger et al.*, 2010; *Bagenal and Delamere*, 2011; *Jia et al.*, 2012; *Sergis et al.*, 2013], or that the durations used in this study underestimate the plasmoid size and therefore mass (due to the trajectory of Cassini through the structures) [*Kivelson and Khurana*, 1995; *Cowley et al.*, 2015].

Chapter 5

Automated Force Free Flux Rope Identification

5.1 Introduction

This Chapter discusses a method by which *in situ* encounters with magnetic flux ropes can be located automatically in spacecraft magnetometer data.

The aim of this Chapter is to present and explain a series of techniques by which flux rope signatures can be automatically identified; this method will then be applied to a large quantity of magnetometer data taken by the MESSENGER spacecraft in orbit around Mercury (Chapter 6). The method includes several widely used analysis techniques, developing and automating criteria that have been used in past manual surveys. Automatically processing years worth of spacecraft data both saves a large amount of time and ensures the search is completely reproducible. This is particularly important at Mercury, where the four years worth of MESSENGER orbital data cover a highly dynamic magnetosphere. Though the techniques have been developed using MESSENGER magnetometer data, they could be applied to other data sets with some adaptation.

Below, the dataset will be summarized. This will be followed by a discussion of the expected magnetic field signature in the data and the selected flux rope model. The process is then discussed with reference to an example detection and several trial intervals. Assumptions and potential adaptations are then discussed.

5.2 Data, Signatures and Model

5.2.1 Data

The method was developed using magnetometer data from the MESSENGER spacecraft [*Solomon et al.*, 2007; *Anderson et al.*, 2007]. Data with a cadence of 20 Hz were used; the short timescales of Hermean magnetotail flux ropes ($\sim 0.74\,s$ [*DiBraccio et al.*, 2015]) necessitate the use of high resolution data. MESSENGER orbited Mercury from 18th March 2011 until 30th April 2015. During this time it performed highly inclined, eccentric orbits with a period of $\sim$ 12 hours (later reduced to $\sim$ 8 hours). This orbit caused MESSENGER to make approximately vertical cuts through the magnetotail plasma sheet several times a day during certain seasons. It is within $\sim$ 25 of these plasma sheet crossings that the process was tested and developed. These crossings are located in the near-Mercury tail, close to midnight in the tail plasma sheet. Orbits were carefully selected to ensure the detections related to flux ropes and not to other processes that occur closer to the magnetopause.

The magnetometer data were used in the aberrated Mercury-Solar-Magnetospheric (henceforth MSM) coordinate system. In this Cartesian system the z-axis ($\hat{Z}_{MSM}$) is aligned with the dipole axis pointing north, the x-direction ($\hat{X}_{MSM}$) traces the Mercury-Sun direction and the y-axis ($\hat{Y}_{MSM}$) completes the right handed set. At Mercury the dipole and rotational axes are approximately aligned, however the magnetic equatorial plane (described by $\hat{X}_{MSM}$ and $\hat{Y}_{MSM}$) is offset north from the planet's geometrical center by $\sim 0.2\,R_M$ [*Anderson et al.*, 2011]. The magnetic field data were corrected for solar wind aberration (aberrated coordinates are indicated with '' notation). This was accomplished using the local orbital velocity of Mercury and assuming a solar wind velocity of $425\,kms^{-1}$.

5.2.2 Magnetotail Flux Rope Signatures

Previous studies have found that flux ropes largely lie in the $\hat{X}$-$\hat{Y}$ plane [*Slavin et al.*, 2003a], generally with their axis in the $\pm\hat{Y}$ direction, travelling in the $\pm\hat{X}$ direction (planetward or tailward) due to the prevailing tail configuration [*DiBraccio et al.*, 2015]. As discussed in Section 1.4.3.4, if a flux rope were to pass directly over the spacecraft with this approximate orientation and velocity then a magnetometer would observe: a bipolar variation in B_Z, a local maximum in B_Y (corresponding to the strong core field along the axis) and a peak in the total field magnitude ($|B|$). This signature is also dependent upon the trajectory of the spacecraft [e.g. *Borg et al.*, 2012; *DiBraccio et al.*, 2015].

5.2.3 Force Free Model

The force free model (Equations 1.42, 1.43 and 1.44), discussed in Section 1.4.3.4 will be used to differentiate between trajectories with large impact parameters and the travelling compression regions that surround the plasmoids as they interact with the lobes [e.g. *Slavin et al.*, 1993].

The assumption that the flux rope is linearly (constant α) force free and cylindrically symmetric will limit the number of flux ropes that are identified by the technique. As it represents lowest energy state of helical magnetic fields, it is therefore perhaps the end point of the evolution of the flux rope morphology [*Priest*, 1990], and more likely to best represent well developed flux ropes. Flux ropes encountered soon after their formation are unlikely to have evolved to the stable equilibrium described by the model. Implications of this assumption are discussed in Section 5.5.1.

5.3 Method

The technique, described below, uses three steps to locate quasi-force free flux ropes within spacecraft magnetometer data. The combination of all three ensures fully automated, rigorous and repeatable flux rope detections.

5.3.1 Baseline Crossing and Peak Detection

The aim of the first step in the technique is to find significant deflections in the B_Z component of the field concurrent with peaks in the $B_{Y'}$ or $|B|$ components of the field. This field signature is discussed in Section 5.2.2 as being the expected result of an equatorial magnetotail flux rope travelling sunward (or tailward) directly over the spacecraft.

This step is similar to the method developed by *Smith et al.* [2016] (Chapter 4) and is illustrated in Figure 1. Once identified, candidates will be further analysed and ultimately accepted or rejected based on the results of the subsequent steps. The algorithm first takes a running average of the B_Z component of the field within a one minute sliding window. The window size was selected specifically for the Mercury data as it was found to trace the 'long' term changes in the field but ignore sharp changes in the field (e.g. flux rope signatures). The running average forms a new baseline through which any deflections of the field must pass. Every instance where B_Z passes through this baseline, henceforth referred to as a crossing, is recorded for further analysis.

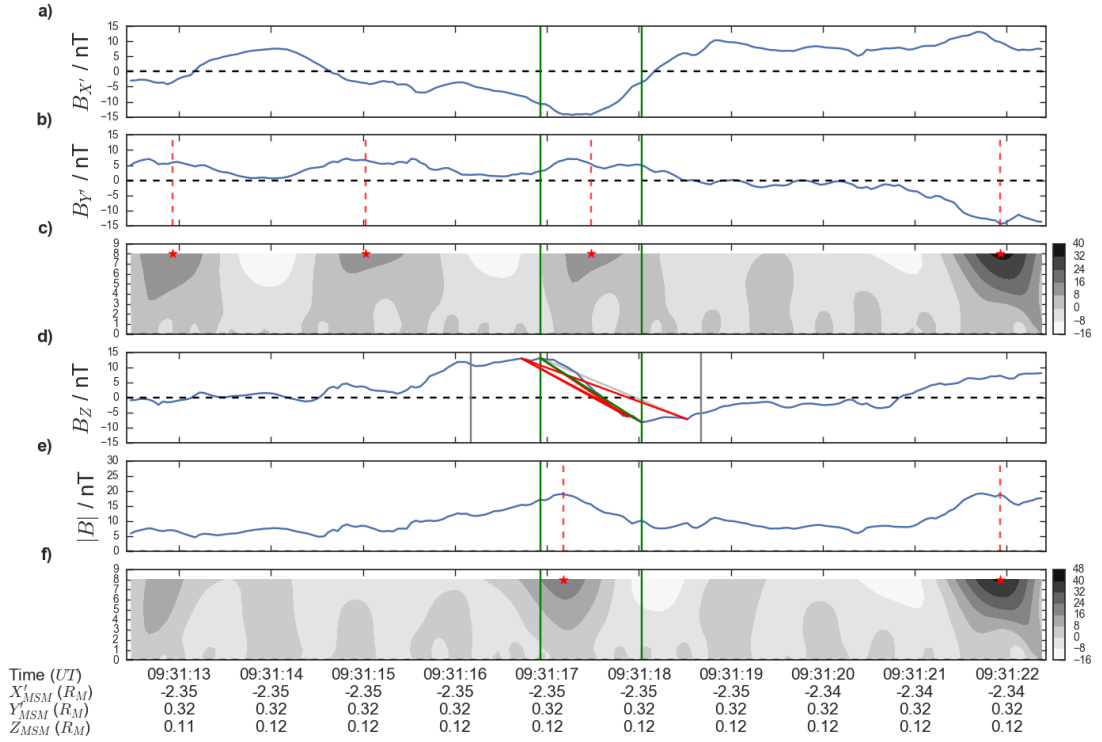

FIGURE 5.1: An example flux rope detection. Panels a, b, d and e show the magnetic field in aberrated MSM coordinates. The grey vertical bars on panel d indicate the maximum length of the event ($\pm 1.25\,s$). The faint grey lines show the first order polynomials interpolated between the potential start/stop pairings that have a value of $r^2 < 0.9$. The red lines indicate those interpolated lines with an $r^2 \geq 0.9$ (calculated from Equation 5.1). The green line shows the final interpolated line selected; with an $r^2 \geq 0.9$ and the largest value of ΔB_Z (from Equation 5.2). The green vertical lines indicate the corresponding selected start and end to the deflection respectively. Panels c and f show the Continuous Wavelet Transform (CWT) of $|B_{Y'}|$ and $|B|$ respectively (with the Ricker wavelet). The color bar indicates the value of the CWT coefficient, while the vertical axis shows the wavelet scale factor. The red stars indicate the locations of the significant peaks in the CWT. The red dashed lines then show the locations of the peaks in the panel of the relevant magnetic field component.

To investigate whether the deflection of the field is significant the method then searches for local maxima and minima of B_Z. Defining the event using the local north-south maxima of the field attempts to find the duration that would be chosen by eye, following the work of *Slavin et al.* [1993], and more recently *Jackman et al.* [2014b]; *Vogt et al.* [2014]; *DiBraccio et al.* [2015]; *Smith et al.* [2016] (Chapter 4). A period extending $1.25\,s$ either side of the crossing (vertical grey bars in Figure 5.1) is examined to find these local extrema. This time window was chosen in order to preferentially select the fluctuations interpreted as flux ropes; *DiBraccio et al.* [2015] reported an average duration of $0.74\,s$.

If the deflection is southward, i.e. the value of B_Z decreases, then all peaks in the field (where the field is larger than at adjacent points) up to $1.25\,s$ before the crossing are selected as potential starts. On the other side, after the crossing, all local minima of the

field (where the field is smaller or more negative than at adjacent points) up to 1.25 s after the crossing are selected as potential ends.

All possible combinations of potential starts and ends are then examined, with the aim of selecting the duration representing the largest and smoothest fluctuation. First order polynomials are interpolated between the various pairs. The interpolations are then compared with the data using the coefficient of determination, given by:

$$r^2 = 1 - \frac{\sum_0^N (B_Z^t - f_t)^2}{\sum_0^N (B_Z^t - \bar{B_Z})^2} \tag{5.1}$$

The start and end pair are located at $t = 0$ and $t = N$ respectively. B_Z^t is the value of B_Z at the point t, $\bar{B_Z}$ is the average of B_Z over all points included. Finally, f_t is the value of the interpolation at time t. If all the data points lie precisely on the polynomial this would yield an r^2 value of 1. The grey, red and green lines on Figure 5.1 show the possible interpolations for the example event.

If the value of r^2 is less than 0.9 (e.g. as for the grey lines in Figure 5.1), and therefore the polynomial represents a poor fit to the data, then the start/end pair is discarded. The magnitude of the deflection, given by:

$$\Delta B_Z = B_Z^0 - B_Z^N \tag{5.2}$$

is then evaluated for all pairs for which $0.9 \leq r^2 \leq 1$ (the green and red lines on Figure 5.1) using Equation 5.2 (B_Z^0 and B_Z^N being the value of the B_Z component of the field at the start and end respectively). The start/end pair with the largest value of ΔB_Z is then selected, defining the event duration, shown by the green line in Figure 5.1. The method defines the limits of the event, shown by the vertical green bars in Figure 5.1. In this case the limits well match those that may have be selected by eye.

The magnitude of the deflection ($|\Delta B_Z|$) is then compared to the standard deviation of the field (σ_{B_Z}), requiring that:

$$\frac{|\Delta B_Z|}{\sigma_{B_Z}} \geq 1 \tag{5.3}$$

where σ_{B_Z} is calculated for the same one minute sliding window as the average of B_Z. If Equation 5.3 is satisfied then the deflection is preliminarily accepted. This threshold is relatively low, however the aim of this step is to find all possible deflections so they may be evaluated by the following methods.

The event duration identified is then inspected for local peaks in $B_{Y'}$ or $|B|$ using wavelet analysis. Figure 5.1 demonstrates this step. The green vertical bars indicate event duration as selected by the previous step. Panels c and f show the results of the Continuous Wavelet Transform (CWT) when applied to $|B_{Y'}|$ and $|B|$ ($\sim$ panels b and e) respectively using the Ricker (or Mexican Hat/Marr) wavelet [*Daubechies*, 1992]. The Ricker wavelet is the normalized second derivative of a gaussian function, importantly featuring a central peak. The CWT and Ricker wavelet combination are commonly used in various fields for pattern matching and peak detection [*Carmona et al.*, 1998; *Du et al.*, 2006]. Panels c and f display time on the horizontal axis and wavelet scale on the vertical axis. The colours indicate the value of the CWT coefficient: strongly positive where the wavelet (with a given scale) matches well with a peak in the data. Local peaks in the CWT coefficient are selected, and those greater than an empirical threshold (designed to preferentially select peaks with a small scale factor), are indicated with red stars. The red dashed lines then indicate the positions of these peaks in the panel of the corresponding component of the field.

If significant peaks are identified in either $B_{Y'}$ or $|B|$ (panels b or e) within the duration indicated by the green and red bars then the deflection is accepted. Figure 5.1 shows an event for which peaks have been identified in both panels. However, only one peak is required as they can be missed by the CWT technique.

This combination of techniques recreates the by-eye selection criteria used by several previous studies [e.g. *Slavin et al.*, 2003a; *DiBraccio et al.*, 2015].

It is possible that the combination of B_Z deflection and peak in $B_{Y'}$ or $|B|$ could be caused by other magnetic structures within the magnetotail. To remove such signatures criteria are then placed on the results of both Minimum Variance Analysis (MVA) and comparison to a model (Sections 5.3.2 and 5.3.3).

5.3.2 Minimum Variance Analysis

The second stage of the process involves Minimum Variance Analysis (MVA); rotating the magnetic field data into a local coordinate system to further check for flux rope-like characteristics. If the magnetic signature is caused by a close encounter with a force-free flux rope then it may be expected that the new coordinate system is distinct and that a clear rotation of the field is apparent (as will be discussed below) [*Slavin et al.*, 1989; *Briggs et al.*, 2011; *DiBraccio et al.*, 2015].

MVA was first developed to find the normal to magnetic discontinuities (e.g. current layers) from magnetometer data [*Sonnerup and Cahill*, 1967]. However, the technique

has also been used to determine the orientation and structure of flux ropes (if the spacecraft passes sufficiently close to the axis and the flux rope satisfies the force free approximation) [e.g. *Sibeck et al.*, 1984; *Elphic et al.*, 1986; *Slavin et al.*, 1989; *Moldwin and Hughes*, 1991; *Xiao et al.*, 2004].

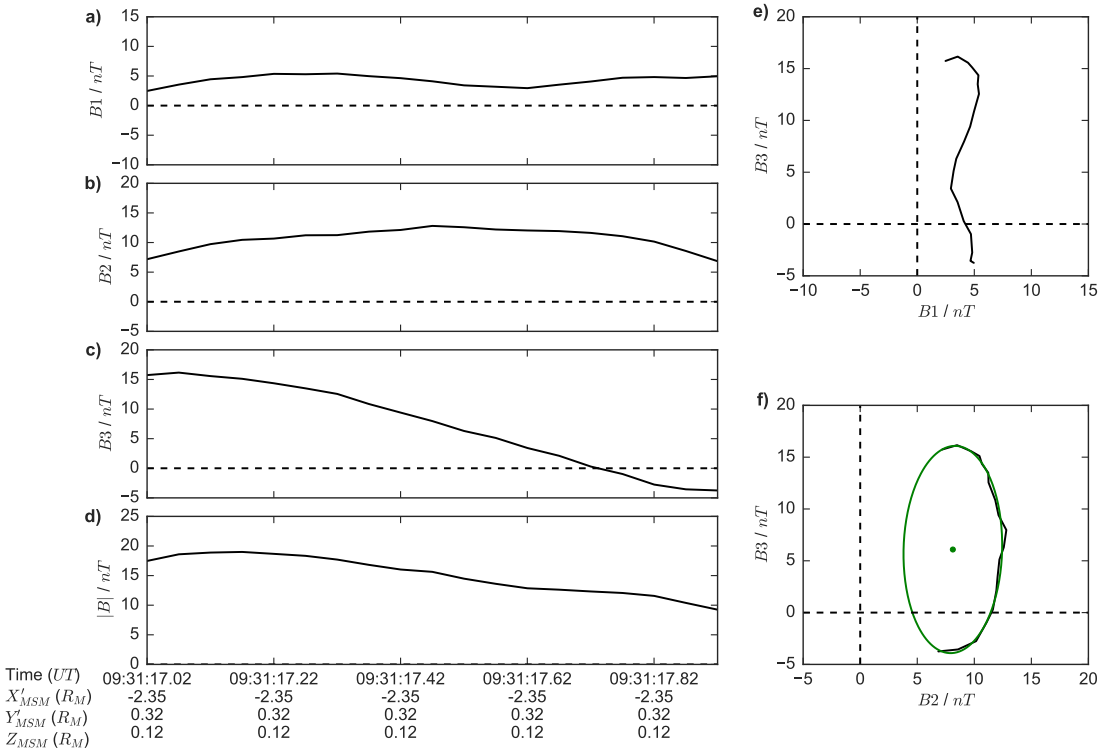

FIGURE 5.2: Results of the MVA analysis on the example flux rope shown in Figures 5.1 and 5.2. The magnetic field is shown in the MVA coordinate system, where B1, B2 and B3 are the field components in the minimum, intermediate and maximum variance directions respectively. Hodograms of the field are also shown. The hodogram displaying B2-B3 (panel f) is over-plotted with the result of the ellipse fitting in green (described in Section 3.2); the green dot is the centre of the fitted ellipse.

MVA outputs three eigenvectors, representing the minimum, intermediate and maximum variation directions ($\mathbf{e_1}$, $\mathbf{e_2}$ & $\mathbf{e_3}$ respectively), and three corresponding eigenvalues (λ_1, λ_2 & λ_3). The three eigenvalues are often quoted in two ratios: the maximum to intermediate ($^{\lambda_3}/_{\lambda_2}$) and the intermediate to minimum ($^{\lambda_2}/_{\lambda_1}$). The relative size of the eigenvalues describes how well the new coordinate system is defined (low ratios suggest the axes are more degenerate [*Khabrov and Sonnerup*, 1998; *Sonnerup and Scheible*, 1998]), so for this work it will be required that both of the ratios are greater than five. *Briggs et al.* [2011], at Mars, placed a limit on $^{\lambda_2}/_{\lambda_1}$ of eight, while *DiBraccio et al.* [2015] placed no limits on either ratio and found $^{\lambda_3}/_{\lambda_2}$ as low as three, and $^{\lambda_2}/_{\lambda_1}$ always less than 12. *DiBraccio et al.* [2015] found that placing thresholds did not change their results and so chose to keep the larger sample for statistical reasons. For this study a threshold is used to help exclude poor quality events (as no manual pre-selection is

performed). Requiring both ratios to be greater than 5 means all three eigenvectors are distinct. No criterion is placed upon the direction of the eigenvectors.

Additionally, the start and end times are varied (from those identified in Section 3.1) by ±10 % of the duration. MVA is performed on all the possible combinations of starts and ends this allows. The amount by which the maximum eigenvalue ratio changes is then calculated by the following:

$$max(\lambda_3/\lambda_2)/mean(\lambda_3/\lambda_2) \leq 1.75 \tag{5.4}$$

If the magnetic structure is well defined, and analysis stable, then the eigenvalue ratio should not change by a large amount, and Equation 5.4 should be satisfied. The limit of 1.75 was determined empirically from running the analysis on the ~ 10 test current sheet crossings.

The pair for which the product of λ_3/λ_2 and λ_2/λ_1 is greatest is then selected, attempting to maximize both ratios (and thereby select the most distinct eigenvectors). Often this is the same as the duration selected in the previous step of the pipeline, or differs by only one data point.

Finally, a clear rotation of the field in a hodogram of the intermediate and maximum field directions is expected when the spacecraft passes through a flux rope. To evaluate this property an ellipse is fitted using least squares minimization to the hodogram trace following the method of *Fitzgibbon et al.* [1999]. The quality of the fit to the data is evaluated using a modified r^2 (Equation 5.5):

$$r^2 = 1 - \frac{\sum_{i=0}^{N} a_i^2}{\sum_{i=0}^{N} c_i^2} \tag{5.5}$$

where the summations are over all data points ($i = 0$ to N), a_i is the radial distance between the point i and the ellipse (point P) and c_i is the radial distance between the centre and the point P on the ellipse. If all points lie directly on the ellipse then $r^2 = 1$. The fit is required to be of a good quality: i.e. $r^2 \geq 0.98$. The ellipse fitting technique requires at least four data points; this imposes a lower limit to the duration of flux rope that can be identified depending on the resolution of the data used. With the $20\,Hz$ MESSENGER data this is $0.2\,s$.

In addition, poor detections are characterized by highly eccentric ellipse fits, therefore for acceptance: $e \leq 0.9$. The ellipse fitting technique is known to have a bias for producing ellipses with low eccentricities [*Fitzgibbon et al.*, 1999]; therefore the fit should meet the criteria if possible.

Figure 5.2 show the results of running MVA on the flux rope shown in Figure 5.1. The expected flux rope characteristics can be seen; little variation in $B1$ (the minimum variance direction), a peak (the core field) in $B2$ and an approximately bipolar signature in $B3$ (the maximum variance direction). If the spacecraft had passed through the center of the flux rope then $B1$ would be 0; $B1$ increases in magnitude as the impact parameter increases. The corresponding eigenvalue ratios are: $^{\lambda_3}/_{\lambda_2} = 13.68$ and $^{\lambda_2}/_{\lambda_1} = 7.22$, with a calculated variation in the maximum to intermediate ratio of 1.383. These values demonstrate a well defined MVA coordinate system with distinct eigenvectors. The ellipse in the $B2$-$B3$ hodogram is a good fit ($r^2 = 0.996$) and is not highly eccentric ($e = 0.849$).

5.3.3 Force Free Flux Rope Fitting

The third and final step of the analysis pipeline attempts to fit the data to a model flux rope. Not only does this provide another set of criteria to exclude poor quality signatures but also allows an estimation of the core field and proximity of the spacecraft to the flux rope axis. The implications of the choice of model are discussed in Section 5.5.1.

The aberrated magnetometer data, within the region identified in Section 5.3.2, is rotated into MVA coordinates and normalized. From there it is transformed into flux rope axial and azimuthal coordinates. The intermediate variance direction is taken to correspond to the axial direction while the azimuthal direction is composed of a combination of the minimum and maximum variance directions. This implicitly assumes that the MVA technique has correctly located the axial direction. This is a good assumption at small impact parameters, however it can be shown to become less valid as the impact parameter increases. Using the force free model an impact parameter of $0.5\,R_0$ results in an angular difference between the intermediate direction and axial direction of $\sim 20^\circ$ [*Xiao et al.*, 2004].

The modelled magnetic field of the flux rope, shown in Equations 1.42 and 1.43, is normalized and computed for impact parameters between 0 and 0.95 (Impact Parameter $= r/R_0$). The results are then compared to the data using a modified χ^2 (χ_1^2), shown in Equation 5.6, as in *DiBraccio et al.* [2015]:

$$\chi_1^2 = \frac{\sum \left((B_{Axial}^{Data} - B_{Axial}^{Model})^2 + (B_{Azimuthal}^{Data} - B_{Azimuthal}^{Model})^2 \right)}{N} \tag{5.6}$$

where the sum is over all N data points, B_{Axial}^{Data} and $B_{Azimuthal}^{Data}$ are the normalized axial and azimuthal components of the field and B_{Axial}^{Model} and $B_{Azimuthal}^{Model}$ are the normalized

axial and azimuthal results of the model. The model is compared to the MVA duration defined in Section 5.3.2, however the fit is allowed to ignore up to the first and last 20% of the data points if this provides a better fit. This flexibility is somewhat analogous to *Slavin et al.* [2003a] allowing the time of closest approach to vary in their fitting. The impact parameter, and duration, with the smallest χ_1^2 is then selected as the best fit. For the flux rope in Figures 1 and 2 the best fit χ_1^2 (of 0.062) was obtained at an impact parameter of $0.33\,R_0$.

Once the best fit to the normalized data has been computed the result is rotated back into MVA coordinates. Another measure of χ^2 is then evaluated comparing the three dimensional fit with the data; χ_2^2 is shown in Equation 5.7 (similar to that used by *Lepping et al.* [1990]):

$$\chi_2^2 = \frac{\sum \left((B_1^{Data} - B_1^{Model})^2 + (B_2^{Data} - B_2^{Model})^2 + (B_3^{Data} - B_3^{Model})^2 \right)}{3N - n} \tag{5.7}$$

where the sum is over all N data points; the differences between all three normalized minimum variance components of the field (as defined in Section 5.3.2) and the model results are calculated and squared. The factor of n here represents the number of free parameters in the fit (taken to be four). For the example flux rope (in Figures 5.1 and 5.2) the value of χ_2^2 calculated was 0.048. The peak axial field calculated by the model is then scaled to equal the peak axial field found in the MVA analysis to provide an estimate of B_0: the core field strength. With the scaling completed the result can be rotated back into MSM coordinates.

With the data compared to the model results, requirements are placed both on the quality of the fit (χ^2) and the best fit impact parameter (IP). If the IP is larger than $0.5\,R_0$ then the MVA technique should be less able to distinguish the axial orientation, and so the events are rejected. In addition, it is required that either χ_1^2 or χ_2^2 is less than 0.15 (and so the flux rope can be well modelled as linearly force-free). Normally the two values of χ^2 are approximately the same.

5.4 Application

To test the efficacy of the method it has been applied to the same dataset as that previously investigated by *DiBraccio et al.* [2015]. During 30 MESSENGER magnetotail current sheet encounters, between 2011 and 2013, *DiBraccio et al.* [2015] identified a total of 49 flux ropes. The three step process independently re-identifies 8 of these. 19 of the flux ropes identified by *DiBraccio et al.* [2015] do not possess greater than 1σ deflections

of the field in the B_Z component, and so are not located by the first step (though they do exhibit significant peaks in B_Y and $|B|$). The remaining flux ropes that are not selected by the method are split evenly between those that did not meet the required MVA criteria and those that did not fit the force free model to the required accuracy (or did but for impact parameters $\geq 0.5\,R_0$).

Figure 5.3 shows the result of the application of the method to two example passages of MESSENGER through the Hermean cross-tail current sheet on 23rd and 24th November 2011. The magnetic field is provided in aberrated MSM coordinates. The flux ropes identified by this method are shaded green. Those identified by *DiBraccio et al.* [2015] and missed by our method are highlighted in red. The top panel, showing data from the 23rd November 2011, was recorded during a period of high solar wind dynamic pressure (due to the impact of a coronal mass ejection) [*Slavin et al.*, 2014]. This caused compression of the dayside magnetopause and very high rates of reconnection on the dayside. Correspondingly, a high rate of flux rope formation and ejection is observed. One flux rope identified by *DiBraccio et al.* [2015] is not recovered around 09 : 25 : 40 due to a large variation in the MVA eigenvalues observed (violating the criterion in Equation 5.4). In the bottom panel a flux rope identified by *DiBraccio et al.* [2015] is not selected due to a large best fit impact parameter ($\geq 0.5\,R_0$).

To further validate the technique it was applied to data from Earth's magnetotail: from the Cluster [*Escoubet et al.*, 1997; *Balogh et al.*, 2001; *Perry et al.*, 2006] and Geotail [*Mukai et al.*, 1994] missions. The method was tested to check if it could recover events from the figures of previous studies. Adapting it for the different timescales, the method identifies both flux ropes shown by *Slavin et al.* [2003a]. Three out of four flux ropes shown by *Borg et al.* [2012] are initially located, though two of these are then discarded as they do not fit the model satisfactorily at the required impact parameters. Both flux ropes shown by *Zhao et al.* [2016] are located, however one is later discarded as it does not sufficiently fit the model.

5.5 Discussion

The method described above represents an automated, consistent method of identifying *in-situ* encounters with cylindrically symmetric, linear (constant-α) flux ropes within spacecraft magnetometer data. In the section below several key assumptions that the process makes are outlined and potential future adaptations are discussed.

5.5.1 Assumptions

The first major assumption made by the analysis pipeline is that the MVA process has correctly determined the orientation of the flux rope. This has been shown in the past to be true in some situations, and to be a better approximation when the spacecraft passes close to the axis [*Xiao et al.*, 2004]. If MVA fails to correctly locate the axial direction then the event will appear to be a poor fit to the model and the flux rope will probably not be identified.

Secondly, the force free model applied assumes that the flux rope is cylindrically symmetrical. It is probable that most flux ropes are in some way distorted through interactions with the surrounding field and plasma. There are alternative models that allow for some deformation, for example those that allow an elliptical or oblate flux rope (e.g. *Hidalgo and Cid* [2002] and *Vandas and Romashets* [2003]). While these models allow more accurate fits of distorted flux ropes they also introduce more free parameters. The purpose of the fit is to provide additional criteria to rule out poor flux rope candidates and allow the estimation of some key parameters. More complex models could be subsequently fit to the successful candidate flux ropes to discern more information about their structure.

Finally, the chosen model assumes that the flux rope is (constant-α) force free; this will result in the exclusion of some flux ropes from the analysis. In fact, as mentioned in Section 5.2.3, the model is likely to be a poor fit to flux ropes that are encountered soon after their formation. This will almost certainly introduce a selection effect. However, without access to high resolution plasma data any model that includes the internal plasma pressure within a flux rope would be poorly constrained. This could result in the inclusion of poor quality events if the plasma parameters that are assumed are not representative of the true environment.

5.5.2 Adaptation

The analysis outlined above could be applied to other large data sets, and used to create a self-consistent catalogue of quasi-force free flux ropes. If used at other planets the time-scales used would require adjustment; i.e. the maximum length of event and duration over which the averages are calculated. Additionally, if simultaneous high-resolution plasma data is available then this could be used to create additional criteria (or modify existing ones). Furthermore, such plasma data would also allow more complex analysis techniques to be employed (e.g. the method of *Rong et al.* [2013] for determining axis orientation). Finally, the method could be applied to virtual spacecraft simulation results, which can shed light on the limitations of *in situ* spacecraft detections.

5.6 Conclusions

A completely automated method of locating cylindrically symmetric, linear (constant-α) flux ropes from spacecraft magnetometer data has been presented. The analysis initially identifies significant ($\Delta B_Z \geq 1\sigma$) deflections in the north-south component of the magnetic field concurrent with peaks in the dawn-dusk component or total field. These candidates are then inspected using MVA to select those for which it is able to determine a well defined coordinate system with a clear rotation of the field. Those identified are then compared to a force free model and the quality of the fit evaluated. The fitting of a model to the magnetic signature allows both the rejection of poor quality events (those likely due to other processes) and the determination of some of the physical parameters of the flux rope (i.e. the radius of the flux rope and core field strength). The pipeline has been tested on data from the MESSENGER mission, and successfully relocates several previously studied flux ropes from *DiBraccio et al.* [2015]. It has also been applied to Earth data from Geotail and Cluster and recovers some prominent examples from the literature [*Slavin et al.*, 2003a; *Borg et al.*, 2012; *Zhao et al.*, 2016]. The method is ideal for application to large data sets whose manual inspection would be time consuming and include unknown biases. The method will be applied to a large quantity of data in Chapter 6, the resulting detections will then be statistically examined with respect to their properties, location and recurrence.

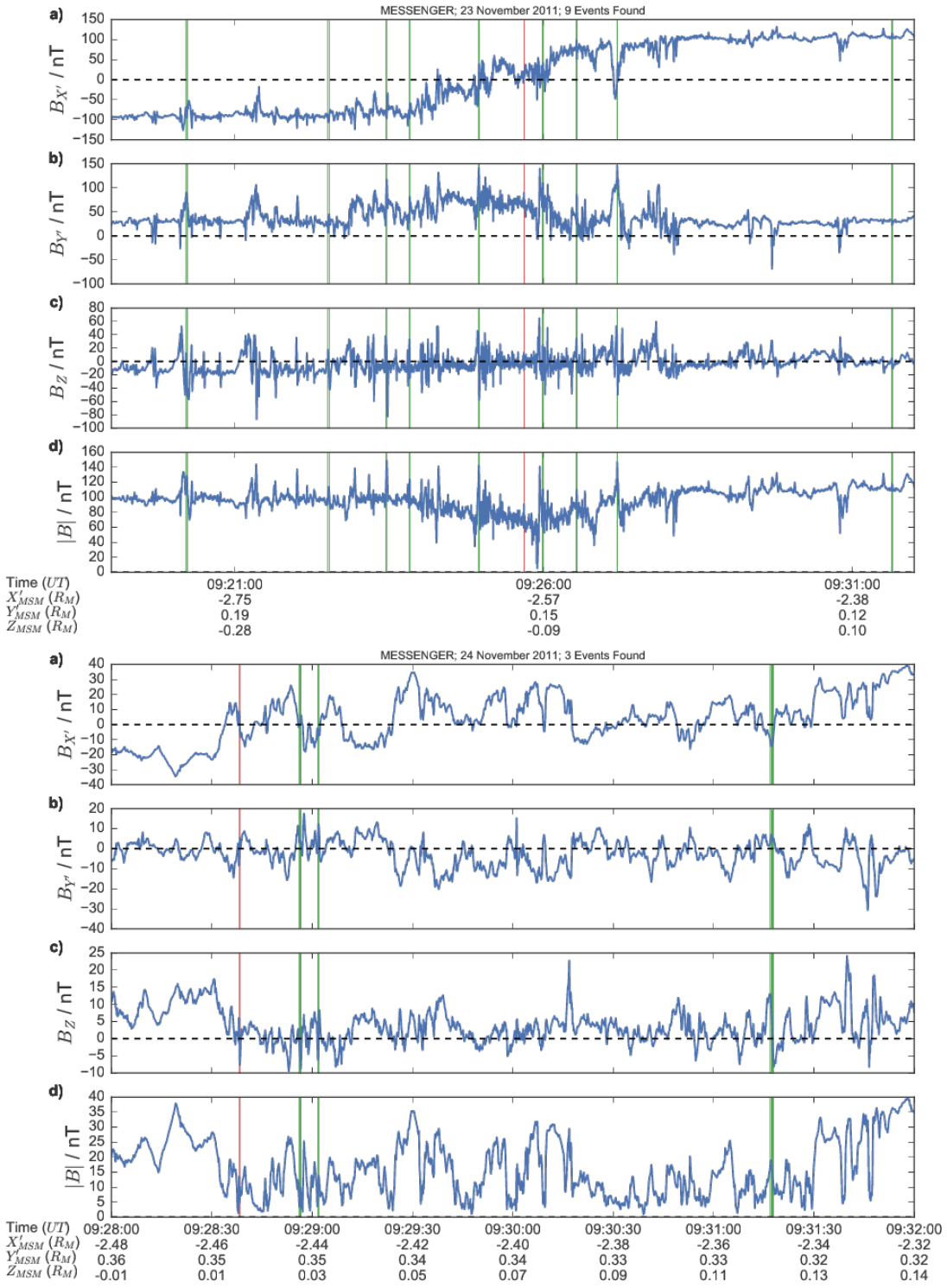

FIGURE 5.3: Two example MESSENGER passages through the Hermean magnetotail current sheet. Magnetic field is provided in aberrated MSM coordinates. Positive force free flux rope detections by the method are indicated with green shading. Flux ropes identified by *DiBraccio et al.* [2015] but missed by this technique are highlighted in red.

Chapter 6

Flux Ropes in the Hermean Magnetotail: Distribution, Properties and Formation

6.1 Introduction

This Chapter discusses the results of the application of the automated force free flux rope identification method (described in the Chapter 5) to 319 plasma sheet intervals.

The aim of the Chapter is to apply a consistent and thorough method to locate *in situ* encounters with magnetic flux ropes in MESSENGER orbital data. The application of this method will enable the largest current survey of flux ropes, casting light on whether inconsistently observed local time asymmetries are the result of limited or biased coverage, or due to the underlying properties of the system. The new automation also allows the identification of smaller flux ropes that may be harder to identify (those that would be less likely to be identified by eye).

Section 6.2 will introduce the data used, the magnetic field signatures of interest and the flux rope magnetic field model utilized. The method will be briefly summarized in Section 6.3. The results of this survey will then be explored with respect to the location, recurrence and motion of the flux ropes. Finally, the structures will be discussed with a focus on their formation and the driving of the Hermean magnetotail.

6.2 Data, Signatures and Models

This section will summarize the data utilized by the study, as well as the signatures of interest and relevant magnetic field models.

6.2.1 Data

The MESSENGER spacecraft [*Solomon et al.*, 2007] orbited Mercury for $\sim$ four years between March 2011 and April 2015. This study utilizes data obtained during this interval from the on-board magnetometer [*Anderson et al.*, 2007]. Data are used at a sampling rate of $20\,Hz$; use of such a high time resolution is necessitated by the short timescales at Mercury; previous work found that flux rope encounters at Mercury generally last for less than three seconds [*Slavin et al.*, 2012a; *DiBraccio et al.*, 2015].

The magnetic field data in this study have been used in the Mercury Solar Magnetospheric (MSM) coordinate system. In this Cartesian system the $\hat{X}_{MSM}$ axis is directed sunward, the $\hat{Z}_{MSM}$ axis is directed northward along the magnetic dipole axis and the $\hat{Y}_{MSM}$ axis completes the right handed system, directed approximately duskward. The origin of the system is offset north from the planetary centre by $\sim 0.2\,R_M$ in accordance with the measured offset of Mercury's dipole field [*Alexeev et al.*, 2008, 2010; *Anderson et al.*, 2008, 2010, 2011; *Johnson et al.*, 2012]. The data have also been aberrated to account for Mercury's orbital motion (using the daily average orbital velocity and an assumed solar wind velocity of $400\,kms^{-1}$). The use of aberrated data is indicated with prime notation (e.g. X'_{MSM}).

MESSENGER's orbit was eccentric and highly inclined, resulting in almost vertical cuts through the magnetotail plasma sheet several times a day during 'hot' and 'warm' season orbits. Magnetic field data from an example passage of MESSENGER through the plasma sheet is shown in Figure 6.1a. MESSENGER began the interval within the southern plasma sheet boundary layer. At approximately 16:17:30 UT the spacecraft passed into the plasma sheet itself, recording diamagnetic depressions of the field indicating the presence of significant plasma. While within the plasma sheet the sign of $B_{X'}$ reversed several times as the spacecraft encountered the cross-tail current layer. MESSENGER exited the plasma sheet at around 16:26:00 UT, and entered the northern plasma sheet boundary layer.

This Chapter uses data collected during a total of 319 plasma sheet encounters, spanning the entirety of the MESSENGER mission. The plasma sheet crossings are those identified and examined by *Poh et al.* [2017a], for more information regarding their selection criteria the interested reader is directed to their study.

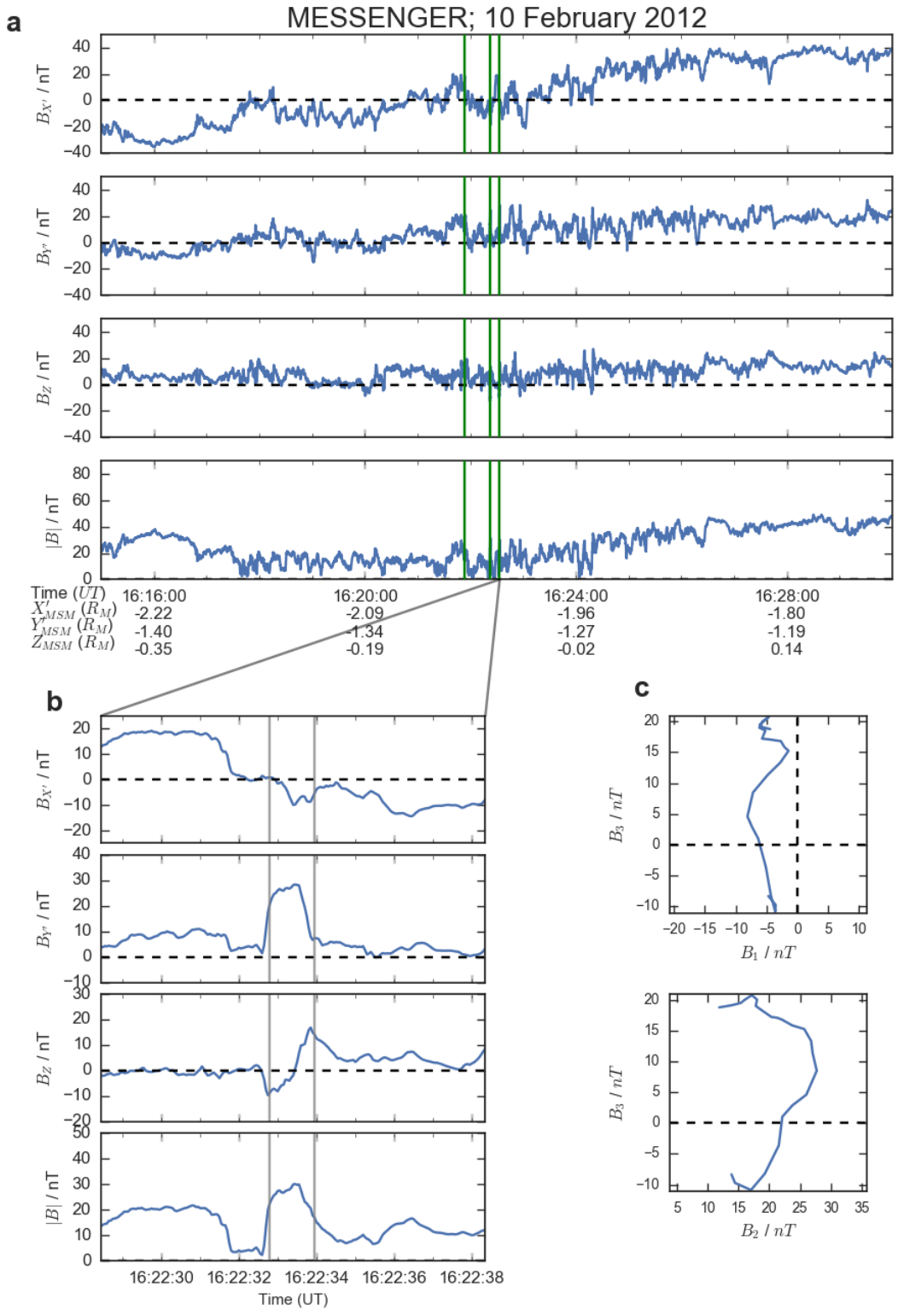

FIGURE 6.1: An illustrative plasma sheet crossing (a) with a zoom in of a flux rope detection (b) and example MVA hodograms (c). Panel (a) shows 15 minutes of 20 Hz MESSENGER magnetometer data in aberrated MSM coordinates; flux rope encounters are shaded green. Panel (b) shows 10 s of data around an *in situ* flux rope encounter. Once more the data are presented in aberrated MSM coordinates. The vertical grey bars indicate the region selected for minimum variance analysis (MVA), the resulting magnetic field hodograms (in the MVA system) are shown in panel (c).

The selection of crossings are evenly distributed across the midnight meridian and cover a range of downtail distances from $\sim 1-3\,R_M$. Limiting the data to intervals confirmed to lie within the plasma sheet reduces the chance of false positive detections from various phenomena including waves, localized compression regions and dynamic events on the magnetopause.

6.2.2 Flux Rope Signatures

The plasma sheet passage displayed in Figure 6.1a included three flux ropes, and Figure 6.1b shows a zoom-in of the magnetic field for one of these flux ropes; deemed to be an approximately cylindrical, linearly force-free structure. The key features of Figure 6.1b are the bipolar deflection in B_Z and the local peaks in $B_{Y'}$ and $|B|$. The spacecraft can be approximated as stationary, as the flux rope moves with a much larger relative velocity ($< v > \sim 465 kms^{-1}$ [*DiBraccio et al.*, 2015]). Previous work has determined that within the magnetotail the prevailing conditions result in the generation of flux ropes in the $\hat{X}_{MSM} - \hat{Y}_{MSM}$ plane, with their core fields approximately in the $\pm\hat{Y}_{MSM}$ direction, that travel either planetward or tailward (in the $\pm\hat{X}_{MSM}$ direction) [*Slavin et al.*, 2003a; *DiBraccio et al.*, 2015; *Sun et al.*, 2016]. This configuration gives rise to a bipolar deflection in the north-south component of the field (B_Z), with peaks in the axial direction ($\sim |B_{Y'}|$) and the total field ($|B|$). This signature is highly dependent on the trajectory through the structure, for example the distance of the spacecraft from the center of the flux rope at the point of closest approach will determine the magnitude of the core field recorded. The signature measured in $B_{X'}$ varies depending on whether the spacecraft encounters both the upper and lower hemispheres of the flux rope; local peaks or bipolar signatures are not uncommon. More detail and figures depicting the result of various relative trajectories can be found in *Borg et al.* [2012] and *DiBraccio et al.* [2015].

Minimum Variance Analysis (MVA) was first applied to spacecraft magnetic field observations for the purpose of identifying the normal to magnetic discontinuities: such as current layers [*Sonnerup and Cahill*, 1967]. The method generates three eigenvalues and eigenvectors; the eigenvectors describe a new coordinate system corresponding to the directions of minimum, intermediate and maximum variance. The degeneracy of the new system can be estimated by comparing the relative sizes of the eigenvalues. A well defined, distinct three dimensional system will be described by eigenvalues that are all significantly different from one another [*Khabrov and Sonnerup*, 1998; *Sonnerup and Scheible*, 1998].

If the spacecraft passes sufficiently close to the axis of a force-free flux rope then MVA can be used to estimate its orientation and structure [*Sibeck et al.*, 1984; *Elphic et al.*, 1986; *Slavin et al.*, 1989; *Moldwin and Hughes*, 1991; *Xiao et al.*, 2004]. When applied to an encounter with a force-free, cylindrically symmetric flux rope MVA would be expected to show a clear bipolar signature in the maximum variance direction ($\hat{\mathbf{e}}_3$), a peak in the intermediate direction ($\hat{\mathbf{e}}_2$) and very little variation in the direction of minimum variance ($\hat{\mathbf{e}}_1$). In fact, if the spacecraft passes directly through the center of the flux rope then the field in the direction of minimum variance will be equal to zero. The combination of the core field peak and the bipolar signature result in a clear rotation of the field in the hodogram of the maximum and intermediate variance directions. This signature is shown in Figure 6.1c).

6.2.3 Flux Rope Field Model

A force-free flux rope model (Equations 1.42, 1.43 and 1.44) is used in this study to estimate some of the physical parameters of the flux rope (e.g. radius and core field) and confirm that the recorded signature is due to the spacecraft's passage through a flux rope.

As discussed in Section 1.4.3.4, the cylindrically symmetric, constant α (linearly) force-free flux rope model represents the lowest energy configuration of helical fields [*Priest*, 1990], and so probably better represents flux ropes observed some time after formation.

6.3 Method

For a full, comprehensive description of the flux rope identification method the reader is directed to *Smith et al.* [2017a] (Chapter 5). In summary, the following steps are used to identify flux rope encounters:

1. Baseline Crossing and Peak Detection: significant deflections of the north-south component of the magnetic field are located.
   (a) Field deflections where $\Delta B_Z \geq 1\sigma$ are selected (that pass through $B_Z = 0$).
   (b) The deflections are required to be coincident with a peak in $|B_Y|$ or $|B|$ (which are identified using a continuous wavelet transform).
2. Minimum Variance Analysis (MVA): a consistent three dimensional magnetic structure is confirmed.

(a) The eigenvalue ratios $^{\lambda_3}/_{\lambda_2}$ and $^{\lambda_2}/_{\lambda_1}$ are required to be ≥ 5.

(b) A small variation in eigenvalue ratios (≤ 1.75) is needed when the limits of the analysis are varied.

(c) The eccentricity of the maximum-intermediate hodogram must be small ($e \leq 0.9$).

3. Force-Free Model Fitting: the structure is confirmed and physical parameters are estimated.

(a) A good fit to the force-free model is required (modified $\chi^2 \leq 0.15$).

(b) The best fit model impact parameter must be small: $r' \leq 0.5$.

The numerical thresholds were determined empirically by application of the method to trial intervals (both at Mercury and at Earth). Two small changes have been made to the method described by *Smith et al.* [2017a] (Chapter 5). Firstly, a criterion that the deflection crosses through $B_Z = 0$ has been added. Physically this corresponds to a requirement that the spacecraft must pass through both the leading and trailing hemispheres of the flux rope. Secondly, the maximum time window considered has been expanded from $2.5\,s$ to $3\,s$.

For some of the following analysis the identifications that satisfy the criteria in points one and two will be used, and these will be referred to as MVA confirmed flux ropes. The motivation for this is to use, when possible, a larger catalogue for greater statistical validity. The flux ropes that are judged to be cylindrically symmetric and linearly force-free, those that also satisfy the criteria in point three, form a subset of this larger catalogue and will be referred to as the force-free subset.

6.4 Statistical Results

A total of 248 MVA confirmed flux ropes were located within the 319 plasma sheet crossings, 74 of which ($\sim 30\%$) satisfactorily fit the force-free model. This force-free fraction is consistent with that determined by *DiBraccio et al.* [2015] ($^{16}/_{49}$ or 33%). It is likely that this fraction is an overestimate; if the flux ropes deviate far from cylindrical and force-free then they are unlikely to be selected based on the results of their MVA properties (and so the total population of flux ropes will be larger than 248).

6.4.1 Location and Frequency

The flux rope detections will now be discussed with respect to their rate and magnetospheric location. To that end, Figure 6.2 includes panels displaying (a) the distribution of MVA confirmed flux rope detections, (b) the distribution of orbital time within the plasma sheet (termed observation time), and (c) the corresponding rate of flux ropes observed per minute. Panels (d) and (e) then show the rate projected onto the X'_{MSM} and Y'_{MSM} axes respectively. The colour bars for Panels (d) and (e) show the plasma sheet observation time binned along the X'_{MSM} and Y'_{MSM} axes, providing an estimate for how well the rates are defined for each bin.

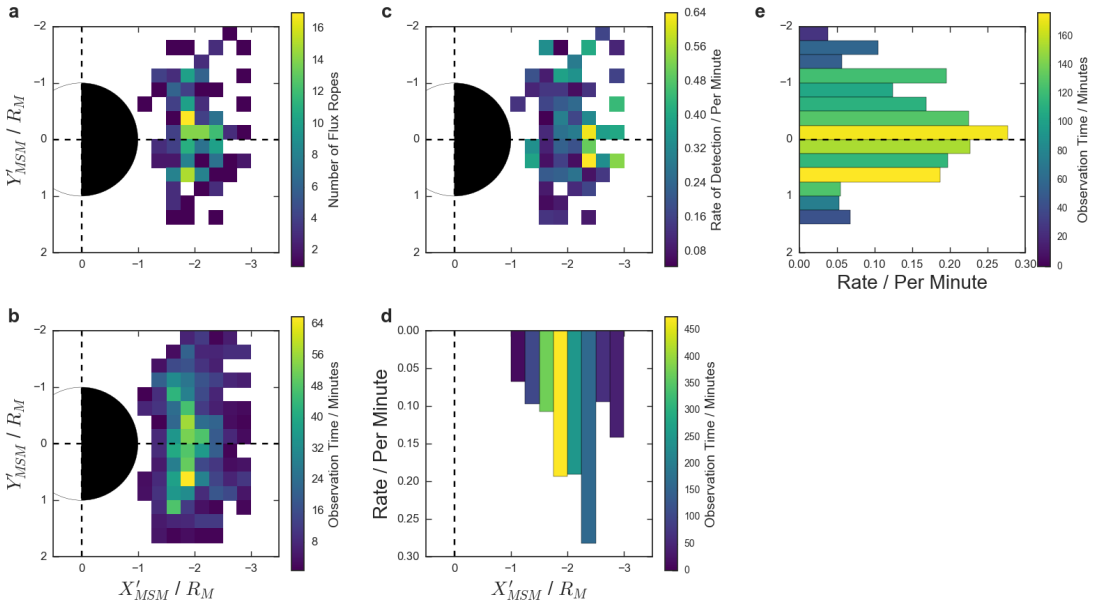

FIGURE 6.2: Histograms showing the distribution of 248 (MVA confirmed) flux ropes within the Hermean magnetotail. Data are binned in 0.25 R_M increments and projected onto the equatorial plane of the MSM coordinate system. Panel (a) describes the distribution of flux rope observations. Panel (b) shows the distribution of plasma sheet observations in minutes per spatial bin. Panel (c) shows the resulting rate of flux rope observations ($^{\#}/_{T}$). Panels (d) and (e) show the rate projected onto the X'_{MSM} and Y'_{MSM} axes respectively. The colour bars for Panels (d) and (e) show the plasma sheet observation time projected onto the X'_{MSM} and Y'_{MSM} axes, this is shown to provide an approximate measure of how well determined (or how much data) has produced the rates for that region.

Figure 6.2 shows the distributions for all MVA confirmed flux ropes, but the equivalent plot for force-free flux ropes shows similar results. Panel (a) shows a slight dawn-dusk asymmetry, with 58% of the detections being located on the dawn side of the tail. This is also found to be the case for those detections confirmed to be force-free; 62% are located on the dawn side of the midnight meridian (not shown).

The 319 plasma sheet crossings can be seen to give coverage over most of the magnetotail (Figure 6.2b). The majority of the coverage can be seen to lie between $1.5 - 2.5\,R_M$

down the tail, and between $-1.5\,R_M \leq Y'_{MSM} \leq 1.5\,R_M$ azimuthally. There is not a significant dawn-dusk asymmetry in the coverage (the plasma sheet observation time follows a $52\% - 48\%$ dawn-dusk split), ruling this out as a cause of the imbalance in the numbers observed in panel (a).

Normalizing the number of flux ropes observed by the time spent within the plasma sheet reveals that although the largest numbers of flux ropes were observed close to the centre of the tail, these also coincide with the locations most often covered by MESSENGER. Panel (d) shows that the rate of flux ropes increases as you move down the tail up until $\sim -2.5\,R_M$. At this point the data coverage is not as comprehensive and so the drop at this point could be due to the relatively small statistics beyond $-2.5\,R_M$ (blue colored bars indicate relatively low observation time). Panel (e) shows the rate across the magnetotail. The distribution is fairly symmetric within the central magnetotail ($Y'_{MSM} \leq \pm 0.5\,R_M$), this corresponds approximately to the region surveyed by *DiBraccio et al.* [2015], where no asymmetries were observed. Outside of the central region it can be seen that flux ropes are more commonly observed at dawn; for the bins covering the $0.5\,R_M$ centered on $\sim Y'_{MSM} = \pm 1$ the rate is three times higher at dawn. This result correlates with recent observations of flux ropes [*Sun et al.*, 2016], statistical field distributions [*Poh et al.*, 2017b], and the origin of precipitating energetic electrons [*Lindsay et al.*, 2015], though is perhaps not as dramatic. A dawn-dusk asymmetry has also been observed for dipolarization fronts [*Sun et al.*, 2016]. This correspondence could be explained by the simulations of *Lu et al.* [2015], who suggest that planetward moving flux ropes may form dipolarization fronts as they re-reconnect with the planetary dipole field. Therefore, any asymmetry would be present in both types of event.

The variation in the rate of flux rope observations across the magnetotail (along the X'_{MSM} axis) suggests that the azimuthal extent of flux ropes within Mercury's magnetotail is limited. *Kiehas et al.* [2013] inferred this to be true for terrestrial flux ropes using multiple spacecraft; the absence of contemporaneous flux rope observations at an adjacent spacecraft suggests a limited azimuthal extent. An alternative explanation could be that flux ropes are not well modelled as cylindrical tubes; that they are distorted for much of their length and as such not as easily identifiable.

The peak rate observed in Panels (d) and (e) is around 0.25 flux ropes per minute, just over three times the rate observed by *Sun et al.* [2016]. It is possible that by selecting those flux ropes for which $\Delta B_Z \geq 1\sigma$ (as opposed to a fixed limit of $\Delta B_Z \geq 15\,nT$ [*Sun et al.*, 2016]) an additional population of small flux ropes will be included. Indeed, if the same selection criterion are applied ($\Delta B_Z \geq 15\,nT$) the number of flux ropes in the catalogue drops from 248 to 120, and the rate reduces to around 0.1 flux ropes per minute, consistent with their result [*Sun et al.*, 2016].

A dawn-dusk asymmetry in the rate of reconnection products has been observed at Earth [*Walsh et al.*, 2014], however the asymmetry is in the opposite direction from that observed by both this and previous studies at Mercury: at Earth flux ropes are more commonly observed pre-midnight [*Slavin et al.*, 2005; *Imber et al.*, 2011]. The peak rate of flux ropes observed at Earth was found to be $\sim 1.2{\times}10^{-3}\,min^{-1}$ [*Imber et al.*, 2011], approximately 200 times smaller than that observed by this work.

The peak rate calculated above ($0.25\,min^{-1}$) is averaged over the plasma sheet observation time and binned along the X'_{MSM} or Y'_{MSM} axes. However, measuring the recurrence in this manner does not fully convey the intermittent nature of the flux rope observations. For example, in Figure 6.1a) three flux ropes are observed during a single plasma sheet crossing. The time from the first to the last flux rope is $\sim 39\,s$, so in this interval the rate of flux rope observation is approximately $5\,min^{-1}$, much higher than the average ($0.25\,min^{-1}$) would have suggested.

Overall, during 61% of the plasma sheet encounters investigated no (MVA confirmed) flux ropes are observed; this fraction increases to 83% when only force-free flux ropes are considered. Figure 6.3a) shows these proportions and also that up to eight flux ropes have been observed in a single crossing. The large fraction of intervals where no flux ropes are observed suggest that reconnection in Mercury's magnetotail is sporadic and occurs in bursts, producing several flux ropes (very rapidly) during each episode before the tail enters a period of relative quiescence. Only 25% of MVA confirmed flux ropes occur in isolation. This fraction is likely to be an upper limit as some flux ropes are likely not identified.

Figure 6.3b) shows the distribution of times between adjacent MVA confirmed flux ropes. In total 124 intervals between adjacent flux ropes are plotted, the vast majority of which are shorter than $\sim 100\,s$. This suggests they are likely related to the same reconnection event within the magnetotail. A similarly short interval between adjacent flux ropes has been observed at Earth [*Imber et al.*, 2011].

6.4.2 Orientation

MVA can be applied to the force-free subset of flux ropes to estimate their approximate orientation [*Sibeck et al.*, 1984; *Elphic et al.*, 1986; *Slavin et al.*, 1989; *Moldwin and Hughes*, 1991; *Xiao et al.*, 2004]. When applied to a force-free flux rope the minimum variance direction ($\hat{\mathbf{e}}_\mathbf{1}$) corresponds to the spacecraft passage through the flux rope, the intermediate vector corresponds to the axial direction ($\hat{\mathbf{e}}_\mathbf{2}$), and the maximum variance vector completes the right handed set ($\hat{\mathbf{e}}_\mathbf{3}$). Figure 6.4 shows these MVA results for the force-free subset of flux ropes. The rows show the results for the minimum, intermediate

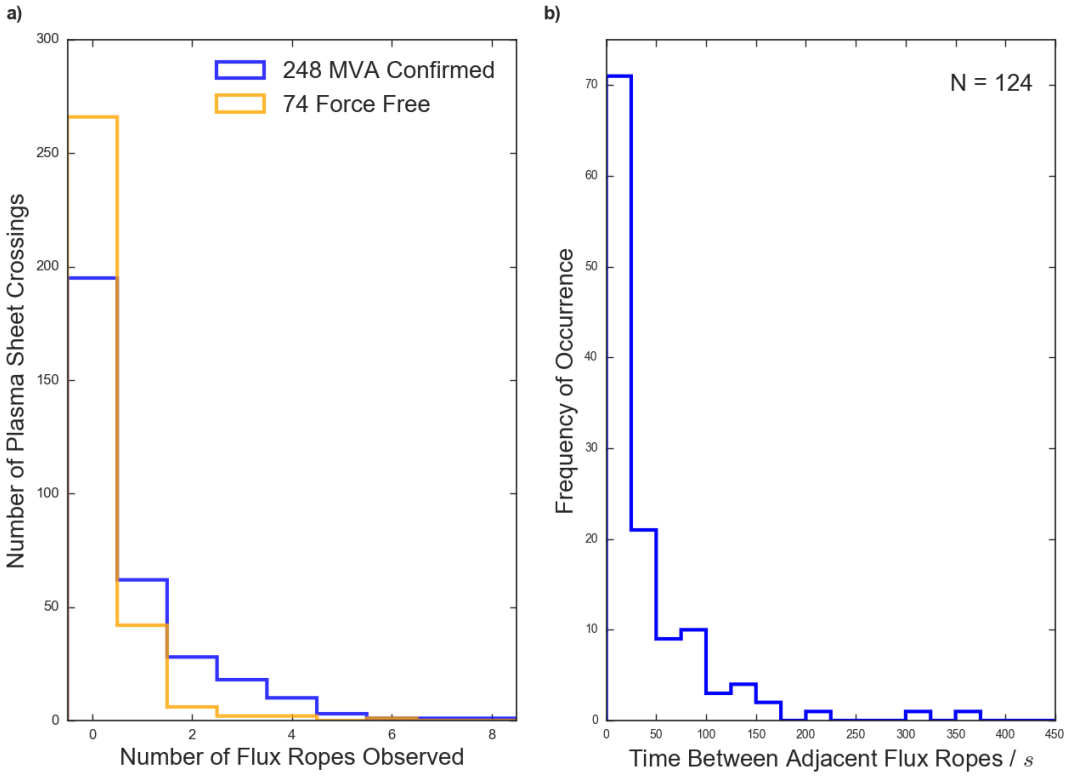

FIGURE 6.3: Panel (a) shows a histogram of the number of MVA confirmed (blue) and force-free (orange) flux ropes observed during each plasma sheet crossing. Panel (b) shows the distribution of times between adjacent MVA confirmed flux ropes.

and maximum variance directions respectively. Meanwhile the columns, from left to right, show the X'_{MSM} - Y'_{MSM} projection, the X'_{MSM} - Z_{MSM} projection and the angular difference between the vectors and an MSM base vector of interest.

For the (a) panels, the minimum variance direction ($\hat{\mathbf{e}}_1$), the vectors largely lie in the X'_{MSM} - Y'_{MSM} plane. Physically, this suggests that the motion of the flux ropes is limited to this plane, as has been observed by previous studies [*Slavin et al.*, 2003a; *DiBraccio et al.*, 2015]. However, the average angular difference between the minimum variance direction and the $\pm\hat{X}'_{MSM}$ axis, is relatively large at 47.5°, the distribution of which in shown in panel (a)(iii).

The (b) panels, showing the results for the intermediate variance direction (($\hat{\mathbf{e}}_2$), representing the approximate direction of the core field show a similar result. The relative magnitude of the vectors is small in panel (b)(ii) compared to that in panel (b)(i). Panel (b)(iii) shows the distribution of angular differences between the intermediate variance direction and the $\pm\hat{Y}'_{MSM}$ axis. Once more this shows a relatively large average angular difference (46.5°), suggesting a large range of flux rope orientations or skews is possible.

Previous studies have commonly observed flux ropes whose axes are tilted in the plane of the magnetic equator at both Earth [*Hughes and Sibeck*, 1987; *Moldwin and Hughes*,

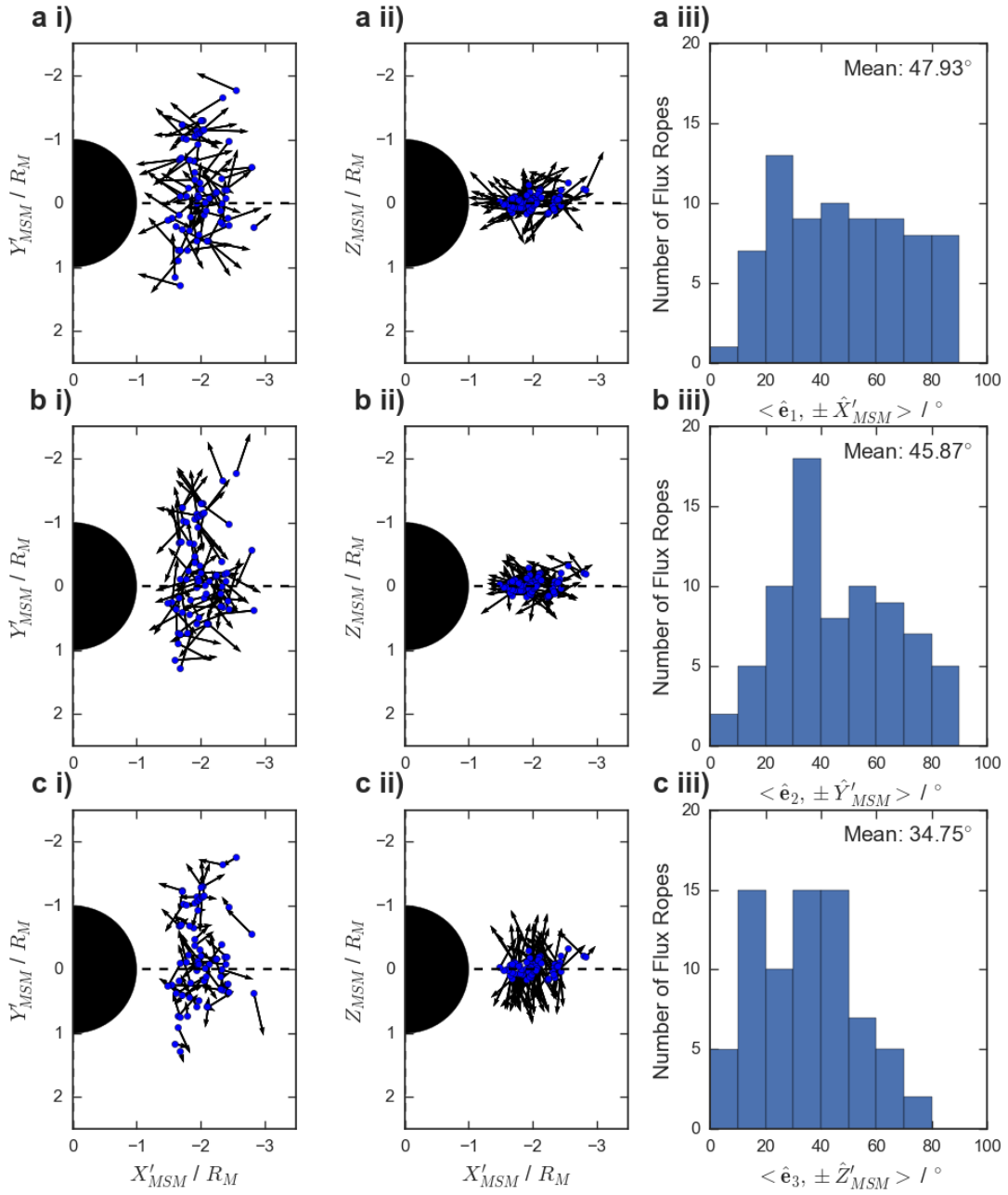

FIGURE 6.4: Minimum Variance Analysis (MVA) results for the 74 force-free flux ropes. The first two columns shows the X'_{MSM} - Y'_{MSM} and X'_{MSM} - Y'_{MSM} projections respectively. The right hand column shows the angular difference in degrees between the variance vectors and the relevant MSM base vector. The rows, from top to bottom, show the minimum, intermediate and maximum variance vectors.

1992; *Slavin et al.*, 2003a; *Kiehas et al.*, 2012] and Mercury [*Sun et al.*, 2016]. *Kiehas et al.* [2012] proposed two potential mechanisms to explain this: (a) spreading of the reconnection site east-west from near midnight resulting in a boomerang-shaped flux rope, and (b) an asynchronous release of the ends of the flux rope, leading to a self consistent tilt. Both formation scenarios (a) and (b) would result in the core field deviating from the $\pm Y'_{MSM}$ direction. Scenario (a) may result in a core field directed

closer to the azimuthal unit vector, $\hat{\phi}$ (e.g. along lines of constant radial distance from the planet). The average angular difference between the intermediate variance direction and the azimuthal unit vector was found to be 46.0°; slightly smaller than found for the $\pm\hat{Y}'_{MSM}$ comparison, but not decisively different. Thus, the results are not sufficient to distinguish between the formation scenarios on a statistical basis, indeed a combination of both processes is possible [*Kiehas et al.*, 2012].

The final row of Figure 6.4, the (c) panels, shows that the maximum variance direction is most often aligned with the $\pm\hat{Z}_{MSM}$ direction. However, the angular difference between the vectors still has a relatively large mean value (34.8°).

The results are broadly consistent with the most recent flux rope survey [*Sun et al.*, 2016], though the mean angular differences reported here are slightly larger. This could be due to a larger dataset, and slightly different selection criteria. Here, for example, no firm limit is placed on the size of the B_Z deflection, and therefore include smaller scale events that could perhaps have more extreme tilts (as they would be more susceptible to local perturbations).

There are several selection effects deserving of mention. Firstly, the preliminary signature sought to identify potential flux ropes (Section 3.1) is a bipolar deflection of B_Z. If the flux ropes do not possess $\Delta B_Z \geq 1\sigma$ then they will not be located by this first step and will therefore not be present in the analysis. It is possible that there are flux ropes excluded from this analysis whose principle axis of variation is poorly aligned with $\pm\hat{Z}_{MSM}$. Secondly, the identification process described in Section 3.2 requires the presence of a peak in $\pm B_Y$ or $|B|$, B_X is not considered and it is possible that some highly skewed flux ropes may not be selected (if the peak in $|B|$ is not correctly identified).

An important consideration when applying this analysis is the accuracy of the MVA technique. When MVA is applied to a model force-free flux rope an impact parameter of $0.5\,R_0$ results in an angular difference of $\sim 20°$ between the intermediate variance direction and the true axial direction [*Xiao et al.*, 2004]. A real force-free flux rope (even where the linear and cylindrical symmetry approximations are well founded) will almost certainly result in a larger discrepancy between the intermediate variance axis and the axial direction. In light of this, the relatively large spreads of angular differences observed in Figure 6.4 are perhaps not unexpected.

6.4.3 Physical Properties

Figure 6.5 shows several histograms detailing the distribution of flux rope parameters observed for the force-free subset. Panels (a) and (b) show the duration and size of

the magnetic field deflections respectively, measured from peak to peak of the bipolar B_Z signature. Panel (c) shows the distribution of impact parameters inferred from the force-free model fit. Panels (d), (e) and (f) show the distributions of the inferred radius (R_0), core field (B_0) and flux context (Φ_{FR}). The first two panels are plotted for the entire MVA confirmed catalogue while the later four only include those confirmed to be force-free.

It is worth noting that there is both a lower and upper cutoff to the duration measured in Figure 6.5a). The techniques used to identify the events require at least four data points, and thus the lower limit to detection is $0.2\,s$. In a similar manner, the maximum event length is $3\,s$; set by the maximum duration explored for the deflection of B_Z. The average duration of $0.83\,s$ for MVA confirmed flux ropes is slightly larger than that obtained by *DiBraccio et al.* [2015] ($0.74\,s$). The small difference could be explained by the cutoff to the duration applied by this work: no such lower limit was applied by *DiBraccio et al.* [2015]. The mean duration of force-free flux ropes ($1.08\,s$) is found to be greater than that of the larger catalogue of MVA confirmed flux ropes; suggesting that smaller duration flux ropes met the force-free criterion less often. Physically, smaller flux ropes could be more likely to correspond to those observed soon after their formation (as discussed in Section 2.3).

The distribution of Figure 6.5b) increases fairly sharply down to $|\Delta B_Z| \sim 10\,nT$. The drop in the distribution below this point could be a result of the requirement that the deflection is greater than the background fluctuations of the field ($|\Delta B_Z| \geq 1\sigma$). It is likely that a population of flux ropes whose magnetic deflections are smaller than 1σ exist, but are not included in this survey. This population may also be missed as a result of the minimum duration of $0.2\,s$ (discussed above).

The distribution of flux rope impact parameters inferred from the force-free fit (Panel (c)) may indicate that the method has resulted in a slight preference for selecting those flux ropes observed at the smallest impact parameters (e.g. ${}^{r}/_{R_0} \leq 0.1$). This could be explained by the requirements placed upon the MVA signature: as the spacecraft passage moves further from the central axis (the impact parameter increases) the MVA results would be expected to be less reliable [*Xiao et al.*, 2004] (and lead to the signature being rejected). Otherwise, the distribution looks fairly constant, as may be expected: the flux ropes would be contained within the plasma sheet, the entirety of which is traversed by the spacecraft.

Figure 6.5d) shows the distribution of best fit flux rope radii, calculated using the observed duration, best fit model impact parameter and an assumed average speed of $465\,kms^{-1}$ [*DiBraccio et al.*, 2015]. The use of an average, and not a local speed is not ideal. *DiBraccio et al.* [2015] measured the Alfvén speed (V_A) of the adjacent plasma

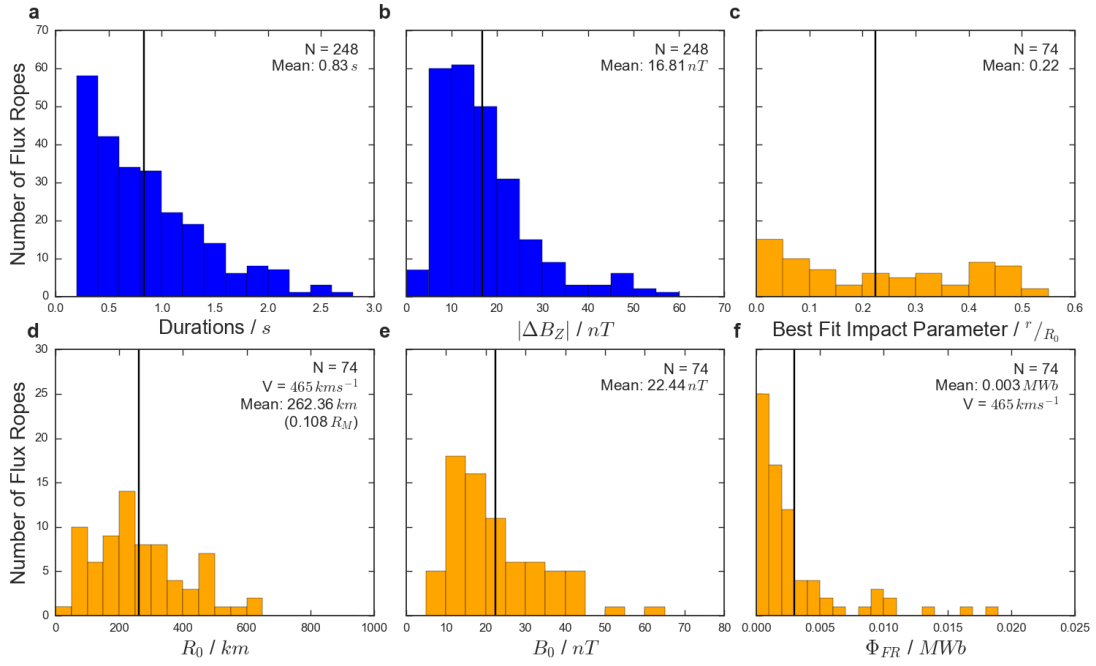

FIGURE 6.5: Histograms showing the distribution of several key flux rope parameters. Panels (a) and (b) are shown for the MVA confirmed flux ropes (in blue) while panels (c)-(f) are only shown for the force-free subset (in orange) as they require parameters from the successful model fit. The means of the distribution are indicated with black vertical bars (and numerically in the upper right of the panels). Panel (a) shows the duration of the flux ropes as measured by the *in situ* spacecraft data, between the extremes of the bipolar B_Z variation. Panel (b) shows the distribution of $|\Delta B_Z|$. Panel (c) shows the distribution of best fit impact parameters from the force-free model fit, panel (d) shows the inferred radius of the flux ropes, calculated assuming a velocity of $465\,kms^{-1}$ and correcting for the impact parameter of the encounter. Panel (e) displays the core fields observed, again inferred from the force-free fit. Panel (f) shows the distribution of flux contained with the flux ropes, calculated using Equation 6.1.

sheet and found values to range from as low as $\sim 100 kms^{-1}$ to over $1000 kms^{-1}$. In addition to this order of magnitude variation in the local plasma sheet it is likely that within the (plasma depleted) reconnection flow the Alfvén speed is higher. For these reasons the radii calculated should be regarded as lower limits. The mean R_0 inferred from the catalogue is $262\,km$ $(0.11\,R_M)$, consistent with previous work [*Slavin et al.*, 2012a; *DiBraccio et al.*, 2015], though slightly smaller; perhaps for the reasons outlined above. A typical plasma sheet density of between 1 and $10\,cm^{-3}$ [*Gershman et al.*, 2014] suggests the ion inertial length in Mercury's magnetotail plasma sheet is $\sim 78 - 228\,km$; a similar order of magnitude to the radius of the observed flux ropes. Therefore, these flux ropes are of similar nature to the ion-scale flux ropes recently identified at the Earth's magnetopause [*Eastwood et al.*, 2016].

The distribution of core field inferred from the force-free fitting (B_0) is provided in Figure 6.5c). The mean B_0 observed is found to be $22.44\,nT$, smaller than that observed by

DiBraccio et al. [2015] ($41\,nT$) and more comparable to that observed at the Earth ($20nT$) [*Slavin et al.*, 2003a].

The flux contained within the flux rope can be obtained from the results of the force-free fit:

$$\Phi_{FR} = \frac{1}{\alpha} 2\pi B_0 R_0^2 J_1(\alpha) \tag{6.1}$$

where Φ_{FR} is the flux content of the flux rope, α is a constant from the force-free fit (taken to be 2.4048 [*Burlaga*, 1988]), B_0 is the strength of the core field, R_0 is the radius of the flux rope and $J_1(\alpha)$ is the first order Bessel function. As this equation requires the radius of the flux rope, it is implicitly dependent on the flux rope velocity (once more assumed to be $465\,kms^{-1}$ [*DiBraccio et al.*, 2015]). The distribution of flux content is displayed in Figure 6.5f). The average Φ_{FR} is found to be $0.003\,MWb$, consistent with the previous estimate of *DiBraccio et al.* [2015]. In comparison, the average flux content of FTEs at Mercury's magnetopause has been found to be $0.06\,MWb$ [*Imber et al.*, 2011], suggesting the flux contained within magnetotail flux ropes is negligible when considering the closure of magnetic flux from the magnetosphere. Therefore, the majority of the flux closure at Mercury must occur during continued lobe reconnection at the x-lines that generate flux ropes [*Richardson et al.*, 1987; *DiBraccio et al.*, 2015].

6.5 Discussion

The survey results will now be discussed with respect to spatial variations across the magnetotail and factors affecting flux rope creation.

6.5.1 Reconnection Location

Although no direct encounters with the NMNL (Near Mercury Neutral Line) are reported by this study, its relative location can be inferred from the direction of motion of the observed flux ropes. In total 55% of the observed flux ropes are moving towards the planet, these flux ropes are observed between 1.25 and $3\,R_M$ down the Hermean tail. On this basis it could be inferred that the NMNL often lies downtail, beyond MESSENGER's orbit ($R \leq 3\,R_M$). This broad result agrees with the preliminary analysis in Section 4.1 and the recent statistical study of *Poh et al.* [2017a], who inferred that the average location of the NMNL was at $X'_{MSM} \sim -3\,R_M$.

Figure 6.6 shows how the distributions of tailward and planetward moving flux ropes compare. Panels (a) and (b) show the distribution of the rates of flux ropes observed in each sector. Qualitatively, they show similar distributions around the midnight ($X'_{MSM} = 0$), however it can be seen that the more distant (downtail) detections post-midnight are almost solely due to planetward moving flux ropes (e.g. $X'_{MSM} \leq -2$). Panel (c) shows the difference between Panels (a) and (b). The majority of sectors are negative (red) indicating that planetward moving flux ropes are more common, especially post-midnight. Again, this perhaps suggests that the location of the NMNL (on average) lies downtail, beyond the coverage of MESSENGER.

Figure 6.6d) shows the rate of tailward and planetward moving (MVA confirmed) flux ropes projected along the X'_{MSM} axis. The distributions are similar for both populations, indicating that the location of the NMNL is likely extremely variable and can, perhaps under strong driving/loading conditions [*Slavin et al.*, 2010], be located very close to the planet. *DiBraccio et al.* [2015] inferred the location of the NMNL to be within ~ 2 and $3\,R_M$ of the planet, a result consistent with a highly mobile x-line within the coverage of MESSENGER.

Figure 6.6e) shows the distribution of flux ropes across the Hermean magnetotail, along the $\hat{Y}'_{MSM}$ axis. The slight dawn-dusk asymmetry, highlighted in Section 4.1, is shown here to be almost entirely due to a portion of the planetward moving flux rope population (red bars). 62% of the planetward moving flux ropes are located dawn-ward of the midnight meridian, compared to 52% of tailward moving flux ropes. This could be explained by the NMNL forming further down the magnetotail on the dawn flank. An asymmetric x-line has been observed at Jupiter, though in the opposite respect: the Jovian x-line is located closer to planet post-midnight [*Vogt et al.*, 2010].

While this is a statistical result, it may be expected that on each occasion the NMNL forms at a given location before retreating down the magnetotail, as was observed during the second [*Slavin et al.*, 2009, 2012a] and third MESSENGER flybys [*Slavin et al.*, 2010]. In these intervals the motion was diagnosed by observing a transition from tailward moving flux ropes (and/or associated traveling compression regions - TCRs) to planetward moving structures (as at Earth [c.f. *Baker et al.*, 1996]). In both flybys the transition between tailward and planetward motion occurred on timescales of the order of minutes to tens of minutes, comparable to the average duration of plasma sheet passages in this study (4.6 minutes). In this statistical work, a transition from tailward to planetward moving (MVA confirmed) flux ropes was observed 34 times, at locations ranging from $X'_{MSM} = -1.35$ to $-2.82\,R_M$ (i.e. across the full scope of this study). A total of 62 chains of more than one (MVA confirmed) flux ropes were observed, and so

55% of flux rope chains show evidence of neutral line retreat, indicating that this is a relatively common occurrence.

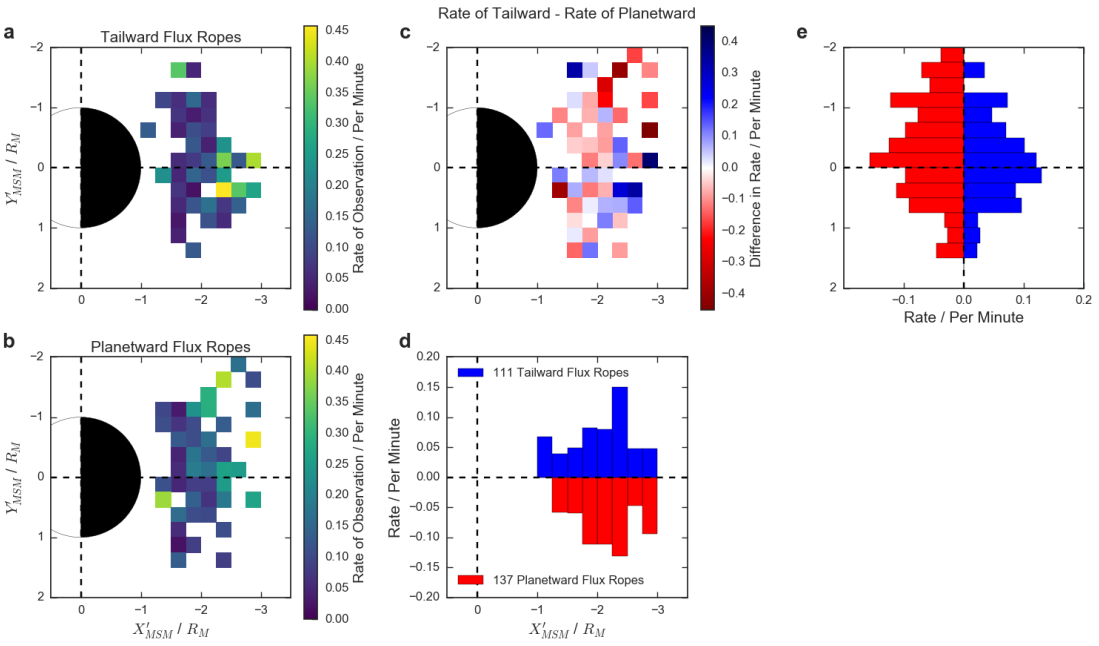

FIGURE 6.6: Histograms showing the rate of observation of 111 tailward (Panel a) and 137 planetward (Panel b) moving MVA confirmed flux ropes. Data are binned in $0.25\,R_M$ increments and projected onto the equatorial plane of the MSM coordinate system. Panel (c) shows the rate of tailward moving flux ropes minus the rate of the planetward moving flux ropes. Positive (blue) values indicate regions where tailward moving flux ropes are observed more often, while negative (red) regions show locations where planetward moving flux ropes are more commonly observed. Panels (d) and (e) show the rates of planetward (red) and tailward (blue) moving flux ropes binned along the X'_{MSM} and Y'_{MSM} axes respectively.

6.5.2 Magnetotail Driving

Reconnection at the dayside magnetopause, if not matched by reconnection in the magnetotail, results in a build up of open flux in the magnetotail lobes. At Earth this is known as the growth phase of a substorm [*Akasofu*, 1964]. This build up of magnetic flux can be observed as an increase in the lobe magnetic field strength [*McPherron et al.*, 1973; *Baker et al.*, 1996] or in the magnetotail flaring angle [*Fairfield*, 1985]. It could be expected that reconnection becomes more likely within the magnetotail as the lobe field strength increases and the plasma sheet thins, magnetospheric phenomena that have been observed at Mercury [*Sun et al.*, 2015]. Ideally this would be explored using data from multiple spacecraft, allowing the simultaneous measurement of lobe field strength and *in situ* flux rope encounters, especially at Mercury where the relative timescales are

very short [*Slavin et al.*, 2009, 2012a]. However, lacking multi-point observations, the average lobe field ($< |B|_{Lobe} >$) was recorded shortly before the each plasma sheet passage (an average of $4m43s$ before). A background model lobe field can then be subtracted:

$$|B|_{Lobe}^{Model}(|X'_{MSM}|) = A|X'_{MSM}|^{G} + B_0 \tag{6.2}$$

where the values of the variables A, G and B_0 were determined to be 86.4, -3.1 and 41.4 respectively by *Poh et al.* [2017a]. The aim of the subtraction is to provide an estimate of whether the lobe field is relatively enhanced or diminished compared to other orbits. Figure 6.7 shows how the difference in lobe field strength is related to the likelihood of flux ropes being observed during a plasma sheet crossing. The fraction of crossings plotted is the number of crossings during which at least one (MVA confirmed) flux rope is observed (for a given lobe field strength) divided by the total number of crossings. The colour bar is used to show the total number of crossings for the relative lobe field strength. For example, during two separate orbital passes the lobe field strength was over $40\,nT$ greater than the model prediction; during both of the subsequent plasma sheet encounters at least one flux rope was observed (giving them both fractions of 1.). It can be clearly seen from Figure 6.7 that the larger the lobe field strength, relative to a background level, the more likely MESSENGER was to observe flux ropes during the plasma sheet passage. Though Figure 6.7 is plotted for the MVA confirmed flux rope catalogue, the same trend is found if the figure is repeated for the force-free subset.

6.5.3 Magnetotail Shear

Previous work at the Earth found a time delayed correlation between the B_Y component of the magnetic field in the IMF and the measured B_Y in the core of flux ropes observed in the centre of the magnetotail. *Moldwin and Hughes* [1992] recorded the hourly average of the IMF and found that 87% of the 39 flux ropes observed had core fields orientated in the same direction. Later, *Slavin et al.* [2003a] reported 79% of the 28 flux rope core fields in their sample agreed with the preceding IMF. More recently, *Borg et al.* [2012] performed a similar study with a sample size of 27, observing only a weak correlation. At Mercury, no contemporaneous upstream measurements of the IMF are possible given the presence of a solitary spacecraft. However, reconnection between the IMF and the dayside magnetopause will result in transport of the IMF B_Y into the magnetotail [*Fairfield*, 1979; *Cowley and Hughes*, 1983; *Petrukovich*, 2011], either through direct convection [*Dungey*, 1965] or asymmetric flux transport [*Tenfjord et al.*, 2015]. Estimates of the timescale for the transport of the IMF from the solar wind to the terrestrial neutral sheet vary between $\sim$ 1 to 3 hours, depending on the solar wind conditions [*Rong et al.*,

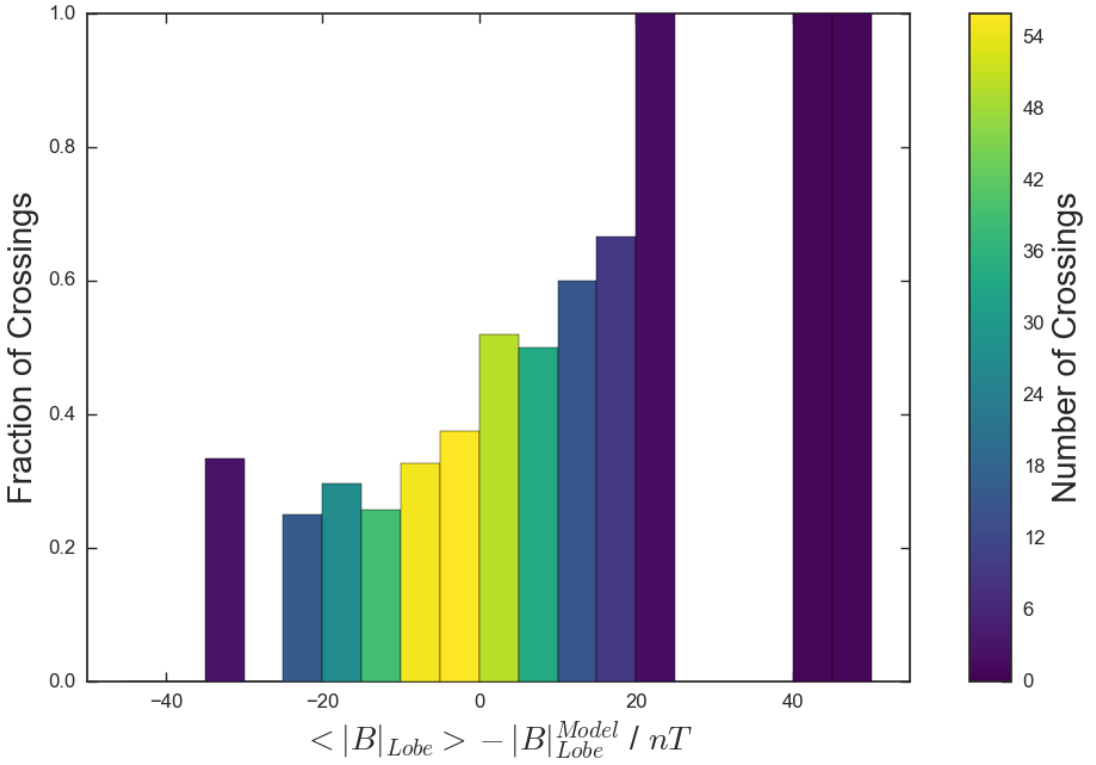

FIGURE 6.7: The fraction of crossings during which (MVA confirmed) flux ropes were observed plotted against the relative lobe field strength measured just prior to the plasma sheet encounter. The model lobe field strength (from Equation 6.2 [*Poh et al.*, 2017a]) is subtracted from the average lobe field (measured shortly before entering the plasma sheet boundary layer) to calculate the relative lobe field strength. The colour bar indicates the number of crossings present in each bin.

2015; *Browett et al.*, 2017]. At Mercury it is likely that this timescale is much shorter owing to the smaller size of the magnetosphere and stronger solar wind modulation [*Burlaga*, 2001; *Slavin et al.*, 2010]. A full consideration of the timescale involved in transfer of the IMF to the neutral sheet at Mercury is both beyond the scope of this work and unlikely to be possible with the single point measurements available. There are two unknown timescales at Mercury of importance to this investigation, the first of which is the time for the IMF B_Y to penetrate the magnetotail. The second is the timescale of variation of B_Y, both in the solar wind and the magnetotail.

The B_Y measured in the magnetotail has several major contributing factors: (a) interaction with the IMF, (b) magnetotail flaring and (c) local fluctuations of the plasma sheet. Source (a) is of primary interest to this study in terms of its effect on the development of the core field of the flux rope [*Moldwin and Hughes*, 1992; *Borg et al.*, 2012]. Source (b), flaring of the magnetotail, is significant in that MESSENGER's orbit lies within the flaring region; *Poh et al.* [2017a] estimated that the flaring region statistically ends

TABLE 6.1: Least-square derived coefficients for Equation 6.3

Coefficient	a	b	c	d	e	f
Value	0.36	-0.43	7.79	2.86	27.3	1.32

at $\sim -3.5\,R_M$ (the extrapolated location where lobe field strength asymptotes). Quantifying the third source of magnetotail B_Y is non-trivial given the relative timescales of the spacecraft motion and plasma sheet fluctuations. Instead, their effect is minimized by selecting lobe intervals at a distance from the plasma sheet. The B_Y component due to the skew of the magnetotail (caused by the angle of solar wind incidence) is assumed to be small, having been corrected for with the use of an aberrated coordinate system (e.g. $B_{Y'}$) [*Fairfield*, 1979].

To isolate the $B_{Y'}$ due to the interaction with the IMF a two dimensional model is used to allow the subtraction of an empirical model flared field. Figure 6.8a) shows a three dimensional plot, where the points indicate the location of the measured lobe intervals and their corresponding values of $B_{Y'}$. The surface and colour bar show the least squares quadratic model fit expressed in Equation 6.3:

$$B_{Y'}^{Model} = a(X'_{MSM})^2 + b(Y'_{MSM})^2 + cX'_{MSM}Y'_{MSM} + dX'_{MSM} + eY'_{MSM} + f \quad (6.3)$$

A linear (planar) fit was also tested and found to result in larger residuals: it did not accurately describe the reduction in flaring with downtail distance. The values of the coefficients obtained from the least squares fit are shown in Table 6.1. The model can be seen to asymptote/flatten at $\sim -3.5\,R_M$, this could be interpreted as the end of the flaring region, consistent with the findings of *Poh et al.* [2017a]. However, the model asymptotes to a non-zero value of $B_{Y'}$, perhaps due to the relative scarcity of data beyond $\sim -2.5\,R_M$. Though the model will describe the average tail flaring of the magnetotail it is likely highly variable and dependent on recent solar wind conditions.

Figure 6.8b) shows the maximum B'_Y measured within the flux rope (as an estimate of the core field strength) plotted against the difference between the lobe field measurement (made prior to the flux rope encounter) and the model value calculated from Equation 6.3. The grey points and error bars show the individual measurements and $\pm 1\sigma$ of the lobe $B_{Y'}$. The blue solid points show the mean and standard error of the mean of the data binned every $5\,nT$. The blue line indicates the best fit to the data (in grey).

The correlation shown by Figure 6.8b) is weak; only 58% of the observed flux ropes have core directions consistent with the preceding lobe field orientations. The first potential

explanation is down to the timescales of the penetration of the IMF and variation of B'_Y. The lobe value is measured (on average) $\sim 5-10$ minutes before the flux ropes are observed, so it is perhaps likely that the B'_Y measured is not the same as that present in the current sheet during the formation of the flux rope. Also, the variation in B'_Y is evident in the relative size of the gray error bars. It is also true that the study includes a large number of small scale flux ropes, whose core orientation and strength is likely to be strongly dependent on the local conditions at their formation; conditions that are not well explored with such broad averaging and unknown timing. Perhaps less critically, the maximum B'_Y measured during the flux rope is a conservative lower limit to the core field of the flux rope; very few encounters will pass directly through the strongest core field at the centre of the flux ropes. Similarly, as shown in Section 4.2, a large number of the observed flux ropes have a significant tilt to their core orientation (in the $X'_{MSM} - Y'_{MSM}$ plane) meaning that the peak B'_Y value will again underestimate the core field strength. Finally, the value of B'_Y due to the flaring of the tail will vary over time depending on recent solar wind conditions; during periods of strong (weak) driving the tail flaring angle will increase (decrease), increasing (reducing) the contribution of tail flaring to the observed B'_Y.

Figure 6.8c) shows the relationship between the average B'_Y measured within the central plasma sheet and the maximum B'_Y measured during the flux rope. 67% of flux ropes are oriented in a manner consistent with prevailing plasma sheet B'_Y, though the error bars (standard deviations) are relatively large indicating that the plasma sheet B'_Y fluctuates significantly. Some inconsistencies would be expected as the local plasma sheet where the flux ropes are formed is not measured, but the plasma sheet before, during and after their passage past the spacecraft. It may be expected that the core fields would correlate strongly with the local Hall field [*Teh et al.*, 2014].

The inverse of the gradient of the linear fit is large, indicating that (statistically) the core fields observed are just over six times the average B'_Y measured in the plasma sheet at a similar time. As mentioned above, the $B^{max}_{Y'}$ plotted here is a lower limit of the core field strength due to the observed flux rope tilt and largely non-zero impact parameters. Though the results are generally consistent with the B'_Y in the nearby plasma sheet resulting in the generation of the core field there are a significant number of exceptions, similar to the observations of *Borg et al.* [2012] at Earth, perhaps due to variations in the strength of the local guide field [*Teh et al.*, 2014].

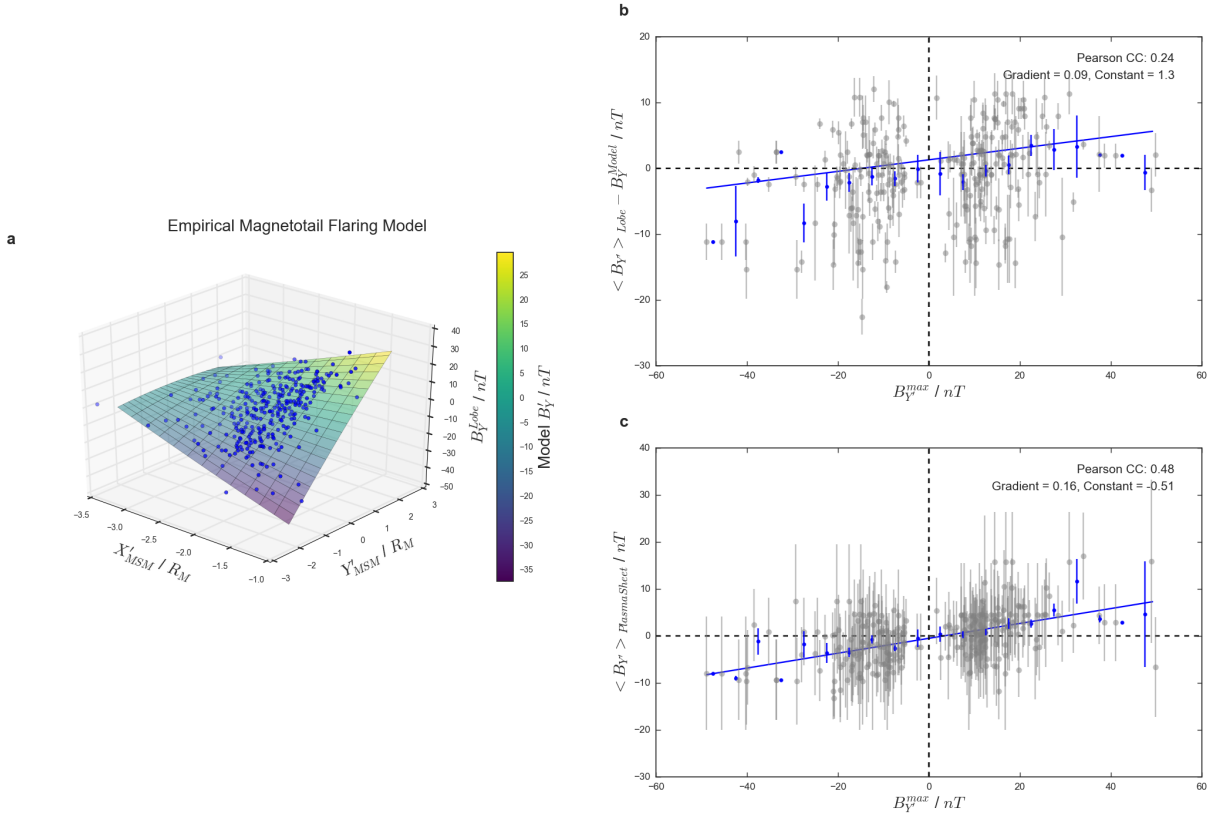

FIGURE 6.8: Panel (a) shows the distribution of B_Y measured across the tail within the lobe (projected onto the $X'_{MSM} - Y'_{MSM}$ plane). The surface shows the least squares quadratic fit to the data, the colour bar corresponds to the resulting modelled value of B_Y. Panel (b) shows the model subtracted value of B_Y measured in the lobe plotted against the maximum B_Y recorded in the 248 MVA confirmed flux ropes. Panel (c) shows the average B'_Y measured within the plasma sheet compared to the maximum B_Y recorded within the 248 MVA confirmed flux ropes. For panels (b) and (c) the grey points indicate individual flux ropes (with the error bars showing $\pm 1\sigma$) while the data are also placed into $5\,nT$ bins, the mean and standard error of the mean are shown in blue. The blue lines show the result of a least squares fit to the grey points. The values of the Pearson correlation coefficient and least squares fit are provided in the top right of the panels.

6.6 Conclusion

The MESSENGER mission provides a wealth of crossings through the magnetotail plasma sheet. An automated method (Chapter 5) has been applied to 319 of these crossings to identify flux ropes. The method initially identifies intervals when the north-south component of the magnetic field passes though zero. These are cross-checked to select those that occur concurrently with peaks (identified using a CWT) in the dawn-dusk component and/or total magnetic field. Flux ropes are then selected as those possessing well defined MVA coordinate systems with clear rotations of the field. In total 248 flux ropes are located, 74 of which are then found to be well represented by a cylindrically symmetric, constant α force-free model.

A small dawn-dusk asymmetry is observed, with 58% of flux ropes observed post-midnight. *In situ* flux rope encounters are intermittent, with 61% of plasma sheet crossings yielding no flux ropes. However, flux rope observations are found to be more likely if the preceding lobe field is relatively enhanced. Flux ropes are observed at up to a rate of $\sim 5\,min^{-1}$ during active intervals, however the average peak rate (post midnight) is only $0.25\,min^{-1}$. Only 25% of flux ropes are observed in isolation; the majority occur in close succession with the time between adjacent flux ropes generally being less than $100\,s$. The radii of the identified force-free flux ropes are found to be of the order of ion inertial length in Mercury's magnetotail plasma sheet.

Minimum Variance Analysis suggests that the majority of the motion of the flux ropes is confined to the $X'_{MSM} - Y'_{MSM}$ plane. It is also found that a large fraction of the flux ropes observed display a significant skew in the $X'_{MSM} - Y'_{MSM}$ plane, perhaps due to an asynchronous release of the ends of the flux ropes, or an east-west spread of the reconnection location.

Very little difference is observed between the downtail distributions of planetward and tailward moving flux ropes identifications, suggesting the x-line is highly mobile over the region surveyed. Across the magnetotail (in the dawn-dusk plane) it is found that the majority of post-midnight identifications are moving planetward, perhaps suggesting the x-line is located further down the tail in this region. In addition, 55% of flux rope chains show some evidence of neutral line retreat.

The effect of the IMF on the flux rope core field orientation is indirectly probed using the lobe and plasma sheet fields. Very weak correlations are found with the lobe field, and a slightly stronger relationship is found with the plasma sheet field. The core field of the flux ropes is found to be ~ 6 times greater than the azimuthal component of the magnetic field in the plasma sheet. The upcoming European Space Agency (ESA) Bepi-Colombo mission to Mercury will be well positioned to shed more light on these topics, with two orbiters allowing multi-point observations.

Ultimately, however detailed a magnetic field survey is performed, the spacecraft measurements represent a single point in a global system. Additionally, the magnetic flux ropes observed are extended structures, and the spacecraft could encounter them in numerous locations and trajectories. The effects of single spacecraft sampling are explored further in Chapter 9.

Chapter 7

Dipolarization Fronts with Associated Energized Electrons in Saturn's Magnetotail

7.1 Introduction

This Chapter investigates the properties and location of dipolarization fronts in Saturn's magnetotail, building on the survey performed in Chapter 4. In particular this work explores the properties of the electron populations that accompany a subset of the previously identified events.

The aim of this work is to investigate the morphology, distribution and plasma character associated with Kronian dipolarization fronts. As discussed in Section 1.4.3.4, dipolarization fronts manifest as localized increases in the north-south component of a planetary magnetic field that propagate towards the planet. In this work the sample is restricted to those that are accompanied by the appearance of energetic electrons. This provides another selection criteria by which to identify the signatures, and also allows an investigation into the sources of electron heating. In particular, the electron energization potentially provides information on the origins of the plasma and also the nature of its planetward propagation. To complement this, the suprathermal composition of the plasma will be analysed to investigate the source populations, and in particular assess whether any material of solar wind origin has been introduced (e.g. as a result of lobe reconnection).

Section 7.2 will provide a summary of the instruments and data used in this study. Section 7.3 will summarize the techniques used to identify the relevant signatures. Section

7.4 will then discuss the identified events and their morphology. This will be followed in Section 7.5 with a discussion of their spatial and temporal distribution. Section 7.6 will then investigate the energization of the observed plasma population. Finally, the relative composition of the heated material will be discussed in Section 7.7.

7.2 Data

Magnetic field data for this study come from the Cassini magnetometer [*Dougherty et al.*, 2004]. The Kronocentric radial theta phi (KRTP) coordinate system is used; this is a spherical polar system: B_r (the radial component) is positive radially outward from Saturn, B_θ (the meridional component) is positive southward and B_ϕ (the azimuthal component) is positive in the direction of corotation. *Jackman et al.* [2009a] showed that this system is suited to distinguish the magnetic signatures due to magnetotail dynamics from other phenomena (e.g. periodic encounters with the magnetotail plasma sheet). Events were identified using data with a one minute cadence; the average duration of a magnetically identified planetward moving event has been found to be $\sim$ 5 minutes [*Smith et al.*, 2016].

Data from Cassini Plasma Spectrometer (CAPS) are used to investigate the *in situ* plasma properties [*Young et al.*, 1998]. The Cassini Electron Spectrometer (ELS) is an electrostatic analyzer, recording electrons between 0.58 and $26,000\,eV$. In general, the ELS instrument does not sample the full $4\pi\,sr$ of the sky, unless Cassini happens to be rolling during the interval of interest. The instrument is mounted on an actuating platform and thus samples $\sim 2\pi\,sr$ of the sky. However, in general the bulk velocity of the electrons in Saturn's magnetosphere is much less than their thermal velocity, meaning the actuation of the instrument generally gives fairly complete pitch-angle distributions within the CAPS energy range [*Arridge et al.*, 2009a]. For this reason any signature of a dynamic event/change in the electron population should be observable regardless of the direction in which CAPS is pointing. The data presented for this study are mostly A-cycle and anode averaged fluxes: flux averaged over 16 consecutive energy sweeps and all 8 anodes. The data are also corrected using geometric factors and energy-dependent efficiencies. For more information on the generation of this data the interested reader is directed to *Thomsen et al.* [2016]. Electron moments such as temperature and density are also used [*Waite and Furman*, 2013]; the techniques that are used to generate the moments are described by *Lewis et al.* [2008] and *Arridge et al.* [2009b]. The CAPS ion mass spectrometer (IMS) is also used to ascertain flow directions.

Data from the Magnetospheric Imaging Instrument (MIMI) [*Krimigis et al.*, 2004] is used to complement the CAPS observations at higher energies. The Low-Energy Magnetospheric Measurement System (LEMMS) is one of three instruments that comprise MIMI. LEMMS measures electrons between $20\,keV$ and several MeV. LEMMS is mounted upon a rotating platform designed to allow sampling of a greater fraction of the three dimensional energetic particle distribution; however during the epochs explored by this work the platform did not rotate and thus LEMMS samples a smaller region of sky (and pitch angles relative to the field). Data from the Charge Mass Spectrometer (CHEMS) instrument is also used by this study. CHEMS is able to measure both the mass and mass per charge of ions with energies between 3 and $236\,keV$ for H^+ and between 8 and $236\,keV$ for O^+. CHEMS is particularly useful in distinguishing ion species with identical m/q ratios and different atomic masses (e.g. H_2^+ and He^{++}). The final constituent of MIMI is the Ion and Neutral Camera (INCA). INCA can record the energy, direction and rough composition of ions between $\sim 7\,keV$ and $3\,MeV$. INCA has a field of view of 120° by 90°. When combined with simultaneous MAG data, INCA can provide detailed pitch angle analysis of the energetic particles within its field of view.

Data from Cassini's orbits in 2006, late 2009 and 2010 were investigated; this combination of data provide good magnetotail coverage at midnight and dawn (2006), as well as at dusk (late 2009 and 2010). A list of magnetopause crossings was used to exclude data from the magnetosheath and solar wind [*Pilkington et al.*, 2015]. Additionally, data from the dayside ($X_{KSM} \geq 0$) and that obtained within a radial distance of $15\,R_S$ were also excluded from the analysis to allow the focus on magnetotail dynamics. Within $\sim 15\,R_S$ the magnetic field becomes more quasi-dipolar and selecting significant southward field deflections becomes more difficult against the larger background field [*Arridge et al.*, 2011b].

7.3 Event Signature & Selection Method

Figure 1 shows an example of a Kronian dipolarization. Panels (a) - (d) show the magnetic field in KRTP coordinates, while panel (e) shows an ELS flux spectrogram. The signatures in both the magnetic field and the energy-flux spectrogram are used to identify the event. The methods by which the relevant magnetic and plasma signatures are located in the data are discussed below.

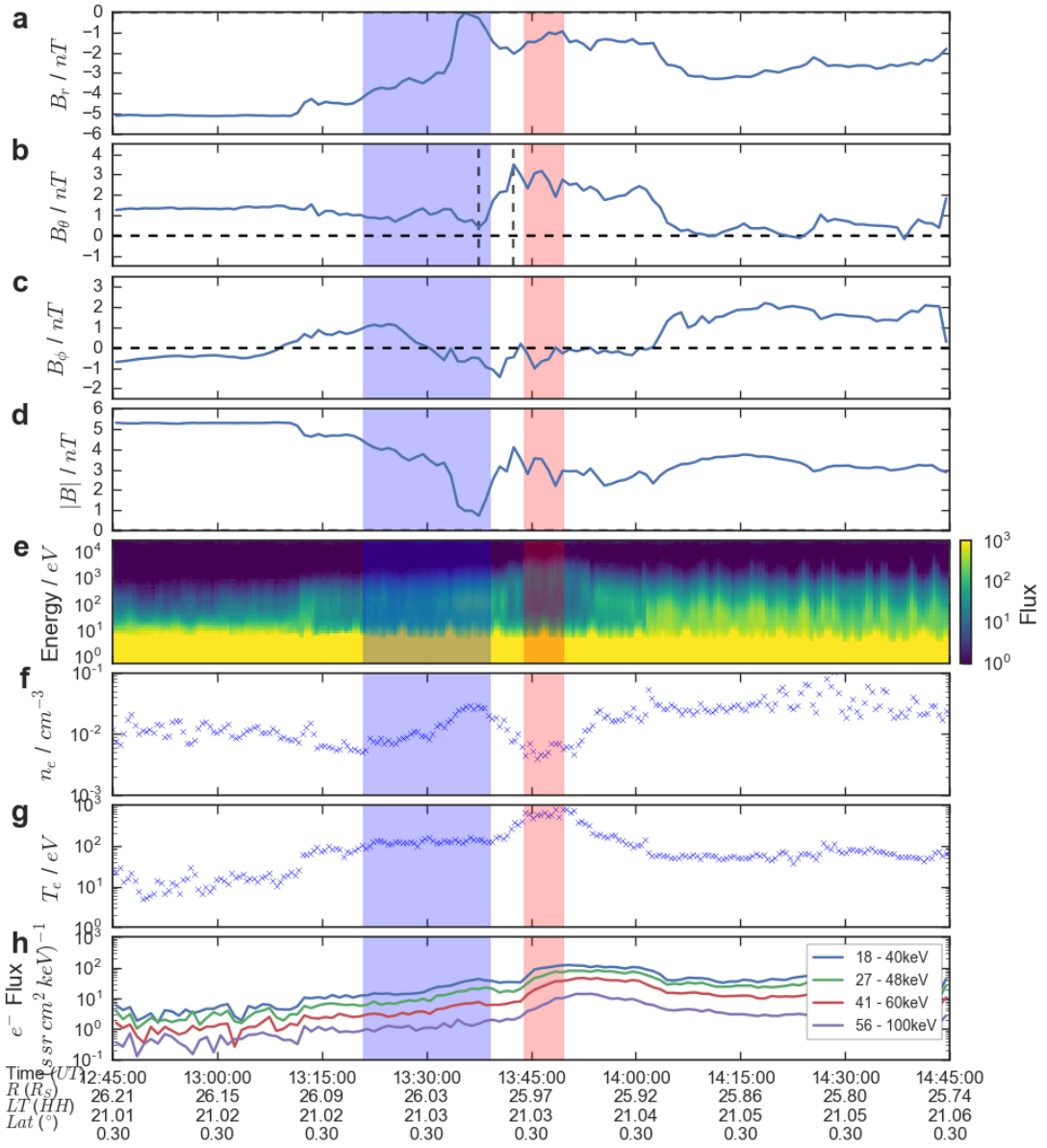

FIGURE 7.1: One hour of Cassini data from day 341 2009. Panels (a) - (d) show magnetometer data in the KRTP coordinate system. Panel (e) shows an ELS flux spectrogram. Panels (f) and (g) show electron density and temperature moments respectively (the methods by which they are calculated are described by *Lewis et al.* [2008] and *Arridge et al.* [2009b]). Panel (h) shows the differential electron flux from the LEMMS instrument in channels ranging between $18 - 100\,keV$. The blue shaded region was identified by the technique described in Section 7.3.2 as the background plasma sheet, while the red shaded region was identified as the energetic electron population following the dipolarization front. The black vertical dashed lines in Panel (b) bracket the magnetic field deflection of interest.

7.3.1 Magnetic Field Deflection

A key signature of a dipolarization is the sharp rotation of the magnetic field in the north-south meridian (an increase in the B_θ component): highlighted in Figure 7.1b between the vertical dashed lines. *Smith et al.* [2016] (Chapter 4) recently developed a technique to locate magnetic field deflections greater than background fluctuations of the field. *Smith et al.* [2016] set the threshold such that deflections must be greater than $1.5\,B_\theta^{RMS}$ (Root-Mean-Square) of the field, calculated for an hour interval surrounding the deflection. In this work, the effect of lowering this threshold is considered for targeted intervals. In the case of the event in Figure 7.1, strong planetward flows precede the magnetic signature (discussed in Section 7.4.3, Figure 7.3), suggesting that the magnetic dipolarization is embedded in the high speed flow.

7.3.2 Electron Energy Enhancement

Terrestrial dipolarization fronts in the literature often involve a magnetic deflection accompanied by a plasma signature: this generally comprises an increase in the flux of higher energy electrons combined with a simultaneous reduction in the fluxes at lower energies [*Deng et al.*, 2010; *Runov et al.*, 2013; *Pan et al.*, 2014b]. This combination leads to an arc-like signature in an electron spectrogram, e.g. that shown in Figure 7.1e centred at around 13:50. Before this time, between 13:15 and 13:40, the main electron population extends between $\sim 20\,eV - 1\,keV$, suggesting Cassini is within the magnetotail plasma sheet [*Arridge et al.*, 2009a]. Following the magnetic field deflection at 13:35, and for approximately 15 minutes, the spacecraft is engulfed by a higher energy population of electrons ($\sim 300\,eV - 5\,keV$). The population returns to something more akin to the previous plasma sheet distribution at approximately 13:55. To locate this arc-like signature a statistical method has been developed. The method is based around quantile-quantile (QQ) plots [*Gilchrist*, 2000]; a technique that allows the direct comparison of two distributions without requiring them to be fit to a model.

Two spectra can be compared using quantile-quantile (QQ) plots [*Gilchrist*, 2000]. This technique allows the direct comparison of two distributions without requiring a specific model to be chosen. In the past it has been applied to solar wind data in order to investigate the variation in several parameters over the solar cycle [*Tindale and Chapman*, 2016]. Figure 7.2 shows the result of comparing two spectra (from the event in Figure 7.1) with the technique. Figure 7.2a shows the magnetic field for a one hour window surrounding a significant southward magnetic field deflection (increase in B_θ). The ELS flux spectrogram for the same interval is shown in Panel (b).

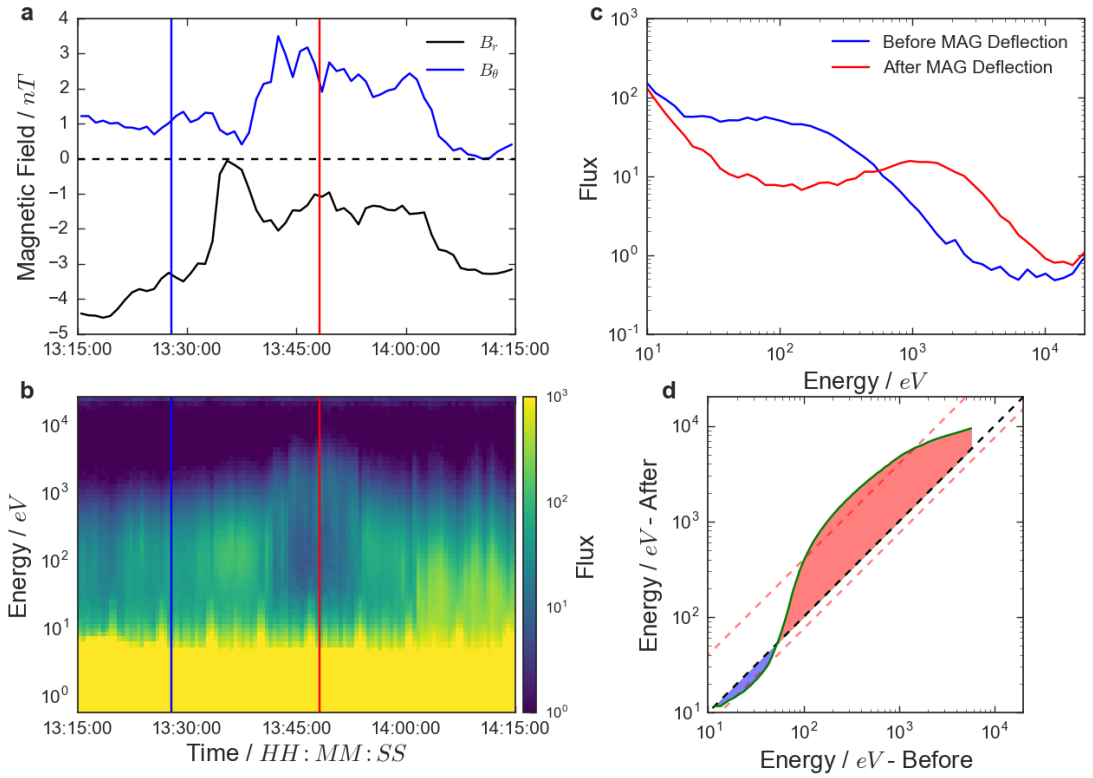

FIGURE 7.2: Figure demonstrating a quantile-quantile (QQ) statistical comparison. Panel (a) shows the B_r (black) and B_θ (blue) components of the magnetic field for one hour surrounding the example dipolarization from Figure 7.1. Panel (b) shows the corresponding electron flux spectrogram around this interval. The vertical red and blue lines on panels (a) and (b) indicate the times of two spectra that have been selected, and are shown in panel (c). Panel (d) shows the resulting QQ plot of the comparison between the two spectra, the black dashed line indicates $y = x$: where the plot would be should the spectra be identical. Regions above (below) $y = x$ have been shaded red (blue). The diagonal red dashed lines indicate the empirical thresholds.

The two example spectra chosen for comparison are shown in Figure 7.2c. The blue distribution is taken within the plasma sheet population (before the dipolarization magnetic signature), while the red is taken within the heated electron population. Each spectrum is first converted into a cumulative distribution function (CDF: C); where $C(x)$ is the probability that the value of the variable $\tilde{x}$ is less than or equal to x ($\tilde{x} \leq x$). Inverting the CDF (creating the iCDF: C^{-1}) provides a method of inferring the energy of the distribution at a given probability.

Two iCDF distributions can then be directly compared, plotting C_1^{-1} against C_2^{-1}; each point then shows the energy of each distribution for a given probability. This is known as a QQ or quantile-quantile plot; an example of which can be seen in Figure 7.2d. If the two distributions are identical ($C_1^{-1} = C_2^{-1}$) then the QQ plot will lie on the line of $y = x$ (the black dashed line in Figure 7.2d. This study concerns the change in plasma distribution during the dipolarization: the difference between the QQ plot and $y = x$.

The characteristic $'S'$ shape shown in Figure 7.2d shows that the spectrum before the dipolarization signature has a larger flux at lower energies (i.e. below around $500\,eV$), while the spectrum taken after the signature is concentrated at higher energies with a relative loss of the lower energy counts. This technique has been specifically designed to search for this type of shift in spectrum based on terrestrial work [*Deng et al.*, 2010; *Runov et al.*, 2013; *Pan et al.*, 2014b]. This signature is common to all previously identified Kronian dipolarizations (that are associated with electron acceleration).

In order to check for this signature the method uses the diagonal red dashed lines in Figure 7.2d, corresponding to $y = 4x$ and $y = 0.75x$. These represent empirical limits required to show strong deviation from the $y = x$ line, i.e. that the populations are significantly different. The limits have been empirically tuned to select those spectra which show the desired characteristic change in electron population. If both diagonal lines are crossed by the QQ curve, then the technique reports that the signature of interest has occurred, subject to the following checks:

1. There are only two changes in the population, i.e. a single clear $'S'$ shape is seen.
2. The $'S'$ shape has the correct orientation: the increase in counts following the magnetic detection is at a higher energy than the dropout.
3. The crossover between the populations occurs between $50\,eV$ and $2\,keV$ (i.e. where the QQ plot crosses through $y = x$).

These criteria were developed from the inspection of trial events (e.g. [*Bunce et al.*, 2005; *Thomsen et al.*, 2013]), and attempts to reproduce the spectra that may have been chosen by-eye. Physically, criterion 1) suggests there must be a simple change in the location of the majority of the population (a shift in energies). The second criterion requires that the shift must be to higher energies. Finally, criterion 3) requires that the change must be from the typical plasma sheet population to something more energetic (i.e. it must not solely be a small increase in counts at the very top of the energy spectrum).

To apply this method to the data set a sliding comparison is performed. Every other spectrum (to minimize computational time) is compared to those spectra spaced between 9 and 30 minutes ahead. If the comparison flags that the characteristic shift in the spectrum has occurred, then the interval is logged. The comparison is applied to the full data set (described in Section 7.2) and then the logged intervals are grouped into regions of 'background' (grouping the catalogue of initial spectra) and 'heated' (grouping the catalogue of 'energized') populations. The grouping is automated, with the following procedure:

In an interval the first lower energy spectra is tagged as 'background'. All identified spectra are then iterated through in chronological order. Subsequent lower energy spectra are grouped into the 'background' category until a higher energy spectrum is encountered. In this manner periods of up to 30 minutes preceding the heated population can be classified as 'background'.

The detections made by the technique are then checked by eye to ensure they represent the phenomenon of interest. The majority of false detections from this method were the result of the presence of anisotropic electron distributions. Additionally, to reduce false detections the spectra were truncated at both low ($\leq 10\,eV$) and high energies ($\geq 20\,keV$). The low energies are dominated by spacecraft photoelectrons while the high energies can be affected by the efficiencies used to correct the data (occasionally magnifying background noise) [c.f. *Thomsen et al.*, 2016].

7.4 Identifications and Morphology

In total 712 significant ($\Delta B_\theta \geq 1.5 B_\theta^{RMS}$) southward magnetic field deflections (termed MAG detections) were located within the data set [*Smith et al.*, 2016] (Chapter 4). In contrast, only 58 intervals of electron energization (termed ELS detections) were identified independently within the same interval of data. When the two sets of detections were cross referenced a total of 17 events were found that exhibited both signatures. Upon manual inspection of the 58 ELS detections it was found that more than 17 were coincident with southward rotations of the field, although the magnitude of some of the deflections was below the empirical threshold ($\Delta B_\theta \leq 1.5 B_\theta^{RMS}$). Lowering the threshold for magnetic field deflections to $\Delta B_\theta \geq B_\theta^{RMS}$ increased the number of coincident electron and magnetic field signatures to 28. These 28 dipolarizations form the catalogue of events for further investigation in this study. A summary of the events and their properties is provided in Table 7.1.

Table 7.2 displays a list of dipolarizations from the literature for comparison with our results. For example, only the dipolarizations reported by *Bunce et al.* [2005], *Thomsen et al.* [2015] and one of those identified by *Thomsen* [2013] show both the magnetic field and electron signatures typical of a terrestrial dipolarization front. It should also be noted that our methods were capable of locating the magnetic and electron signatures of all the events in Table 7.2.

Table 7.1: Catalogue of Kronian dipolarizations and properties.

	Date & Time	$\lvert\Delta B_\theta\rvert$ / nT	LT / HH	R / R_S	Lat / °	Group/Isolated	CAPS/ELS Moments?	PA Spectra (FA/P/None)[a]	LEMMS e^-?	CHEMS?
0	04/03/2006 00:41	-0.98	3.00	42.01	0.14	I	N	-	N	N
1	18/03/2006 04:24	-3.98	5.88	25.93	-0.15	I	N	-	N	N
2	25/04/2006 02:40	-1.77	5.12	33.72	-0.07	G	N	-	Y	N
3	25/04/2006 02:40	-1.77	5.12	33.72	-0.07	G	N	-	Y	N
4	25/04/2006 13:54	-1.44	5.31	31.07	-0.09	I	Y	FA	Y	Y
5	19/05/2006 19:49	-1.83	4.02	25.35	0.02	I	Y	FA	Y	N
6	20/05/2006 06:37	-2.87	4.30	22.36	0.00	G	Y	FA	N	N
7	20/05/2006 07:09	-2.26	4.32	22.18	-0.01	G	N	-	N	N
8	20/05/2006 07:35	-2.08	4.33	22.10	-0.01	G	Y	FA	N	N
9	21/05/2006 04:01	-3.68	5.35	15.25	-0.12	I	Y	FA	Y	Y
10	21/07/2006 21:16	-4.71	2.42	21.76	0.33	I	Y	FA	Y	Y
11	15/08/2006 04:32	-3.23	2.67	19.24	-0.37	G	Y	FA	N	Y
12	15/08/2006 05:19	-3.47	2.70	18.99	-0.51	G	Y	FA	Y	Y
13	15/08/2006 05:50	-2.62	2.73	18.82	-0.59	G	Y	P	N	N
14	25/08/2006 04:02	-2.00	23.07	45.82	11.61	I	N	-	Y	N
15	07/09/2006 13:12	-2.67	2.17	22.76	1.09	I	N	-	N	N
16	07/09/2006 16:15	-4.56	2.26	21.99	0.76	G	Y	FA	Y	N
17	07/09/2006 16:59	-2.67	2.28	21.84	0.70	G	Y	FA	Y	Y
18	16/09/2006 03:50	-1.08	0.08	36.65	14.32	I	Y	FA	N	Y
19	08/10/2006 07:09	-1.78	1.53	28.07	8.33	G	Y	FA	Y	Y
20	08/10/2006 08:06	-1.47	1.55	27.91	8.16	G	Y	FA	Y	Y
21	09/10/2006 12:48	-2.80	2.16	22.01	1.78	I	Y	FA	Y	Y
22	04/11/2006 06:21	-1.54	1.20	27.97	18.56	I	Y	FA	Y	Y
23	07/12/2009 13:38	-3.09	21.03	25.98	0.30	I	Y	FA	Y	Y
24	18/03/2010 17:06	-1.51	20.89	22.93	0.38	I	N	-	Y	N
25	19/03/2010 21:17	-3.41	22.03	13.91	0.34	I	Y	None	Y	Y
26	25/04/2010 04:57	-1.05	20.52	26.05	0.15	I	N	-	Y	N
27	28/11/2010 06:34	-1.97	20.54	22.54	-0.07	I	Y	FA	N	N

[a] FA = Field aligned, P = Perpendicular, None = No structure

7.4.1 Dipolarizations lacking an energetic electron signature

As outlined above, the vast majority ($^{695}/_{712}$) of significant southward magnetic field deflections are unaccompanied by the expected electron signature of a dipolarization front. Looking to the literature, the two dipolarizations discussed by *Russell et al.* [2008] and *Jackman et al.* [2015] both lacked electron heating signatures and were observed while Cassini was at a relatively large distance from the current sheet centre ($|B_R| \geq 2\,nT$). Far from the center of the current sheet the electron counts can be expected to be relatively weak. It is therefore possible that these events did result in electron heating, but that this heated population is limited in vertical (or latitudinal) extent. In addition, the technique used to select the signatures (Section 7.3.2) requires the presence of a background plasma sheet population with which the heated population can be compared. Therefore many dipolarization signatures (from the perspective of the magnetic field) may be observed outside of the plasma sheet where the electron counts are too low to result in a CAPS-based detection. The technique is also fairly specific and it is likely that it is insensitive to some forms of heating that could be displayed.

However on inspection, $^{475}/_{695}$ events show an average value of $|B_R| \leq 2\,nT$ during the field deflection, suggesting Cassini was reasonably close to the current sheet and thus the CAPS instrument would have been capable of sampling plasma sheet electrons. Indeed, during the dipolarization presented by *Jackman et al.* [2013] the current sheet was encountered both shortly before and after the magnetic field signature, suggesting that Cassini should have encountered a latitudinally confined energetic electron population (certainly following the magnetic field deflection). This suggests that either some southward magnetic field deflections and dipolarizations do not result in heated electrons, or that the dipolarizing heated electron flux is also limited in azimuthal width.

At Earth, the energetic electron flux has been shown to be dependent upon the spacecraft location relative to the dipolarization front; with observations on the dusk side of the front showing lower electron flux [*Runov et al.*, 2013]. The electron drifts that lead to this asymmetric signature over the front could explain a good fraction of the detections. In addition, terrestrial observations suggest that only magnetic field deflections associated with enhanced dawn-dusk electric fields are associated with energetic particle flux [*Gabrielse et al.*, 2012; *Liu et al.*, 2016]. Unfortunately, it is not possible to test this with the data available from Cassini at Saturn.

Yao et al. [2017a] recently proposed two drivers of dipolarizations at Saturn, the first of which is the main target of this study: reconnection driven fronts. The second type,

with a similar magnetic field signature is instead attributed to a disruption of the cross-tail current systems. This current disruption, while resulting in a rotation of the field, may not be very efficient at energizing the electron population [*Yao et al.*, 2017a]. Furthermore, this mechanism would not manifest with a sharp boundary between distinct plasma populations, potentially meaning that these type of events would not selected by our method (Appendix B). Additionally, there are other magnetospheric processes or structures that can result in a sudden tilting of the magnetic field. For example, Alfvénic waves or crossing into different magnetospheric structures can rotate the orientation of the magnetic field. Such structures include the low latitude boundary layer [*Masters et al.*, 2011] (located near the magnetopause) and the magnetotail plasma sheet [e.g. *Jackman et al.*, 2009a].

Moving towards the magnetotail current sheet would have the effect of reducing the value of B_R and increasing n_e. If the 10 minutes preceding and following the deflection of the field are compared, it is found that only $^{50}/_{695}$ events show a B_R reduction of at least $1\,nT$ coupled with a greater than 10% increase in n_e. This interpretation cannot therefore explain the majority of the MAG detections.

It could be concluded that the majority of the MAG detections (that lack coincident electron energization signatures) are due to a combination of the relative location of the spacecraft, disruption of the magnetotail current systems or passages into adjacent magnetospheric structures. The first possibility would suggest that the energetic electron population is much more limited in spatial extent than the magnetic field signature, as is the case at Earth [e.g. *Runov et al.*, 2013]. The second suggestion would imply that disruption of the current systems is much more common than reconnection driven dipolarization fronts, or that the effect covers a wider azimuthal region. More work is needed in the future to distinguish between these possibilities.

7.4.2 Electron signatures lacking a significant rotation of the magnetic field

In total, 30 ELS detections were made, uncoupled to strong southward field rotations. Energetic electron signatures lacking a corresponding magnetic field signature are often observed at the Earth. At the Earth these signatures are often energy dispersed, suggesting a non-local generation mechanism [*Duan et al.*, 2014]. It has been suggested that they are due to dipolarization fronts propagating past the spacecraft, dawn-ward or dusk-ward of the spacecraft position [*Gabrielse et al.*, 2016]. However, on inspection of the high energy electron data available from LEMMS the events in the catalog do not appear to be energy dispersed (given a cadence of $60\,s$). Therefore, these events could

	$\lvert\Delta B_\theta\rvert$	Increase in Energetic Electrons
Bunce et al. [2005]	$3.5\,nT$	Y
Russell et al. [2008]	$1.6\,nT$	N
Jackman et al. [2013][a]	$0.8\,nT$	N
Thomsen et al. [2013]	$3.41\,nT$/none	Y/N
Thomsen et al. [2015]	$0.98\,nT$	Y
Jackman et al. [2015]	$2.4\,nT$	N

[a] Three were discussed; two were previously reported [*Bunce et al.*, 2005; *Russell et al.*, 2008].

TABLE 7.2: Table summarizing several Kronian dipolarizations from the literature.

be due to a different phenomenon to those observed at Earth, or the dispersion could be weak (such that the cadence of the data is insufficient). For example, they could be paired with magnetic field rotations that are small relative to background fluctuations of the field (and so do not meet the threshold values used by this work), or lag behind the front to such an extent ($\geq\sim$ 30 minutes) that it is not possible for the automated method to pair the two. Delayed energetic fluxes have been observed at the Earth [e.g. *Runov et al.*, 2011]. Alternatively, it is possible that the energy dispersion is less apparent at Saturn due to the dominance of corotational motion: the drifts of electrons monitored by LEMMS (i.e. with energies between $20\,keV$ and several MeV) are still largely dominated by corotation. In general, dispersion signatures are rare in this data set beyond $\sim 15\,R_S$. Gradient/curvature drifts that may cause dispersions would become more apparent towards the upper end of the energy range. Resonant acceleration by wave activity could also result in electron heating.

7.4.3 Case Study

An example of an event where both a strong magnetic field deflection and energetic electron signature were detected was introduced above in Figure 7.1. Figures 7.1f and (g) show the derived electron density and temperature respectively. Finally, panel (h) shows the LEMMS energetic electron flux for four energy channels between 18 and $100\,keV$. The vertical blue and red shaded regions represent those selected by the technique (discussed in Section 7.3.2) as ambient plasma sheet and energetic population respectively. The properties of the electron moments within these regions will be explored later, in Section 7.6. During this event Cassini was located at a radial distance of $26\,R_S$, a local time of 21:00 and a latitude of 0.3°. This represents the earliest local time at which a dipolarization has been observed *in situ* at Saturn prior to this work.

The combination of magnetic field deflection and electron energy enhancement used to identify the event can be seen in panels (b) and (e) at around 13:40. Meanwhile, panels f and g show that the change in electron spectrogram corresponds to an increase

in the electron temperature and a reduction in the density, as is seen in terrestrial dipolarizations [e.g. *Runov et al.*, 2015]. This is a feature common to all of the 28 events identified (likely a result of the specificity of the selection method employed) and will be explored in more detail in Section 7.6. Figure 7.1h shows how the energetic population observed by the ELS instrument (shown in panel (e): electrons up to 26 keV) can extend up to several hundred keV. Figure 7.1h also demonstrates that the increase in energetic electron counts is dispersionless: all energy channels increase within one minute of each other. This mirrors terrestrial dipolarizations, where the bursts of energetic electrons that accompany dipolarization fronts are often dispersionless [*Apatenkov et al.*, 2007; *Duan et al.*, 2014; *Gabrielse et al.*, 2014]. A total of $^{19}/_{28}$ dipolarization fronts show an increase in LEMMS electron counts (Table 7.1), all of which are dispersionless.

Figure 7.3a shows all-sky images from the CAPS instrument for the dipolarization in Figure 7.1. In these all-sky images the centre of the circle represents the anti-Saturnward look direction (radially out from the planet), the inner dashed circle represents directions 90° from this, and the outer edge represents the Saturnward direction. The hollow triangle indicates the direction of strict corotation. The flow preceding the dipolarization front (the first two panels) can be seen to be coming from between the anti-Saturnward and corotational directions and represents a broad inflow. The flow is coming from slightly above the horizontal which can be explained as the spacecraft was below the current sheet (from the sign of B_r in Figure 7.1a). The broad inflow can be interpreted as a result of the compression of the plasma sheet ahead of the dipolarization front. Following the passage of the front (in the right hand panel) the flow can be seen to become more collimated. The velocity of the plasma during this interval can be calculated to be $\sim 1200\,kms^{-1}$, almost five times the strict corotational velocity at this radial distance. Therefore, this represents a very energetic period of inflow, many times the ambient flow speed of the plasma [*McAndrews et al.*, 2009; *Thomsen et al.*, 2013]. Unfortunately the viewing of CAPS is not often in a direction such that inflowing plasma is within the field of view. For this reason it is not possible to examine the flows statistically.

MIMI/INCA (with its large field of view) enables us to observe the pitch angle (α) distribution of H^+ between $\sim 80 - 180°$ for energies between 5 and 227 keV. The distribution during the event is shown in Figure 7.3b. Time advances along the x-axis while energy increases vertically. Pitch angle contours are labelled and shown in black. Following the passage of the dipolarization front ($\sim$ 13:37 onwards), features of an anisotropic pitch angle distribution become apparent for approximately 10 minutes (3 panels). The most consistent feature (across all energies) of the heated dipolarizing flow is a population at approximately $\alpha = 90°$. This is likely a flow anisotropy, however it is also possible that adiabatic betatron acceleration plays a role in its generation, as the heated flow has moved to a region of higher field strength. The distributions can

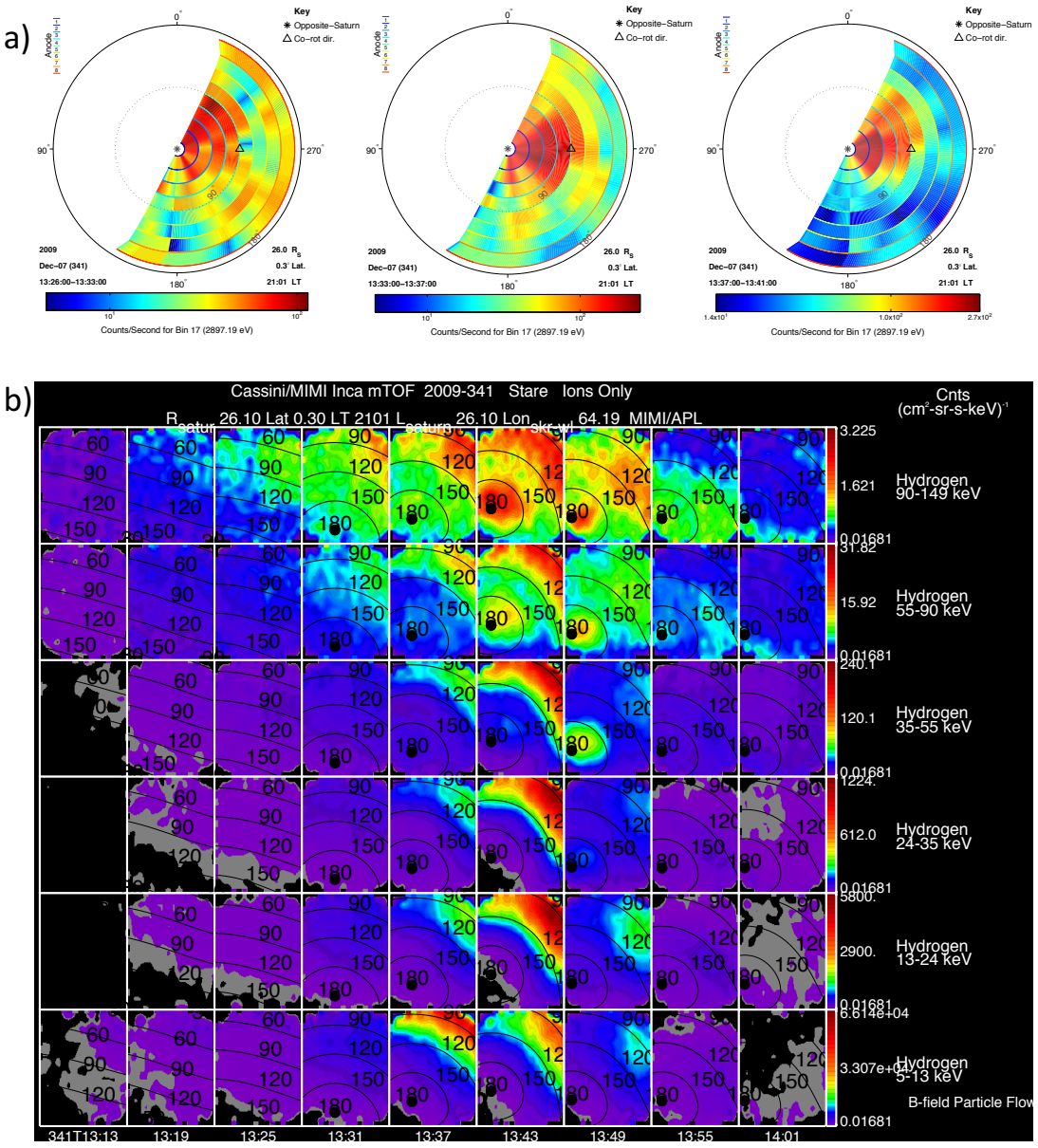

FIGURE 7.3: (a) CAPS/IMS all-sky images for three intervals around the dipolarization in Figure 7.1. The centre of each plot represents the anti-Saturnward look direction (as if the observer is looking along the radial unit vector of the planet), and the radial distance away from the centre is proportional to the polar angle relative to the anti-Saturnward direction. Therefore, the dashed circle represents a direction 90° from the radial direction and the outside of the circle represents the Saturnward direction . The corotational direction is indicated by the triangle on the right hand side of each circle. The colours indicate the counts per second at an energy per charge of 2897 eV. The times used to integrate the counts are shown below each panel. White regions correspond to look directions not covered by CAPS in this interval. (b) INCA angular distributions for H+ between 13:13 and 14:01. Pitch angle contours are shown in black for 60°, 90°, 120° and 150°. The panels advance in time across the bottom axis and increase in energy moving up the panels. Note that the colour bars showing counts $(cm^2 - sr - s - keV)^{-1}$ are different for each row (energy).

also be seen to vary with energy, as is observed at the Earth [e.g. *Ashour-Abdalla et al.*, 2011; *Duan et al.*, 2014; *Pan et al.*, 2014b; *Birn et al.*, 2017; *Runov et al.*, 2017]. For example, at energies above $\sim 90\,keV$ the presence of a field aligned population becomes apparent; a population that could be generated by Fermi-type acceleration as the length of the flux tubes decreases.

7.5 Distribution and Frequency

The distribution of the identified events across the Kronian magnetotail will now be investigated. The panels of Figure 7.4 show the spatial distribution of the 28 events for which both a magnetic field deflection and electron energy enhancement were identified.

Figure 7.4a also includes dipolarizations presented in the literature for comparison. Dipolarizations can be seen to occur across most of the magnetotail, though the majority occur post-midnight ($^{22}/_{28}$). Figure 7.4b shows the 28 detections highlighted in blue if they occurred within 3 hours of another event [*Jackman et al.*, 2014b; *Smith et al.*, 2016] and red if they were isolated. The three hour time interval was selected by scaling a 30 minute time scale previously used at the Earth [*Slavin et al.*, 1993]. Grouped events are solely seen post-midnight, while isolated events are seen across the entire magnetotail. In total, just over half ($^{16}/_{28}$) occur in isolation.

Figure 7.4c shows how the size of the magnetic field signature varies according to the location of the event. In general, the more distant events from the planet can be seen to possess smaller field deflections. This could be a feature of Kronian dipolarization fronts, however it could also be a selection effect. In this study the magnetic deflection is required to be greater than a threshold based on the RMS (Root-Mean-Square) of the field. The meridional field component increases in magnitude as the radial distance decreases: this will result in small field deflections (such as those observed in the deep tail) not being selected at small radial distances. This would be more consistent with the terrestrial work of *Runov et al.* [2015], who found that the magnitude of field deflection is fairly invariant with geocentric distance. Alternatively, *Ashour-Abdalla et al.* [2015] noted in their modelling that dipolarization fronts steepen as they approach the Earth; this could potentially be the Kronian equivalent.

Finally, Figure 7.4d shows the locations of the events with (blue) and without (red) corresponding increases in LEMMS ($E_{e^-} \geq 20\,keV$) count rates. As mentioned in Section 7.4.3, $^{10}/_{28}$ events do not show a simultaneous increase in high energy electrons, but this does not appear to be an effect of their location: they are spread across the magnetotail with no clear preference. As LEMMS has limited pitch angle coverage, the possibility of

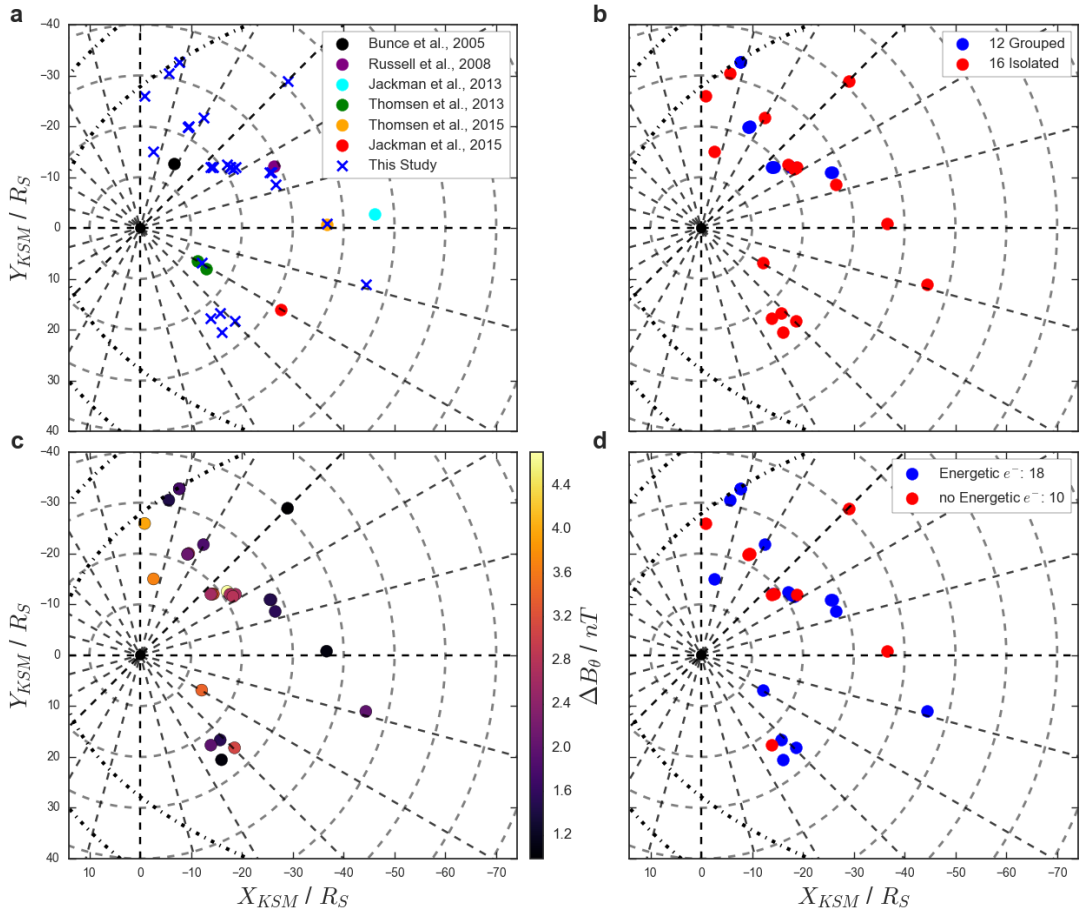

FIGURE 7.4: Equatorial projections of Saturn's magnetotail, each hour of local time and every $10\,R_S$ of radial distance are indicated with black dashed lines. The black dot-dash lines indicate the location of the *Kanani et al.* [2010] magnetopause model for $P_{SW}^{Dynamic} = 0.1\,nPa$ and $0.01\,nPa$. Each panel displays the locations of the 28 detections for which both electron energizations and southward magnetic field deflections ($\geq B_\theta^{RMS}$) were observed. Panel (a) includes the detections from the literature (described in Table 7.2). Panel (b) shows the events coloured blue if they occur within a group (i.e. within 3 hours of an adjacent event [c.f. *Jackman et al.*, 2014b; *Smith et al.*, 2016]), or red if they are isolated. Panel (c) shows the events with a colour bar according to the size of the magnetic field deflection with which they are associated. Panel (d) shows the events for which an increase in the LEMMs ($E_{e^-} \geq 20\,keV$) rates are observed (in blue), with the examples for which no increase (or a decrease) are observed (in red).

anisotropic energetic electron distributions reducing the detection efficiency of the high energy counterpart of the dipolarizations cannot be excluded, even though Earth-based observations would be more consistent with isotropic energetic electron populations [e.g. *Walsh et al.*, 2011]. It is also possible that the energization for these events does not extend beyond the CAPS energy range (above $\sim 26\,keV$), a possibility if the spacecraft was located closer to the reconnection site during these intervals (and the higher energy populations are mostly generated by non-local mechanisms). If this was the case, it might be expected that the events for which higher T_{e^-} were recorded would be more

likely to show increases in LEMMS. Indeed, $^{6}/_{7}$ of the events with the highest T_{e^-} in the dipolarizing material and $^{8}/_{9}$ events with the highest fractional increase in T_{e^-} show increases in LEMMS counts.

7.6 Plasma Heating

The properties of the hot, tenuous population following the dipolarization front (e.g. that highlighted in red in Figure 7.1) will now be examined in more detail. Insufficient counts were recorded to analyze the ion populations involved in any of the events, but there were sufficient electron counts to produce usable moments for $^{19}/_{28}$ of the events.

The CAPS/ELS pitch angle (PA) spectra were inspected for the 19 events with sufficient electron counts. The PA coverage of CAPS/ELS during these intervals was generally limited to around half of the full 180° distribution. However, all 19 events afforded sufficient coverage to identify when the distributions fell into two broad categories: field aligned (peaking towards 0° or 180°) or perpendicular (peaking around $\sim$ 90°). In total, $^{18}/_{19}$ events show anisotropic distributions. The vast majority (17 events) showed higher electron fluxes approaching field aligned orientations; perhaps suggesting that the majority of the heated low-energy electron population was generated by the (non-local) Fermi heating mechanism as the flux tubes contract towards the planet (as has been suggested by *Yao et al.* [2017b]).

Figures 7.5a and (b) show density-temperature plots for the electron populations before and after the passage of the dipolarization front respectively. It should be noted that the spacecraft is not tracking the planetward moving plasma population, and so the 'before' measurement is simply taken as representative of the ambient plasma sheet (for the purposes of comparison). Panels (a) and (b) are plotted on the same axes scales for comparison. It can be seen that between the two panels all points move upward and to the left: the electron temperature increase is coupled with a decrease in the density. The colours of the points indicate the radial distance at which the event was encountered. The colours demonstrate that the events furthest from the planet occupy the bottom left of the distribution while those closest to the planet fill the upper right. *Runov et al.* [2015] performed a similar analysis at the Earth and observed an analogous trend. In general, those dipolarizations observed at greater radial distances are more likely to be closer to the site of reconnection. With a shorter propagation distance, and associated smaller change in field strength, the effects of non-local mechanisms (e.g betatron and Fermi heating) would be smaller in magnitude, as has been found at the Earth [e.g. *Birn et al.*, 2014; *Pan et al.*, 2014b; *Runov et al.*, 2015].

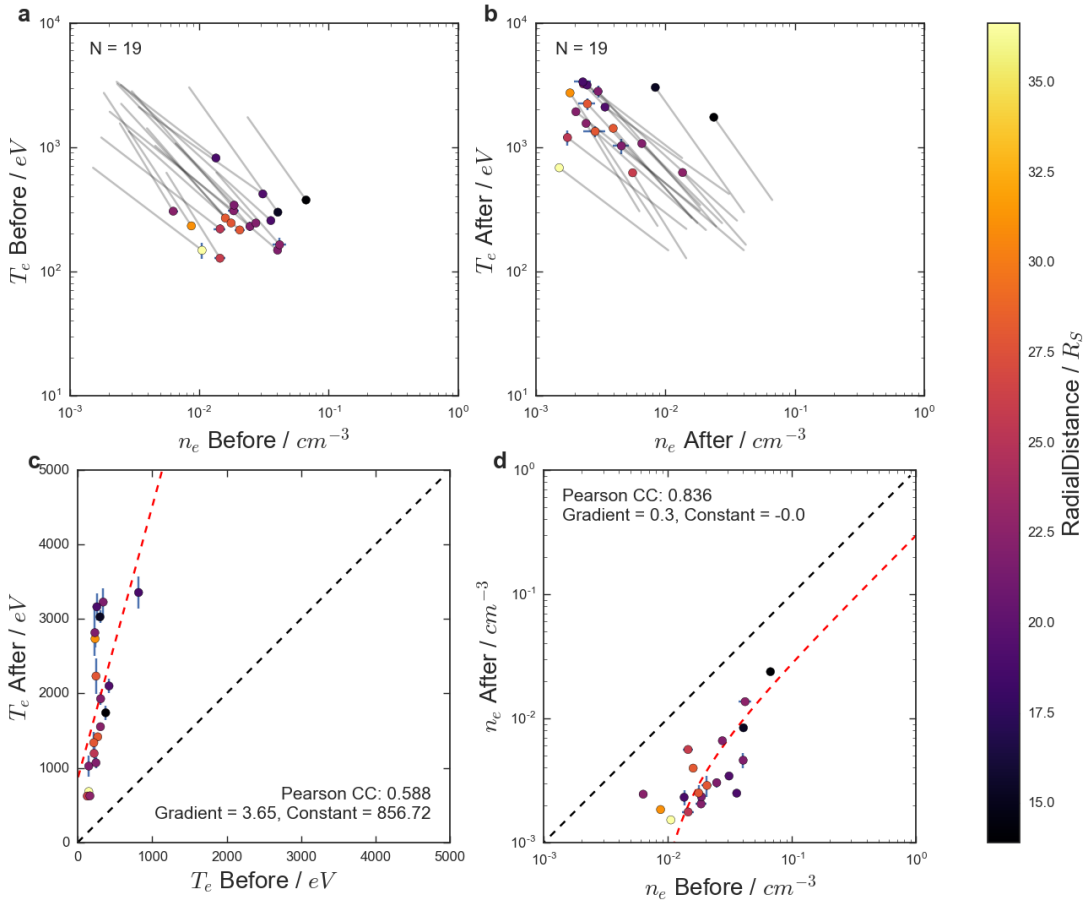

FIGURE 7.5: Panels (a) and (b) show the electron density plotted against the electron temperature for before (a) and after (b) the dipolarization front. These panels are plotted on the same axes scale for direct comparison. The gray lines indicate how the events move in density-temperature space. Panels (c) (and (d)) show the electron temperature (density) before the front plotted against the electron temperature (density) after the passage of the front. The points and error bars provided are the mean and standard error of the mean respectively. The diagonal black dashed line shows the location of $y = x$: where the points would lie if there was no change during the passage of the front. The red dashed lines indicate least squares linear fits to the data; the details of the fit parameters are provided on the panels. The colour bar for all four panels indicates the radial distance at which the spacecraft encountered the event.

Figures 7.5c and (d) show how the electron temperature and density vary within each event. Panel (c) shows the electron temperature before the front compared to that measured after its passage, while panel (d) shows the same but for the electron density. The gradients of the linear ($y = mx + c$) least-squares fits show that, on average, the temperature increases by between a factor three and four, while the density drops by around a factor of three. The temperature best fit contains a significant constant value ($\sim 900\,eV$). This constant could be interpreted as the minimum temperature increase caused by mechanisms local to the reconnection site [e.g. *Fu et al.*, 2017], though there is also likely a selection effect present: small changes in temperature are less likely to be identified. In addition the fit is strongly affected by the point that lies to the upper

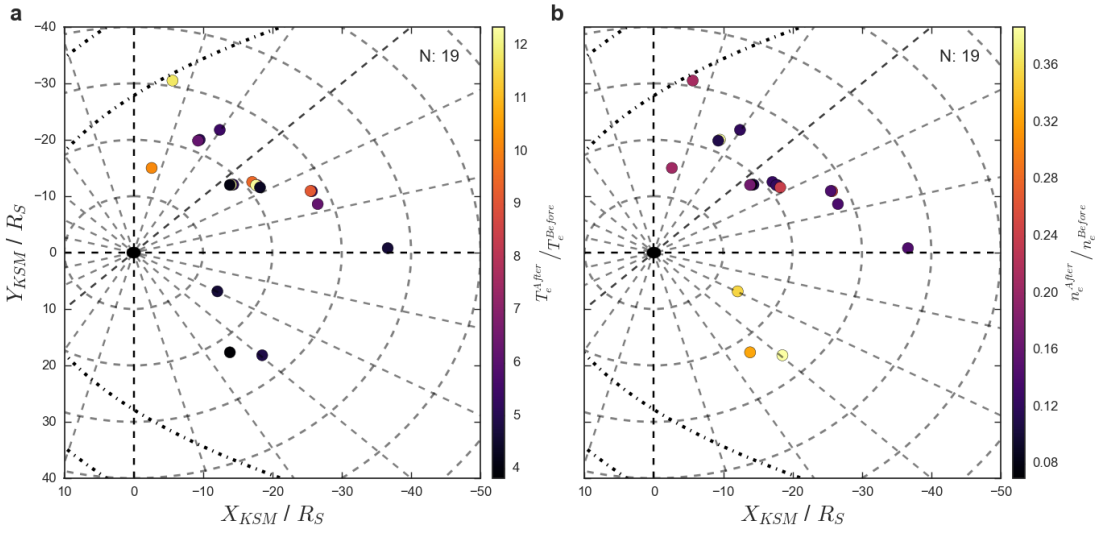

FIGURE 7.6: Equatorial projections of Saturn's magnetotail, as in Figure 7.4. The panels display the 19 events for which electron moments were available both before and after the passage of the front. Panel (a) shows the fractional temperature change over the event, while Panel (b) shows the fractional change in density.

right at $T_e \sim 1\,keV$. When this point is excluded from the fit the average fractional temperature change (gradient) increases to a factor of six.

The changes in electron temperature and density will be explored with respect to their location within the magnetotail. Equatorial projections of the magnetotail are shown in Figure 7.6. The colour bar of Figure 7.6a shows the fractional increase in T_e following the passage of the dipolarization front ($^{T_e^{After}}/_{T_e^{Before}}$) while the color bar of Figure 7.6b shows the fractional change in n_e ($^{n_e^{After}}/_{n_e^{Before}}$). The panels only include those events for which sufficient electron moments are available, as above ($^{19}/_{28}$). It should be noted that the fractional temperature increases are almost all larger than the average calculated using the best fit in Figure 7.5c. This is likely a result of the arbitrary use of a linear fit and the outlier (discussed above).

The events pre-midnight can be seen to possess relatively small temperature increases (factors of ~ 4 in Figure 7.6a) and preserve the greatest fraction of their density ($30-40\%$ in Figure 7.6b), perhaps suggesting that they are observed when the spacecraft is closer to the reconnection site. As discussed above, the further the events have propagated from the reconnection site, the greater the magnitude of non-local heating mechanisms. These pre-midnight dipolarization fronts could be related to the Vasyliunas cycle stretching, as the mass loaded flux tubes rotate around the dusk flank and are no longer confined by the magnetopause.

In contrast, the events post-midnight show a much greater range of variation of plasma properties: some show very large heating factors (10-12 fold increase), while others are

more similar to those observed pre-midnight. These observations could be explained by a larger variation in x-line location in the post-midnight region of the magnetotail, with the dipolarizations propagating from different downtail locations. Experiencing a more significant change in total field strength would explain the greater possible heating observed post-midnight. Additionally, if the distance between the effective mirror points shrinks significantly, then the plasma would be more dramatically heated. Finally, the range of densities measured after the dipolarization also vary from 10% to 30% of that measured within the ambient plasma sheet

7.7 Composition

The dipolarizations will now be investigated with respect to the relative composition of their plasma. In general, the plasma sheet would be expected to be populated by ions of internal magnetospheric origin, comprising both light ions (e.g. H^+ and H_2^+) and heavier water group ions (W^+) from Enceladus (e.g. O^+, OH^+, H_2O^+ and H_3O^+). The presence of species that are more prevalent in the solar wind (e.g. He^{++}) could act as an indication that the reconnection process has involved the closure of open field lines, e.g. related to the Dungey cycle. Fortunately, the CHEMS instrument is capable of distinguishing several of the ion species and charge states of interest: e.g. He^{++} and H_2^+ (of external and internal origin respectively). It should be noted that CHEMS measures the composition of the suprathermal ($E \geq\sim 10\,keV$) plasma, which may differ from that of the thermal plasma ($E \sim 100\,eV$) due to species dependent heating and loss mechanisms.

Figure 7.7 shows example CHEMS PHA (pulse-height analysis) data. Figure 7.7a shows the counts ($\sim 10\,keV \leq E \leq 236\,keV$) integrated over an interval of ambient plasma sheet preceding a dipolarization front on day 282 2006, while Figure 7.7b shows the integrated counts obtained within the heated population following the front. Mass per charge vs. mass boxes for specific species of interest are shown, as are the number of counts and their compositional fraction. As mentioned above, He^{++} (marked in red) and H_2^+ (marked in blue) are indistinguishable based solely upon mass per charge histograms (i.e. along the x-axis and the upper histograms).

For this study, the addition of atomic mass information allows us to unambiguously differentiate internal from external plasma populations. The abundances of He^{++} and W^+ group ions will be compared before and after the passage of the front. In the example shown in Figure 7.7 it can be seen that the W^+ group fraction drops by a factor of two between the intervals. The He^{++} fraction increases slightly, but not significantly compared to the change in W^+. H^+ is not directly used as a tracer as it could originate

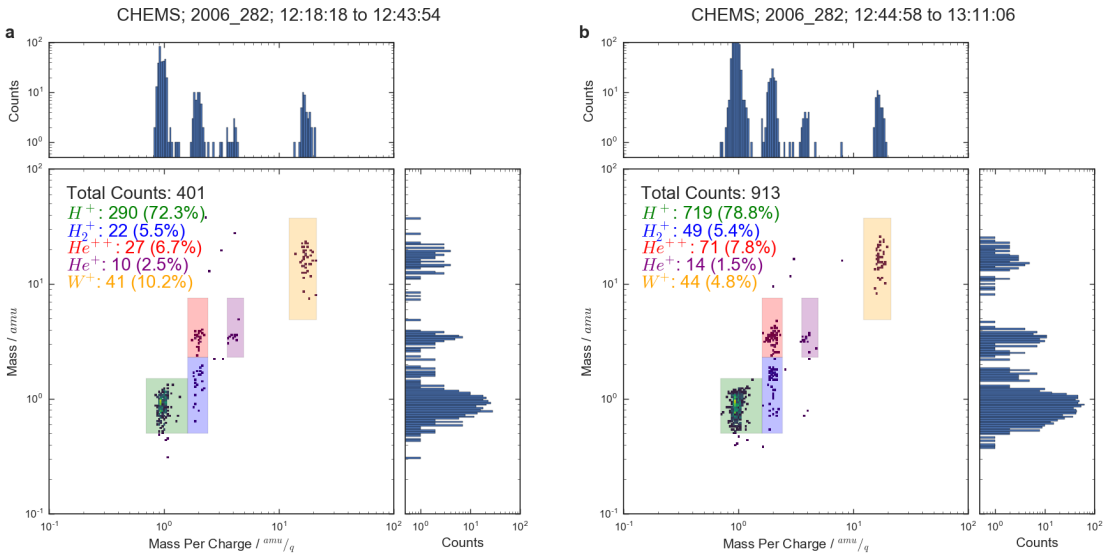

FIGURE 7.7: CHEMS PHA (pulse-height analysis) data (a) before the dipolarization and (b) within the heated population following the front on 9 October 2006. Coloured boxes are placed on the histogram to indicate the locations of specific species relevant to this study. The corresponding counts and fractional compositions are displayed in the upper left of each panel.

from Saturn's ionosphere, Enceladus, Titan or the solar wind [*Glocer et al.*, 2007; *Felici et al.*, 2016]. Combining the reduction in W^+ with the relatively steady He^{++} suggests that this dipolarization is associated with the release of a plasmoid (unobserved on the tailward/distant side of the reconnection site), in which the heavy W^+ group ions have been preferentially lost [c.f. *Badman and Cowley*, 2007; *Thomsen et al.*, 2013, 2014b]. If the reconnection had proceeded to involve lobe field then the He^{++} fraction would have been expected to increase. Also, while the integration times for both panels are similar ($\sim$ 26 minutes) the counts in the second interval are much higher, providing additional evidence that significant heating has occurred.

Figure 7.8 explores the composition of the dipolarizations statistically, showing equatorial projections of the magnetotail. Figure 7.8 shows the 15 dipolarizations which provided sufficient CHEMS counts ($\geq$ 30) both before and after the dipolarization front. Sufficient counts were required in both intervals as the scale height has been found to vary for different ion species in the plasma sheet [*Kellert et al.*, 2009; *Sergis et al.*, 2011]; motion of the plasma sheet could change the composition and so the comparison must be made with immediately adjacent material. The panels on the left show the relative abundances measured before the passage of the front, while the panels on the right show the fractional changes in those abundances measured within the dipolarizing material (i.e. a value of two would indicate a doubling in fractional abundance). The events displayed in the right hand panel are plotted in grey if the change was not statistically

significant (at the $p = 0.1$ level). Therefore, red indicates significant decreases in the fractional abundance/ratio, while blue shows a large increase.

Figure 7.8a shows the W^+ group fraction before the passage of the dipolarization front. A large range in water group fraction is observed, with fractions ranging between ~ 0 and 40 %. Figure 7.8b then shows the relative change in $\% W^+$ within the dipolarizing material relative to the previous panel. Just under half of the events ($^6/_{15}$) show a significant depletion of W^+ relative to the preceding ambient plasma sheet. This could either be as a result of the reconnection of lobe field, or the preferential loss of equatorial heavy W^+ ions in departing plasmoids [e.g. *Badman and Cowley*, 2007; *Thomsen et al.*, 2013, 2014b]. Two events display a significant increase in W^+ fraction.

Similarly, Figures 7.8c and (d) show the He^{++} fraction in the ambient plasma sheet and the relative change within the dipolarizing material. It can be seen that the He^{++} fraction is, in general, much smaller than the W^+ group fraction. The ambient plasma sheet (Figure 7.8c) generally contains less than 5 $\% He^{++}$, with only one interval recording a higher fraction than this. One event, located $\sim 35\, R_S$ down the tail at midnight, shows a strong increase from 2 % to 13 % He^{++} (saturating the color bar in 7.8d). Such an increase suggests that perhaps open field lines have been closed during this event, leading to the inclusion of more plasma of solar wind origin. The vast majority of events ($^{13}/_{15}$) show no significant change in He^{++} %. This is likely related to the small number of He^{++} counts generally recorded (and the resulting large statistical uncertainties).

The bottom four panels investigate the ratios of several light ion species and their relative changes. These light ion ratios should be insensitive to plasmoid release (unlike the more equatorially confined W^+ group) and thus provide another indicator of potential Dungey-style reconnection. H_2^+ has an internal source, and thus it could be illuminating to compare its abundance to He^{++}. Figures 7.8e and (f) show the ratios of $^{H_2^+}/_{He^{++}}$ before the passage of the front and the relative change within the dipolarizing material. A decrease in the $^{H_2^+}/_{He^{++}}$ fraction, coupled with a depletion of W^+ and increase in He^{++} would be conclusively indicative of Dungey-type lobe reconnection. Figure 7.8f does highlight one event for which the ratio decreases (which also displayed a strong reduction in W^+ in Figure 7.8b). This event is located postmidnight at $\sim 20\, R_S$ and a local time of 0200.

Unfortunately, the ratio of H_2^+ and He^{++} is statistically insignificant (at the $p = 0.1$ level) for $^8/_{15}$ events, likely due to the sparsity of He^{++}. For this reason Figures 7.8g and (h) investigate the ratio of H_2^+ to H^+. While H^+ (and therefore this ratio) is not a decisive diagnostic of external/lobe involvement (as it has both internal and external sources) a relative increase in its abundance (compared to H_2^+) combined with other significant changes in the panels above (e.g. a significant decrease in W^+) would be

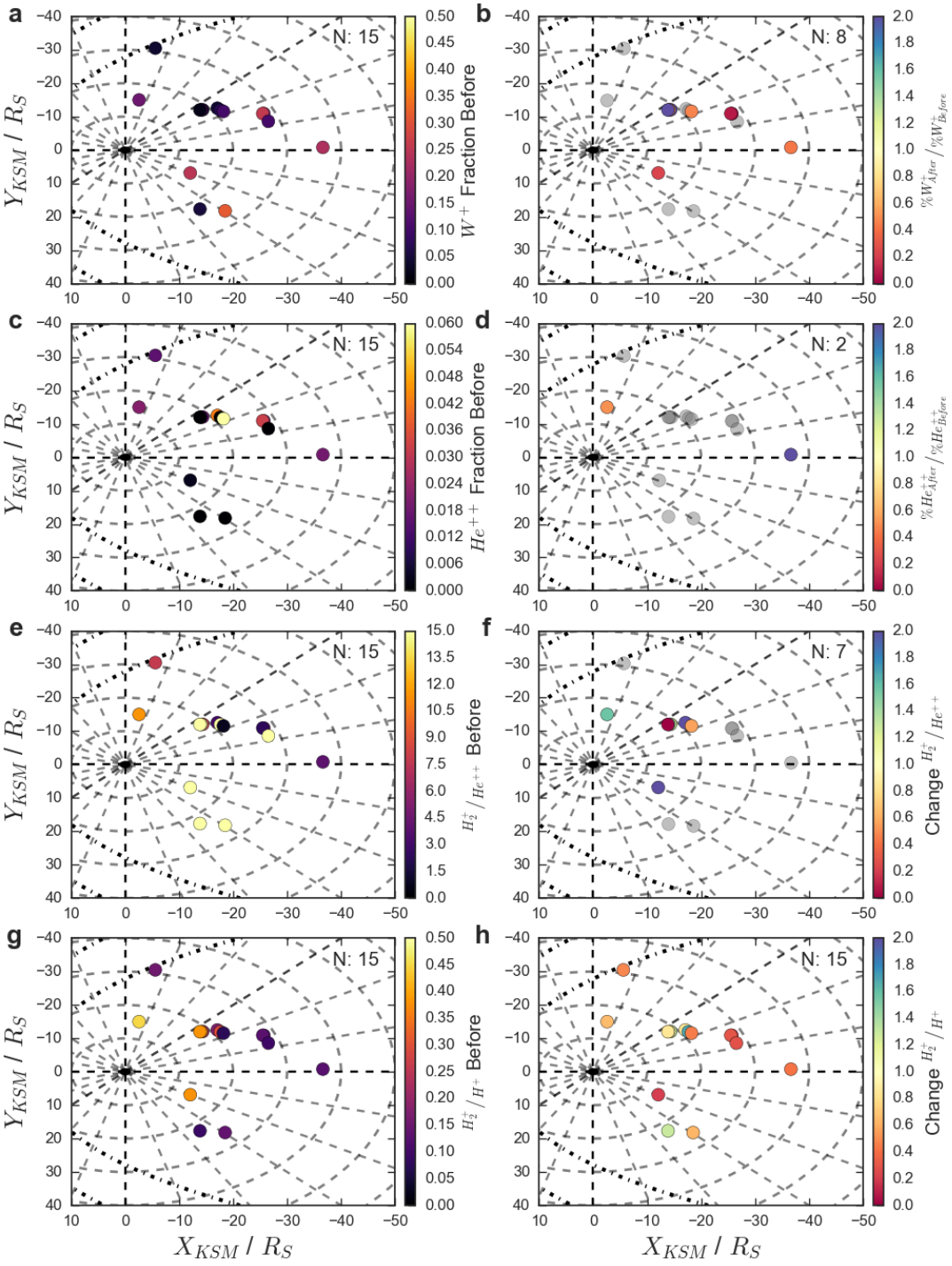

FIGURE 7.8: Equatorial projections of Saturn's magnetotail, as in Figures 7.4 and 7.6. The panels display the 15 events for which sufficient CHEMS counts (≥ 30) were collected in both the background and heated populations. Panels (a) and (c) show the fractional population of W^+ and He^{++} observed before the passage of the front respectively. Panels (b) and (d) show the change in W^+ and He^{++} fractions observed in the dipolarizing material relative to the background (panels a and c): blue/green indicates the fraction has increased while red/orange indicates a reduction. Panels (e) and (g) then show the ratios of $^{H_2^+}/_{He^{++}}$ and $^{H_2^+}/_{H^+}$ before the front, while panels (f) and (h) chart the relative change in the ratios within the dipolarizing material.

suggestive of lobe involvement. Likely due to the large numbers of counts in both species, all 15 events show significant ($p \leq 0.1$) changes in Figure 7.8h. Both events highlighted above (located at $35\,R_S$ and $20\,R_S$) show strong decreases in this ratio, building on the evidence of the above panels. These two events are located fairly deep in the tail or post-midnight. It has been suggested that reconnection cannot proceed onto open field lines until the flux tubes have rotated past midnight [e.g. *Thomsen et al.*, 2013], consistent with this result.

The complete absence of W^+ group ions would not necessarily be expected from a dipolarization resulting from Dungey-type reconnection of open field lines, even assuming that 'pure lobe' reconnection is possible. *Thomsen et al.* [2015] argue that some W^+ can originate in the mantle, and be subsequently involved in lobe reconnection. Additionally, a combination of terrestrial work and modelling has suggested that plasma from the adjacent plasma sheet becomes entrained in the reconnection outflow [*Eastwood et al.*, 2015]. This mechanism would also suggest that Dungey-type dipolarizations that have propagated from deep within the tail would be expected to contain significant W^+ accumulated during their propagation. For these reasons the presence of W^+ is not a decisive indicator of purely Vasyliunas-type reconnection.

7.8 Conclusions

Analysis of dipolarization fronts within Saturn's magnetotail has been presented. Southward deflections of the magnetic field were first identified, as were intervals where an energized electron population was present. In total, 28 events with clear signatures in both the magnetic field and CAPS ELS data have been analyzed. The vast majority of significant southward field rotations ($\geq 95\%$) were unaccompanied by the required change in electron population, while 48% of identified electron signatures were coincident with large rotations of the field. The large number of southward field deflections not coincident with significant changes in the electron energy distribution could be due to the spacecraft's location relative to the current sheet, inefficient heating from disruption of cross tail current systems or changes in the spacecraft's magnetospheric environment.

An example dipolarization (showing terrestrial-like properties) was presented displaying a strong southward field rotation coupled with a reduction in the density and a heating of the electron population. The high energy electron counts increased in a dispersionless fashion following the passage of the front. The direction and speed of plasma flow were found to be planetward and around five times the corotational velocity. The pitch

angle spectra show significant counts in both the perpendicular and field aligned orientations, which can be explained by flow anisotropies and the non-local betatron and Fermi mechanisms heating the plasma during it's planetward passage.

Dipolarizations were identified over the majority of the magnetotail, but most were located post-midnight ($^{22}/_{28}$). Several chains of dipolarizations were observed (a chain defined as multiple events, each separated by less than three hours). These chains of dipolarizations were solely observed post-midnight. The dipolarizations observed furthest from the planet were found to possess smaller deflections of the magnetic field, while the largest deflections were identified closest to the planet. This is likely a selection effect, as the threshold deflection size increases at smaller radial distances (corresponding to the stronger meridional field component).

The majority of the low energy ($E \leq 26\,keV$) dipolarizing electron populations were found to have large relative fluxes in the field aligned orientations, possibly as the result of Fermi-type heating mechanisms. The electron temperature and density were found to be anti-correlated following the passage of the dipolarization front. The electron temperature increased by factors of around six, while the density dropped by a factor of approximately three. Pre-midnight dipolarizations were found to be accompanied by the smallest relative heating and density depletions while those post-midnight displayed a much larger range of temperature and density variation. This could perhaps be explained by a more consistent x-line forming closer to the planet pre-midnight, while post-midnight the location of the x-line varies over a much larger range of radial distances. If this were the case then post-midnight the dipolarizing material could travel over larger distances, increasing the magnitude of non-local heating effects.

The composition of the heated dipolarizing flows was compared to that of the adjacent ambient plasma sheet. Six of the events (40%) show significant ($p \leq 0.1$) reductions in W^+ group fraction, which could be caused by the preferential loss of equatorial heavy ions in departing plasmoids or the closure of open field lines. Two of these events also show other compositional changes suggestive of the reconnection of open field lines.

Chapter 8

Multi-Instrument Investigation of the Location of Saturn's Magnetotail X-Line

8.1 Introduction

This Chapter discusses an indirect, multi-instrument investigation of the Kronian magnetotail X-line. It focuses on two case studies that were first identified during the survey described in Chapter 4.

The aim of this Chapter is to present two case studies, showing variability in the location of the magnetotail reconnection site. An extensive catalogue of reconnection products, identified from their magnetic signature [*Smith et al.*, 2016] (Chapter 4), were investigated from a multi-instrument perspective to infer the location of the spacecraft relative to the magnetotail x-line. The first interval is inferred to be the result of multiple x-lines; evidenced by a quick succession of discrete reconnection products (plasmoids and dipolarizations). The time intervals over which these flows operate are an order of magnitude shorter than that those described in the past [c.f. *Thomsen et al.*, 2013, 2015; *Arridge et al.*, 2015b]. The second example shows the retreat of an x-line deeper into the magnetotail; this phenomena is inferred from the changing plasma signature recorded by Cassini.

Section 7.2 describes the instrumentation used within the study. Section 7.3 presents two case studies, while Section 7.4 discusses their implications in terms of x-line width and magnetospheric dynamics. Section 7.5 then summarizes and concludes.

8.2 Instrumentation

Data from the Cassini magnetometer [*Dougherty et al.*, 2004] are used in this study. Magnetic field data are presented in KRTP (Kronocentric-Radial-Theta-Phi) coordinates: a planet centered spherical polar system in which the radial component is directed outward from the planet, the theta (or meridional) component is positive southward and the azimuthal component is positive in the direction of planetary rotation (corotation). This coordinate system has been shown to be well suited to distinguish transient magnetospheric phenomena from periodic encounters with the magnetotail plasma sheet [*Jackman et al.*, 2009a].

The magnetic field data are complemented by the thermal electron and ion data from the Cassini Plasma Spectrometer (CAPS) [*Young et al.*, 1998]. The Cassini Electron Spectrometer (ELS) observes the electron population between $0.58\,eV$ and $26\,keV$, while the Ion Mass Spectrometer (IMS) measures ions with an energy per charge between $1\,eV/e$ and $50\,keV/e$. During most intervals the CAPS instrument does not see the full $4\,\pi sr$ of the sky, unless the spacecraft happens to be rolling. Instead, an actuating platform allows sampling of $\sim 2\,\pi sr$ of the sky. Electron moments (i.e. n_e and T_e) derived from ELS data are also used, and the methods by which these moments are derived are described by *Lewis et al.* [2008] and *Arridge et al.* [2009b].

The thermal plasma data from CAPS are complemented by the suprathermal populations observed by the Magnetospheric Imaging Instrument (MIMI) [*Krimigis et al.*, 2004]. In particular, data from the Charge Mass Spectrometer (CHEMS) are presented. CHEMS measures the mass and mass per charge of ions between 3 and $236\,keV$ for H^+ and between 8 and $236\,keV$ for O^+. The collection of both mass and mass per charge information enables the separation of ion species such as H_2^+ and He^{++}, an ability that is crucial to determining whether the plasma is of internal (H_2^+) or external (He^{++}) origin.

Finally, data from the Radio and Plasma Wave Science (RPWS) [*Gurnett et al.*, 2004] instrument provides a more global picture of the magnetospheric dynamics. The RPWS instrument allows monitoring of the Saturn Kilometric Radiation (SKR), typically observed between frequencies of $3\,kHz$ and $1.2\,MHz$ [*Kaiser and Desch*, 1984; *Lamy et al.*, 2008].

8.3 Results

A catalogue of reconnection products [*Smith et al.*, 2016] (Chapter 4), identified from Cassini's magnetometer data, was investigated with data from multiple instruments in order to probe the distance of Cassini from the reconnection sites in Saturn's magnetotail. Two case studies are presented showing the motion or formation of magnetotail x-lines on short timescales. The first example shows the products of short-lived or azimuthally narrow x-lines on the dusk flank. The second example shows the tailward motion of an x-line (or series of x-lines) post-midnight over a quarter of a planetary rotation.

8.3.1 Case Study 1: Pre-Midnight Multiple X-Lines

In this example, Cassini was approximately $33\,R_S$ ($1\,R_S = 60268\,km$) from the planet on an inbound trajectory at 20:00 hrs local time and a latitude close to the rotational equator (0.12°). It should be noted that the dipole equator is offset northward from the rotational equator by $\sim 0.04\,R_S$ [*Dougherty et al.*, 2005b]. Seven hours of Cassini MAG and CAPS/ELS data are shown in Figure 8.1. Figure 8.2 shows CAPS/IMS viewing plots for the intervals highlighted (with corresponding letters above the axes) in Figure 8.1. The coloured bars represent the orientation of the associated plasma flow relative to corotation (also shown in Panel g). The angle relative to the corotational direction (α) was calculated from plots such as those displayed in Figure 8.2: the angular separation between the peak of the observed counts and the corotational direction was evaluated. α is defined such that positive values indicate outflow, and it has been calculated for all times during which sufficient ion counts were recorded. Red bars indicate strong outflow ($\alpha > 30°$), orange represents slightly weaker outflow ($20° < \alpha < 30°$) while yellow shows those within 20° of corotation and thus fairly consistent with this, given uncertainties in the measurement (as in *Thomsen et al.* [2013]). Triangles indicate those intervals for which the peak flow is not within the field of view of the instrument, and therefore represent upper limits. The blue interval shows a time during which the region of sky just outside of corotation is visible and the peak is outside of this location (consistent with inflow), alternatively grey intervals show those for which the peak is not observed, but the instrument cannot confirm that the increasing counts continue beyond corotation.

At the start of the interval, between 05:00 and 05:30, the thermal plasma flows appear to be fairly corotational, consistent with previous statistical studies of the dominant flow patterns observed at Saturn [*McAndrews et al.*, 2009; *Thomsen et al.*, 2013]. An example of an all-sky viewing plot for this configuration is presented in Figure 8.2a. Notably, the peak of the ion counts can be seen to coincide with the angle 90° from the

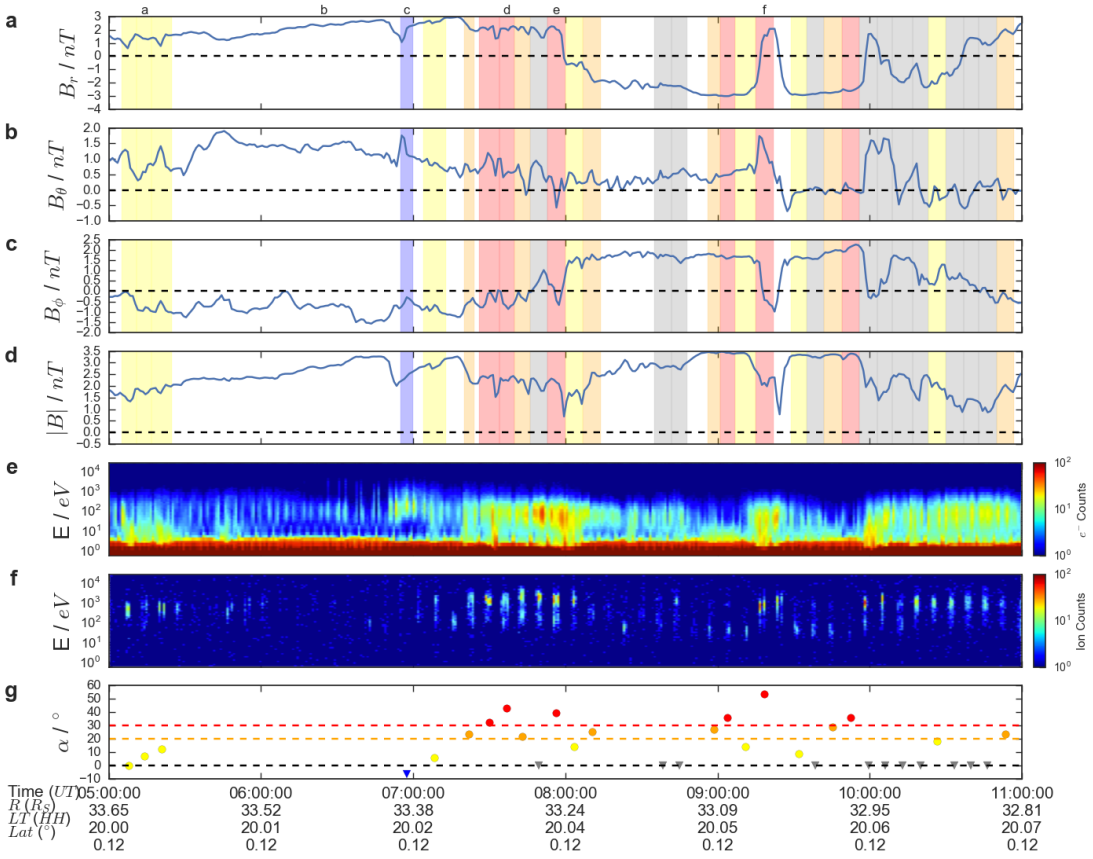

FIGURE 8.1: Seven hours of Cassini data from day 040 2010 from 05:00 - 12:00 UT. Panels (a) - (d) shows one minute resolution magnetometer data in the spherical polar KRTP (Kronocentric-Radial-Theta-Phi) coordinate system. Panel (e) shows a CAPS/ELS electron spectrogram, where the counts have been averaged over all anodes. Panel (f) shows the ion spectrogram from anode 5, which generally showed the greatest counts during the interval. The vertical shaded regions outline the integration times used to produce the CAPS/IMS all sky viewing plots, some of which feature in Figure 8.2. These intervals were analysed to determine the angular separation between the peak of the counts and the direction of corotation (α), plotted in panel (g). Positive values of alpha represent outflow, while negative show inflow. During several intervals the peak of the flow was not observed within the field of view of CAPS/IMS, therefore only the derivation of upper limits were possible and are indicated with triangles in panel (g). Yellow regions (and points) show intervals where α was less than 20°, orange shows those between 20 and 30°, while those for which $\alpha \geq 30°$ are shown in red. The blue region shows an interval during which inflow can be inferred, while grey regions show those consistent with either inflow or corotation (i.e. the peak was not within the field of view). Six intervals are marked with letters at the top, which correspond to the relevant panels of Figure 8.2.

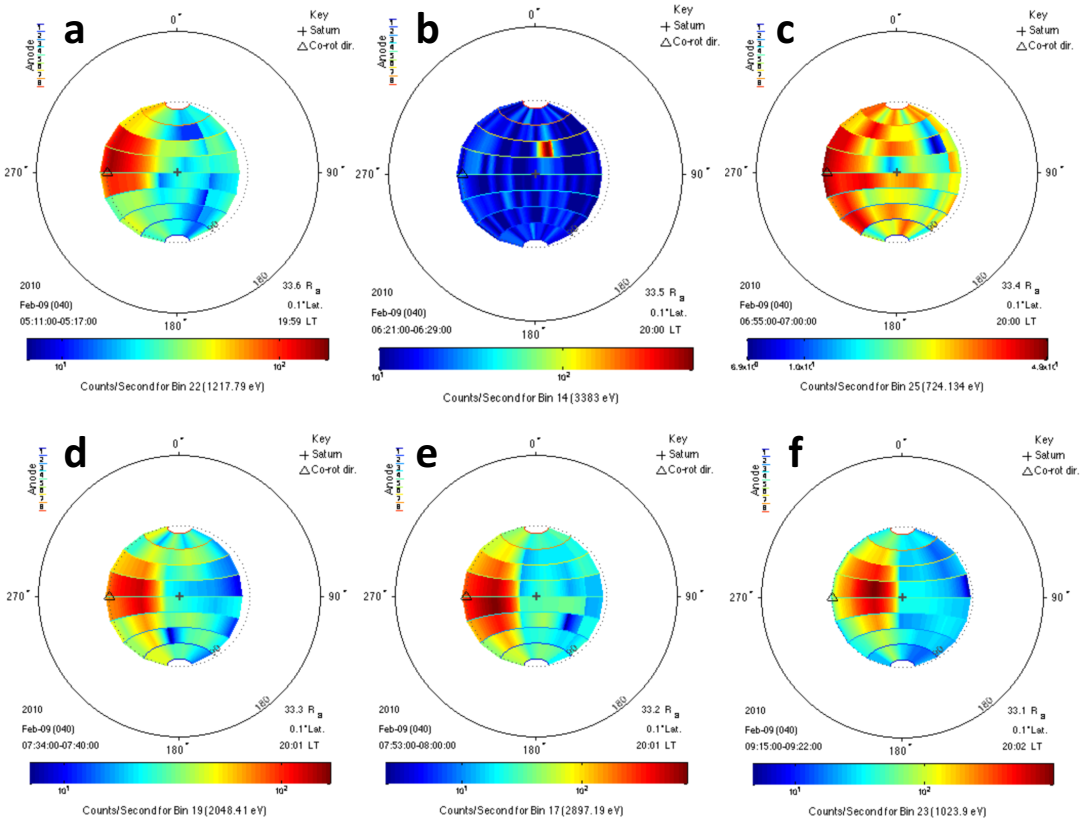

FIGURE 8.2: CAPS/IMS all-sky viewing plots (CAPS/ELS in Panel b) detailing the origin of counts during the intervals defined at the top of Figure 8.1. The centre of the plots represents the Saturnward looks direction (i.e. along the radial unit vector in the $-\hat{r}$ direction). The dotted circle represents directions a polar angle of 90° from this, including the corotational direction (indicated with a triangle). The outer circle represents the anti-Saturnward direction. White regions show those areas of the full $4\pi sr$ not covered by the CAPS instrument during the given integration time (itself shown in the bottom left of each panel). The colours represent the count rate originating from that sector of sky. The CAPS/IMS energy bin used to produce the panel is provided at the bottom of each.

planetward direction, corresponding to an α of 0 (Figure 8.1g). Following this, between approximately 06:00 and 06:30, the radial component of the field increases while the temperature of the electron population appears to decrease. This could be indicative of field line stretching, perhaps as more heavily mass-loaded flux tubes have rotated around the dusk flank and are no longer supported by the magnetopause.

Shortly after $\sim$ 06:30 narrow vertical bars (indicating a highly anisotropic population) appear in the electron energy flux spectrogram at around $1\,keV$ (Figure 8.1e). These correspond to a population of energetic field aligned electrons (confirmed in Figure 8.2b). *Mitchell et al.* [2009] inferred similar field aligned distributions to be related to auroral currents. These electrons are followed at 06:50 by a southward rotation of the field in Figure 8.1b. This rotation of the field is accompanied by a small energization of the

electron population: a signature that has been recently used to identify Kronian dipolarization fronts [*Smith et al.*, 2018] (Chapter 7). Unfortunately, the CAPS instrument was oriented such that it was mostly looking toward the planet at this time (hence only in a position to detect plasma flowing outward from the planet and into the detector), and so cannot definitively confirm the presence of an inflowing plasma population. However, Figure 8.2c shows that the plasma counts increase towards the edge (left) of the field of view, extrapolating or fitting to this distribution would result in an flow originating from at least 5° outside of corotation (shown by the blue triangle in Figure 8.1g). This would be consistent with the field rotation and small electron energization, indicating a dipolarization of the field. Following the dipolarization, the flow returns to something more indicative of corotation flow (shown by the yellow shaded region and an $|\alpha| < 5°$). It is worth noting that inflow from dipolarizations may not be expected to travel radially inward at Saturn (as discussed in Section 2.3); Figure 8.2c is consistent with an inflow originating between the anti-Saturnward (outer edge of the circle) and corotational direction (as discussed and observed by *Thomsen et al.* [2013]). The duration of the inflow period was relatively short at ~ 10 minutes, shorter than the 30 minute to several hour intervals previously reported at Saturn [e.g. *Thomsen et al.*, 2013, 2015; *Jackman et al.*, 2015].

Between approximately 07:30 and 07:50 a period of fairly significant outflow is observed (one of the intervals is displayed in Figure 8.2d). The azimuthal component of the magnetic field also changes sign, moving to a leading (or swept-forward) configuration. Then, at 07:54, the field is deflected through $B_\theta = 0$, briefly turning northward. This, coupled with observations that the plasma flow during this interval has a very significant outward component ($\alpha \sim 40°$) suggests that this could be the trailing edge of a plasmoid that has formed as the field has stretched downtail. The lack of a clear, preceding strong southward field deflection would indicate that the tailward hemisphere of the plasmoid is not encountered, or that the magnetic structure is not symmetric [e.g. *Cowley et al.*, 2015]. Though not a large field deflection ($\Delta B_\theta \sim 1\,nT$) the outflow is significant compared to the adjacent measurements. The outflow is shown in Figure 8.2e, where the peak of the ion counts can be seen to arrive from inward of the position of strict corotation (the hollow triangle). If this does represent a plasmoid, then an x-line may have formed planetward (and duskward) of the spacecraft. Alternatively, the original x-line (associated with the dipolarization front) may have moved planetward, passing by the spacecraft which was located in the adjacent northern magnetotail lobe (from the large positive value of B_r in this interval). The strong outflow and field deflection are only observed for a short period (during one 7 minute integration for the outflow) before the flow angle reduces back towards corotation.

Just over an hour after the first plasmoid was observed a second passed over the spacecraft, at around 09:15. The large, bipolar field deflection in B_θ is once more accompanied by outflow originating between the planetward and corotational directions (Figure 8.2f), as before. The return of the plasma towards corotational flow between the two plasmoids could indicate that this is due to a separate instance of reconnection, that an x-line has formed planetward and duskward of the spacecraft.

To summarize, in the space of just over three hours (just under a third of a planetary rotation) it could be inferred that Cassini observed three distinct products of reconnection. The first product, a dipolarization front, originating tailward of the spacecraft, while the later plasmoids formed between the spacecraft and the planet. The thermal plasma flows during the interval show a strong corotational influence but differ significantly from ambient azimuthal flow.

8.3.2 Case Study 2: Post-Midnight Tailward Motion

For the second example Cassini was located post-midnight at around 02:30 hrs local time, $\sim 20\,R_S$ from the planet and latitudinally close to the rotational equator ($|Lat| < 1°$). Figure 8.3 shows four hours of MAG data (Figure 8.3a - d) and thermal electron energy flux from CAPS/ELS (Panel e). The derived electron temperature is presented in Figure 8.3f.

Three clear dipolarizations are marked with vertical red dashed lines. These were identified based on the strong southward deflections (Figure 8.3b) and the change in electron population in Figure 8.3e. The change in electron population corresponds to an increase in the electron temperature and a reduction in the density of the dipolarizing material [c.f. *Smith et al.*, 2018]. There are several other signatures present that could be dipolarizations (e.g. at 03:25 and 05:45); however they are not as clear as the three that are marked. The viewing of the CAPS instrument during this interval is purely inwards, towards the planet and thus is unable to confirm the presence of an inflowing plasma population (or flow changes such as those in Figure 8.2).

Chains of dipolarizations are not uncommon in Saturn's magnetotail [*Smith et al.*, 2016, 2018], however this event is particularly significant as it shows a clear increase in the T_e of the dipolarizing electron population with each subsequent dipolarization (highlighted with red shading in Figure 8.3f). Before the first dipolarization the ambient plasma sheet has a temperature of $\sim 160\,eV$; this increases to around $600\,eV$ following the first dipolarization. The second and third dipolarizing populations then show average electron temperatures of $2.2\,keV$ and $3.4\,keV$ respectively. For context, Saturn's ambient

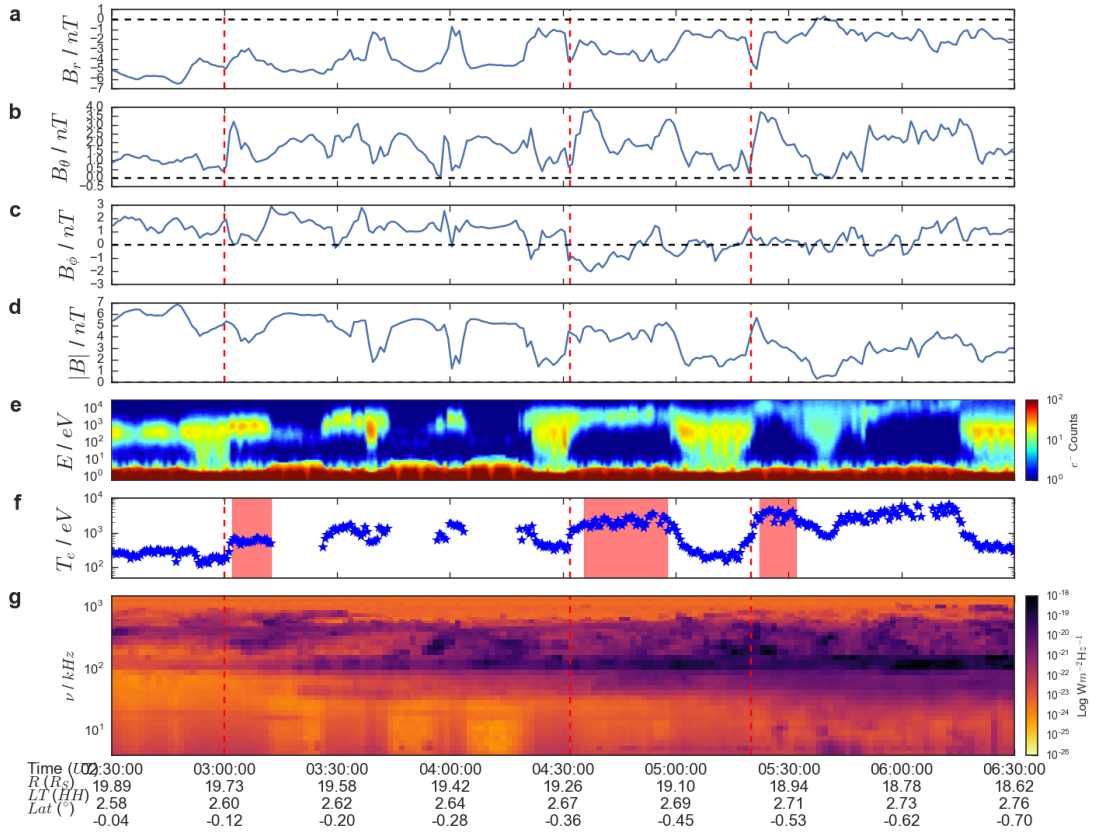

FIGURE 8.3: Cassini data from day 227 2006 between 02:30 and 06:30 UT. Panels (a) - (e) are presented as in Figure 8.1. Panel (f) shows the electron temperature: calculated using the methods described by *Lewis et al.* [2008] and *Arridge et al.* [2009b]. The red shading indicates the energetic/heated electron populations identified by *Smith et al.* [2018]. Panel (g) displays a frequency-time spectrogram of the radio emissions from the RPWS instrument.

(undisturbed) plasma sheet electron population is typically around 100 eV [*Arridge et al.*, 2009a]. The T_e change is shown in combination with the changing n_e in Figure 8.4a.

The ion counts within the CAPS/IMS energy range (i.e. $E \leq 26\,keV$) are very low for these events, and so the MIMI suite of instruments is required to determine the composition of the dipolarizing material. CHEMS observes the suprathermal plasma population ($E \geq\sim 10\,keV$), which could differ from the thermal population if species dependent heating or loss processes are significant. Figure 8.4b shows the composition of the three heated intervals identified in Figure 8.3f. The first two heated intervals ('03:02 - 03:12' and '04:35 - 04:57') show markedly similar compositions, with W^+ group fractions of over 40 % and very little He^{++}. However, for the last interval ('05:22 - 05:32') a strong fractional reduction in W^+ is observed, while H_2^+ and H^+ fractional abundances are seen to increase.

Figure 8.3g shows the RPWS data during the interval of interest, allowing us a more global perspective of auroral dynamics. Shortly after 03:00 UT the intensity of the main

band SKR emission increases (between approximately 100 and 400 kHz [*Kaiser and Desch*, 1984; *Lamy et al.*, 2008]). This intensification is observed in both left and right handed polarizations (not shown) indicating emission from both northern and southern hemispheres. The emission continues to intensify throughout the plotted interval and gradually extends to lower frequencies (i.e. towards $\sim 10 - 20\,kHz$ around 06:00 UT). This characteristic change in the SKR is known as a Low Frequency Extension (LFE). In the past LFEs have been linked with both tail reconnection [*Jackman et al.*, 2009b; *Lamy et al.*, 2013; *Reed et al.*, 2018] and increases in solar wind dynamic pressure [*Badman et al.*, 2008; *Lamy et al.*, 2010]. It should be noted that RPWS data is not included in Figure 8.1, as during that interval the radio intensity is much weaker.

8.4 Discussion

The case studies are now discussed with respect to their implications for magnetospheric dynamics.

8.4.1 Case Study 1: Pre-Midnight Multiple X-Lines

Given the location of the spacecraft (post-dusk) it is likely that the first example shows episodes of reconnection related to the Vasyliunas cycle (considering a flow regime comparable to Figure 2 of *Cowley et al.* [2004b]). As mass laden flux tubes rotate around the dusk flank they are no longer supported by the magnetopause and so can stretch down the magnetotail. As the flux tubes become stretched, the oppositely directed field lines either side of the magnetotail current sheet grow closer together, increasing the local gradient of the field, and eventually leading to reconnection. The presence of significant thermal water group ions (of internal origin) in this interval supports this inference: this is the reconnection of closed flux.

The durations of the identified flows (10 - 30 minutes) are less than the 30 minutes to several hours typically reported at Saturn [e.g. *Thomsen et al.*, 2013, 2015; *Arridge et al.*, 2015b]. These durations are much more in-line with the duration of the magnetic field signatures observed [e.g. *Jackman et al.*, 2014b; *Smith et al.*, 2016]. The short durations suggest (given the fast rotation of the Saturnian system) that either the x-lines are extremely limited in azimuth, or that they form and disperse on very short timescales. A duration of 10 minutes and a velocity of 345 kms^{-1} (the corotational plasma flow velocity at this radial distance [*McAndrews et al.*, 2009]), translates to a channel width of 3.4 R_S (or ~ 0.4 hours of local time). This value is likely to represent an upper limit; the typically observed (sub-) corotational velocities at this radial distance are around

$100 - 200\,kms^{-1}$ [*McAndrews et al.*, 2009; *Thomsen et al.*, 2013]. This is, therefore, a relatively small scale process compared to those previously observed. Small scale, patchy reconnection was suggested for the Jovian magnetosphere by *Bagenal* [2007], and more recently *Thomsen et al.* [2014a] and *Delamere et al.* [2015b] invoked a planetary wind, or 'reconnection drizzle' respectively on Saturn's dusk flank to explain their observations. The fact that the observed flows are not radial, and have a considerable corotational component, suggests that the reconnection products formed at earlier local times. It has been suggested, from observations of northward magnetic field excursions on the dayside, that reconnection can initiate pre-dusk in the dayside magnetosphere [*Delamere et al.*, 2015b].

8.4.2 Case Study 2: Post-Midnight Tailward Motion

The mechanisms that heat the plasma behind a dipolarization front are a combination of those local to the reconnection site itself [e.g. *Phan et al.*, 2014; *Fu et al.*, 2017] and the heating that occurs during the propagation of the front towards the planet, e.g. adiabatic Fermi and betatron acceleration [e.g. *Ashour-Abdalla et al.*, 2011; *Fu et al.*, 2011; *Birn et al.*, 2013, 2014; *Pan et al.*, 2014a] and non-adiabatic wave activity [e.g. *Grigorenko et al.*, 2016] (non-local processes). At the terrestrial magnetopause, *Phan et al.* [2014] derived an empirical relation between the electron heating at the reconnection site (ΔT_e) and the Alfvén speed and plasma density of the reconnection inflow. Transposing the empirical relationship to Saturn's magnetotail requires extrapolation beyond the parameter space explored at the terrestrial magnetopause (due to the lower field strengths and plasma densities) and so should perhaps be interpreted with caution. However, using the measured lobe field strengths and the heated electron density (as a proxy for the inflowing population) leads to the conclusion that the local electron heating would be fairly significant (of the order of several hundred eV) but unable to explain the majority of the observed temperature change. Nonetheless, the empirical relationship suggests that a reduction in the inflowing plasma density would result in increased electron heating [*Phan et al.*, 2014], though of an insufficient magnitude to fully explain the observations.

The majority of the electron heating can thus be attributed to further processing post-reconnection (i.e. non-local heating effects). Therefore, as the magnitude of the heating increases significantly with subsequent events it could be inferred that the material has travelled a greater distance and that the site of reconnection is (or distinct sites are) receding deeper into the tail. *Arridge et al.* [2015b] observed an interval during which Cassini passed through a tailward moving reconnection site, and therefore this is perhaps a common occurrence. X-lines that retreat tailward are often observed at the Earth

[e.g. *Eastwood et al.*, 2010; *Alexandrova et al.*, 2015] and also at Jupiter [*Kronberg et al.*, 2005; *Kasahara et al.*, 2011]. Therefore, the second example likely shows an interval during which a reconnection site, or a series of reconnection sites, can be inferred to move down the magnetotail, further from the spacecraft. Figure 8.4a shows that the subsequent events move up and to the left in density-temperature space: the increasing temperatures are accompanied by reducing densities.

It is also noteworthy that clear reconnection related activity is observed for a period of around three hours, almost a third of a planetary rotation. This suggests that the reconnection site/sites are either relatively stationary with respect to local time, or are very widely extended (covering ≥ 7 hours of local time).

The composition of the plasma can help determine whether the observed dipolarization is a result of the closure of open lobe field lines (and thus is Dungey cycle related), or purely involves closed field lines (and so is more likely part of the internally driven Vasyliunas cycle). It has been postulated that the closure of open field cannot occur until the equatorial, mass loaded closed field has been reconnected and depleted [e.g. *Thomsen et al.*, 2013].

For purely Vasyliunas cycle, closed field reconnection, it would be expected that the dipolarizing material would contain significant plasma of internal origin: including H^+, H_2^+ and heavier water group ions (W^+) such as O^+, OH^+, H_2O^+ and H_3O^+. If the reconnection has proceeded to involve the closure of lobe field lines, then species of solar wind origin (such as He^{++}) may be expected to be included. It should be noted that H^+ has both internal (e.g. Saturn's ionosphere and its moons) and external (i.e. the solar wind) sources, and is thus not a good discriminator.

As mentioned above, the first two intervals ('03:02 - 03:12' and '04:35 - 04:57') show similar (and predominantly internal) compositions, with over $40\,\%W^+$ group and little He^{++}. However, the suprathermal count rate measured is markedly different, increasing from $10.4\,min^{-1}$ to $56.7\,min^{-1}$ (not shown). This could be a result of the plasma in the second event having been subject to greater heating, increasing the proportion of ambient plasma accelerated into the energy range of CHEMS ($E \geq\sim 10\,keV$). The similar composition, and strong W^+, is suggestive of the reconnection of closed field, and therefore indicating they are likely Vasyliunas-cycle related.

The final interval shows a strong reduction in W^+ group fraction; to less than 10%. If this were indicative of open flux closure, then it may be expected that it would be replaced by H^+ and He^{++}. However, instead the fractions of H_2^+ and H^+ increase. Due to the strong presence of H_2^+, little if any lobe flux was closed during this event. Instead it is possible that this event was associated with the reconnection of slightly

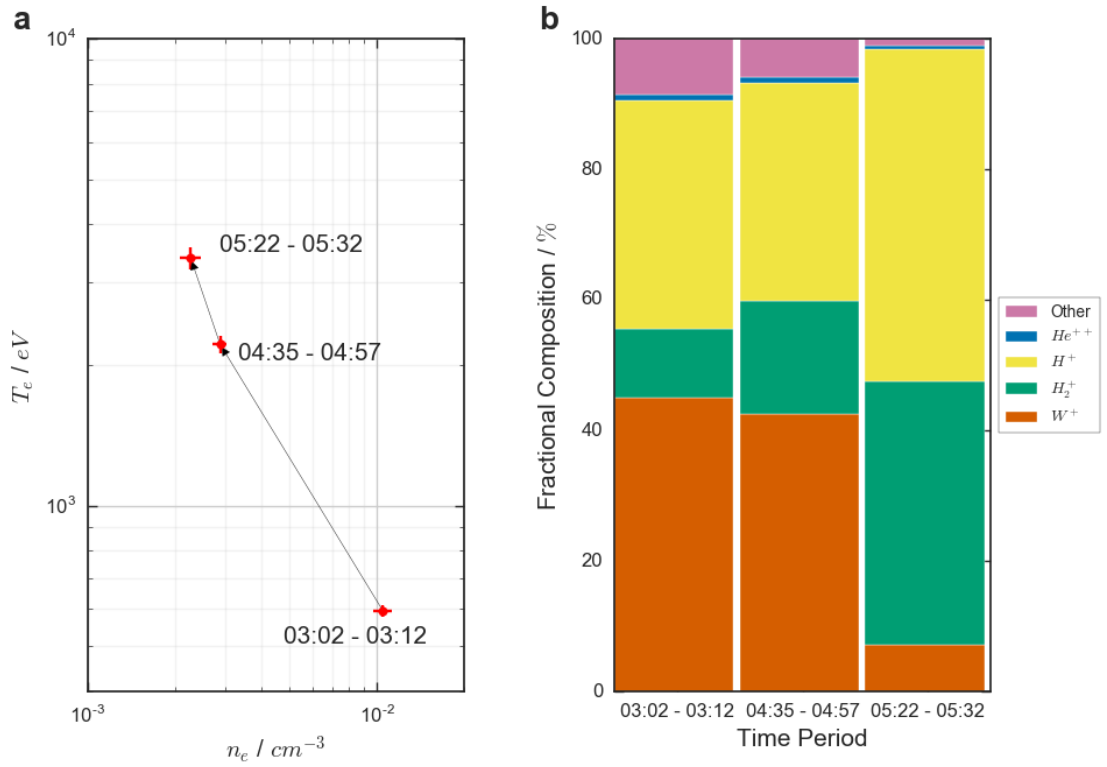

FIGURE 8.4: Cassini data summarizing the three dipolarizations in terms of a) electron temperature and density and b) suprathermal composition. Panel a displays the mean and standard error of the mean of the electron temperature and density moments [*Lewis et al.*, 2008; *Arridge et al.*, 2009b] within the heated regions (highlighted in Figure 8.3f). The suprathermal composition in panel b is derived from the CHEMS instrument, integrated over the same integrals as above.

higher latitude, more W^+ depleted field, and the release of a plasmoid. The plasmoid would act to preferentially remove the equatorial heavy W^+ group ions [*Badman and Cowley*, 2007; *Thomsen et al.*, 2013, 2014b]. Though the T_e of this event is the largest of the three events, the suprathermal count rate in this event reduces to $37.3\,min^{-1}$ (from $56.7\,min^{-1}$ in the previous dipolarizing interval). This could be explained by the reconnection occurring within a region of lower density, and thus less plasma was available to be boosted into the suprathermal regime. Overall, this interval could be the *in situ* signature of the progression of reconnection to higher latitude, W^+ depleted flux tubes.

The field aligned currents that stimulate the intensification of the SKR (and cause the LFE) are associated with the precipitation of $\sim 1-20\,keV$ electrons into Saturn's atmosphere, producing UV (Ultra-Violet) aurora [*Lamy et al.*, 2010; *Mutel et al.*, 2010; *Tao et al.*, 2014; *Gustin et al.*, 2017]. The link between magnetotail reconnection, LFEs and auroral forms at Saturn was first postulated by *Cowley et al.* [2005]. During SOI (Saturn Orbit Insertion), *Bunce et al.* [2005] observed the first event combining a magnetic field deflection, heated plasma (i.e. a dipolarization) and an LFE. Later, *Jackman et al.*

[2013] investigated several dipolarizations, their associated field aligned currents, and auroral imagery from an event inferred to be reconnection related. Unfortunately, no contemporaneous auroral imagery is available for the interval in the second case study; however given both the *in situ* and RPWS data it is likely that auroral emission would have been observed post-midnight [e.g. *Lamy et al.*, 2013]. *In situ*, the lack of species prevalent in the solar wind (e.g. He^{++}) would suggest that the associated auroral emission would likely not approach the poleward boundary of the main oval [c.f. *Nichols et al.* [2014]].

8.5 Conclusions

Two examples of Saturn's magnetotail x-lines forming and moving on short timescales have been presented. In the first example three reconnection related structures are observed, inferred to originate from at least two x-lines. The entire interval considered only spans around a third of a planetary rotation. The related thermal plasma flows only last for a small fraction of those previously reported [*Thomsen et al.*, 2013, 2015; *Arridge et al.*, 2015b]. This suggests that either the x-lines are extremely limited azimuthally ($\sim 3.4\,R_S$) or operate for very short intervals before dissipating, perhaps constituting "reconnection drizzle" as postulated by *Delamere et al.* [2015b]. The interval is inferred to form a part of the Vasyliunas cycle as fresh, mass laden flux tubes rotate around the dusk flank and reconnect. In particular, this event is in sharp contrast to that described by [*Thomsen et al.*, 2015], which represented a (rare) example of sustained lobe reconnection.

In the second example tailward motion of a magnetotail x-line, or series of x-lines, can be inferred. The composition of the suprathermal plasma ($\geq$ several keV) is not indicative of lobe reconnection during this interval, and is instead suggestive of the shedding of W^+ rich flux tubes that must precede reconnection of lobe flux. The interval is coincident with an intensification and lowering of the frequency of the SKR emission, likely related to the field aligned currents generated by the magnetotail reconnection.

Chapter 9

Evaluating Single Spacecraft Observations of Planetary Magnetotails with Simple Monte Carlo Simulations

9.1 Introduction

This chapter describes a pair of Monte Carlo based techniques designed to estimate the inherent selection effects of single spacecraft surveys in terms of: a) orbital sampling and b) placing criteria on the properties of the magnetic signature.

This Chapter is divided into two main sections. Section 9.2 aims to investigate the effects of orbital sampling on the results of statistical surveys. This work is motivated by a series of recent surveys that have made contrasting observations. The first observed an evenly distributed flux rope population across the magnetotail [*DiBraccio et al.*, 2015], while the second observed a population heavily biased towards the dawn flank [*Sun et al.*, 2016]. The surveys differed principally in their orbital coverage. Section 9.3 will then investigate the effects that placing selection criteria on the required magnetic field will impose on statistical surveys. This investigation is motivated by the observation that changing the magnetic field signature selection criteria appears to change the inferred rate of flux rope encounters in the Hermean magnetotail (Chapter 6) [*Smith et al.*, 2017b].

Section 9.2.1 describes the Monte Carlo model designed to evaluate orbital selection effects. Section 9.2.2 then considers the general results of the model, investigating the

effects of varying the model parameters and the choice of orbits sampling. Section 9.2.3 then compares the results of the model to those of the survey in Chapter 6 [*Smith et al.*, 2017b], allowing investigation of the intrinsic properties Mercury system (including of the neutral line location and extent).

Section 9.3.1 then discusses the Monte Carlo based technique designed to estimate selection effects. This will be followed in Section 9.3.2 by a discussion of the criterion employed by two recent surveys of MESSENGER spacecraft data in the Hermean magnetotail [*Sun et al.*, 2016; *Smith et al.*, 2017b]. The method will then be used to estimate the underlying distributions from which the results of Chapter 6 [*Smith et al.*, 2017b] were identified. Finally, the recurrence of Hermean magnetotail flux ropes will be discussed, using the technique to estimate the unseen or unidentified fractions of the population.

9.2 Orbital Selection

9.2.1 The Model

In this section the design and properties of the orbital sampling model will be discussed, along with some of the implicit assumptions of such a setup.

9.2.1.1 Model Set-up

The orbit of MESSENGER resulted in plasma sheet crossings that were separated by $\sim 8-12$ hours, much longer than the time-scale on which global Hermean magnetospheric dynamics operate. Additionally, during just under half of all MESSENGER plasma sheet crossings there were short periods during which the products of a (likely single) reconnection interval could be observed [*Smith et al.*, 2017b] (Chapter 6). Therefore, for the purposes of this work each plasma sheet crossing is treated as independent (from adjacent crossings), and it is assumed that (at most) one instance of tail reconnection may occur. If this model were adapted for comparison with other surveys/environments then the validity of these assumptions would need to be re-evaluated.

The Cartesian Mercury Solar Magnetospheric (MSM) coordinate system is used in this study. In this system, the $\hat{X}_{MSM}$ axis points towards the Sun, the $\hat{Z}_{MSM}$ axis is aligned with the magnetic dipole and directed northward, and the $\hat{Y}_{MSM}$ axis completes the right handed set (pointing duskward). The model forms a two dimensional plane (the equivalent of the $X_{MSM}-Y_{MSM}$ plane), approximating the plasma sheet on the nightside

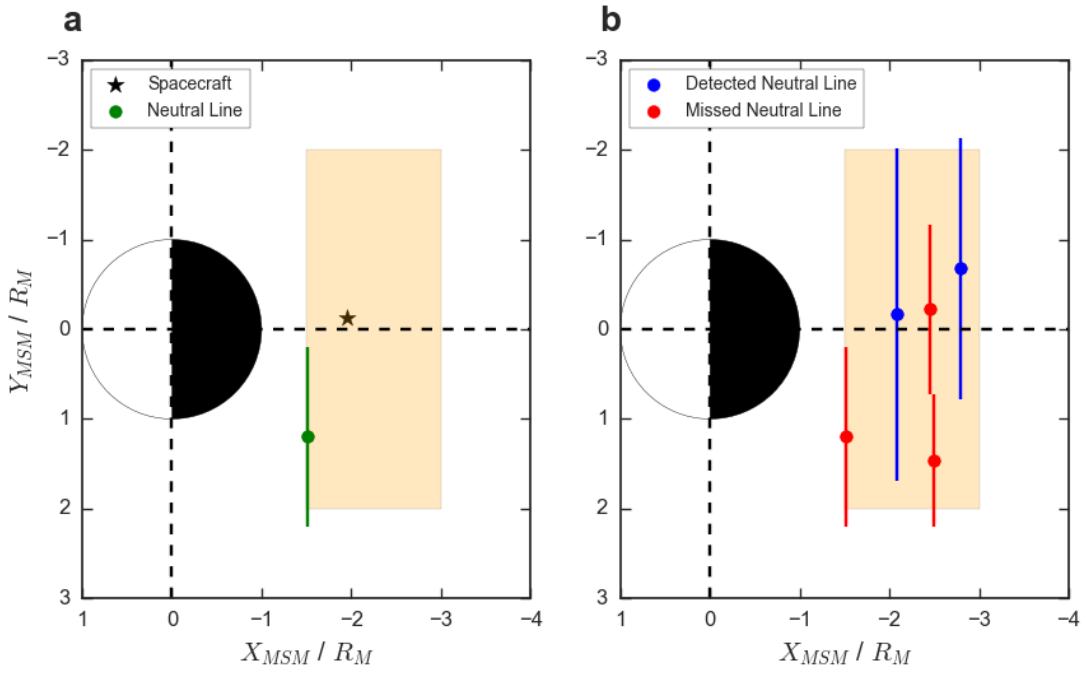

FIGURE 9.1: Schematic describing the model set-up. Panel (a) shows an example orbit, with a randomly generated spacecraft location (black star) and neutral line (in green). The orange shaded region shows the limit of the uniform distributions used to generate the orbits and neutral line centres. Panel (b) shows the results of 10 orbits where the reconnection probability has been set to 50%. The blue neutral lines show those that were spatially coincident with the generated spacecraft locations during that orbit, while the red neutral lines show those that were missed by their respective spacecraft.

of the planet. The model is set up to simulate a given number of orbits, and for each orbit the following are generated:

1. Spacecraft Location (X_{MSM} and Y_{MSM})
2. Plasma Sheet Dwell Time

where the location will initially be drawn from a uniform distribution, while the dwell time will be drawn from a database of current sheet crossings identified in the MESSENGER data [*Poh et al.*, 2017a]. This initial set-up simulates a spacecraft dataset with completely even coverage (i.e. with no orbital bias), which may represent the ideal scenario for a large statistical survey. During a fraction of orbits (an adjustable parameter) reconnection is deemed to have occurred. Initially the probability is set to 50% of orbital passes, and for each of these a neutral line is generated. The effects of changing this probability will be explored further in Sections 9.2.2. In reality, the probability of observing a flux rope during a crossing of the Hermean plasma sheet has been found to scale with the magnitude of the preceding lobe magnetic field strength [*Smith et al.*, 2017b] (Chapter 6). The generated neutral line has the following properties:

- Neutral Line Center (X_{MSM} and Y_{MSM})
- Neutral Line Width (W_{NL})

This set-up is illustrated in Figure 9.1a. The orange shaded area shows the region within which the spacecraft and neutral line could be generated, roughly representing MESSENGER's coverage of Mercury's magnetotail. An example generated spacecraft location (black star) and neutral line (green point and line) are shown in Figure 9.1a.

As a first approximation, the neutral line is considered to generate a single flux rope moving planetward and a single flux rope moving tailward, with azimuthal widths provided by the extent of the neutral line. If the neutral line and spacecraft are spatially coincident (along the Y_{MSM} axis) then the neutral line is considered to be 'detected'. Selection effects, i.e. those that would cause the flux rope to not be identified even when encountering the spacecraft, are considered in Section 9.3.

The model allows a map to be constructed where flux ropes (and associated neutral lines) are detected and where they are missed, purely as a result of the spacecraft coverage. Figure 9.1b shows the results of 10 orbits. Five neutral lines have been generated (i.e. 50% of the orbits are associated with reconnection). The red neutral lines show those that were not spatially coincident with their respective spacecraft and so were missed, while the blue neutral lines show those that generated flux ropes that passed over the randomly placed spacecraft. In accordance with expectation, though with a small sample size, it can be seen in Figure 9.1b that the wider neutral lines were detected, while the smaller ones were missed by the random sampling. This effect will be further explored in Sections 9.2.2.

It should be noted that no boundary effects are considered (e.g. the dawn or dusk magnetopause). Instead, the boundaries are implicitly provided by the limits of the spacecraft orbit and neutral line centres simulated. This does mean that some portion of the neutral line width may be outside of the region within which the spacecraft could observe it. Therefore, if the centre of the neutral line is placed at the edge of the spacecraft's orbital region then the effective length of the neutral line could be up to a factor of two shorter than that explicitly generated.

9.2.2 Recovery of the Intrinsic Distribution

To begin, the distributions that are recovered by (or inferred from) the virtual spacecraft will be compared to those that would be obtained with complete magnetotail coverage (i.e. the true or intrinsic distribution). This provides a measure of the effectiveness of

TABLE 9.1: The initial distributions from which the model parameters were drawn

Parameter	Distribution	Minimum	Maximum
X_{MSM}^{SC}	Uniform	$-3\,R_M$	$-1.5\,R_M$
Y_{MSM}^{SC}	Uniform	$-2\,R_M$	$2\,R_M$
X_{MSM}^{NMNL}	Uniform	$-3\,R_M$	$-1.5\,R_M$
Y_{MSM}^{NMNL}	Uniform	$-2\,R_M$	$2\,R_M$
W_{NL}	Uniform	$2\,R_M$	$2.5\,R_M$

the spacecraft sampling, and can be evaluated as a function of the number of orbits, orbital selection or properties of the dynamic structures of interest (e.g. recurrence or extent).

9.2.2.1 Increasing the Number of Orbits

In this section, the model results will be discussed while drawing the spacecraft position (X_{MSM}^{SC}, Y_{MSM}^{SC}), neutral line centre (X_{MSM}^{NMNL}, Y_{MSM}^{NMNL}) and neutral line width (W_{NL}) from uniform distributions, the details of which are provided in Table 9.1. The reconnection probability is initially set to 0.5. It should be noted that these correspond to initial test parameters, selected to demonstrate the effects of increasing the random sampling. The parameters will be further investigated in Section 9.2.2.2.

As orbits are added it is possible to build dawn-dusk maps of the distribution of flux ropes observed. Figure 9.2 explores how the addition of orbits affects the comparison between the inferred and 'true' distributions (i.e. the distribution that would be obtained if the entire tail were monitored by spacecraft). Figures 9.2a and 9.2b show the results after 100 and 500 randomly distributed orbits respectively. The top panels show the number of flux ropes observed by the spacecraft, the middle shows the spacecraft cumulative dwell time, while the bottom shows the inferred rate in blue. The red bars in the lower panels represent the distribution observed if the entire tail were monitored, i.e. the 'true' distribution. It is possible to compare the recovered and 'true' distributions using a χ^2 metric; the values of which are shown above Figures 9.2a and 9.2b. The lower the value of this measure, the closer the observed rate matches the value that would be recovered with complete magnetotail coverage.

Between 100 and 500 orbits the intrinsic/true distributions (red) do not change significantly: the underlying distribution is fairly settled. However, after 100 orbits have been completed the randomly located spacecraft has not adequately sampled the tail, and so the χ^2 is high: the observed distribution poorly represents the underlying distribution. In contrast, once 500 orbits have been performed the system has been much better sampled, and the χ^2 has dropped by a factor of ~ 8.

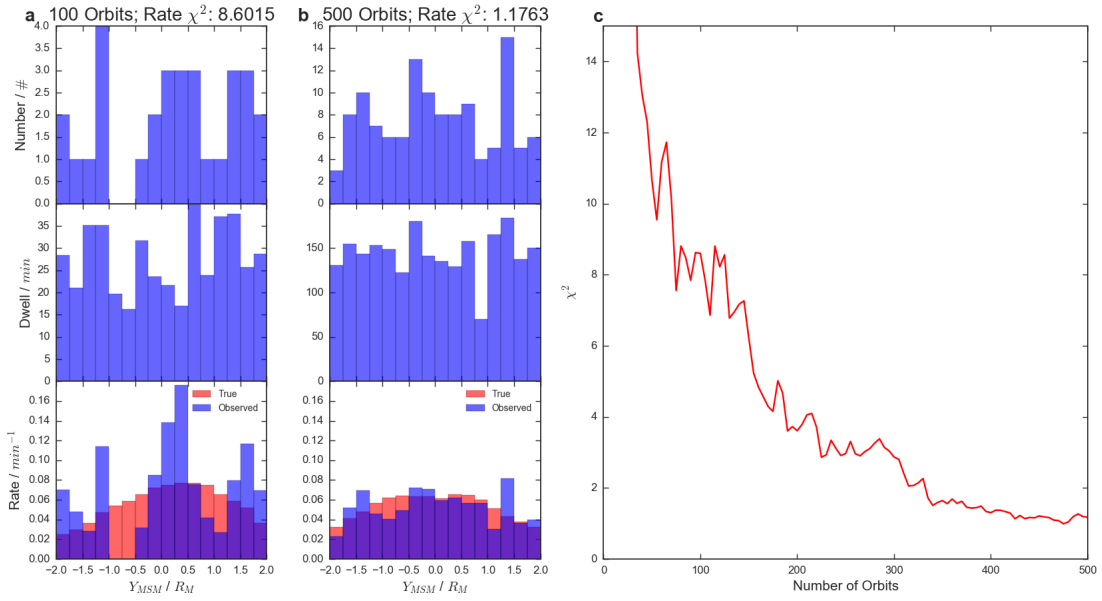

FIGURE 9.2: Figure showing how the observed/inferred rate of flux ropes measured across the model magnetotail compare to the 'true' distribution after 100 orbits (a), 500 orbits (b) and as a function of orbits (c). For the left and centre panels the top row shows the number of flux ropes observed per bin, the middle shows the cumulative spacecraft dwell time and the bottom shows the inferred rate (blue) and 'true' rate (red) given complete spacecraft coverage. The model parameters are provided in Table 9.1.

Figure 9.2c shows how the χ^2 (between the true and inferred distributions) varies as a function of the number of orbital passes. Overall, the χ^2 can be seen to drop rapidly with the addition of more orbits. Eventually this effect is saturated and the χ^2 plateaus after $\sim 300-350$ orbits. There are some exceptions to this behaviour, with small jumps observed, perhaps when a region is temporarily over sampled and the stochastic nature of the modelled reconnection boosts the rate in a region to an unrepresentative value.

Figure 9.3a shows the median variation in χ^2 as a function of orbits (for 1000 sets of orbital passes, or iterations, which has the effect of removing the random fluctuations). It can be seen that the value of the median χ^2 drops steadily until around $\sim 250-300$ orbits at which point diminishing returns begin to apply and the addition of more orbits does not significantly reduce the χ^2. Therefore it could be said that, for the parameters selected, at least 200-300 orbits should be considered before commenting conclusively on the measured cross-tail distribution. Figure 9.3b shows the median number of flux ropes observed as a function of the number of orbits, allowing the inference that the ~ 250 orbit limit equates to a sample size of ~ 60 flux ropes.

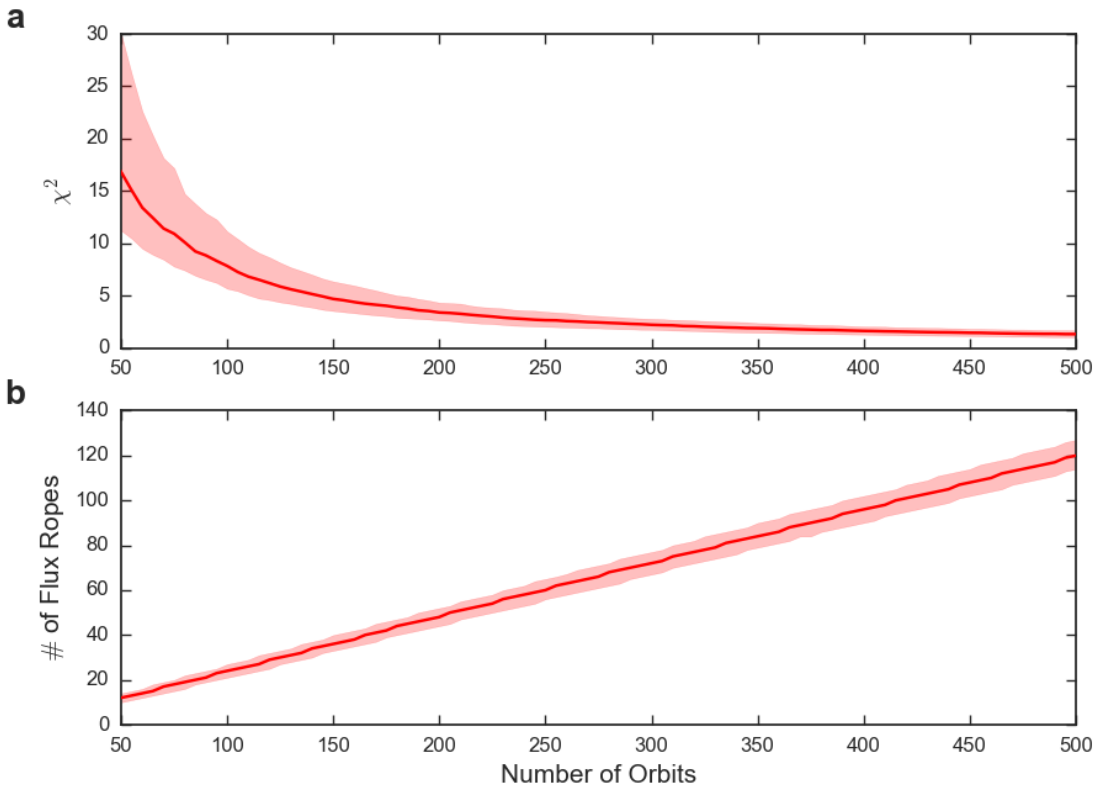

FIGURE 9.3: Figure showing the median χ^2 between the inferred and 'true' cross-tail distributions (a) and median number of flux ropes observed (b) as a function of the number of orbits performed (after 1000 iterations of the model). The limits of the red shaded region represent the interquartile range. The model parameters are provided in Table 9.1.

9.2.2.2 Varying System Parameters

The effects of varying several model parameters will now be explored. For example, one of the key model parameters is the width of the neutral line. Figures 9.2 and 9.3 were created with a uniform distribution of neutral line widths between 2 and 2.5 R_M (Table 9.1). Figure 9.4a shows how the median χ^2 varies for a range of neutral line widths (with the probability of reconnection fixed at 0.5). It should be noted that the χ^2 metric cannot be evaluated if the 'true' value for a bin is zero; therefore the averages in Figures 9.4a and 9.4c only begin at the point at which every cross-tail bin (in every iteration) had observed at least a single flux rope. For narrow neutral lines (e.g. those 10% of the model magnetotail: 0.4 R_M, in red) the χ^2 is both higher and drops slower than for the wider neutral lines. This is likely a result of the fact that smaller reconnection products will be observed less often by the spacecraft, and thus the observed distribution is always less representative of the full distribution. This can be seen in Figure 9.4b, where the number of flux ropes observed for those spanning 10% of the tail only reaches ~ 20 after 500 orbits. This is approximately the number that may be expected by simply taking the number of orbits and then multiplying through by the probability of reconnection

and the fractional extent of the neutral lines ($N \sim 500 \times 0.5 \times 0.1 = 25$). It should be noted that the effective sampling can be improved by increasing the width of the bins considered (i.e. the bin width could be said to be inappropriately narrow in Figure 9.2a).

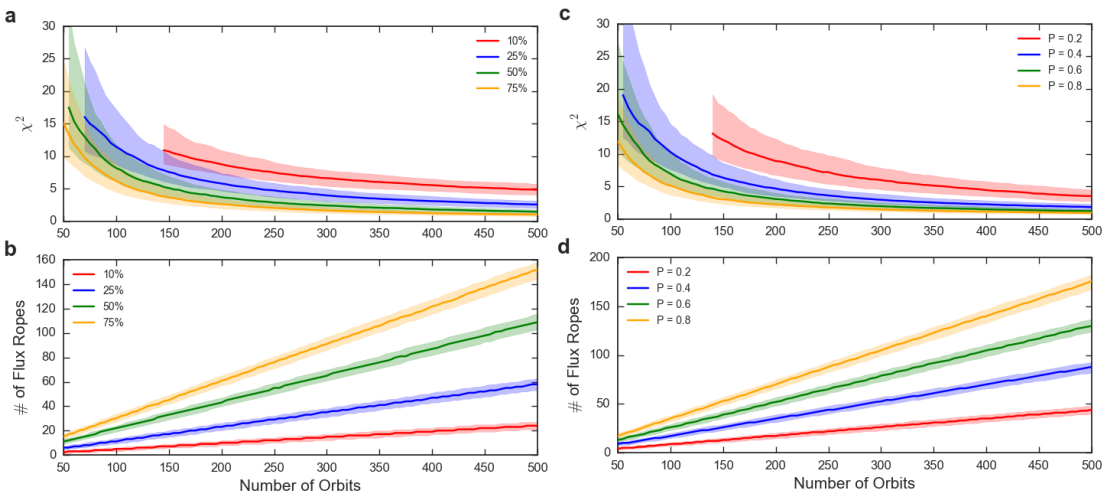

FIGURE 9.4: The median χ^2 of 1000 iterations of the Monte Carlo (top) and the median number of flux ropes observed (bottom) for four different widths of neutral line (a and b) as a percentage of the width of the tail ($4\,R_M$), and four different reconnection probabilities (c and d). The limits of the shaded regions represent the interquartile range. For the panels in which the width is varied (a and b) the probability is fixed at 0.5, while for the panels in which the probability is varied (c and d) the width is fixed at 50% of the tail width (i.e. $2\,R_M$). The remaining model parameters are as shown in Table 9.1.

Another interesting parameter to test is the probability of reconnection occurring during an orbital pass. Figure 9.4c shows how the median χ^2 varies for four selected probabilities (with the width fixed at 50% of the model tail width: $2\,R_M$). For a low probability (0.2, in red) the measured χ^2 is relatively high, once more linked to the low number of flux rope encounters (Figure 9.4d). In contrast, if the probability is high (e.g. 0.8, in yellow) then very few orbits are needed to adequately describe the tail, potentially as few as ~ 150 orbits.

More generally, this technique allows the quantification of the common sense results: if the dynamic structures of interest are more azimuthally confined or less likely to be produced, then more orbits are required to constrain their distribution. Another interesting result that may be inferred from Figure 9.4 is that the χ^2 distributions do not correspond or scale linearly with the number of flux ropes observed, i.e. there is not a pre-determined number of flux ropes that is required to accurately assess the distribution (independent of the physical parameters of the structures). Additionally, the orbits during which no dynamic products are observed need to be accounted for when the spatial distributions are considered.

9.2.2.3 Orbit Selection

Sections 9.2.2.1 and 9.2.2.2 drew the spacecraft locations from uniform distributions (Table 9.1). However, uniform spacecraft coverage is often not possible for large surveys; therefore the effects of uneven coverage will now be explored. In the survey of the Hermean tail described by Chapter 6 [*Smith et al.*, 2017b] a catalogue of 319 plasma sheet crossings was used (first identified by *Poh et al.* [2017a]).

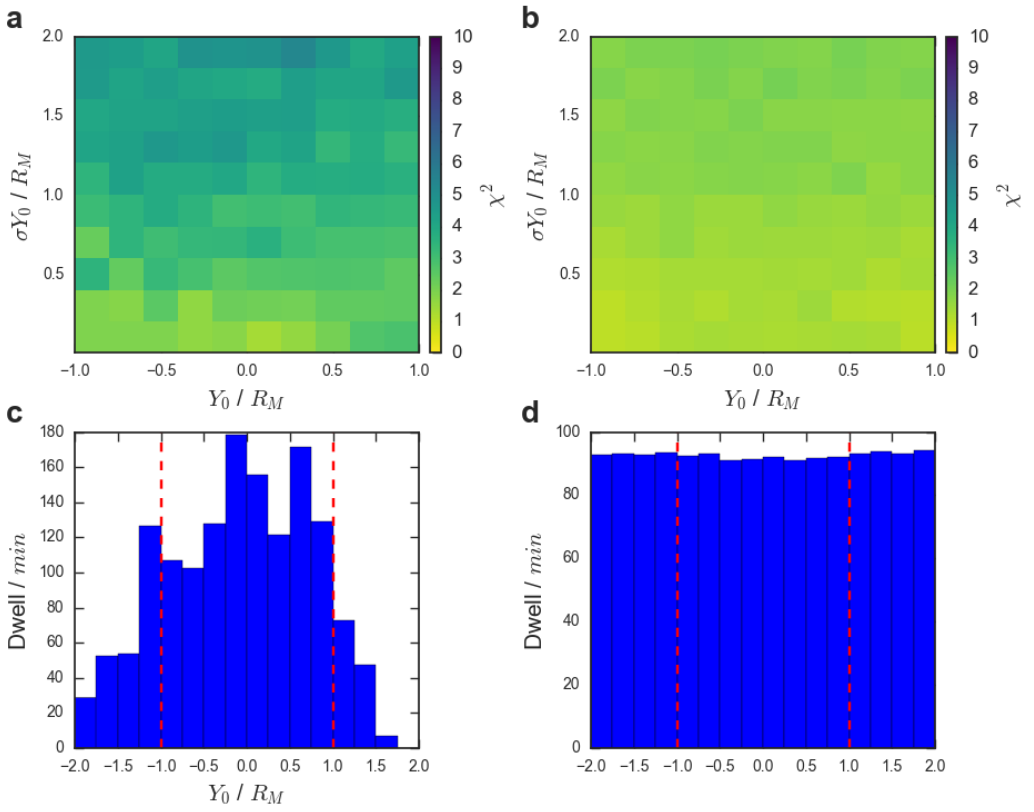

FIGURE 9.5: (Top) The mean χ^2 obtained between the intrinsic (true) and inferred spatial distributions after 319 orbits where the centre of the neutral line is drawn from normal distributions described by Y_0 and σY_0. The means are calculated from a sample of 10,000 iterations. The results are shown for MESSENGER's orbits as selected by *Poh et al.* [2017a] (a) and for randomly (and uniformly) distributed orbits (b). (Bottom) The cumulative dwell time within each spatial bin across the magnetotail for the orbits selected by *Poh et al.* [2017a] (c) and the mean dwell time per spatial bin for the uniformly distributed orbits (d). The red vertical dashed lines present in the lower panels represent the total width of the region plotted in the upper panels.

The effects of uneven spacecraft coverage will depend on the relative locations of both the spacecraft and the structures of interest. Therefore, for this investigation the uniform flux rope distributions are exchanged for normal distributions with a centre and width defined by Y_0 and σY_0. The reconnection probability is set to 0.5, while the neutral line width remains between 2 and 2.5 R_M (as above). Figure 9.5 compares the effectiveness

of the orbit selection used by Chapter 6 [*Smith et al.*, 2017b] (Figure 9.5a) with the same number of orbits (319) uniformly distributed over the magnetotail (Figure 9.5b). The quality with which the true distribution is recovered is quantified with a χ^2 metric (as above); this has been repeated 10,000 times for randomly selected combinations of Y_0 and σY_0. The results of the 10,000 iterations have then been averaged, and the mean per bin is presented in Figures 9.5a and 9.5b. The lower panels show the spatial sampling used by the *Smith et al.* [2017b] (Chapter 6) survey (9.5c) and the mean of the uniformly distributed orbits (9.5d).

The 319 uniformly distributed orbits can be seen to well capture the underlying distribution (Figure 9.5b), with low (≤ 2) values of the χ^2 obtained for both narrow (low σY_0) and wide distributions (high σY_0) when the centres are located anywhere across the centre of the magnetotail ($-1\,R_M \leq Y_0 \leq 1\,R_M$). In contrast, the orbits used by Chapter 6 [*Smith et al.*, 2017b] can be seen to give poorer comparisons for most of the simulated distributions (Figure 9.5a). The reduced spacecraft coverage beyond $Y_{MSM} = \pm 1\,R_M$ (Figure 9.5c) in particular results in more poorly recovered distributions at larger values of σY_0 and towards $Y_0 \sim 1\,R_M$.

However, even if the inferred distributions may not well represent the underlying distributions it does not necessary follow that it is impossible to uniquely identify the intrinsic distribution. It is possible that use of the Monte Carlo method would still result in the inference of the correct underlying distribution. In the future, this technique could be used to evaluate the effectiveness of a given spacecraft's orbital coverage for observing statistical distributions of various transient features.

9.2.3 Spatial Distributions at Mercury

The model can be used to compare a given set of observations with various intrinsic distributions (each generated by unique set of system parameters). For this study the results of Chapter 6 [*Smith et al.*, 2017b] will be used for comparison. In order to make the comparisons valid either the model or the results of the survey require adjustment; for example clusters of up to 8 flux ropes were observed during a single plasma sheet crossing (a feature not present in the model). A mechanism could be added to the model to allow the generation of multiple flux ropes, however to keep the number of free parameters low (and minimize possible degeneracies) the results of Chapter 6 [*Smith et al.*, 2017b] have instead been reprocessed. This has been performed such that multiple detections within the same plasma sheet crossing are only counted as a single detection. For intervals when the orientation of flux ropes changed during a crossing, then the orientation is taken as that which dominated the interval.

Firstly, the dawn-dusk distribution of flux ropes will be considered. This will allow some of the physical parameters of the Mercury system to be estimated, e.g. probability of reconnection and neutral line width. Once these parameters have been estimated, the model may be set-up to provide an overall rate of flux rope detections that is consistent with observations. This will then allow the location of the Near Mercury Neutral Line (NMNL) to be explored by further investigation of the relative rates of planetward and tailward moving structures.

9.2.3.1 Dawn-Dusk Distribution

Firstly, the uniformly distributed spacecraft locations are replaced with those orbits performed by MESSENGER during the original survey [Chapter 6: *Smith et al.*, 2017b]. Secondly, the uniform distributions from which the neutral line locations were drawn (in Sections 9.2.2.1 and 9.2.2.2) are exchanged for normal distributions. This allows parametrization in terms of a distribution centre (Y_0) and a distribution width (σY_0), as in Section 9.2.2.3. The final variables employed are the probability of reconnection during an orbital pass (P) and the width of the neutral lines (W_{NL}). The model can then be run, for the MESSENGER orbits, for millions of iterations with random combinations of the four parameters (Y_0, σY_0, P and W_{NL}). Each iteration (consisting of the 319 orbits performed by MESSENGER) can be compared to the observed cross-tail distribution from the survey [Chapter 6: *Smith et al.*, 2017b], and a χ^2 metric derived for each combination of parameters.

Over three million parameter combinations have been tested. However, as the model is stochastic there can be fairly considerable variations in the χ^2 obtained between very similar combinations of parameters. Such variability can be inferred from the interquartile ranges displayed in Figures 9.3 and 9.4. To remove this variability, which may obscure the general trends, the results are smoothed in four dimensional parameter space using a histogram binning method. The choice of four dimensional bin size does affect the final results, though this is likely a result of the density of the four dimensional sampling: if more combinations of parameters are simulated (and therefore the density of four dimensional sampling increased) then the bin size can be reduced while the final result retains the same trends. In this case, the bin sizes were reduced as much as possible (thereby increasing the resolution) while retaining the smoothness of the underlying trends.

The resulting four dimensional parameter space was then sampled using an affine-invariant Markov chain Monte Carlo (MCMC) ensemble sampler [*Foreman-Mackey et al.*, 2012], in order to estimate the Bayesian posterior probability density functions (PPDF):

the probability distribution of the variables given the evidence presented by the sampling. Figure 9.6 shows the results of the MCMC sampling. The six panels in the lower left (b, d, e, g, h and i) represent the one, two and three sigma contours projected onto all possible combinations of two parameters. The panels along the uppermost diagonal (a, c, f and j) represent the PPDF functions marginalized for each of the four parameters considered. The blue dots/lines represent the medians of the marginalized PPDFs. It should be noted that the medians may not be co-located with visible peaks if the full distributions are not present within the simulation limits, therefore it is perhaps more constructive to draw conclusions from the peaks and shapes of the marginalized distributions (if they extend beyond the simulated parameter space).

Firstly, the distribution in Figure 9.6a shows that the results of the survey are most consistent with neutral line distribution marginally offset dawnward of midnight ($Y_0 = -0.37^{+1.21}_{-1.02}\,R_M$), though the midnight meridian is within 1σ. The observations are also most consistent with a relatively broad neutral line distribution (Figure 9.6c), indicating a substantial amount of variability between orbital passes. The sampling provided by the selected MESSENGER orbits (Figure 9.5c) has been shown to poorly recover broad distributions: this likely results in the lack of an 'edge' to the distributions on the broad side (with large σY_0).

Secondly, the median width of the neutral line is found to be $2.16^{+0.96}_{-0.98}\,R_M$, just over half the width of the model magnetotail (Figure 9.6f). However, this should be regarded as an upper limit as there is no consideration of the magnetopause boundary, and so the effective width of the neutral line will be between 1.08 and $2.16\,R_M$ (depending on the location of the neutral line centre). It is also clear from the shape of the W_{NL} distribution in Figure 9.6f that larger neutral lines (i.e. to the right of the peak of the distribution) are more consistent with the survey results, rather than those $\lesssim 1.6\,R_M$. Finally from the marginalized distributions, the median probability of a neutral line forming during a plasma sheet crossing is found to be $0.52^{+0.22}_{-0.19}$. This result is intuitive: Chapter 6 [*Smith et al.*, 2017b] found that during 39 % of crossings flux ropes were observed. Accounting for occasions where the spacecraft was not co-located with the neutral line will result in a fraction greater than 39%.

Figure 9.6 also shows the covariances between the parameters. For example, from Figure 9.6d, if the width of the neutral line is larger, then the distribution centre (Y_0) is required to be offset further towards dawn. This is shown by the diagonal slope formed by the probability contours, from upper left to middle bottom. This is necessary to explain the relative lack of observations duskward of $\sim 1\,R_M$ [Chapter 6: *Smith et al.*, 2017b]. If the neutral lines are wider, then a more central distribution would result in the observation of significant numbers of flux ropes close to dusk. The same relationship can be seen

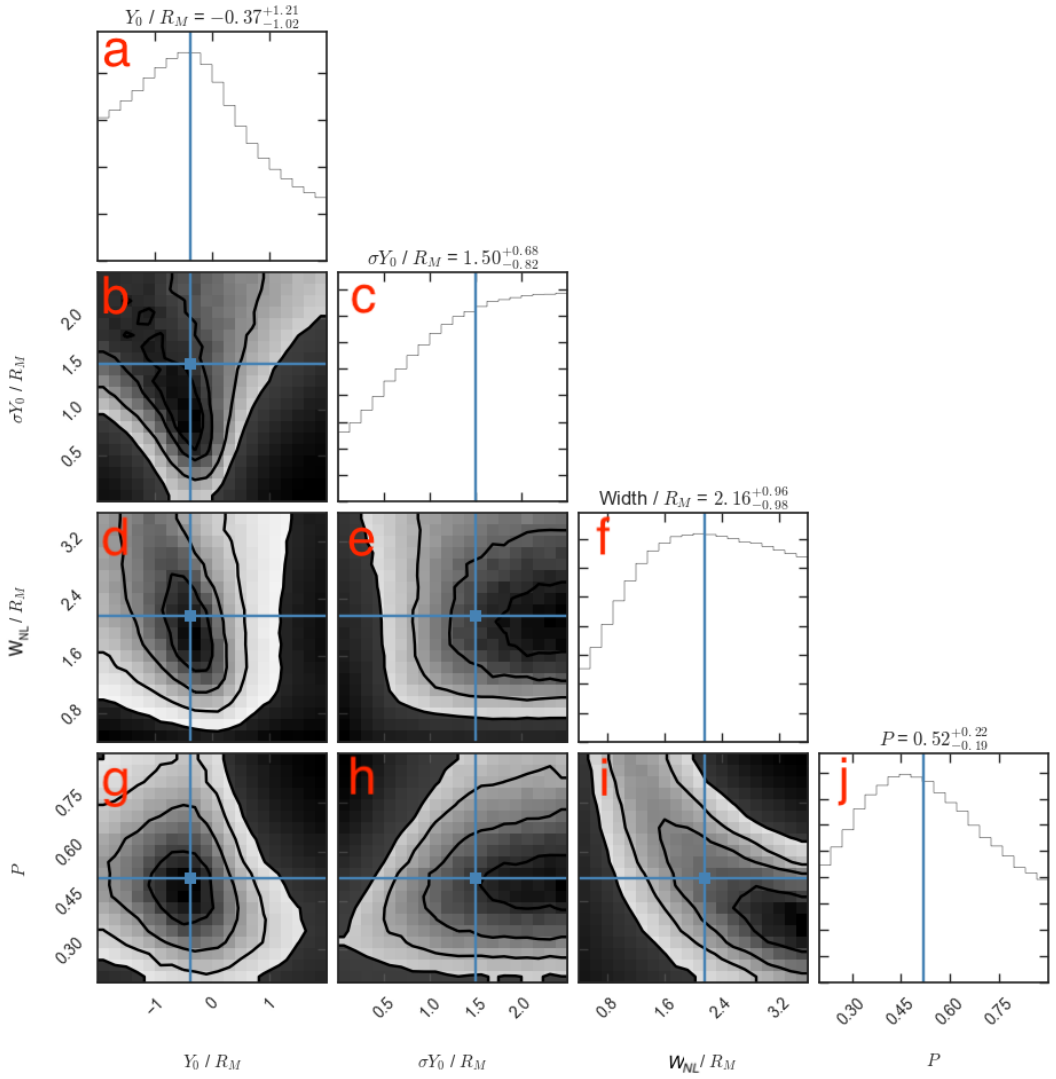

FIGURE 9.6: The posterior probability distributions of the model parameters: Y_0, σY_0, W_{NL} and P. The uppermost diagonal elements (a, c, f, j) show the marginalized posterior probability distribution for each parameter in turn while the lower left panels (b, d, e, g, h and i) show two dimensional projections for all combinations of parameters. The solid lines in the lower left show the one, two and three sigma contours. The blue lines, points and values above the diagonal panels indicate the medians of each distribution. The confidence limits provided for the median values are 1σ.

in the σY_0 vs. Y_0 panel (Figure 9.6b), where the contours slope from upper left to lower middle. Physically this can be interpreted as a broader distribution requiring that the centre be offset further towards dawn. Finally, a classically expected degeneracy is quantified by the panel showing the projection onto width (W_{NL}) vs. probability (P) space (Figure 9.6i): if there is a greater probability of reconnection occurring, then the neutral lines are required to be narrower and vice-versa.

9.2.3.2 Downtail Neutral Line Location

The previous section allowed the basic parameters of the model to be estimated, i.e. those which provide a rate of flux rope observations that best match the survey results. The downtail location of the neutral line can now be investigated by using the derived parameters and comparing the relative rates of the tailward and planetward moving distributions. For this, the x-line location is parametrized in terms of a distribution centre (X_0) and a width (σX_0) (which physically corresponds to variation between individual orbits).

Over a million iterations were performed with random selected combinations of X_0 and σX_0. The planetward and tailward distributions were each compared to the respective results from the survey in Chapter 6 [*Smith et al.*, 2017b], and two χ^2 metrics evaluated (for the planetward and tailward distributions separately). As with Section 9.2.3.1, the results were smoothed using a histogram and the parameter space sampled using an affine-invariant Markov chain Monte Carlo sampler [*Foreman-Mackey et al.*, 2012]. The results are displayed in Figures 9.7a and 9.7b for the tailward and planetward moving distributions respectively. The formats are similar to Figure 9.6.

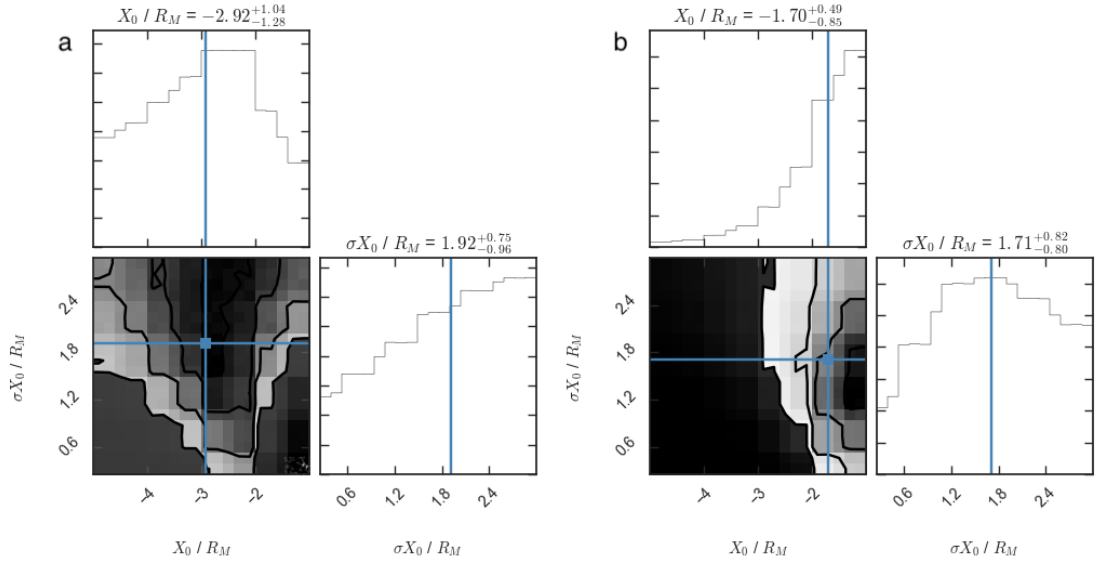

FIGURE 9.7: The posterior probability distributions for the tailward (a) and planetward (b) distributions of flux ropes. The formats are similar to Figure 9.6.

The results for the tailward distribution (Figure 9.7a) give a median neutral line location of $X_0 = -2.92^{+1.04}_{-1.28}$, and favour a relatively broad distribution (in σX_0). This result is consistent with a previous statistical study: *Poh et al.* [2017a] inferred the location to be on average at $\sim -3\,R_M$ (using an independent method).

However, the results for the comparison of the planetward moving distribution (Figure 9.7b) are not consistent with that found for the tailward population, with a median neutral line location of $-1.70^{+0.49}_{-0.85}$ appearing most consistent. The x-line location inferred from the tailward moving population ($X_0 \sim -3\,R_M$) would result in too high a rate of planetward moving flux ropes, much greater than is observed. Therefore the x-line is inferred to be closer to the planet. It is also clear that simply increasing the variability in the location of the x-line (i.e. increasing σX_0, moving up in Figure 9.7b) is insufficient to account for this effect. In other words, the contours in Figure 9.7b do not allow the x-line to move deeper into the tail (left) if the variability in location is greater (σX_0 increases). The lack of self-consistency in the neutral line location suggests that there is some physics of the underlying system not captured by the simple parametrization.

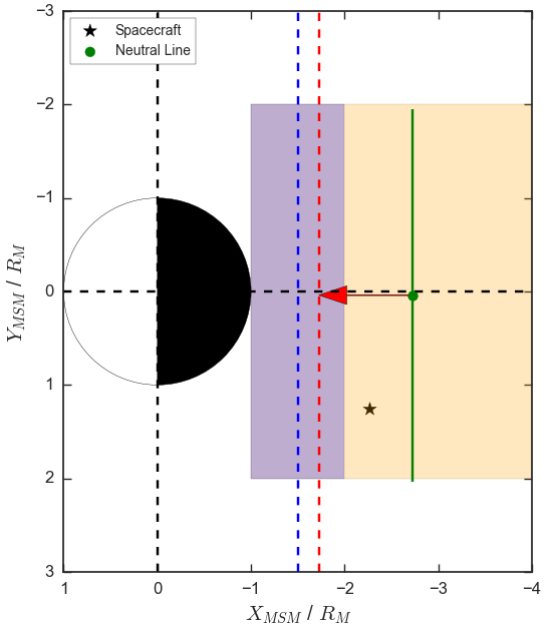

FIGURE 9.8: Schematic describing the two dimensional model set-up, adapted from that in Figure 9.1. The additions are shown by a maximum travel distance, indicated with the red arrow and vertical dashed line, and a distance of closest approach indicated with a blue shaded region and vertical dashed line.

To investigate this, additional parameters are added to the model. The first consideration is that there is perhaps some maximum distance that the flux rope can travel from the x-line, at which point it becomes unrecognisable as a flux rope, parametrized as a distance A. Physically this could correspond to the flux rope becoming distorted, such that it is not well approximated by the force free model, or perhaps forming a dipolarization front [e.g. *Lu et al.*, 2015]. This travel distance is represented by the red arrow and dashed line in Figure 9.8. Therefore, in order to observe the flux rope, the spacecraft would have to be located tailward of the red dashed line. The second mechanism added to the model is a distance of closest approach to the planet by the flux

rope, parametrized with X_{Min} and some variation in this value (σX_{Min}). Physically this could represent the distance at which the flux rope halts its planetward motion, re-reconnecting with the planetary field [*Slavin et al.*, 2003a]. This region is represented by the blue dashed line (X_{Min}) and shaded region (σX_{Min}) in Figure 9.8. As with the maximum travel distance (A), the spacecraft must be located tailward of the distance of closest approach in order to observe a flux rope.

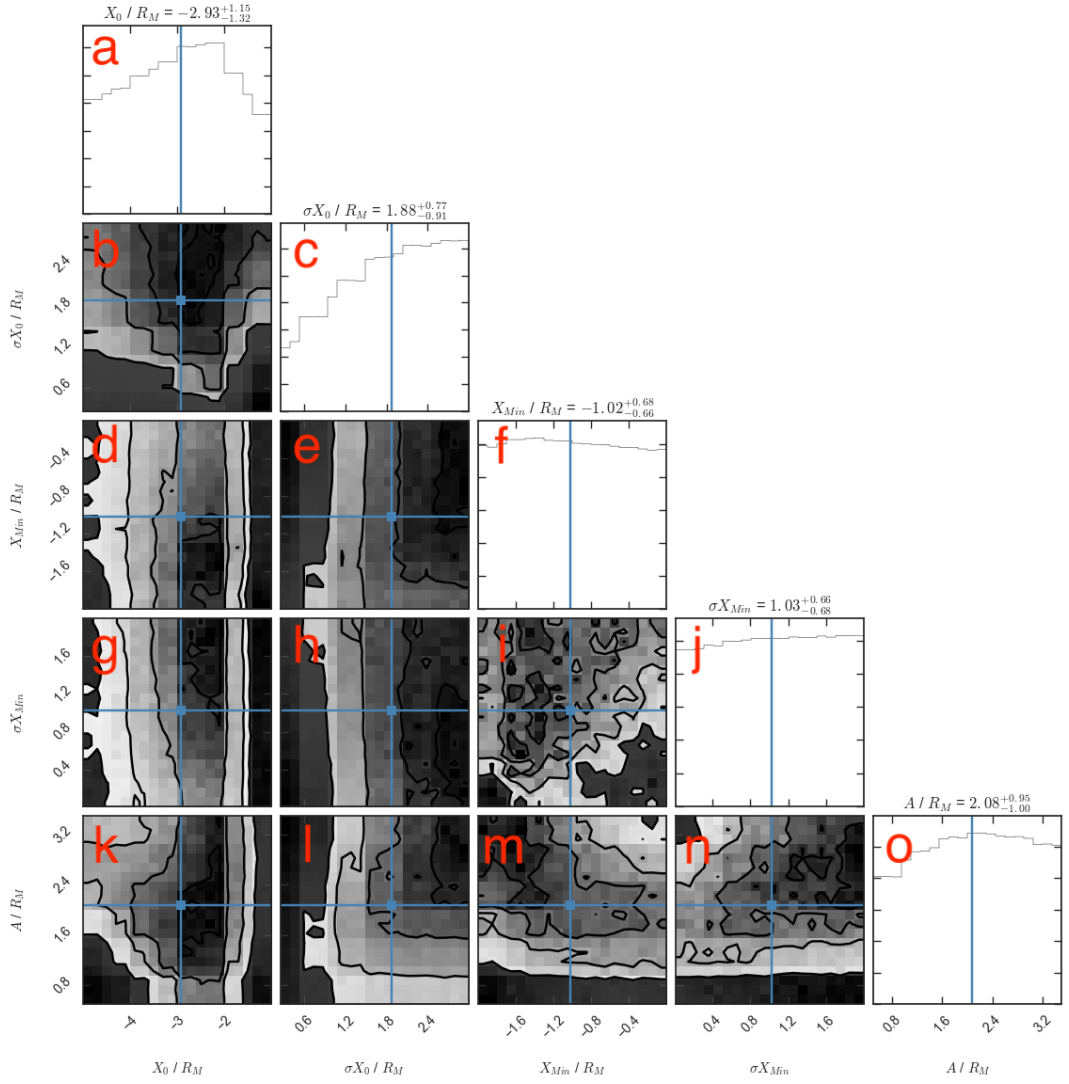

FIGURE 9.9: The posterior probability distributions of the model (X_0 and σX_0) including parameters for potential loss mechanisms planetward of the x-line (A, X_{Min} and σX_{Min}). The format is the same as for Figure 9.6 and 9.7.

Figure 9.9 shows the results of the model with the addition of these parameters (for the planetward distribution). The addition of the loss terms has reduced the median value of X_0 such that it is now fully consistent with both the tailward distributions in Figure 9.7a and previous studies [e.g. *Poh et al.*, 2017a] (with a median $X_0 = -2.93^{+1.15}_{-1.32}$). This

suggests that some form of dissipation planetward of the neutral line is fundamentally important at Mercury within the region surveyed by MESSENGER.

Once more, the median values quoted above the diagonal panels in Figure 9.9 should be regarded with a degree of caution as the full distributions are not within the simulated parameter space. It is also clear that the parametrization of the loss terms is not entirely physical: the marginalized distributions do not show a clear peak for X_{Min}, σX_{Min} or A. However, the addition of these dissipation mechanisms does allow the x-line location to be self-consistent. Additionally, a faint relationship is observed between X_{Min} and A (Figure 9.9m): increasing the size of the quasi-dipolar region (decreasing X_{Min}) increases the maximum travel distance (A) that is consistent with the observations. Physically this would correspond to a larger 'quasi-dipolar region' negating the requirement for a maximum travel distance, and vice versa.

9.3 Magnetic Signature Selection

9.3.1 Model and Method

In this Section the chosen flux rope model and the Monte Carlo method used to probe the effects of selection criteria are discussed.

9.3.1.1 The Force Free Model

The force free model (Equations 1.42, 1.43 and 1.44) is used to allow the transformation from the intrinsic properties of the flux ropes to the observable quantities (on which the constraints are generally placed). The observable quantities most commonly constrained include the duration of the magnetic signature, the magnitude of the field deflection (in the north-south field component) and the size of the peak in the axial or total field. Figure 9.10e shows two projections of a spacecraft trajectory through a model flux rope.

The model allows, with the application of some simple assumptions, that a combination of four intrinsic parameters will completely describe the magnetic signature of the flux rope encounter: velocity, radius (r_0), core field (B_0) and distance of closest approach to the flux rope axis (the impact parameter: r'_{Min}). Firstly, if it is assumed that the flux rope is oriented such that the axial field is directed along the dawn-dusk axis, then it follows that the field deflection in the north-south field component will be solely due to the changing azimuthal component of the flux rope ($\mathbf{B}_{Az}$). From Equation 1.43 it can be seen that the magnitude of the azimuthal component in the leading and trailing hemispheres of the flux rope ($r' = 1$) will be solely determined by the value of the core

field ($|B_0|$). Meanwhile, the closest approach to the flux rope axis (r'_{Min}), or the impact parameter, will control the orientation of the axial field relative to the north-south unit vector. Therefore, combining the impact parameter (r'_{Min}) and the core field strength will allow the calculation of the field deflection in the north-south field component: ΔB_Z. This is shown in Figure 9.10b. As may be expected, the largest field deflections are found for flux ropes with the strongest core fields (B_0) that are encountered at small impact parameters (r'_{Min}). It can be seen that the impact parameter has a relatively small effect up until around $r'_{Min} \geq 0.6\, r_0$, at which point the substantial change in the curvature of the field begins to considerably reduce the magnitude of the north-south field deflection.

Secondly, if it is assumed that the relative velocity of the spacecraft is negligible, and that the flux rope moves either planetward or tailward from its origin then a combination of its velocity, radius (r_0) and the impact parameter (r'_{Min}) will allow the determination of the duration of the magnetic signature of the flux rope (i.e. the duration of the peak to peak field deflection, sometimes known as the "characteristic time" [*Kawano et al.*, 1992]). This ignores any signature that may be created by the magnetic field draped around the flux rope. The duration of the magnetic signature is shown for combinations of flux rope radii and velocities for impact parameters of $r'_{Min} = 0$ and $r'_{Min} = 0.75$ in Figures 9.10c and 9.10d respectively. It should be noted that Figures 9.10c and 9.10d are plotted with the same colour scale for ease of comparison. As is intuitive, faster moving, smaller flux ropes produce shorter magnetic signatures and vice versa. Additionally, if the impact parameter is increased then the duration of the signature will be reduced (e.g. from comparing Figures 9.10c and 9.10d).

9.3.2 Evaluating Selection Bias

It is possible to simulate many thousands of flux rope encounters, randomly selecting combinations of flux rope radius (r_0), core field strength (B_0), velocity and the impact parameter (r'_{Min}) of the spacecraft trajectory. For each simulated flux rope encounter, the magnitude of the resulting field deflection (ΔB_Z), the duration of the signature (ΔT) and the magnitude of the peaks in the axial and total field (B_Y^{Max} and $|B|^{Max}$) can be calculated (as demonstrated in Figure 9.10). It is then possible to compare these values to the selection criteria enforced by recent surveys. Where values need to be compared to the background fluctuations of the field (e.g. the standard deviation) these values are randomly drawn from a set of 319 MESSENGER plasma sheet crossings [*Poh et al.*, 2017a].

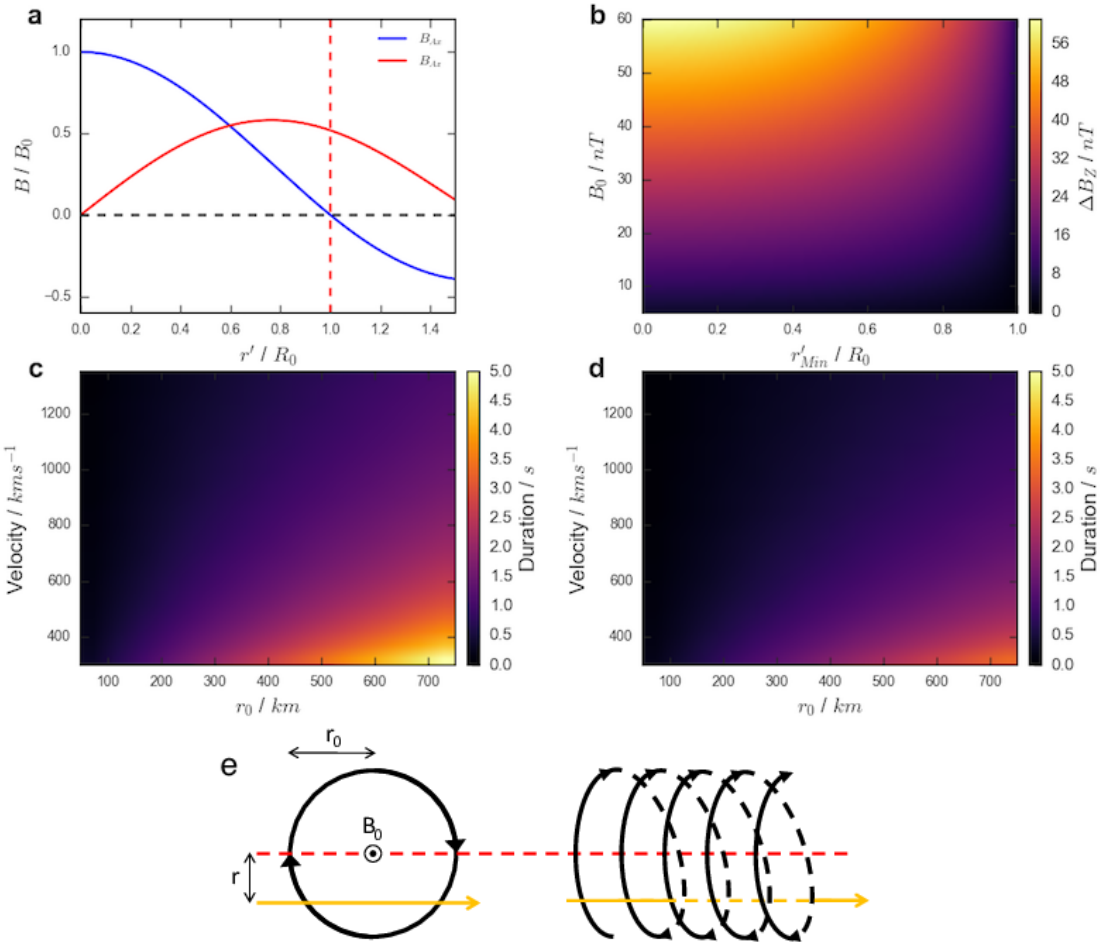

FIGURE 9.10: Figure illustrating the use of the force-free model in transforming from intrinsic properties to observable quantities. Equations 1.42 and 1.43 are shown in panel (a). Panel (b) shows how the combination of core field and impact parameter combine to provide the field deflection in the B_Z component (given the assumptions in the text). Panels (c) and (d) show how the combination of flux rope velocity and radius combine to provide the duration of the magnetic signatures for $r' = 0$ and 0.75 respectively. Panel (e) shows two projections of an example spacecraft trajectory (yellow) though a model flux rope (where black lines indicate the magnetic field).

For each combination of physical parameters it is possible to determine the fraction of flux ropes that would be identified by a given survey. This allows the recovery of combinations of parameters to be evaluated, and any interdependence quantified. Below, two recent surveys of the Hermean magnetotail (including Chapter 6) will be evaluated and compared [*Sun et al.*, 2016; *Smith et al.*, 2017b]. Initially the four intrinsic parameters will be drawn from uniform distributions. One million random combinations were simulated.

9.3.2.1 Application to the Sun et al., 2016 Flux Rope Survey

Sun et al. [2016] performed a survey of 98 intervals during which MESSENGER crossed

through the magnetotail plasma sheet. The MESSENGER magnetometer data were searched with an automated method, and the following criteria placed upon any field signature:

1. $|\Delta B_Z| \geq 15nT$
2. $|B_Y^{Max}| \geq \overline{|B_Y|} + 5\,nT$
3. $|B|^{Max} \geq \overline{|B|} + 5\,nT$
4. $0.15s \leq \Delta T \leq 5s$

where $\overline{|B_Y|}$ and $\overline{|B|}$ are the average of the B_Y component and total field respectively (for the time period from $0.5\,s$ before the start of the event until $0.5\,s$ after), while $|B_Y^{Max}|$ and $|B|^{Max}$ are the absolute values of the peaks in the field. Checks were also performed upon the field rotation observed in minimum variance coordinates, and to ensure that the point of inflection (of the field rotation) was coincident with the peak in the axial field. These criteria have not been explicitly recreated in this study as they would not reject any of the signatures generated (due to the use of the force-free model). In total, *Sun et al.* [2016] located 39 flux ropes.

Figure 9.11 shows the effects of applying the *Sun et al.* [2016] criteria listed above to the randomly generated force-free flux ropes (described above). The four intrinsic flux rope parameters are shown across the bottom while a histogram of the fraction of flux ropes recovered for each are shown along the top of each column (diagonally: panels a, c, f, j). The six lower left panels then show the possible combinations of the parameters (panels b, d, e, g, h, i), with the color indicating the fraction of the generated flux ropes that were recovered given the selection criteria.

Figure 9.11a shows the recovery fraction as a function of the impact parameter. It can be seen that even if the spacecraft passes through the centre of the flux rope ($r'_{Min} = 0$) only 60% of the generated flux ropes are identified. The recovery fraction can then be seen to drop off increasingly quickly as the impact parameter increases. There are two main contributing factors to this; the first is that structures with weak core fields will result in small deflections of the field (from quasi-force-free configurations). The second factor is that as the impact parameter increases (i.e. the spacecraft trajectory is further removed from the centre of the structure), the magnitude of the north-south field deflection will reduce due to the curvature of the flux rope: this will also have the effect of reducing the duration of the signature. The combination of these factors can be seen in Figure 9.11b, showing impact parameter against B_0, where as the impact parameter increases a larger core field is required for identification. Figure 9.11d shows

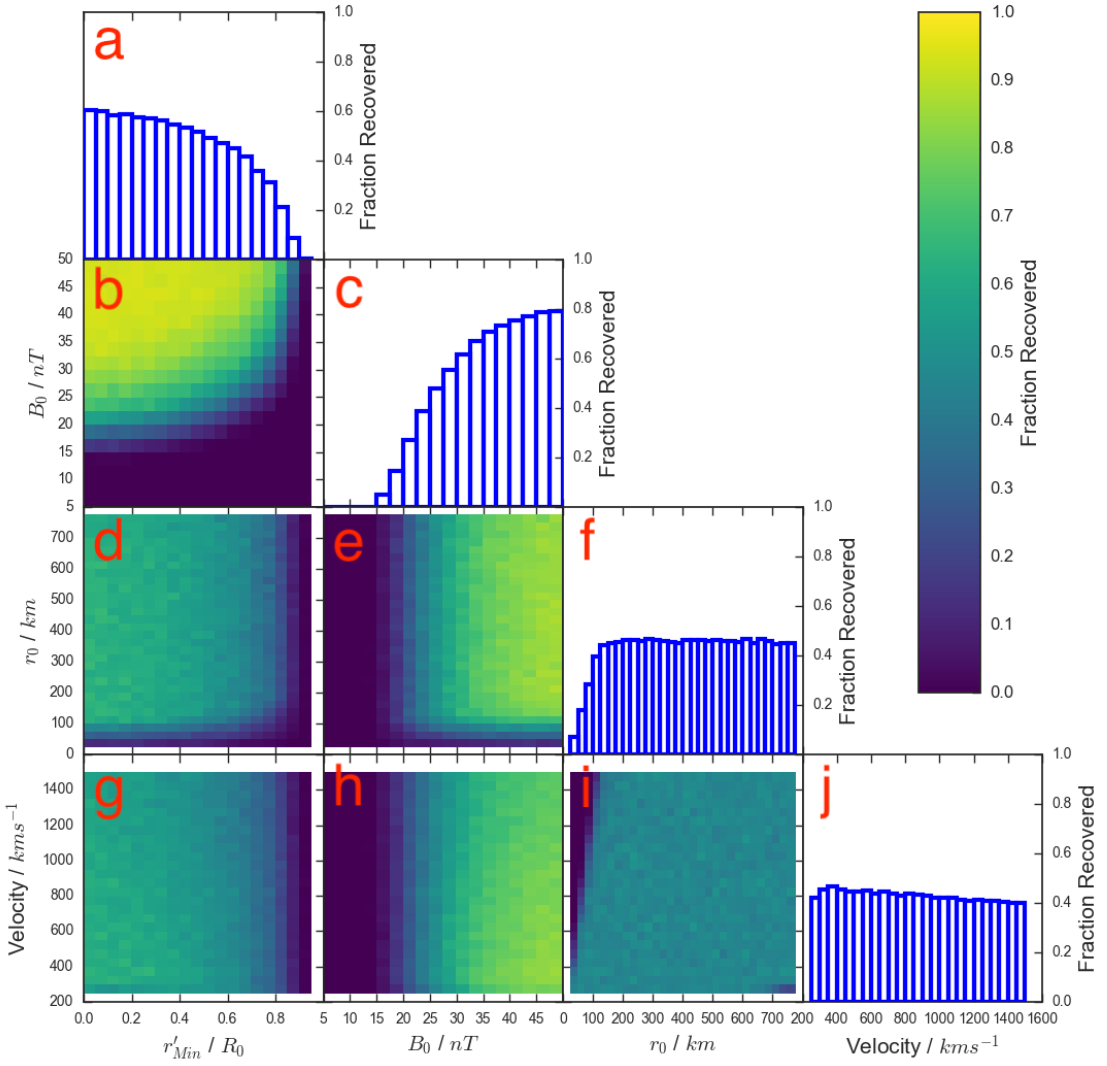

FIGURE 9.11: A four dimensional grid showing how the selection criteria of *Sun et al.* [2016] affects the fraction of flux ropes identified as a function of the intrinsic properties of the flux ropes. The diagonal panels show the fraction of flux ropes recovered as a function of the four intrinsic parameters (panels a, c, f, j). The six panels in the lower left show all combinations of the four parameters (panels b, d, e, g, h, i), while the color indicates the fractional recovery for flux ropes in that region of parameter space.

the reduction in recovery fraction for lower values of r_0 ($\leq 100\,km$) and higher values of r'_{Min} ($\geq 0.7\,r_0$), both of which result in a decreased duration of the field signature.

Figure 9.11c shows the recovery fraction as a function of core field, highlighting how the effectiveness of the survey decreases significantly below a core field of $\sim 20\,nT$. Therefore, if there is a significant fraction of the intrinsic population that possesses small core fields ($\leq 20\,nT$), then they will be poorly represented by the identified sample. This has important consequences for the inferred rate of flux rope generation, and thereby

magnetotail reconnection. Figures 9.11e and 9.11h are both dominated by the reduction in efficiency at low values of the core field.

The time criterion used by *Sun et al.* [2016] can be seen to relatively evenly sample the tested radius parameter space (Figure 9.11f), exhibiting a drop at only very small flux ropes ($r_0 \leq 100\,km$). Meanwhile, Figure 9.11j shows that the velocity recovery is even for the range of values tested. The radius and velocity fractional recoveries are combined in Figure 9.11i, and appear fairly flat for the majority of the parameter space. The principle exception being small ($r_0 \leq 100\,km$) flux ropes, for which there is a clear relation with the velocity (such that the product of the velocity and r_0 must be greater than $0.15\,s$). If a statistical study is concerned with the relative shape of an observed distribution, then the shape of the recovery distribution is a fundamentally important property of the selection criteria adopted.

9.3.2.2 Application to the Smith et al., 2017 Flux Rope Survey (Chapter 6)

For comparison, *Smith et al.* [2017b] (described in Chapter 6) performed an automated search of 319 plasma sheet crossings (first identified by *Poh et al.* [2017a]). The following key selection criteria were placed upon the magnetic signatures:

1. $\Delta B_Z \geq 1\sigma B_Z$
2. $r'_{Min} \leq 0.5$
3. $0.25s \leq \Delta T \leq 3s$

where σB_Z is the local standard deviation of the B_Z component and r'_{Min} is the impact parameter of the flux rope encounter. Several other criteria were also placed upon the signature; described by *Smith et al.* [2017a] (Chapter 5). The criteria based on the quality of model fit and results of the minimum variance analysis have not been included, they would not reject the model field signatures generated by the force-free model. In addition, *Smith et al.* [2017a] (Chapter 5) employed a wavelet transform in order to locate peaks in the axial and total field; this has also not been recreated by the method. In total *Smith et al.* [2017b] (Chapter 6) located 248 flux ropes, of which 74 were found to be well fitted by the force-free model. The quasi-force-free subset will be used for comparison in Section 9.3.3 (as their relative trajectory could be sufficiently well modelled).

Figure 9.12 details the effects of the criteria above in the same format as Figure 9.11. One of the stand out properties of Figure 9.12 is the impact of imposing the selection

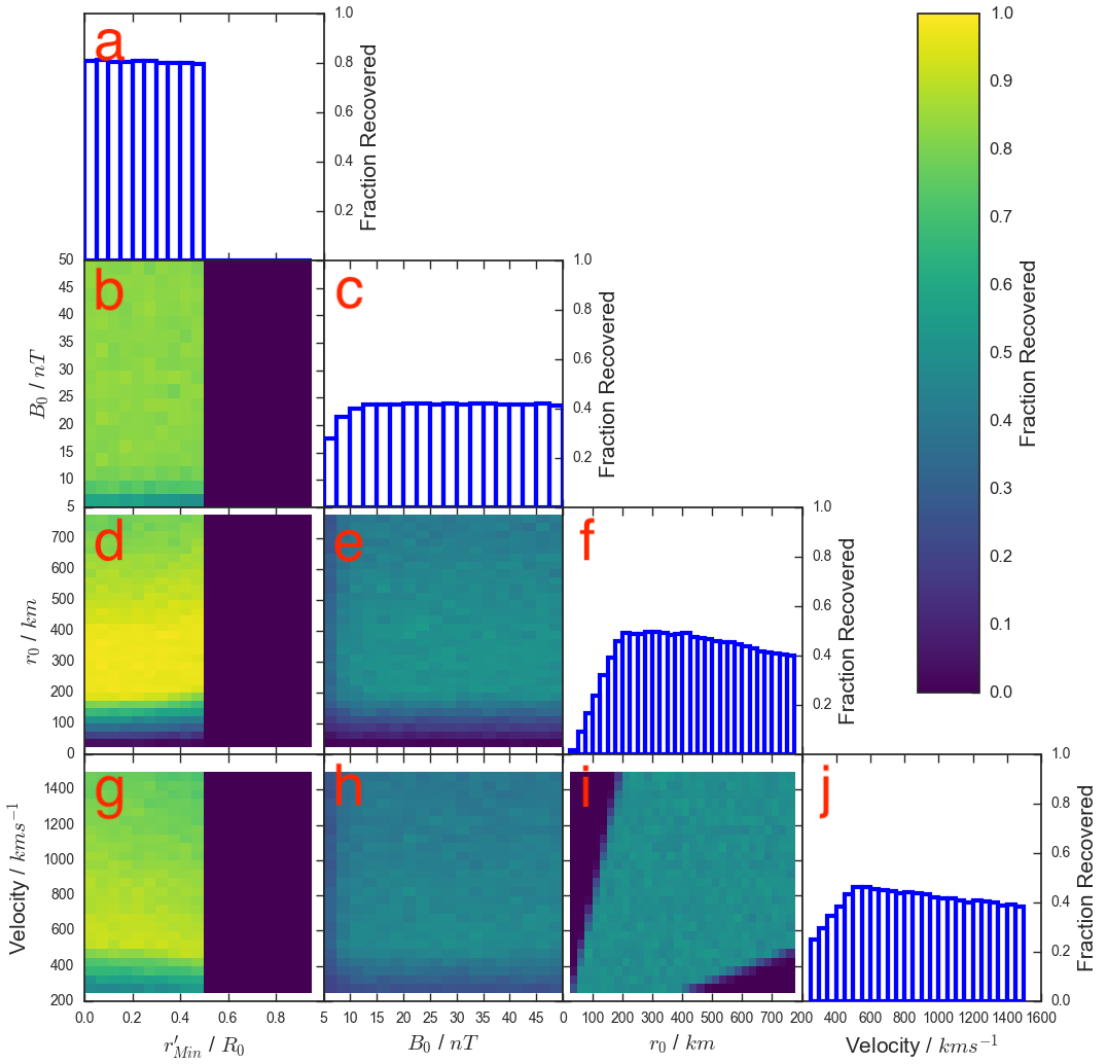

FIGURE 9.12: A four dimensional grid showing how the selection criteria of *Smith et al.* [2017b] (Chapter 6) affects the fraction of flux ropes recovered as a function of the intrinsic properties of the flux ropes. The format is as in Figure 9.11.

criterion regarding the impact parameter ($r'_{Min} \geq 0.5$). This immediately reduces the fraction of flux ropes identified by a factor of two (as the impact parameter can be drawn from a uniform distribution). However it can seen that there is a fairly flat fractional recovery within this cut-off in Figure 9.12a, in contrast to the shape of the fractional recovery shown in Figure 9.11a. This is a result of requiring the deflection to be greater than 1σ of the background; in practical terms this is approximately a factor of three reduction in threshold ($1\sigma \sim 5\,nT$). The reduced threshold also leads to a larger peak fractional recovery as a function of impact parameter (~ 0.8 compared to the ~ 0.6 shown in Figure 9.11a). Figure 9.12c also shows a fairly flat recovery as a function of core field, once more in contrast to Figure 9.11c. Therefore the criteria employed in Chapter 6 [*Smith et al.*, 2017b] more evenly samples the population of flux ropes with

small core fields (e.g. $B_0 \leq 20\,nT$), compared to the criteria used by *Sun et al.* [2016].

Figure 9.12i shows the recovery fraction projected onto the radius against velocity space and shows that both small, fast moving and large slow moving flux ropes are poorly sampled by the *Smith et al.* [2017b] (Chapter 6) criteria. This has the result of distorting the recovery fraction distribution as a function of both radius and velocity (Figure 9.12f and j). This shape of fractional recovery distribution will have significant effects on the inferred distributions from the survey, and should be taken into account when interpreting the results.

9.3.2.3 Interpretation and Limitations

There are several important factors to note when interpreting the results of Figures 9.11 and 9.12. The first is that the absolute magnitude of the recovery fractions is dependent upon the extent of the parameter space sampled (e.g. the lower limit of the core field, B_0). If the parameter space were extended then it is likely that the additional flux ropes would be poorly recovered by the selection criteria (as they have not been designed to select those structures). This would have the effect of reducing all of the inferred fractional recoveries. Therefore, the absolute magnitudes of the recovery fractions should be interpreted with caution. To minimize the effects of overextending the parameter space, the limits were selected based upon the Hermean magnetotail flux ropes observed by previous works [e.g. *DiBraccio et al.*, 2015; *Sun et al.*, 2016; *Smith et al.*, 2017b].

A second consideration is that the generation of the parameters is completely independent. However, if a pair of parameters were known to be correlated then this sampling may be unrepresentative. A related issue is the choice of distribution from which the parameters are drawn. In Figures 9.11 and 9.12, the four model parameters have been drawn from uniform distributions as a simple first approximation. If the absolute shape and parameters of the intrinsic distributions were known, then they should be used. However, as discussed above with regards to the extent of the parameter space, the main impact of the choice of distribution would be to change the absolute magnitudes of the recovery distributions. As an example, *Fermo et al.* [2011] suggested that the distribution of flux rope radii may follow an exponentially decreasing tail. This would imply that there are more small flux ropes than there are large, and so a uniformly distributed population will under-generate small flux ropes. This has implications for the overall magnitudes of the recovery distribution: smaller flux ropes are less likely to be identified and so correcting for this effect would reduce the overall fraction recovered.

To test this further, Figure 9.13 shows the selection criteria of *Smith et al.* [2017b] (Chapter 6) applied to flux ropes generated from distributions that are perhaps more representative of the intrinsic distributions. The impact parameter (r'_{Min}) is still drawn from a uniform distribution; the relative distance of the spacecraft from the flux rope axis should be completely random. The flux rope radii are drawn from an exponential distribution with a mean of $250\,km$; the choice of distribution is consistent with modelling efforts [*Fermo et al.*, 2010, 2011] and terrestrial magnetopause flux rope observations [*Akhavan-Tafti et al.*, 2018], while the mean is taken from a recent survey of Hermean magnetotail flux ropes [*Smith et al.*, 2017b] (Chapter 6). The core field (B_0) is also drawn from an exponential distribution with a mean of $22.5\,nT$; where the shape is consistent with previous Hermean magnetotail surveys [e.g. *DiBraccio et al.*, 2015], and the mean is once more taken from a recent survey [*Smith et al.*, 2017b] (Chapter 6). Finally, the velocity is drawn from a normal distribution with a mean of $450\,kms^{-1}$ and a standard deviation of $200\,kms^{-1}$; this is consistent with terrestrial magnetotail studies [*Moldwin and Hughes*, 1992; *Slavin et al.*, 2003a], and also similar to the Alfvén velocity observed in the Hermean plasma sheet [*DiBraccio et al.*, 2015].

Overall, comparing the results with the uniform source distributions (Figure 9.12) with those produced with the source distributions described above (Figure 9.13), the main result is that all of the recovery fractions have dropped by a factor of approximately two. This is a result of the increased sampling of those flux ropes with smaller radii (r_0) and core fields (B_0). As the source distributions used to produce Figure 9.13 are not fully constrained, for the remains of the study the recovery fractions with uniform distributions (i.e. Figure 9.12) will be used. For the majority of the later Sections the shape of the distribution will be of more importance than the absolute magnitude of the recovery fraction. In Section 9.3.3.2 the magnitudes are important, and therefore the estimates obtained for the intrinsic rate should be regarded as lower limits.

Finally, in all surveys, especially those undertaken automatically by algorithms, cuts must be made to distinguish the events of interest from other magnetotail phenomena. While this analysis can show the effects of the selection criteria on underlying populations (and potentially aid the placement of those limits) it only shows one factor that will affect the quality of the survey. For example, to maximize the derived recovery efficiencies it would be ideal to place no (or very low) thresholds. However, this would lead to a very large number of spurious or nuisance identifications which would inhibit or mislead the conclusions of the survey. Care must be taken therefore to balance these competing considerations, for example through the use of contingency tables and metrics such as the Heidke skill score [*Heidke*, 1926]: a technique often used in space weather forecasting [e.g. *Stephenson and Stephenson*, 2000; *Pulkkinen et al.*, 2013].

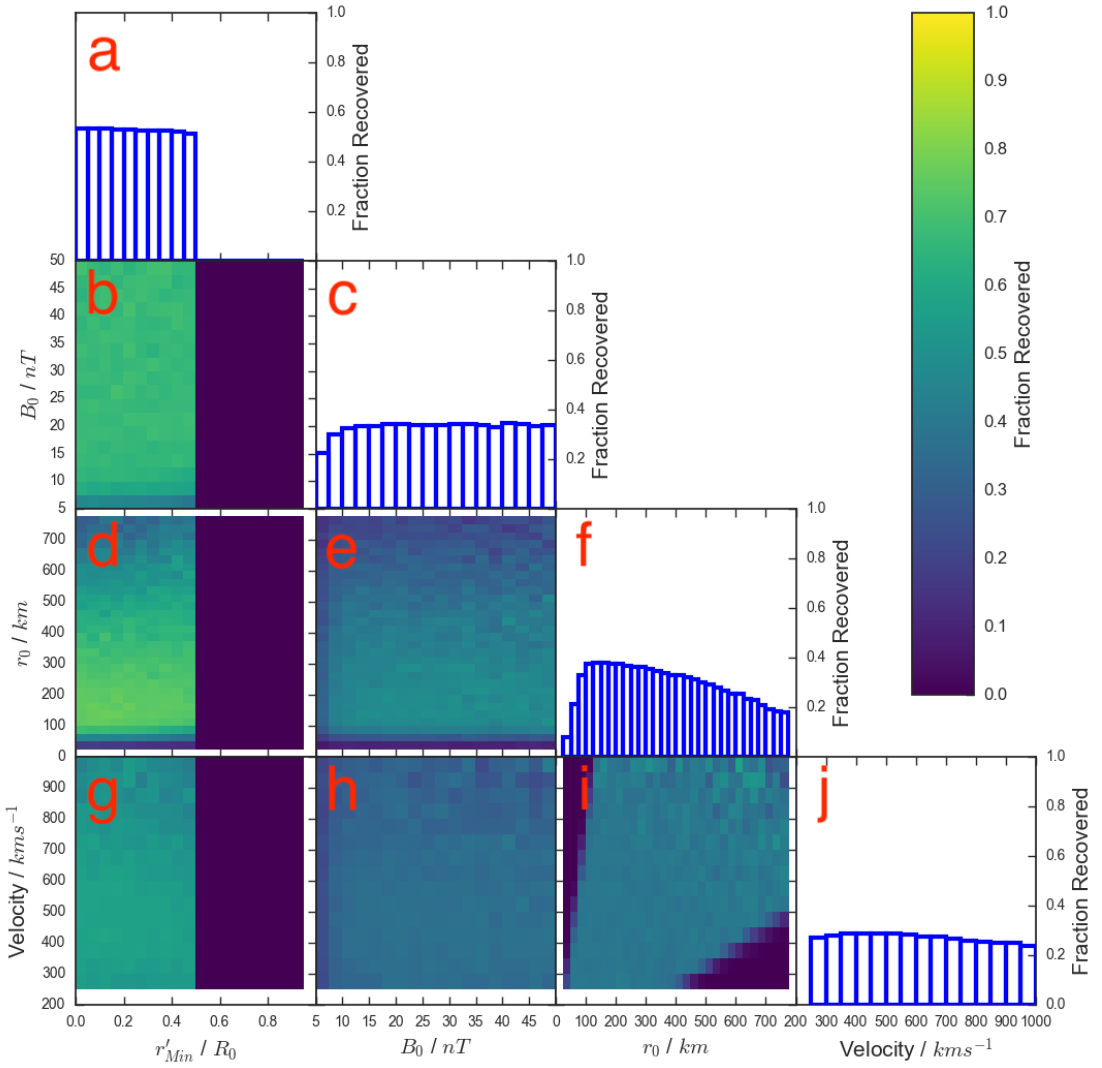

FIGURE 9.13: A four dimensional grid showing how the selection criteria of *Smith et al.* [2017b] (Chapter 6) affects the fraction of flux ropes recovered as a function of the intrinsic properties of the flux ropes. The format is as in Figures 9.11 and 9.12. However, the four parameters are now drawn from the following distributions: r'_{Min} from a uniform distribution between 0 and 1; B_0 from an exponential distribution with a mean of $22.5\,nT$; r_0 from an exponential distribution with a mean of $250\,km$; and Velocity from a normal distribution with a mean of $450 \pm 200\,kms^{-1}$. It should be noted that the upper end of the velocity range has been truncated (compared to Figure 9.12) due to poor sampling with the selected distributions.

9.3.3 Application

The evaluation of the fractional recovery of flux ropes (as a function of underlying parameters) enables further interpretation of survey results. This is particularly crucial where the surveys are compared with statistical results from modelling, investigations that are not subject to the same instrumental constraints. Below, the impact of selection effects will be evaluated when interpreting histograms of an observed property. The effects on the inferred rate of flux rope observations will then be investigated.

9.3.3.1 Distribution of Properties

Figure 9.14 demonstrates the impact of selection effects on an intrinsic distribution. Figure 9.14a shows a synthetic distribution of flux rope radii, where the distribution has been drawn from an exponential with a mean of 450 km. The exponential distribution was chosen as appropriate from the modelling work of *Fermo et al.* [2010], while the choice of mean is consistent with previous work on Hermean magnetotail flux ropes [*DiBraccio et al.*, 2015]. Figure 9.14b shows the fractional recovery of flux ropes as a function of radius (Figure 9.12f), given the selection criteria employed by *Smith et al.* [2017b] (Chapter 6). Therefore, accounting for selection effects (combining Figures 9.14a and b) would result in the observed distribution shown in Figure 9.14c (in blue). This distribution is consistent with that observed by previous studies: displaying an exponential tail at larger radii and a drop off at the smallest spatial scales [e.g. *Fear et al.*, 2007; *Fermo et al.*, 2011]. The results obtained by *Smith et al.* [2017b] (Chapter 6) are shown in red in Figure 9.14c for context, though it should be noted that their estimates were obtained using an average Hermean plasma sheet Alfvén velocity (and not the actual flux rope velocity).

Previously, studies have fitted the tail of the distribution of observed flux rope radii to an exponential function ($\propto e^{-r/r_0}$) [e.g. *Fermo et al.*, 2011; *Akhavan-Tafti et al.*, 2018]. Following this, if the tail of the observed distribution in Figure 9.14c (i.e. $r > 200\,km$) is fitted to an exponential function, the mean radius recovered is not consistent with the original generated distribution ($\overline{r_0} = 392.9 \pm 6.2\,km$). Therefore for this intrinsic distribution (and set of selection criteria) fitting to the tail of the distribution does not appear to overcome the selection effects of the survey. However, this may not be the case for all studies and will depend strongly on the shape of the recovery distribution (i.e. Figure 9.14b) relative to the intrinsic distribution.

Ideally, it would be a simple process to divide the distribution of an observed property (e.g. the flux rope radius or core field strength) by the recovery fraction and thus obtain an estimate of the intrinsic distribution (i.e. to go from Figure 9.14c to 9.14a). For example, if only 20% of flux ropes with a given radius will be identified with a set of selection criteria, then the n flux ropes observed are representative of an intrinsic $\frac{n}{0.2} = 5n$ flux ropes. If the quality of the data were sufficient then this could be done trivially.

However, the flux ropes observed by MESSENGER were identified solely upon their magnetic signature, and lack simultaneous, high cadence plasma observations [e.g. *DiBraccio et al.*, 2015; *Smith et al.*, 2017b]. In this case it is perhaps not appropriate to perform the correction on the inferred radii (as they are calculated with the aid of

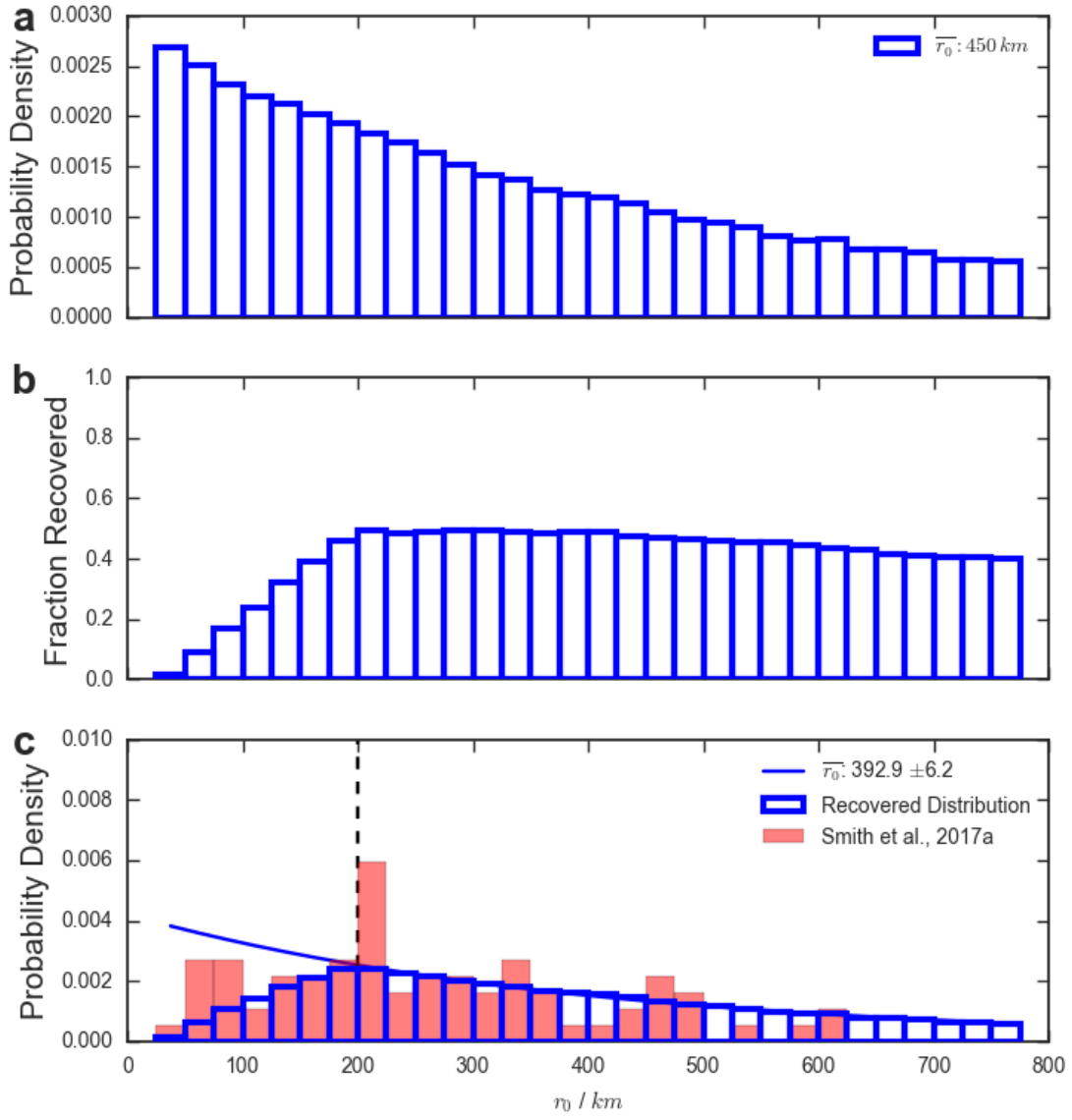

FIGURE 9.14: Panel (a) shows a randomly generated distribution of radii drawn from an exponential distribution with a mean of 450 km. Panel (b) shows the recovery fraction of flux ropes as a function of radius with the criteria of *Smith et al.* [2017b] (Chapter 6), while panel (c) shows the resulting distribution of radii that would be observed. In panel (c) the observations of *Smith et al.* [2017b] (Chapter 6) are provided in red as an example. The solid blue line shows the results of exponential fits to the tail of recovered distribution ($r > 200\,km$: represented by the vertical black dashed line).

an average Alfvén velocity). Therefore, the comparisons should be made between the modelled and observed durations.

Figure 9.15a shows an example distribution of flux rope radii, drawn from an exponential distribution with a mean r_0 of 450 km (as above). When a spacecraft passes through a flux rope it will generally not pass directly through the centre of the structure, and will instead create a chord through the flux rope (assuming the structure can be approximated as a cylindrical structure and is encountered normal to its axis). *Akhavan-Tafti*

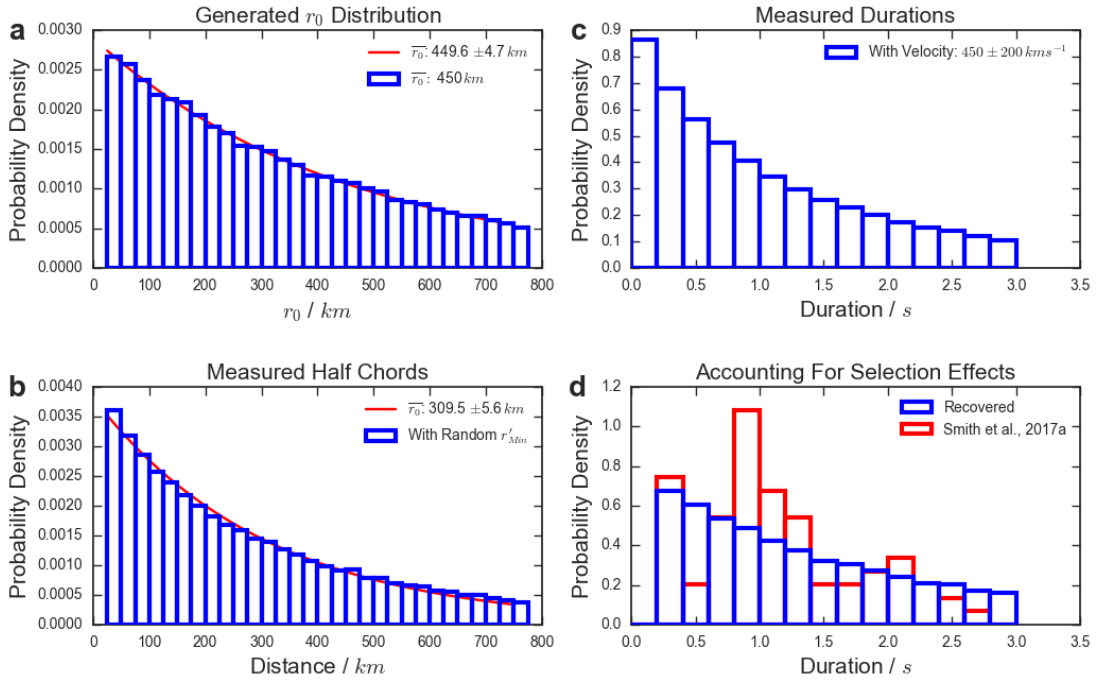

FIGURE 9.15: Panel (a) shows an exponentially distributed set of flux rope radii with a mean of 450 km, while panel (b) shows the distribution of radii once corrected for the impact parameter of the encounter. Panel (c) shows the duration of the signatures that would be recorded assuming a normally distributed velocity, and panel (d) shows the distribution of durations that would be observed with the selection criteria of *Smith et al.* [2017b] (Chapter 6). The solid red lines show exponential fits to the distributions in (a) and (b).

et al. [2018] recently highlighted the importance of correcting for this effect in statistical studies of subsolar magnetopause FTEs. Figure 9.15b shows the distribution of measured half chords when Figure 9.15a is corrected with randomly selected impact parameters (r'_{Min}). Fitting this distribution to an exponential would result in the inference of a smaller mean radius than is correct [*Akhavan-Tafti et al.*, 2018].

Next, the distribution of half chords is converted to the duration of the magnetic signature, often defined as the time between the peaks of the bipolar signature [e.g. *Kawano et al.*, 1992; *Slavin et al.*, 1993]. Physically this corresponds to the time between the leading and trailing edges of the flux rope. To make this conversion, the velocity of each flux rope is required. In this case, the velocities are drawn from a normal distribution with a mean of 450 kms^{-1} and a standard deviation of 200 kms^{-1}. This distribution was chosen as it is consistent with previous observations of terrestrial flux ropes [*Moldwin and Hughes*, 1992; *Slavin et al.*, 2003a] and measurements of the Hermean magnetotail Alfvén velocity [*DiBraccio et al.*, 2015]. The resulting distribution of durations is shown in Figure 9.15c. Several velocity distributions were tested and the changes were found to have a relatively small effect on the resulting distribution of durations.

Finally, the distribution in Figure 9.15c is sampled with the selection criteria employed by *Smith et al.* [2017b] (Chapter 6); this results in the distribution shown in blue in Figure 9.15d. The actual distribution observed by *Smith et al.* [2017b] (Chapter 6) is also shown in red. It is then possible to compare the results with that of *Smith et al.* [2017b] (Chapter 6) while varying the mean of the input distribution. Performing this fit allows the mean of the distribution of quasi-force-free flux rope radii to be calculated as $589^{+273}_{-269}\,km$. The large uncertainties could be improved with a larger database of observed events.

9.3.3.2 Inferred Rate

Each flux rope will occupy a unique location in the four-dimensional parameter space described by Figures 9.11 and 9.12. In principle it would be possible to use the probability of recovering each individual flux rope as a weighting factor. Correcting each observation for the probability of its identification can then provide a rate of flux rope generation that is more reflective of the system.

However, for application to the survey in Chapter 6 [*Smith et al.*, 2017b] it is more appropriate to apply this correction to the recovery fractions in a two dimensional parameter space described by ΔB_Z and the duration of the signature: Figure 9.16a. The reason for this is the velocity of each individual flux rope is not known, meaning the radius is not known definitively.

In total, Chapter 6 [*Smith et al.*, 2017b] identified 74 quasi-force-free flux ropes, the distribution of which is shown in Figure 9.16b as a function of deflection size (ΔB_Z) and duration. Correcting each of these detections by the probability shown in Figure 9.16a suggests that these 74 identifications are representative of a total of 181 quasi-force-free flux ropes.

The survey in Chapter 6 [*Smith et al.*, 2017b] considered a total of 1482 minutes of MESSENGER plasma sheet observations. With 74 observed flux ropes this corresponds to an average rate of observation of $0.05\,min^{-1}$. Correcting each flux rope for the probability of its identification increases the total number of flux ropes, and therefore the inferred rate of flux ropes encountered in the Hermean magnetotail increases to $0.12\,min^{-1}$. For context, the rate of terrestrial magnetotail flux rope observations is around $0.7 \times 10^{-3} min^{-1}$ [*Imber et al.*, 2011]. Future work should involve running such terrestrial observations through the techniques described, so the inferred values can be fully compared.

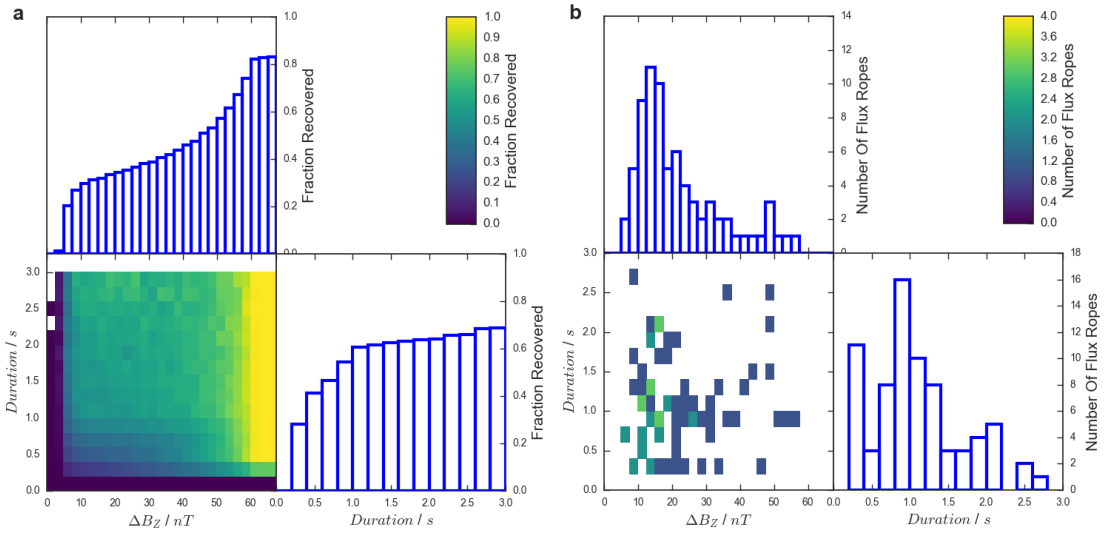

FIGURE 9.16: The fractional recovery of model flux ropes as a function of deflection size (ΔB_Z) and duration, for the criteria of Chapter 6 [*Smith et al.*, 2017b] (a). The distribution of quasi-force-free flux ropes observed in Chapter 6 [*Smith et al.*, 2017b] (b).

9.4 Conclusions

9.4.1 Orbital Selection

In the first part of this Chapter, a Monte Carlo based analysis technique has been presented and applied to a single spacecraft survey of Mercury's magnetotail. Firstly, synthetic, randomly distributed orbits were tested to determine the number of orbits required to obtain a good estimate of the underlying intrinsic distributions of magnetotail flux ropes. The required number of orbits was shown to be heavily dependent upon the properties of the system and the flux ropes themselves, e.g. the width of the structures and the probability of their occurrence. The efficacy of two different orbital sampling regimes were compared; the uniformly distributed orbits were found to best infer the majority of intrinsic distributions tested.

Secondly, many iterations with different combinations of model parameters were performed and compared to the results of Chapter 6 [*Smith et al.*, 2017b]. The survey results were found to be most consistent with an x-line that is offset dawnward of midnight by $\sim 0.4\,R_M$. Azimuthally wider flux ropes (e.g. $\geq 2\,R_M$) were found to be more consistent with the results, rather than narrower structures. The statistical downtail location of the x-line was then probed. The distribution of tailward moving flux ropes allowed the recovery of a statistical location consistent with previous studies [e.g. *Poh et al.*, 2017a]. However, the distribution of planetward moving structures returned a result that was both inconsistent with previous work in the literature and with the results

obtained from the comparison to the tailward moving distribution. This discrepancy could be resolved with the addition of parameters describing dissipation mechanisms planetward of the reconnection site (e.g. a 'maximum travel distance' or 'distance of closest approach').

9.4.2 Magnetic Signature Selection

In the second half of this Chapter, a Monte Carlo based method has been presented; this technique allows the estimation of the fraction of events that are identified, as a function of various underlying parameters of the flux ropes. The evaluation of the fractional recovery of flux ropes can allow the observed distributions of properties to be corrected, providing insight into the underlying distributions present. An application of this was shown with regards to the distribution of flux rope radii observed in the Hermean magnetotail (e.g. from Chapter 6). In this case, the subsequent fit is made to the distribution of durations observed (due to the lack of simultaneous high resolution plasma data). The most consistent result is found with a distribution with a mean radius of $589^{+273}_{-269}\,km$.

Finally, each individual identification can be corrected for the likelihood that it would be made. For example, small flux ropes may be under-represented as they are more difficult and thus less likely to be identified. Following this, the 74 quasi-force-free flux ropes observed by Chapter 6 [*Smith et al.*, 2017b] are indicative of an total population of 181 flux ropes. This has the effect of increasing the overall rate of flux ropes in the Hermean tail from $0.05\,min^{-1}$ to $0.12\,min^{-1}$, a value that is approximately 180 times that previously observed in the terrestrial magnetotail, indicating the hugely dynamic nature of the Hermean magnetotail.

Chapter 10

Summary and Future Work

10.1 Introduction

This Chapter summarises the results of the Chapters 4 - 9, showing the progress that has been made by this thesis. Potential future avenues of work are also discussed.

10.2 Reconnection in Saturn's Magnetotail

Chapters 4, 7 and 8 investigated reconnection in Saturn's magnetotail, including developing methods of automatically locating the signatures of *in situ* encounters between Cassini and reconnection related structures.

Previous work at Saturn had highlighted a discrepancy between the amount of plasma entering the magnetosphere, primarily through the ionisation of the Enceladus neutral torus, and the mass lost through reconnection events (i.e. plasmoids) in the magnetotail. In addition, the impact of the solar wind on Saturn's magnetospheric dynamics is an active area of research. This is the context in which the study described by Chapter 4 began.

10.2.1 Chapter 4: A Comprehensive Magnetic Field Survey

In order to make a comprehensive estimation of the mass lost through plasmoid events, the Kronian magnetotail magnetic field was surveyed for strong deflections of the north-south meridional component. This survey was performed by an algorithm designed to select strong deflections of the field, above the level of background fluctuations. In

addition to the 2006 deep tail orbits considered by previous works, data were also included from 2009/2010 orbits that covered a previously unconsidered region around the dusk flank. The addition of these orbits provided a more complete view of the Kronian magnetotail.

When normalized to the observing time, reconnection related events were most commonly observed post-midnight. More infrequent detections were made around the dusk flank. The increase in the rate of detections post-midnight could be indicative of the growing instability of the mass laden flux tubes as they rotate across the tail. The location of the reconnection site, inferred from the orientation and type of reconnection product, appeared to be highly variable though most commonly located between ~ 20 and $30\,R_S$ away from the planet. Using generous upper estimates for the plasmoid volume, the estimated mass loss through plasmoids was still insufficient, by an order of magnitude to explain the mass addition from Enceladus. Concerning solar wind interaction, only a very short statistical post plasmoid plasma sheet (PPPS) was observed following the catalogue of plasmoids. This suggests that the majority of events do not possess significant PPPSs, and therefore open flux may be closed in few, large scale events.

In the future, the large catalogue created by this study could be used to further investigate specific phenomena (e.g. dipolarizations in Chapter 7) and the dynamics of the magnetotail (e.g. Chapter 8) using multiple instruments. The relationship between the events and both solar wind and internal driving could also be examined in detail. Additionally, the mass imbalance should be approached using multi-instrument case studies and comparisons to global models. Critically, the largest sources of uncertainty in the mass loss determination should be re-examined. This includes detailed investigation of the mass input, quantifying the mass addition from magnetopause reconnection and kelvin-helmholtz instability driven vortices. Loss processes should also be further investigated, for example constraints should be placed on the azimuthal extent of plasmoids as well as a determination of the loss through the magnetopause flanks.

10.2.2 Chapter 7: Dipolarization Fronts Associated with Energetic Electrons

Building on Chapter 4, dipolarization fronts were selected for further investigation, including information on the thermal electron population associated with the events. This was for two main reasons; firstly from terrestrial literature they may be expected to be accompanied by a population of energized electrons: this signature provides an additional selection criteria to locate the structures, while the characteristics of the electron

heating allows their generation and propagation to be probed. Secondly, the composition of the plasma that follows the dipolarization may be indicative of the plasma involved in reconnection, crucially allowing insight into whether lobe field was involved.

From an initial sample of 712 potential field deflections (identified in Chapter 4), 28 were found to be coincident with the appearance of a more energetic electron population. The distribution of the 28 events was strongly asymmetric across the magnetotail, with 79% located dawnward of midnight. Approximately half of the events (43%) were found within 3 hours of another identification, all of which were located postmidnight. The associated energetic electron populations exhibited increases in temperature (by factors of $4-12$) and decreases in density (by factors of $3-10$). The heating characteristics were asymmetric across the tail, with the premidnight events possessing the smallest relative changes in temperature and density. This could be related to a more variable (and potentially distant) postmidnight reconnection site. A strong depletion of water group species was observed in 40% of events, possibly related to loss of the heavy, equatorially confined material in plasmoids. The suprathermal composition of two events indicated the presence of plasma of solar wind origin, potentially the signature of lobe reconnection.

Further work should be performed in the future to investigate how the 28 identifications differ (magnetically) from the original sample of 712; e.g. looking into the presence (or absence) of high frequency magnetic field fluctuations that often accompany terrestrial dipolarization fronts. Additional studies could also develop our understanding of the plasma flow accompanying dipolarizations; comparing and contrasting the observations with those made in the terrestrial magnetosphere. The auroral counterparts of dipolarizations could also be used to constrain the recurrence and azimuthal extent of Kronian dipolarizations.

10.2.3 Chapter 8: Multi-Instrument Case Studies of Saturn's Magnetotail X-Line

The catalogue created in the process of Chapter 4's investigation contains a trove of interesting events, potential case studies that could illuminate some of the current open questions at Saturn. For example, previous surveys had suggested that the location of the reconnection site, in terms of radial distance from the planet, was variable; precluding the determination of a statistical x-line.

Chapter 8 described a pair of case studies showing intervals during which the x-line could be inferred to move or form on relatively short timescales. In the first case study, the spacecraft initially observed a dipolarization, followed shortly by a series of plasmoids. Therefore, the spacecraft was first located planetward of a reconnection site, and a short

time later was tailward of a second x-line. The thermal plasma flows were short, lasting for $\sim 10\,minutes$, indicating the reconnection was either bursty or limited in azimuth. If this is a result of azimuthally confined reconnection, then the flows were of the order of $\sim 3\,R_S$ or 0.4 hours of local time wide. The second case study presented a series of dipolarizations in which the temperature of the heated electron population increased with subsequent events. This was interpreted as the signature of a reconnection site (or series of sites) moving down the magnetotail, leading to increased non-local heating during the planetward propagation of the material.

In the future further events identified by Chapter 4 could be analysed from a multi instrument perspective: this would allow studies such as an investigation of the abundance and properties of lobe reconnection in Saturn's magnetotail. Future studies could use the correlation between *in situ* magnetotail dynamics and auroral radio signatures to help constrain the azimuthal extent of the magnetotail signatures (or the auroral radio viewing region). Additionally, the properties of the electron heating could be further explored: pitch angle modelling could be employed to trace the origins of the heated population.

10.3 Reconnection in Mercury's Magnetotail

Chapters 5, 6 and 9 investigated the distribution, occurrence and properties of flux ropes in the Hermean magnetotail.

Previous work identified an even distribution of flux rope observations in the centre of the Hermean tail using MESSENGER orbital data. A later study expanded the survey region, and observed a strong dawnward offset in their observations. This asymmetry has been observed in studies of other magnetospheric phenomena at Mercury, therefore this thesis set out to perform the most comprehensive survey of the Hermean tail to evaluate the distribution and properties of the flux ropes. The role of selection effects, from orbital selection and placing criterion on the properties of the magnetic signatures, were also investigated.

10.3.1 Chapter 5: Flux Rope Identification Method

In Chapter 5, a series of methods were presented which, when combined, allow for the repeatable and automated identification of *in situ* flux rope encounters. Initially, above background ($> 1\sigma$) deflections of the north-south field component are identified. The deflections were then checked to ensure they were coincident with peaks in either the

axial or total field (using a continuous wavelet transform). The three components of the magnetic field surrounding the candidate deflections were then processed with MVA to assess whether they could be processed into a well defined coordinate system with a clear rotation of the field. Finally, a model was fit to the signature, allowing the rejection of spurious events and also the estimation of some of the key parameters of the flux rope. The technique was developed and verified using data from MESSENGER, as well as the terrestrial Cluster and Geotail missions; recovering known flux rope events.

The technique was applied to MESSENGER data in Chapter 5, but more generally in the future it could be applied to terrestrial datasets to create a very large catalogue of flux ropes that would be of great use to the community. The technique would require some adaptation, for example the timescales investigated to define the magnetic signature would need to be adjusted. Additionally, in an environment (such as the Earth) where high resolution plasma measurements are available, criteria could be added and more complex modelling employed. The techniques could also be further developed, for example using machine learning classification methods to determine the defining characteristics of flux ropes from comparison with pre-existing catalogues.

10.3.2 Chapter 6: Hermean Magnetotail Flux Rope Survey

Chapter 6 described the largest current survey of flux ropes in the Hermean magnetosphere. The methods from Chapter 5 were used to locate *in situ* flux rope encounters within 319 MESSENGER current sheet crossings. In total, 248 flux ropes were identified, of which 74 satisfactorily fit the cylindrically symmetric, constant α force-free model. A slight dawn-dusk asymmetry was observed in the detections, with a greater abundance observed closer to the dawn than to the dusk flank. The flux rope observations were made intermittently, with just under half of the plasma sheet intervals being associated with flux rope encounters. The peak rate of flux ropes was found to be very high ($\sim 5\,min^{-1}$) during active intervals. The inferred neutral line location was found to be highly variable, with no clear distinction between the distribution of planetward and tailward moving structures. The effects of the IMF on the orientation of the flux rope core field were examined, and weak correlations observed between the flux rope core field and the preceding lobe field.

In the future, especially with the arrival of Bepi-Columbo in 2025, the coupling between the solar wind and Mercury's magnetotail dynamics should be examined in greater detail. For example, the relationship between the dawn-dusk component of the IMF and that within Mercury's magnetotail current sheet should be studied. Further, this could then be linked to the core field orientation of magnetotail flux ropes. Additionally, with two

orbiters the mission would be ideally placed to investigate the evolution and propagation of magnetotail flux ropes.

10.3.3 Chapter 9: Evaluating Single Spacecraft Surveys with Monte Carlo Simulations

While the techniques introduced in Chapters 5, and applied in Chapter 6, represent a thorough and detailed survey of the Hermean magnetotail field, they still represent single point measurements of a magnetosphere. There are two main reasons why flux ropes may be generated and not be identified in the spacecraft data: the first is that the spacecraft is in a location that is not covered by the flux rope. A Monte Carlo model was developed to assess the underlying distribution of flux ropes, given the orbit of MESSENGER and the detections made in Chapter 6. It was found that the results of the survey were most consistent with a neutral line offset dawnward of midnight by $\sim 0.4\,R_M$, with a width around $\sim 50\%$ of the Hermean magnetotail. Large variability of the neutral line in the downtail direction was unable to reproduce the observed distributions of planetward and tailward structures. However, including dissipation terms planetward of the neutral line produced consistent results, suggesting that these mechanisms are important.

The second reason why flux rope encounters may be missed is that the signature is not recognised by the survey as belonging to a flux rope. This is particularly a problem if the flux ropes are represented by small magnetic signatures, both in terms of deflection size and duration. The results of Chapter 6 and a recent survey [*Sun et al.*, 2016] were evaluated, and each was found to preferentially select a different subset of the underlying population. A Monte Carlo method was developed to correct for these selection effects, and applied to the observed distribution of flux rope radii. In addition, accounting for undetected flux ropes increased the average rate in the Hermean magnetotail by a factor of ~ 2.5.

In the future this type of modelling could be applied to the terrestrial magnetotail, allowing the investigation of the underlying distributions therein. If these techniques were adapted for the Kronian magnetosphere then the dominance of corotation would need to be implemented in some fashion. The techniques could also be used in statistical studies of FTEs on the dayside magnetopause. This would require considerable adaptation, for example the orientation and propagation directions of the model flux ropes would need to be carefully considered.

Bibliography

Achilleos, N., C. S. Arridge, C. Bertucci, C. M. Jackman, M. K. Dougherty, K. K. Khurana, and C. T. Russell (2008), Large-scale dynamics of Saturn's magnetopause: Observations by Cassini, *Journal of Geophysical Research: Space Physics*, *113*(11), doi:10.1029/2008JA013265.

Acuña, M. H. (2002), Space-based magnetometers, *Review of Scientific Instruments*, *73*(11), 3717–3736, doi:10.1063/1.1510570.

Acuña, M. H., and N. F. Ness (1980), The magnetic field of Saturn: Pioneer 11 observations, *Science*, *207*(4429), 444–446, doi:10.1126/science.207.4429.444.

Akasofu, S.-I. (1964), The development of the auroral substorm, *Planetary and Space Science*, *12*(4), 273–282, doi:10.1016/0032-0633(64)90151-5.

Akhavan-Tafti, M., J. A. Slavin, G. Le, J. P. Eastwood, R. J. Strangeway, C. T. Russell, R. Nakamura, W. Baumjohann, R. B. Torbert, B. L. Giles, D. J. Gershman, and J. L. Burch (2018), MMS Examination of FTEs at the Earth's Subsolar Magnetopause, *Journal of Geophysical Research: Space Physics*, *123*(2), 1224–1241, doi:10.1002/2017JA024681.

Alexandrova, A., R. Nakamura, V. S. Semenov, and T. K. M. Nakamura (2015), Motion of reconnection region in the Earth's magnetotail, *Geophysical Research Letters*, *42*(12), 4685–4693, doi:10.1002/2015GL064421.

Alexeev, I. I., E. S. Belenkaya, S. Y. Bobrovnikov, J. A. Slavin, and M. Sarantos (2008), Paraboloid model of Mercury's magnetosphere, *Journal of Geophysical Research: Space Physics*, *113*(12), doi:10.1029/2008JA013368.

Alexeev, I. I., E. S. Belenkaya, J. A. Slavin, H. Korth, B. J. Anderson, D. N. Baker, S. A. Boardsen, C. L. Johnson, M. E. Purucker, M. Sarantos, and S. C. Solomon (2010), Mercury's magnetospheric magnetic field after the first two MESSENGER flybys, *Icarus*, *209*(1), 23–39, doi:10.1016/j.icarus.2010.01.024.

Allen, R. C., D. G. Mitchell, C. P. Paranicas, D. C. Hamilton, G. Clark, A. M. Rymer, S. K. Vines, E. C. Roelof, S. M. Krimigis, and J. Vandegriff (2018), Internal Versus External Sources of Plasma at Saturn: Overview From Magnetospheric Imaging Investigation/Charge-Energy-Mass Spectrometer Data, *Journal of Geophysical Research: Space Physics*, doi:10.1029/2018JA025262.

Anderson, B. J., M. H. Acuña, D. A. Lohr, J. Scheifele, A. Raval, H. Korth, and J. A. Slavin (2007), The magnetometer instrument on MESSENGER, *Space Science Reviews*, *131*(1-4), 417–450, doi:10.1007/s11214-007-9246-7.

Anderson, B. J., M. H. Acuña, H. Korth, M. E. Purucker, C. L. Johnson, J. A. Slavin, S. C. Solomon, and R. L. McNutt (2008), The Structure of Mercury's Magnetic Field from MESSENGER's First Flyby, *Science*, *321*(5885), 82–85, doi:10.1126/science.1159081.

Anderson, B. J., M. H. Acuña, H. Korth, J. A. Slavin, H. Uno, C. L. Johnson, M. E. Purucker, S. C. Solomon, J. M. Raines, T. H. Zurbuchen, G. Gloeckler, and R. L. McNutt (2010), The magnetic field of Mercury, *Space Science Reviews*, *152*(1-4), 307–339, doi:10.1007/s11214-009-9544-3.

Anderson, B. J., C. L. Johnson, H. Korth, M. E. Purucker, R. M. Winslow, J. A. Slavin, S. C. Solomon, R. L. McNutt, J. M. Raines, and T. H. Zurbuchen (2011), The Global Magnetic Field of Mercury from MESSENGER Orbital Observations, *Science*, *333*(6051), 1859–1862, doi:10.1126/science.1211001.

Anderson, B. J., C. L. Johnson, H. Korth, R. M. Winslow, J. E. Borovsky, M. E. Purucker, J. A. Slavin, S. C. Solomon, M. T. Zuber, and R. L. McNutt (2012), Low-degree structure in Mercury's planetary magnetic field, *Journal of Geophysical Research E: Planets*, *117*(12), doi:10.1029/2012JE004159.

Anderson, J. D., and G. Schubert (2007), Saturn's gravitational field, internal rotation, and interior structure., *Science (New York, N.Y.)*, *317*(5843), 1384–7, doi:10.1126/science.1144835.

Andrews, D. J., A. J. Coates, S. W. H. Cowley, M. K. Dougherty, L. Lamy, G. Provan, and P. Zarka (2010), Magnetospheric period oscillations at Saturn: Comparison of equatorial and high-latitude magnetic field periods with north and south Saturn kilometric radiation periods, *Journal of Geophysical Research: Space Physics*, *115*(A12), n/a–n/a, doi:10.1029/2010JA015666.

Angelopoulos, V., W. Baumjohann, C. F. Kennel, F. V. Coroniti, M. G. Kivelson, R. Pellat, R. J. Walker, H. Lühr, and G. Paschmann (1992), Bursty bulk flows in

the inner central plasma sheet, *Journal of Geophysical Research*, *97*(A4), 4027, doi: 10.1029/91JA02701.

Angelopoulos, V., C. F. Kennel, F. V. Coroniti, R. Pellat, M. G. Kivelson, R. J. Walker, C. T. Russell, W. Baumjohann, W. C. Feldman, and J. T. Gosling (1994), Statistical characteristics of bursty bulk flow events, *Journal of Geophysical Research*, *99*(A11), 21,257, doi:10.1029/94JA01263.

Apatenkov, S. V., V. A. Sergeev, M. V. Kubyshkina, R. Nakamura, W. Baumjohann, A. Runov, I. Alexeev, A. Fazakerley, H. Frey, S. Muhlbachler, P. W. Daly, J. A. Sauvaud, N. Ganushkina, T. Pulkkinen, G. D. Reeves, and Y. Khotyaintsev (2007), Multi-spacecraft observation of plasma dipolarization/injection in the inner magnetosphere, *Ann. Geophys.*, *25*(3), 801–814, doi:10.5194/angeo-25-801-2007.

Arridge, C. S., K. K. Khurana, C. T. Russell, D. J. Southwood, N. Achilleos, M. K. Dougherty, A. J. Coates, and H. K. Leinweber (2008), Warping of Saturn's magnetospheric and magnetotail current sheets, *Journal of Geophysical Research: Space Physics*, *113*(8), 13, doi:10.1029/2007JA012963.

Arridge, C. S., H. J. McAndrews, C. M. Jackman, C. Forsyth, A. P. Walsh, E. C. Sittler, L. K. Gilbert, G. R. Lewis, C. T. Russell, A. J. Coates, M. K. Dougherty, G. A. Collinson, A. Wellbrock, and D. T. Young (2009a), Plasma electrons in Saturn's magnetotail: Structure, distribution and energisation, *Planetary and Space Science*, *57*(14-15), 2032–2047, doi:10.1016/j.pss.2009.09.007.

Arridge, C. S., L. K. Gilbert, G. R. Lewis, E. C. Sittler, G. H. Jones, D. O. Kataria, A. J. Coates, and D. T. Young (2009b), The effect of spacecraft radiation sources on electron moments from the Cassini CAPS electron spectrometer, *Planetary and Space Science*, *57*(7), 854–869, doi:10.1016/j.pss.2009.02.011.

Arridge, C. S., N. André, K. K. Khurana, C. T. Russell, S. W. H. Cowley, G. Provan, D. J. Andrews, C. M. Jackman, A. J. Coates, E. C. Sittler, M. K. Dougherty, and D. T. Young (2011a), Periodic motion of Saturn's nightside plasma sheet, *Journal of Geophysical Research: Space Physics*, *116*(11), 22, doi:10.1029/2011JA016827.

Arridge, C. S., N. André, H. J. McAndrews, E. J. Bunce, M. H. Burger, K. C. Hansen, H. W. Hsu, R. E. Johnson, G. H. Jones, S. Kempf, K. K. Khurana, N. Krupp, W. S. Kurth, J. S. Leisner, C. Paranicas, E. Roussos, C. T. Russell, P. Schippers, E. C. Sittler, H. T. Smith, M. F. Thomsen, and M. K. Dougherty (2011b), Mapping magnetospheric equatorial regions at Saturn from Cassini prime mission observations, *Space Science Reviews*, *164*(1-4), 1–83, doi:10.1007/s11214-011-9850-4.

Arridge, C. S., M. Kane, N. Sergis, K. K. Khurana, and C. M. Jackman (2015a), Sources of Local Time Asymmetries in Magnetodiscs, *Space Science Reviews*, *187*(1-4), 301–333, doi:10.1007/s11214-015-0145-z.

Arridge, C. S., J. P. Eastwood, C. M. Jackman, G.-K. Poh, J. A. Slavin, M. F. Thomsen, N. André, X. Jia, A. Kidder, L. Lamy, A. Radioti, D. Reisenfeld, N. Sergis, M. Volwerk, A. P. Walsh, P. Zarka, A. Coates, and M. K. Dougherty (2015b), Cassini in situ observations of long-duration magnetic reconnection in Saturn's magnetotail, *Nature Physics*, *12*(3), 268–271, doi:10.1038/nphys3565.

Aschenbrenner, H., and G. Goubau (1936), Eine Anordnung zur Registrierung rascher magnetischer Storungen, *Hochfrequenztechnik und Elektroakustik*, *47*(6), 177–181.

Ashour-Abdalla, M., M. El-Alaoui, M. L. Goldstein, M. Zhou, D. Schriver, R. Richard, R. Walker, M. G. Kivelson, and K. J. Hwang (2011), Observations and simulations of non-local acceleration of electrons in magnetotail magnetic reconnection events, *Nature Physics*, *7*(4), 360–365, doi:10.1038/nphys1903.

Ashour-Abdalla, M., G. Lapenta, R. J. Walker, M. El-Alaoui, and H. Liang (2015), Multiscale study of electron energization during unsteady reconnection events, *Journal of Geophysical Research: Space Physics*, *120*(6), 4784–4799, doi:10.1002/2014JA020316.

Axford, W. I., and C. O. Hines (1961), A Unifying Theory Of High-Latitude Geophysical Phenomena and Geomagnetic Storms, *Canadian Journal of Physics*, *39*(10), 1433–1464, doi:10.1139/p61-172.

Azari, A. R., M. W. Liemohn, X. Jia, M. F. Thomsen, D. G. Mitchell, N. Sergis, A. M. Rymer, G. B. Hospodarsky, C. Paranicas, and J. Vandegriff (2018), Interchange Injections at Saturn: Statistical Survey of Energetic H+ Sudden Flux Intensifications, *Journal of Geophysical Research: Space Physics*, *123*, 4692–4711, doi:10.1029/2018JA025391.

Badman, S. V., and S. W. H. Cowley (2007), Significance of Dungey-cycle flows in Jupiter's and Saturn's magnetospheres, and their identification on closed equatorial field lines, *Annales Geophysicae*, *25*(4), 941–951, doi:10.5194/angeo-25-941-2007.

Badman, S. V., E. J. Bunce, J. T. Clarke, S. W. H. Cowley, J. C. Gérard, D. Grodent, and S. E. Milan (2005), Open flux estimates in Saturn's magnetosphere during the January 2004 Cassini-HST campaign, and implications for reconnection rates, *Journal of Geophysical Research: Space Physics*, *110*(A11), 16, doi:10.1029/2005JA011240.

Badman, S. V., S. W. H. Cowley, J. C. Gérard, and D. Grodent (2006), A statistical analysis of the location and width of Saturn's southern auroras, *Annales Geophysicae*, *24*(12), 3533–3545, doi:10.5194/angeo-24-3533-2006.

Badman, S. V., S. W. H. Cowley, L. Lamy, B. Cecconi, and P. Zarka (2008), Relationship between solar wind corotating interaction regions and the phasing and intensity of Saturn kilometric radiation bursts, *Ann. Geophys*, *26*, 3641–3651.

Badman, S. V., C. M. Jackman, J. T. Clarke, and J. D. Nichols (2012), Open flux in Saturn's magnetosphere, *Icarus*, *14*, 7508, doi:http://dx.doi.org/10.1016/j.icarus.2013.12.004.

Badman, S. V., A. Masters, H. Hasegawa, M. Fujimoto, A. Radioti, D. Grodent, N. Sergis, M. K. Dougherty, and A. J. Coates (2013), Bursty magnetic reconnection at Saturn's magnetopause, *Geophysical Research Letters*, *40*(6), 1027–1031, doi:10.1002/grl.50199.

Badman, S. V., C. M. Jackman, J. D. Nichols, J. T. Clarke, and J.-C. Gérard (2014), Open flux in Saturn's magnetosphere, *Icarus*, *231*, 137–145, doi:10.1016/j.icarus.2013.12.004.

Bagenal, F. (2007), The magnetosphere of Jupiter: Coupling the equator to the poles, *Journal of Atmospheric and Solar-Terrestrial Physics*, *69*, 387–402, doi:10.1016/j.jastp.2006.08.012.

Bagenal, F., and P. A. Delamere (2011), Flow of mass and energy in the magnetospheres of Jupiter and Saturn, *Journal of Geophysical Research: Space Physics*, *116*(5), 17, doi:10.1029/2010JA016294.

Baker, D. N., E. W. Hones, D. T. Young, and J. Birn (1982), The possible role of ionospheric oxygen in the initiation and development of plasma sheet instabilities, *Geophysical Research Letters*, *9*(12), 1337–1340, doi:10.1029/GL009i012p01337.

Baker, D. N., J. A. Simpson, and J. H. Eraker (1986), A Model of Impulsive Acceleration and Transport of Energetic Particles in Mercury's Magnetosphere, *Journal of Geophysical Research*, *91*(1), 8742–8748, doi:10.1029/JA091iA08p08742.

Baker, D. N., T. I. Pulkkinen, V. Angelopoulos, W. Baumjohann, and R. L. McPherron (1996), Neutral line model of substorms: Past results and present view, *Journal of Geophysical Research: Space Physics*, *101*(A6), 12,975–13,010, doi:10.1029/95JA03753.

Balogh, A., T. Beek, R. Forsyth, P. Hedgecock, R. Marquedant, E. Smith, D. Southwood, and B. Tsurutani (1992), The magnetic field investigation on the ULYSSES mission - Instrumentation and preliminary scientific results, *Astronomy and Astrophysics Supplement Series (ISSN 0365-0138)*, *92*, 221–236.

Balogh, A., C. M. Carr, M. H. Acuña, M. W. Dunlop, T. J. Beek, P. Brown, K.-H. Fornacon, E. Georgescu, K.-H. Glassmeier, J. Harris, G. Musmann, T. Oddy, and K. Schwingenschuh (2001), The Cluster Magnetic Field Investigation: overview of in-flight performance and initial results, *Annales Geophysicae*, *19*(10/12), 1207–1217, doi:10.5194/angeo-19-1207-2001.

Baumjohann, W., and R. A. Treumann (2012), *Basic Space Plasma Physics*, Imperial College Press, doi:10.1142/p850.

Baumjohann, W., G. Paschmann, and H. Lühr (1990), Characteristics of high-speed ion flows in the plasma sheet, *Journal of Geophysical Research*, *95*(A4), 3801, doi:10.1029/JA095iA04p03801.

Baumjohann, W., A. Roux, O. Le Contel, R. Nakamura, J. Birn, M. Hoshino, A. T. Y. Lui, C. J. Owen, J.-A. Sauvaud, A. Vaivads, D. Fontaine, and A. Runov (2007), Dynamics of thin current sheets: Cluster observations, *Annales Geophysicae*, *25*(6), 1365–1389, doi:10.5194/angeo-25-1365-2007.

Belenkaya, E. S., I. I. Alexeev, M. S. Blokhina, S. W. H. Cowley, S. V. Badman, V. V. Kalegaev, and M. S. Grigoryan (2007), IMF dependence of the open-closed field line boundary in Saturn's ionosphere, and its relation to the UV auroral oval observed by the Hubble Space Telescope, *Annales Geophysicae*, *25*(5), 1215–1226, doi:10.5194/angeo-25-1215-2007.

Birn, J., and K. Schindler (2002), Thin current sheets in the magnetotail and the loss of equilibrium, *Journal of Geophysical Research*, *107*(A7), 1117, doi:10.1029/2001JA000291.

Birn, J., M. Hesse, R. Nakamura, and S. Zaharia (2013), Particle acceleration in dipolarization events, *Journal of Geophysical Research: Space Physics*, *118*(5), 1960–1971, doi:10.1002/jgra.50132.

Birn, J., A. Runov, and M. Hesse (2014), Energetic electrons in dipolarization events: Spatial properties and anisotropy, *Journal of Geophysical Research: Space Physics*, *119*(5), 3604–3616, doi:10.1002/2013JA019738.

Birn, J., A. Runov, and X.-Z. Zhou (2017), Ion velocity distributions in dipolarization events: Distributions in the central plasma sheet, *Journal of Geophysical Research: Space Physics*, *122*(8), 8014–8025, doi:10.1002/2017JA024230.

Bittencourt, J. A. (2004), *Fundamentals of Plasma Physics Third Edition*, vol. 49, 3rd ed., 197–197 pp., Springer New York, New York, NY, doi:10.1007/978-1-4757-4030-1.

Blanc, M., D. J. Andrews, A. J. Coates, D. C. Hamilton, C. M. Jackman, X. Jia, A. Kotova, M. Morooka, H. T. Smith, and J. H. Westlake (2015), Saturn Plasma Sources and Associated Transport Processes, *Space Science Reviews*, *192*(1-4), 237–283, doi:10.1007/s11214-015-0172-9.

Borg, A. L., M. G. G. T. Taylor, and J. P. Eastwood (2012), Annales Geophysicae Observations of magnetic flux ropes during magnetic reconnection in the Earth's magnetotail, *Annales Geophysicae*, *30*(1992), 761–773, doi:10.5194/angeo-30-761-2012.

Bothmer, V., R. Kallenbach, B. Klecker, and E. Marsch (1999), The Solar Origin of Corotating Interaction Regions and Their Formation in the Inner Heliosphere, *Space Science Reviews*, *89*, 141–178, doi:10.1023/A.

Boudouridis, A., E. Zesta, L. R. Lyons, P. C. Anderson, and D. Lummerzheim (2004), Magnetospheric reconnection driven by solar wind pressure fronts, *22*, 1367–1378.

Briggs, J. A., D. A. Brain, M. L. Cartwright, J. P. Eastwood, and J. S. Halekas (2011), A statistical study of flux ropes in the Martian magnetosphere, *Planetary and Space Science*, *59*(13), 1498–1505, doi:10.1016/j.pss.2011.06.010.

Broadfoot, A. L., M. J. Belton, P. Z. Takacs, B. R. Sandel, D. E. Shemansky, J. B. Holberg, J. M. Ajello, S. K. Atreya, T. M. Donahue, H. W. Moos, J. L. Bertaux, J. E. Blamont, D. F. Strobel, J. C. McConnell, A. Dalgarno, R. Goody, and M. B. McElroy (1979), Extreme ultraviolet observations from Voyager 1 encounter with Jupiter, *Science*, *204*(4396), 979–982, doi:10.1126/science.204.4396.979.

Browett, S. D., R. C. Fear, A. Grocott, and S. E. Milan (2017), Timescales for the penetration of IMF By into the Earth's magnetotail, *Journal of Geophysical Research: Space Physics*, *122*(1), 579–593, doi:10.1002/2016JA023198.

Bunce, E. J., S. W. H. Cowley, and J. A. Wild (2003), Azimuthal magnetic fields in Saturn's magnetosphere: effects associated with plasma sub-corotation and the magnetopause-tail current system, *21*.

Bunce, E. J., S. W. H. Cowley, D. M. Wright, A. J. Coates, M. K. Dougherty, N. Krupp, W. S. Kurth, and A. M. Rymer (2005), In situ observations of a solar wind compression-induced hot plasma injection in Saturn's tail, *Geophysical Research Letters*, *32*(20), 1–4, doi:10.1029/2005GL022888.

Bunce, E. J., C. S. Arridge, J. T. Clarke, A. J. Coates, S. W. Cowley, M. K. Dougherty, J. C. Gérard, D. Grodent, K. C. Hansen, J. D. Nichols, D. J. Southwood, and D. L. Talboys (2008), Origin of Saturn's aurora: Simultaneous observations by Cassini and the Hubble Space Telescope, *Journal of Geophysical Research: Space Physics*, *113*(9), doi:10.1029/2008JA013257.

Burch, J. L., J. Goldstein, T. W. Hill, D. T. Young, F. J. Crary, A. J. Coates, N. André, W. S. Kurth, and E. C. Sittler (2005), Properties of local plasma injections in Saturn's magnetosphere, *Geophys. Res. Lett*, *32*, 14–2, doi:10.1029/2005GL022611.

Burkholder, B., P. A. Delamere, X. Ma, M. F. Thomsen, R. J. Wilson, and F. Bagenal (2017), Local time asymmetry of Saturn's magnetosheath flows, *Geophysical Research Letters*, *44*(12), 5877–5883, doi:10.1002/2017GL073031.

Burlaga, L. F. (1988), Magnetic clouds and force-free fields with constant alpha, *Journal of Geophysical Research*, *93*(7), 7217, doi:10.1029/JA093iA07p07217.

Burlaga, L. F. (2001), Magnetic fields and plasmas in the inner heliosphere: Helios results, *Planetary and Space Science*, *49*(14-15), 1619–1627, doi:10.1016/S0032-0633(01)00098-8.

Burton, M. E., B. Buratti, D. L. Matson, and J.-P. Lebreton (2001), The Cassini/Huygens Venus and Earth flybys: An overview of operations and results, *Journal of Geophysical Research: Space Physics*, *106*(A12), 30,099–30,107, doi:10.1029/2001JA900088.

Burton, M. E., M. K. Dougherty, and C. T. Russell (2009), Model of Saturn's internal planetary magnetic field based on Cassini observations, *Planetary and Space Science*, *57*(14-15), 1706–1713, doi:10.1016/j.pss.2009.04.008.

Cao, H., C. T. Russell, U. R. Christensen, M. K. Dougherty, and M. E. Burton (2011), Saturn's very axisymmetric magnetic field: No detectable secular variation or tilt, doi:10.1016/j.epsl.2011.02.035.

Carmona, R., W.-L. Hwang, and B. Torresani (1998), *Practical Time-Frequency Analysis, Volume 9: Gabor and Wavelet Transforms, with an Implementation in S (Wavelet Analysis and Its Applications)*, *Wavelet Analysis and Its Applications*, vol. 9, 490 pp., Elsevier Science.

Chapman, S., and V. C. A. Ferraro (1931), A New Theory of Magnetic Storms, *Terrestrial Magnetism and Atmospheric Electricity*, *36*(2), 77, doi:10.1029/TE036i002p00077.

Chen, Y., and T. W. Hill (2008), Statistical analysis of injection/dispersion events in Saturn's inner magnetosphere, *Journal of Geophysical Research: Space Physics*, *113*(7), doi:10.1029/2008JA013166.

Chen, Y., T. W. Hill, A. M. Rymer, and R. J. Wilson (2010), Rate of radial transport of plasma in Saturn's inner magnetosphere, *J. Geophys. Res*, *115*, doi:10.1029/2010JA015412.

Cheng, C. (2004), Physics of Substorm Growth Phase, Onset, and Dipolarization, *Space Science Reviews*, *113*(1/2), 207–270, doi:10.1023/B:SPAC.0000042943.59976.0e.

Christon, S. P. (1987), A comparison of the Mercury and Earth magnetospheres: Electron measurements and substorm time scales, *Icarus*, *71*(3), 448–471, doi: 10.1016/0019-1035(87)90040-6.

Clarke, J. T., J. C. Gérard, D. Grodent, S. Wannawichian, J. Gustin, J. Connerney, F. Crary, M. Dougherty, W. Kurth, S. W. Cowley, E. J. Bunce, T. Hill, and J. Kim (2005), Morphological differences between Saturn's ultraviolet aurorae and those of Earth and Jupiter, *Nature*, *433*(7027), 717–719, doi:10.1038/nature03331.

Coleman, P. J., L. Davis, and C. P. Sonett (1960), Steady Component of the Interplanetary Magnetic Field: Pioneer V, *Physical Review Letters*, *5*(2), 43–46, doi: 10.1103/PhysRevLett.5.43.

Cowley, S., and M. Lockwood (1992), Excitation and decay of solar wind-driven flows in the magnetosphere- ionosphere system, *Annales Geophysicae*, *10*, 103–115.

Cowley, S. W. H. (1981), Magnetospheric asymmetries associated with the y-component of the IMF, *Planetary and Space Science*, *29*(1), 79–96, doi:10.1016/0032-0633(81) 90141-0.

Cowley, S. W. H., and E. J. Bunce (2001), Origin of the main auroral oval in Jupiter's coupled magnetosphere-ionosphere system, *Planetary and Space Science*, *49*, 1067–1088.

Cowley, S. W. H., and E. J. Bunce (2003), Corotation-driven magnetosphere-ionosphere coupling currents in Saturn's magnetosphere and their relation to the auroras, *21*, 1691–1707.

Cowley, S. W. H., and W. J. Hughes (1983), Observation of an IMF sector effect in the Y magnetic field component at geostationary orbit, *Planetary and Space Science*, *31*(1), 73–90, doi:10.1016/0032-0633(83)90032-6.

Cowley, S. W. H., E. J. Bunce, and J. M. O'Rourke (2004a), A simple quantitative model of plasma flows and currents in Saturn's polar ionosphere, *Journal of Geophysical Research*, *109*(A5), A05,212, doi:10.1029/2003JA010375.

Cowley, S. W. H., E. J. Bunce, and R. Prangé (2004b), Saturn's polar ionospheric flows and their relation to the main auroral oval, *Annales Geophysicae*, *22*(4), 1379–1394, doi:10.5194/angeo-22-1379-2004.

Cowley, S. W. H., S. V. Badman, E. J. Bunce, J. T. Clarke, J. C. Gérard, D. Grodent, C. M. Jackman, S. E. Milan, and T. K. Yeoman (2005), Reconnection in a rotation-dominated magnetosphere and its relation to Saturn's auroral dynamics, *Journal of Geophysical Research: Space Physics*, *110*(A2), doi:10.1029/2004JA010796.

Cowley, S. W. H., J. D. Nichols, and C. M. Jackman (2015), Down-tail mass loss by plasmoids in Jupiter's and Saturn's magnetospheres, *Journal of Geophysical Research A: Space Physics*, *120*(8), 6347–6356, doi:10.1002/2015JA021500.

Daubechies, I. (1992), *Ten Lectures on Wavelets*, vol. 61, 357 pp., SIAM, doi:10.1137/1.9781611970104.

Davis, L., and E. J. Smith (1990), A model of Saturn's magnetic field based on all available data, *Journal of Geophysical Research*, *95*(A9), doi:10.1029/JA095iA09p15257.

De La Haye, V., J. H. Waite, R. E. Johnson, R. V. Yelle, T. E. Cravens, J. G. Luhmann, W. T. Kasprzak, D. A. Gell, B. Magee, F. Leblanc, M. Michael, S. Jurac, and I. P. Robertson (2007), Cassini Ion and Neutral Mass Spectrometer data in Titan's upper atmosphere and exosphere: Observation of a suprathermal corona, *Journal of Geophysical Research: Space Physics*, *112*(7), 16, doi:10.1029/2006JA012222.

Delamere, P. A., and F. Bagenal (2013), Magnetotail structure of the giant magnetospheres: Implications of the viscous interaction with the solar wind, *Journal of Geophysical Research: Space Physics*, *118*(11), 7045–7053, doi:10.1002/2013JA019179.

Delamere, P. A., R. J. Wilson, and A. Masters (2011), Kelvin-Helmholtz instability at Saturn's magnetopause: Hybrid simulations, *Journal of Geophysical Research: Space Physics*, *116*(10), doi:10.1029/2011JA016724.

Delamere, P. A., R. J. Wilson, S. Eriksson, and F. Bagenal (2013), Magnetic signatures of Kelvin-Helmholtz vortices on Saturn's magnetopause: Global survey, *Journal of Geophysical Research: Space Physics*, *118*(1), 393–404, doi:10.1029/2012JA018197.

Delamere, P. A., F. Bagenal, C. Paranicas, A. Masters, A. Radioti, B. Bonfond, L. Ray, X. Jia, J. Nichols, and C. Arridge (2015a), Solar Wind and Internally Driven Dynamics: Influences on Magnetodiscs and Auroral Responses, *Space Science Reviews*, *187*(1-4), 51–97, doi:10.1007/s11214-014-0075-1.

Delamere, P. A., A. Otto, X. Ma, F. Bagenal, and R. J. Wilson (2015b), Magnetic flux circulation in the rotationally driven giant magnetospheres, *Journal of Geophysical Research: Space Physics*, *120*(6), 4229–4245, doi:10.1002/2015JA021036.

Delcourt, D. C. (2013), On the supply of heavy planetary material to the magnetotail of mercury, *Annales Geophysicae*, *31*(10), 1673–1679, doi:10.5194/angeo-31-1673-2013.

Deng, X., M. Ashour-Abdalla, M. Zhou, R. Walker, M. El-Alaoui, V. Angelopoulos, R. E. Ergun, and D. Schriver (2010), Wave and particle characteristics of earthward electron injections associated with dipolarization fronts, *Journal of Geophysical Research: Space Physics*, *115*(9), doi:10.1029/2009JA015107.

Desroche, M., F. Bagenal, P. A. Delamere, and N. Erkaev (2013), Conditions at the magnetopause of Saturn and implications for the solar wind interaction, *Journal of Geophysical Research: Space Physics*, *118*(6), 3087–3095, doi:10.1002/jgra.50294.

Dewey, R. M., J. A. Slavin, J. M. Raines, D. N. Baker, and D. J. Lawrence (2017), Energetic Electron Acceleration and Injection During Dipolarization Events in Mercury's Magnetotail, *Journal of Geophysical Research: Space Physics*, *122*(12), 12,170–12,188, doi:10.1002/2017JA024617.

DiBraccio, G. A., J. A. Slavin, S. A. Boardsen, B. J. Anderson, H. Korth, T. H. Zurbuchen, J. M. Raines, D. N. Baker, R. L. McNutt, and S. C. Solomon (2013), MESSENGER observations of magnetopause structure and dynamics at Mercury, *Journal of Geophysical Research: Space Physics*, *118*(3), 997–1008, doi:10.1002/jgra.50123.

DiBraccio, G. A., J. A. Slavin, S. M. Imber, D. J. Gershman, J. M. Raines, C. M. Jackman, S. A. Boardsen, B. J. Anderson, H. Korth, T. H. Zurbuchen, R. L. McNutt, and S. C. Solomon (2015), MESSENGER observations of flux ropes in Mercury's magnetotail, *Planetary and Space Science*, *115*, 77–89, doi:10.1016/j.pss.2014.12.016.

Dougherty, M. K., S. Kellock, D. J. Southwood, A. Balogh, E. J. Smith, B. T. Tsurutani, B. Gerlach, K. H. Glassmeier, F. Gleim, C. T. Russell, G. Erdos, F. M. Neubauer, and S. W. H. Cowley (2004), The Cassini Magnetic Field Investigation, *Space Sci Rev.*, *114*(1-4), 331–383.

Dougherty, M. K., N. Achilleos, N. Andre, C. S. Arridge, A. Balogh, C. Bertucci, M. E. Burton, S. W. Cowley, G. Erdos, G. Giampieri, K. H. Glassmeier, K. K. Khurana, J. Leisner, F. M. Neubauer, C. T. Russell, E. J. Smith, D. J. Southwood, and B. T. Tsurutani (2005a), Cassini magnetometer observations during Saturn orbit insertion, *Science*, *307*(5713), 1266–1270, doi:10.1126/science.1106098.

Dougherty, M. K., N. Achilleos, N. Andre, C. S. Arridge, A. Balogh, C. Bertucci, M. E. Burton, S. W. Cowley, G. Erdos, G. Giampieri, K. H. Glassmeier, K. K. Khurana, J. Leisner, F. M. Neubauer, C. T. Russell, E. J. Smith, D. J. Southwood, and B. T. Tsurutani (2005b), Cassini magnetometer observations during Saturn orbit insertion, *Science*, *307*(5713), 1266–1270, doi:10.1126/science.1106098.

Dougherty, M. K., K. K. Khurana, F. M. Neubauer, C. T. Russell, J. Saur, J. S. Leisner, and M. E. Burton (2006), Identification of a dynamic atmosphere at Enceladus

with the Cassini magnetometer, *Science*, *311*(5766), 1406–1409, doi:10.1126/science.1120985.

Du, P., W. A. Kibbe, and S. M. Lin (2006), Improved peak detection in mass spectrum by incorporating continuous wavelet transform-based pattern matching, *Bioinformatics*, *22*(17), 2059–2065, doi:10.1093/bioinformatics/btl355.

Duan, A. Y., J. B. Cao, M. Dunlop, and Z. Q. Wang (2014), Energetic electron bursts in the plasma sheet and their relation with BBFs, *Journal of Geophysical Research: Space Physics*, *119*(11), 8902–8915, doi:10.1002/2014JA020169.

Dungey, J. W. (1961), Interplanetary magnetic field and the auroral zones, *Physical Review Letters*, *6*(2), 47–48, doi:10.1103/PhysRevLett.6.47.

Dungey, J. W. (1963), The structure of the exosphere or adventures in velocity space, in *Geophysics, The Earth's Environment*, p. 550, Gordon and Breach.

Dungey, J. W. (1965), The length of the magnetospheric tail, *Journal of Geophysical Research*, *70*(7), 1753–1753, doi:10.1029/JZ070i007p01753.

Eastman, T. E., E. W. Hones, S. J. Bame, and J. R. Asbridge (1976), The magnetospheric boundary layer: Site of plasma, momentum and energy transfer from the magnetosheath into the magnetosphere, *Geophysical Research Letters*, *3*(11), 685–688, doi:10.1029/GL003i011p00685.

Eastwood, J. P., and S. A. Kiehas (2015), Origin and Evolution of Plasmoids and Flux Ropes in the Magnetotails of Earth and Mars, in *Magnetotails in the Solar System*, pp. 269–287, American Geophysical Union (AGU), doi:10.1002/9781118842324.ch16.

Eastwood, J. P., T. D. Phan, M. Øieroset, and M. A. Shay (2010), Average properties of the magnetic reconnection ion diffusion region in the Earth's magnetotail: The 2001-2005 Cluster observations and comparison with simulations, *Journal of Geophysical Research: Space Physics*, *115*(8), doi:10.1029/2009JA014962.

Eastwood, J. P., T. D. Phan, R. C. Fear, D. G. Sibeck, V. Angelopoulos, M. Ieroset, and M. A. Shay (2012a), Survival of flux transfer event (FTE) flux ropes far along the tail magnetopause, *Journal of Geophysical Research: Space Physics*, *117*(8), doi:10.1029/2012JA017722.

Eastwood, J. P., J. J. Videira, D. A. Brain, and J. S. Halekas (2012b), A chain of magnetic flux ropes in the magnetotail of Mars, *Geophysical Research Letters*, *39*(3), doi:10.1029/2011GL050444.

Eastwood, J. P., M. V. Goldman, H. Hietala, D. L. Newman, R. Mistry, and G. Lapenta (2015), Ion reflection and acceleration near magnetotail dipolarization fronts associated with magnetic reconnection, *Journal of Geophysical Research: Space Physics*, *120*(1), 511–525, doi:10.1002/2014JA020516.

Eastwood, J. P., T. D. Phan, P. A. Cassak, D. J. Gershman, C. Haggerty, K. Malakit, M. A. Shay, R. Mistry, M. Øieroset, C. T. Russell, J. A. Slavin, M. R. Argall, L. A. Avanov, J. L. Burch, L. J. Chen, J. C. Dorelli, R. E. Ergun, B. L. Giles, Y. Khotyaintsev, B. Lavraud, P. A. Lindqvist, T. E. Moore, R. Nakamura, W. Paterson, C. Pollock, R. J. Strangeway, R. B. Torbert, and S. Wang (2016), Ion-scale secondary flux ropes generated by magnetopause reconnection as resolved by MMS, *Geophysical Research Letters*, *43*(10), 4716–4724, doi:10.1002/2016GL068747.

Elphic, R. C., C. A. Cattell, K. Takahashi, S. J. Bame, and C. T. Russell (1986), ISEE1 and 2 observations of magnetic flux ropes in the magnetotail: FTE's in the plasma sheet?, *Geophysical Research Letters*, *13*(7), 648–651, doi:10.1029/GL013i007p00648.

Eraker, J. H., and J. A. Simpson (1986), Acceleration of charged particles in Mercury's magnetosphere, *Journal of Geophysical Research*, *91*(A9), 9973, doi:10.1029/JA091iA09p09973.

Escoubet, C. P., R. Schmidt, and M. L. Goldstein (1997), Cluster - Science and Mission Overview, in *The Cluster and Phoenix Missions*, vol. 79, edited by P. Escoubet, C., R. Schmidt, and C. T. Russell, 1 ed., pp. 11–32, Springer Netherlands, doi:10.1007/978-94-011-5666-0_1.

Fairfield, D. H. (1979), On the average configuraton of the geomagnetic tail, *Journal of Geophysical Research: Space Physics*, *84*(A5), 1950–1958, doi:10.1029/JA084iA05p01950.

Fairfield, D. H. (1985), Solar wind control of magnetospheric pressure (CDAW 6), *Journal of Geophysical Research*, *90*(A2), 1201, doi:10.1029/JA090iA02p01201.

Fairfield, D. H. (1992), On the Structure of the Distant Magnetotail: ISEE 3, *J. Geophys. Res.*, *97*(A2), 1403–1410, doi:10.1029/91ja02388.

Fear, R., S. Milan, A. Fazakerley, C. Owen, T. Asikainen, M. Taylor, E. Lucek, H. Reme, I. Dandouras, and P. Daly (2007), Motion of flux transfer events: a test of the Cooling model, *Annales de Geophysique*, *25*(1978), 1669–1690, doi:10.5194/angeo-25-1669-2007.

Fear, R. C., and S. E. Milan (2012), The IMF dependence of the local time of transpolar arcs: Implications for formation mechanism, *Journal of Geophysical Research: Space Physics*, *117*(3), doi:10.1029/2011JA017209.

Felici, M., C. S. Arridge, A. J. Coates, S. V. Badman, M. K. Dougherty, C. M. Jackman, W. S. Kurth, H. Melin, D. G. Mitchell, D. B. Reisenfeld, and N. Sergis (2016), Cassini observations of ionospheric plasma in Saturn's magnetotail lobes, *Journal of Geophysical Research A: Space Physics*, *121*(1), 338–357, doi:10.1002/2015JA021648.

Fermo, R. L., J. F. Drake, and M. Swisdak (2010), A statistical model of magnetic islands in a current layer, *Citation: Physics of Plasmas*, *17*, doi:10.1063/1.3286437.

Fermo, R. L., J. F. Drake, M. Swisdak, and K. J. Hwang (2011), Comparison of a statistical model for magnetic islands in large current layers with Hall MHD simulations and Cluster FTE observations, *Journal of Geophysical Research: Space Physics*, *116*(9), doi:10.1029/2010JA016271.

Fitzgibbon, A., M. Pilu, and R. B. Fisher (1999), Direct least squares fitting of ellipses.pdf, *IEEE Transactions On Pattern Analysis and Machine Intelligence*, *21*(5), 476–480.

Fleshman, B. L., P. A. Delamere, and F. Bagenal (2010), A sensitivity study of the Enceladus torus, *J. Geophys. Res.*, *115*(E4), E04,007, doi:10.1029/2009je003372.

Foreman-Mackey, D., D. W. Hogg, D. Lang, and J. Goodman (2012), emcee: The MCMC Hammer, *Publications of the Astronomical Society of the Pacific*, *125*(925), 306–312, doi:10.1086/670067.

Forsyth, R. J., A. Balogh, E. J. Smith, G. Erdös, and D. J. McComas (1996), The underlying Parker spiral structure in the Ulysses magnetic field observations, 1990-1994, *Journal of Geophysical Research: Space Physics*, *101*(A1), 395–403, doi:10.1029/95JA02977.

Freeman, M. P., and S. K. Morley (2009), No evidence for externally triggered substorms based on superposed epoch analysis of IMF Bz, *Geophysical Research Letters*, *36*(21), L21,101, doi:10.1029/2009GL040621.

Fu, H. S., Y. V. Khotyaintsev, M. André, and A. Vaivads (2011), Fermi and betatron acceleration of suprathermal electrons behind dipolarization fronts, *Geophysical Research Letters*, *38*(16), doi:10.1029/2011GL048528.

Fu, H. S., A. Vaivads, Y. V. Khotyaintsev, M. André, J. B. Cao, V. Olshevsky, J. P. Eastwood, and A. Retinò (2017), Intermittent energy dissipation by turbulent reconnection, *Geophysical Research Letters*, *44*(1), 37–43, doi:10.1002/2016GL071787.

Fuselier, S. A., R. Frahm, W. S. Lewis, A. Masters, J. Mukherjee, S. M. Petrinec, and I. J. Sillanpaa (2014), The location of magnetic reconnection at Saturn's magnetopause:

A comparison with Earth, *Journal of Geophysical Research: Space Physics*, *119*(4), 2563–2578, doi:10.1002/2013JA019684.

Gabrielse, C., V. Angelopoulos, A. Runov, and D. L. Turner (2012), The effects of transient, localized electric fields on equatorial electron acceleration and transport toward the inner magnetosphere, *Journal of Geophysical Research: Space Physics*, *117*(10), doi:10.1029/2012JA017873.

Gabrielse, C., V. Angelopoulos, A. Runov, and D. L. Turner (2014), Statistical characteristics of particle injections throughout the equatorial magnetotail, *Journal of Geophysical Research: Space Physics*, *119*(4), 2512–2535, doi:10.1002/2013JA019638.

Gabrielse, C., C. Harris, V. Angelopoulos, A. Artemyev, and A. Runov (2016), The role of localized inductive electric fields in electron injections around dipolarizing flux bundles, *Journal of Geophysical Research: Space Physics*, *121*(10), 9560–9585, doi:10.1002/2016JA023061.

Gabrielse, C., V. Angelopoulos, C. Harris, A. Artemyev, L. Kepko, and A. Runov (2017), Extensive Electron Transport and Energization via Multiple, Localized Dipolarizing Flux Bundles, *Journal of Geophysical Research: Space Physics*, *122*(5), 5059–5076, doi:10.1002/2017JA023981.

Gershman, D. J., J. A. Slavin, J. M. Raines, T. H. Zurbuchen, B. J. Anderson, H. Korth, D. N. Baker, and S. C. Solomon (2014), Ion kinetic properties in Mercury's pre-midnight plasma sheet, *Geophysical Research Letters*, *41*(16), 5740–5747, doi:10.1002/2014GL060468.

Gershman, D. J., J. M. Raines, J. A. Slavin, T. H. Zurbuchen, T. Sundberg, S. A. Boardsen, B. J. Anderson, H. Korth, and S. C. Solomon (2015), MESSENGER observations of multiscale Kelvin-Helmholtz vortices at Mercury, *Journal of Geophysical Research: Space Physics*, *120*(6), 4354–4368, doi:10.1002/2014JA020903.

Gilchrist, W. G. (2000), *Statistical Modelling with Quantile Functions Statistical Modelling with Quantile Functions*, CRC Press.

Glocer, A., T. I. Gombosi, G. Toth, K. C. Hansen, A. J. Ridley, and A. Nagy (2007), Polar wind outflow model: Saturn results, *Journal of Geophysical Research: Space Physics*, *112*(1), doi:10.1029/2006JA011755.

Gosling, J., and V. Pizzo (1999), Formation and Evolution of Corotating Interaction Regions and their Three Dimensional Structure, *Space Science Reviews*, *89*(1/2), 21–52, doi:10.1023/A:1005291711900.

Gosling, J. T., M. F. Thomsen, S. J. Bame, R. C. Elphic, and C. T. Russell (1991), Observations of reconnection of interplanetary and lobe magnetic field lines at the high-latitude magnetopause, *Journal of Geophysical Research: Space Physics*, *96*(A8), 14,097–14,106, doi:10.1029/91JA01139.

Grigorenko, E. E., E. A. Kronberg, P. W. Daly, N. Y. Ganushkina, B. Lavraud, J. A. Sauvaud, and L. M. Zelenyi (2016), Origin of low proton-to-electron temperature ratio in the Earth's plasma sheet, *Journal of Geophysical Research A: Space Physics*, *121*(10), 9985–10,004, doi:10.1002/2016JA022874.

Grigorenko, E. E., E. A. Kronberg, and P. W. Daly (2017), Heating and acceleration of charged particles during magnetic dipolarizations, *Cosmic Research*, *55*(1), 57–66, doi:10.1134/S0010952517010063.

Gurnett, D. A., W. S. Kurth, D. L. Kirchner, G. B. Hospodarsky, T. F. Averkamp, P. Zarka, A. Lecacheux, R. Manning, A. Roux, P. Canu, N. Cornilleau-Wehrlin, P. Galopeau, A. Meyer, R. Boström, G. Gustafsson, J.-E. Wahlund, L. Åhlen, H. O. Rucker, H. P. Ladreiter, W. Macher, L. J. C. Woolliscroft, H. Alleyne, M. L. Kaiser, M. D. Desch, W. M. Farrell, C. C. Harvey, P. Louarn, P. J. Kellogg, K. Goetz, and A. Pedersen (2004), The Cassini Radio and Plasma Wave Investigation, *Space Science Reviews*, *114*(1-4), 395–463, doi:10.1007/s11214-004-1434-0.

Gustin, J., D. Grodent, A. Radioti, W. Pryor, L. Lamy, and J. Ajello (2017), Statistical study of Saturn's auroral electron properties with Cassini/UVIS FUV spectral images, *Icarus*, *284*, 264–283, doi:10.1016/J.ICARUS.2016.11.017.

Hansen, C. J. (2006), Enceladus' Water Vapor Plume, *Science*, *311*(5766), 1422–1425, doi:10.1126/science.1121254.

Hansen, C. J., L. Esposito, A. I. Stewart, J. Colwell, A. Hendrix, W. Pryor, D. Shemansky, and R. Wast (2006), Enceladus' water vapor plume, *Science*, *311*(5766), 1422–1425, doi:10.1126/science.1121254.

Hasegawa, H., M. Fujimoto, T.-D. Phan, H. Rème, A. Balogh, M. W. Dunlop, C. Hashimoto, and R. TanDokoro (2004), Transport of solar wind into Earth's magnetosphere through rolled-up KelvinHelmholtz vortices, *Nature*, *430*(7001), 755–758, doi:10.1038/nature02799.

Heidke, P. (1926), Berechnung Des Erfolges Und Der Güte Der Windstärkevorhersagen Im Sturmwarnungsdienst, *Geografiska Annaler*, *8*(4), 301–349, doi:10.1080/20014422.1926.11881138.

Henderson, M. G., G. D. Reeves, R. D. Belian, and J. S. Murphree (1996), Observations of magnetospheric substorms occurring with no apparent solar wind/IMF

trigger, *Journal of Geophysical Research: Space Physics*, *101*(A5), 10,773–10,791, doi:10.1029/96JA00186.

Hidalgo, M. A., and C. Cid (2002), Elliptical cross-section model for the magnetic topology of magnetic clouds, *October*, *29*(13), 13–16, doi:10.1029/2001GL013875.

Hill, T. (1979), Inertial limit on corotation, *Journal of Geophysical Research*, *84*(A11), 6554, doi:10.1029/JA084iA11p06554.

Hill, T. W., A. M. Rymer, J. L. Burch, F. J. Crary, D. T. Young, M. F. Thomsen, D. Delapp, N. André, A. J. Coates, and G. R. Lewis (2005), Evidence for rotationally driven plasma transport in Saturn's magnetosphere, *Geophys. Res. Lett*, *32*, 14–10, doi:10.1029/2005GL022620.

Hill, T. W., M. F. Thomsen, M. G. Henderson, R. L. Tokar, A. J. Coates, H. J. McAndrews, G. R. Lewis, D. G. Mitchell, C. M. Jackman, C. T. Russell, M. K. Dougherty, F. J. Crary, and D. T. Young (2008), Plasmoids in Saturn's magnetotail, *Journal of Geophysical Research: Space Physics*, *113*(1), 1–16, doi:10.1029/2007JA012626.

Hones, E. W. (1977), Substorm processes in magnetotail - comments on hot tenuous plasmas, fireballs, and boundary-layers in Earth's magnetotail, *Journal of Geophysical Research-Space Physics*, *82*(35), 5633–5640.

Hsu, T.-S., and R. L. McPherron (2004), Average characteristics of triggered and nontriggered substorms, *Journal of Geophysical Research*, *109*(A7), A07,208, doi:10.1029/2003JA009933.

Huang, S. Y., M. Zhou, X. H. Deng, Z. G. Yuan, Y. Pang, Q. Wei, W. Su, H. M. Li, and Q. Q. Wang (2012), Kinetic structure and wave properties associated with sharp dipolarization front observed by Cluster, *Annales Geophysicae*, *30*(1), 97–107, doi:10.5194/angeo-30-97-2012.

Huang, S. Y., H. S. Fu, Z. G. Yuan, M. Zhou, S. Fu, X. H. Deng, W. J. Sun, Y. Pang, D. D. Wang, H. M. Li, H. M. Li, and X. D. Yu (2015), Electromagnetic energy conversion at dipolarization fronts: Multispacecraft results, *Journal of Geophysical Research A: Space Physics*, *120*(6), 4496–4502, doi:10.1002/2015JA021083.

Hubert, B., M. Palmroth, T. V. Laitinen, P. Janhunen, S. E. Milan, A. Grocott, S. W. H. Cowley, T. Pulkkinen, and J.-C. Gérard (2006), Compression of the Earth's magnetotail by interplanetary shocks directly drives transient magnetic flux closure, *Geophysical Research Letters*, *33*(10), doi:10.1029/2006GL026008.

Hughes, W. J., and D. G. Sibeck (1987), On the 3-dimensional structure of plasmoids, *Geophysical Research Letters*, *14*(6), 636–639, doi:10.1029/GL014i006p00636.

Hundhausen, A. J. (1972), *Coronal Expansion and Solar Wind*, *Physics and Chemistry in Space*, vol. 5, Springer Berlin Heidelberg, Berlin, Heidelberg, doi:10.1007/978-3-642-65414-5.

Hunt, G. J., S. W. H. Cowley, G. Provan, E. J. Bunce, I. I. Alexeev, E. S. Belenkaya, V. V. Kalegaev, M. K. Dougherty, and A. J. Coates (2014), Field-aligned currents in Saturn's southern nightside magnetosphere: Subcorotation and planetary period oscillation components, *Journal of Geophysical Research: Space Physics*, *119*(12), 9847–9899, doi:10.1002/2014JA020506.

Hwang, K. J., M. L. Goldstein, E. Lee, and J. S. Pickett (2011), Cluster observations of multiple dipolarization fronts, *Journal of Geophysical Research: Space Physics*, *116*(4), doi:10.1029/2010JA015742.

Ieda, A., S. Machida, T. Mukai, Y. Saito, T. Yamamoto, A. Nishida, T. Terasawa, and S. Kokubun (1998), Statistical analysis of the plasmoid evolution with Geotail observations, *Journal of Geophysical Research*, *103*(A3), 4453, doi:10.1029/97JA03240.

Iess, L., D. J. Stevenson, M. Parisi, D. Hemingway, R. A. Jacobson, J. I. Lunine, F. Nimmo, J. W. Armstrong, S. W. Asmar, M. Ducci, and P. Tortora (2014), The Gravity Field and Interior Structure of Enceladus, *Science*, *344*(6179), 78–80, doi:10.1126/science.1250551.

Imber, S. M., J. A. Slavin, H. U. Auster, and V. Angelopoulos (2011), A THEMIS survey of flux ropes and traveling compression regions: Location of the near-Earth reconnection site during solar minimum, *Journal of Geophysical Research: Space Physics*, *116*(A2), doi:10.1029/2010JA016026.

Imber, S. M., J. A. Slavin, S. A. Boardsen, B. J. Anderson, H. Korth, R. L. McNutt, and S. C. Solomon (2014), MESSENGER observations of large dayside flux transfer events: Do they drive Mercury's substorm cycle?, *Journal of Geophysical Research: Space Physics*, *119*(7), 5613–5623, doi:10.1002/2014JA019884.

Jackman, C. M., and C. S. Arridge (2011a), Solar Cycle Effects on the Dynamics of Jupiter's and Saturn's Magnetospheres, *Solar Physics*, *274*(1-2), 481–502, doi:10.1007/s11207-011-9748-z.

Jackman, C. M., and C. S. Arridge (2011b), Statistical properties of the magnetic field in the Kronian magnetotail lobes and current sheet, *Journal of Geophysical Research: Space Physics*, *116*(5), 8, doi:10.1029/2010JA015973.

Jackman, C. M., N. Achilleos, E. J. Bunce, S. W. H. Cowley, M. K. Dougherty, G. H. Jones, S. E. Milan, and E. J. Smith (2004), Interplanetary magnetic field at 9

AU during the declining phase of the solar cycle and its implications for Saturn's magnetospheric dynamics, *Journal of Geophysical Research*, *109*(A11), A11,203, doi: 10.1029/2004JA010614.

Jackman, C. M., C. T. Russell, D. J. Southwood, C. S. Arridge, N. Achilleos, and M. K. Dougherty (2007), Strong rapid dipolarizations in Saturn's magnetotail: In situ evidence of reconnection, *Geophysical Research Letters*, *34*(11), 5, doi:10.1029/ 2007GL029764.

Jackman, C. M., R. J. Forsyth, and M. K. Dougherty (2008a), The overall configuration of the interplanetary magnetic field upstream of Saturn as revealed by Cassini observations, *Journal of Geophysical Research: Space Physics*, *113*(8), doi: 10.1029/2008JA013083.

Jackman, C. M., C. S. Arridge, N. Krupp, E. J. Bunce, D. G. Mitchell, H. J. McAndrews, M. K. Dougherty, C. T. Russell, N. Achilleos, G. H. Jones, and A. J. Coates (2008b), A multi-instrument view of tail reconnection at Saturn, *Journal of Geophysical Research: Space Physics*, *113*(11), doi:10.1029/2008JA013592.

Jackman, C. M., C. S. Arridge, H. J. McAndrews, M. G. Henderson, and R. J. Wilson (2009a), Northward field excursions in Saturn's magnetotail and their relationship to magnetospheric periodicities, *Geophysical Research Letters*, *36*(16), 5, doi:10.1029/ 2009GL039149.

Jackman, C. M., L. Lamy, M. P. Freeman, P. Zarka, B. Cecconi, W. S. Kurth, S. W. H. Cowley, and M. K. Dougherty (2009b), On the character and distribution of lower-frequency radio emissions at Saturn and their relationship to substorm-like events, *Journal of Geophysical Research: Space Physics*, *114*(8), doi:10.1029/2008JA013997.

Jackman, C. M., C. S. Arridge, J. A. Slavin, S. E. Milan, L. Lamy, M. K. Dougherty, and A. J. Coates (2010), In situ observations of the effect of a solar wind compression on Saturn's magnetotail, *J. Geophys. Res.*, *115*(A10), doi:10.1029/2010ja015312.

Jackman, C. M., J. A. Slavin, and S. W. Cowley (2011), Cassini observations of plasmoid structure and dynamics: Implications for the role of magnetic reconnection in magnetospheric circulation at Saturn, *Journal of Geophysical Research: Space Physics*, *116*(10), 9, doi:10.1029/2011JA016682.

Jackman, C. M., N. Achilleos, S. W. H. Cowley, E. J. Bunce, A. Radioti, D. Grodent, S. V. Badman, M. K. Dougherty, and W. Pryor (2013), Auroral counterpart of magnetic field dipolarizations in Saturn's tail, *Planetary and Space Science*, *82-83*, 34–42, doi:10.1016/j.pss.2013.03.010.

Jackman, C. M., C. S. Arridge, N. André, F. Bagenal, J. Birn, M. P. Freeman, X. Jia, A. Kidder, S. E. Milan, A. Radioti, J. A. Slavin, M. F. Vogt, M. Volwerk, and A. P. Walsh (2014a), Large-scale structure and dynamics of the magnetotails of Mercury, Earth, Jupiter and Saturn, *Space Science Reviews*, *182*(1-4), 85–154, doi:10.1007/s11214-014-0060-8.

Jackman, C. M., J. A. Slavin, M. G. Kivelson, D. J. Southwood, N. Achilleos, M. F. Thomsen, G. A. Dibraccio, J. P. Eastwood, M. P. Freeman, M. K. Dougherty, and M. F. Vogt (2014b), Saturn's dynamic magnetotail: A comprehensive magnetic field and plasma survey of plasmoids and traveling compression regions and their role in global magnetospheric dynamics, *Journal of Geophysical Research: Space Physics*, *119*(7), 5465–5494, doi:10.1002/2013JA019388.

Jackman, C. M., M. F. Thomsen, D. G. Mitchell, N. Sergis, C. S. Arridge, M. Felici, S. V. Badman, C. Paranicas, X. Jia, G. B. Hospodarksy, M. Andriopoulou, K. K. Khurana, A. W. Smith, and M. K. Dougherty (2015), Field dipolarization in Saturn's magnetotail with planetward ion flows and energetic particle flow bursts: Evidence of quasi-steady reconnection, *Journal of Geophysical Research: Space Physics*, *120*(5), 3603–3617, doi:10.1002/2015JA020995.

Jasinski, J. M., C. S. Arridge, L. Lamy, J. S. Leisner, M. F. Thomsen, D. G. Mitchell, A. J. Coates, A. Radioti, G. H. Jones, E. Roussos, N. Krupp, D. Grodent, M. K. Dougherty, and J. H. Waite (2014), Cusp observation at Saturn's high-latitude magnetosphere by the Cassini spacecraft, *Geophysical Research Letters*, *41*(5), 1382–1388, doi:10.1002/2014GL059319.

Jasinski, J. M., J. A. Slavin, C. S. Arridge, G. Poh, X. Jia, N. Sergis, A. J. Coates, G. H. Jones, and J. H. Waite (2016), Flux transfer event observation at Saturn's dayside magnetopause by the Cassini spacecraft, *Geophysical Research Letters*, *43*(13), 6713–6723, doi:10.1002/2016GL069260.

Jasinski, J. M., J. A. Slavin, J. M. Raines, and G. A. DiBraccio (2017), Mercury's solar wind interaction as characterized by magnetospheric plasma mantle observations with MESSENGER, *Journal of Geophysical Research: Space Physics*, doi:10.1002/2017JA024594.

Jia, X., and M. G. Kivelson (2012), Driving Saturn's magnetospheric periodicities from the upper atmosphere/ionosphere: Magnetotail response to dual sources, *Journal of Geophysical Research: Space Physics*, *117*(A11), n/a–n/a, doi:10.1029/2012JA018183.

Jia, X., K. C. Hansen, T. I. Gombosi, M. G. Kivelson, G. Tóth, D. L. Dezeeuw, and A. J. Ridley (2012), Magnetospheric configuration and dynamics of Saturn's magnetosphere: A global MHD simulation, *Journal of Geophysical Research: Space Physics*, *117*(5), 22, doi:10.1029/2012JA017575.

Johnson, C. L., M. E. Purucker, H. Korth, B. J. Anderson, R. M. Winslow, M. M. H. Al Asad, J. A. Slavin, I. I. Alexeev, R. J. Phillips, M. T. Zuber, and S. C. Solomon (2012), MESSENGER observations of Mercury's magnetic field structure, *Journal of Geophysical Research E: Planets*, *117*(12), doi:10.1029/2012JE004217.

Jurac, S., and J. D. Richardson (2005), A self-consistent model of plasma and neutrals at Saturn: Neutral cloud morphology, *Journal of Geophysical Research: Space Physics*, *110*(A9), A09,220, doi:10.1029/2004JA010635.

Kaiser, M. L., and M. D. Desch (1984), Radio emissions from the planets Earth, Jupiter, and Saturn, *Reviews of Geophysics*, *22*(4), 373, doi:10.1029/RG022i004p00373.

Kanani, S. J., C. S. Arridge, G. H. Jones, A. N. Fazakerley, H. J. McAndrews, N. Sergis, S. M. Krimigis, M. K. Dougherty, A. J. Coates, D. T. Young, K. C. Hansen, and N. Krupp (2010), A new form of Saturn's magnetopause using a dynamic pressure balance model, based on in situ, multi-instrument Cassini measurements, *Journal of Geophysical Research: Space Physics*, *115*(6), 1–11, doi:10.1029/2009JA014262.

Kane, M., D. G. Mitchell, J. F. Carbary, and S. M. Krimigis (2014), Plasma convection in the nightside magnetosphere of Saturn determined from energetic ion anisotropies, *Planetary and Space Science*, *91*, 1–13, doi:10.1016/j.pss.2013.10.001.

Karimabadi, H., T. B. Sipes, H. White, M. Marinucci, A. Dmitriev, J. K. Chao, and J. Driscoll (2007), Data Mining in Space Physics: 1. The MineTool Algorithm, *Journal of Geophysical Research-Space Physics*, *112*(A11), 1–49.

Karimabadi, H., T. B. Sipes, Y. Wang, B. Lavraud, and a. Roberts (2009), A new multivariate time series data analysis technique: Automated detection of flux transfer events using Cluster data, *Journal of Geophysical Research*, *114*(A6), A06,216, doi:10.1029/2009JA014202.

Kasahara, S., E. A. Kronberg, N. Krupp, T. Kimura, C. Tao, S. V. Badman, A. Retinò, and M. Fujimoto (2011), Magnetic reconnection in the Jovian tail: X-line evolution and consequent plasma sheet structures, *Journal of Geophysical Research: Space Physics*, *116*(11), 15, doi:10.1029/2011JA016892.

Kawano, H., S. Kokubun, and K. Takahashi (1992), Survey of Transient Magnetic Field Events in the Dayside Magnetosphere, *Journal of Geophysical Research*, *97*(A7), 10,677–10,692, doi:10.1029/92JA00369.

Keiling, A., C. M. Jackman, and P. A. Delamere (2015), *Magnetotails in the Solar System*, book section Origin and, pp. 1–407, John Wiley & Sons, Inc, doi:10.1002/9781118842324.

Kellert, S., E. J. Bunce, A. J. Coates, and S. W. Cowley (2009), Thickness of Saturn's ring current determined from north-south Cassini passes through the current layer, *Journal of Geophysical Research: Space Physics*, *114*(4), doi:10.1029/2008JA013942.

Kessel, R. L., S.-H. Chen, J. L. Green, S. F. Fung, S. A. Boardsen, L. C. Tan, T. E. Eastman, J. D. Craven, and L. A. Frank (1996), Evidence of high-latitude reconnecting during northward IMF: Hawkeye observations, *Geophysical Research Letters*, *23*(5), 583–586, doi:10.1029/95GL03083.

Khabrov, A., and B. U. Sonnerup (1998), Error estimates for minimum variance analysis, *Jgr*, *103*(A4), 6641–6651, doi:10.1029/97JA03731.

Kidder, A., C. S. Paty, R. M. Winglee, and E. M. Harnett (2012), External triggering of plasmoid development at Saturn, *Journal of Geophysical Research: Space Physics*, *117*(7), doi:10.1029/2012JA017625.

Kiehas, S. A., V. Angelopoulos, A. Runov, M. B. Moldwin, and C. Mstl (2012), On the formation of tilted flux ropes in the Earth's magnetotail observed with ARTEMIS, *Journal of Geophysical Research: Space Physics*, *117*(5), doi:10.1029/2011JA017377.

Kiehas, S. A., V. Angelopoulos, A. Runov, and S. S. Li (2013), On the azimuthal size of flux ropes near lunar orbit, *Journal of Geophysical Research: Space Physics*, *118*(7), 4415–4424, doi:10.1002/jgra.50425.

Kivelson, M. G., and K. K. Khurana (1995), Models of flux ropes embedded in a Harris neutral sheet: Force-free solutions in low and high beta plasmas, *Journal of Geophysical Research*, *100*(A12), 23,637–23,646, doi:10.1029/95JA01548.

Kivelson, M. G., and D. J. Southwood (2005), Dynamical consequences of two modes of centrifugal instability in Jupiter's outer magnetosphere, *Journal of Geophysical Research: Space Physics*, *110*(A12), 15, doi:10.1029/2005JA011176.

Kivelson, M. G. M. G., and C. T. C. T. Russell (1995), Introduction to Space Physics, p. 568.

Kmigis, S. M., D. G. Mitchell, D. C. Hamilton, N. Krupp, S. Livi, E. C. Roelof, J. Dandouras, T. P. Armstrong, B. H. Mauk, C. Paranicas, P. C. Brandt, S. Bolton, A. F. Cheng, T. Choo, G. Gloeckler, J. Hayes, K. C. Hsieh, W. H. Ip, S. Jaskulek, E. P. Keath, E. Kirsch, M. Kusterer, A. Lagg, L. J. Lanzerotti, D. LaVallee, J. Manweiler, R. W. McEntire, W. Rasmuss, J. Saur, F. S. Turner, D. J. Williams, and J. Woch

(2005), Dynamics of Saturn's magnetosphere from MIMI during Cassini's orbital insertion, *Science*, *307*(5713), 1270–1273, doi:10.1126/science.1105978.

Korth, H., B. J. Anderson, D. J. Gershman, J. M. Raines, J. A. Slavin, T. H. Zurbuchen, S. C. Solomon, and R. L. McNutt (2014), Plasma distribution in Mercury's magnetosphere derived from MESSENGER Magnetometer and Fast Imaging Plasma Spectrometer observations, *Journal of Geophysical Research: Space Physics*, *119*(4), 2917–2932, doi:10.1002/2013JA019567.

Krimigis, S. M., T. P. Armstrong, W. I. Axford, C. O. Bostrom, G. Gloeckler, E. P. Keath, L. J. Lanzerotti, J. F. Carbary, D. C. Hamilton, and E. C. Roelof (1982), Low-energy hot plasma and particles in Saturn's magnetosphere, *Science*, *215*(4532), 571–577, doi:10.1126/science.215.4532.571.

Krimigis, S. M., J. F. Carbary, E. P. Keath, T. P. Armstrong, L. J. Lanzerotti, and G. Gloeckler (1983), General characteristics of hot plasma and energetic particles in the Saturnian magnetosphere: Results from the Voyager spacecraft, *Journal of Geophysical Research: Space Physics*, *88*(A11), 8871–8892, doi:10.1029/JA088iA11p08871.

Krimigis, S. M., D. G. Mitchell, D. C. Hamilton, S. Livi, J. Dandouras, S. Jaskulek, T. P. Armstrong, J. D. Boldt, A. F. Cheng, G. Gloeckler, J. R. Hayes, K. C. Hsieh, W.-H. Ip, E. P. Keath, E. Kirsch, N. Krupp, L. J. Lanzerotti, R. Lundgren, B. H. Mauk, R. W. McEntire, E. C. Roelof, C. E. Schlemm, B. E. Tossman, B. Wilken, and D. J. Williams (2004), Magnetosphere Imaging Instrument (MIMI) on the Cassini Mission to Saturn/Titan, *Space Science Reviews*, *114*(1-4), 233–329, doi:10.1007/s11214-004-1410-8.

Kronberg, E. A., J. Woch, N. Krupp, A. Lagg, K. K. Khurana, and K. H. Glassmeier (2005), Mass release at Jupiter: Substorm-like processes in the Jovian magnetotail, *Journal of Geophysical Research: Space Physics*, *110*(A3), n/a—-n/a, doi:10.1029/2004JA010777.

Lai, H. R., H. Y. Wei, C. T. Russell, C. S. Arridge, and M. K. Dougherty (2012), Reconnection at the magnetopause of Saturn: Perspective from FTE occurrence and magnetosphere size, *Journal of Geophysical Research: Space Physics*, *117*(5), doi:10.1029/2011JA017263.

Lamy, L., P. Zarka, B. Cecconi, R. Prangé, W. S. Kurth, and D. A. Gurnett (2008), Saturn kilometric radiation: Average and statistical properties, *Journal of Geophysical Research: Space Physics*, *113*(7), doi:10.1029/2007JA012900.

Lamy, L., P. Schippers, P. Zarka, B. Cecconi, C. S. Arridge, M. K. Dougherty, P. Louarn, N. Andr, W. S. Kurth, R. L. Mutel, D. A. Gurnett, and A. J. Coates (2010), Properties of Saturn kilometric radiation measured within its source region, *Geophysical Research Letters*, *37*(12), doi:10.1029/2010GL043415.

Lamy, L., R. Prangé, W. Pryor, J. Gustin, S. V. Badman, H. Melin, T. Stallard, D. Mitchell, and P. C. Brandt (2013), Multispectral simultaneous diagnosis of Saturn's aurorae throughout a planetary rotation, *Journal of Geophysical Research: Space Physics*, *118*(8), 4817–4843, doi:10.1002/jgra.50404.

Lee, L. C., and Z. F. Fu (1985), A theory of magnetic flux transfer at the Earth's magnetopause, *Geophysical Research Letters*, *12*(2), 105–108, doi:10.1029/GL012i002p00105.

Lepping, R. P., J. A. Jones, and L. F. Burlaga (1990), Magnetic field structure of interplanetary magnetic clouds at 1 AU, *Journal of Geophysical Research*, *95*(A8), 11,957, doi:10.1029/JA095iA08p11957.

Lepping, R. P., D. H. Fairfield, J. Jones, L. A. Frank, W. R. Paterson, S. Kokubun, and T. Yamamoto (1995), Crosstail magnetic flux ropes as observed by the GEOTAIL spacecraft, *Geophysical Research Letters*, *22*(10), 1193–1196, doi:10.1029/94GL01114.

Lepping, R. P., J. A. Slavin, M. Hesse, J. Jones, and A. Szabo (1996), Analysis of magnetotail flux ropes with strong core fields: ISEE 3 observations, *Earth, Planets and Space*, *48*(5-6), 589–601, doi:10.5636/jgg.48.589.

Lewis, G. R., N. André, C. S. Arridge, A. J. Coates, L. K. Gilbert, D. R. Linder, and A. M. Rymer (2008), Derivation of density and temperature from the Cassini-Huygens CAPS electron spectrometer, *Planetary and Space Science*, *56*(7), 901–912, doi:10.1016/j.pss.2007.12.017.

Lindsay, S. T., M. K. James, E. J. Bunce, S. M. Imber, H. Korth, A. Martindale, and T. K. Yeoman (2015), MESSENGER X-ray observations of magnetosphere-surface interaction on the nightside of Mercury, *Planetary and Space Science*, *125*, 72–79, doi:10.1016/j.pss.2016.03.005.

Liu, J., V. Angelopoulos, A. Runov, and X.-Z. Zhou (2013), On the current sheets surrounding dipolarizing flux bundles in the magnetotail: The case for wedgelets, *Journal of Geophysical Research: Space Physics*, *118*(5), 2000–2020, doi:10.1002/jgra.50092.

Liu, J., V. Angelopoulos, X. J. Zhang, D. L. Turner, C. Gabrielse, A. Runov, J. Li, H. O. Funsten, and H. E. Spence (2016), Dipolarizing flux bundles in the cis-geosynchronous

magnetosphere: Relationship between electric fields and energetic particle injections, *Journal of Geophysical Research A: Space Physics*, *121*(2), 1362–1376, doi:10.1002/2015JA021691.

Liu, X., T. W. Hill, R. A. Wolf, S. Sazykin, R. W. Spiro, and H. Wu (2010), Numerical simulation of plasma transport in Saturn's inner magnetosphere using the Rice Convection Model, *Journal of Geophysical Research: Space Physics*, *115*(12), doi:10.1029/2010JA015859.

Lockwood, M., and S. W. H. Cowley (1992), Ionospheric convection and the substorm cycle, in *The First International Conference on Substorms, ICS-1*, pp. 99—-109.

Lu, S., Q. Lu, Y. Lin, X. Wang, Y. Ge, R. Wang, M. Zhou, H. Fu, C. Huang, M. Wu, and S. Wang (2015), Dipolarization fronts as earthward propagating flux ropes: A three-dimensional global hybrid simulation, *Journal of Geophysical Research A: Space Physics*, *120*(8), 6286–6300, doi:10.1002/2015JA021213.

Lundquist, S. (1950), Magneto-hydrostatic fields, *Ark. Fysik*, *2*, 361–365.

Lyons, L. R., G. T. Blanchard, J. C. Samson, R. P. Lepping, T. Yamamoto, and T. Moretto (1997), Coordinated observations demonstrating external substorm triggering, *Journal of Geophysical Research: Space Physics*, *102*(A12), 27,039–27,051, doi:10.1029/97JA02639.

Ma, X., A. Otto, and P. A. Delamere (2014), Interaction of magnetic reconnection and Kelvin-Helmholtz modes for large magnetic shear: 2. Reconnection trigger, *Journal of Geophysical Research: Space Physics*, *119*(2), 808–820, doi:10.1002/2013JA019225.

Ma, X., P. Delamere, A. Otto, and B. Burkholder (2017), Plasma Transport Driven by the Three-dimensional Kelvin-Helmholtz Instability, *Journal of Geophysical Research: Space Physics*, doi:10.1002/2017JA024394.

Malaspina, D. M., and J. T. Gosling (2012), Two spacecraft observations of magnetic discontinuities in the solar wind with STEREO, *Journal of Geophysical Research: Space Physics*, *117*(4), doi:10.1029/2011JA017375.

Masters, A. (2015), The dayside reconnection voltage applied to Saturn's magnetosphere, *Geophysical Research Letters*, *42*(8), 2577–2585, doi:10.1002/2015GL063361.

Masters, A., N. Achilleos, C. Bertucci, M. Dougherty, S. Kanani, C. Arridge, H. McAndrews, and A. Coates (2009), Surface waves on Saturn's dawn flank magnetopause driven by the Kelvin-Helmholtz instability, *Planetary and Space Science*, *57*(14-15), 1769–1778, doi:10.1016/J.PSS.2009.02.010.

Masters, A., N. Achilleos, M. G. Kivelson, N. Sergis, M. K. Dougherty, M. F. Thomsen, C. S. Arridge, S. M. Krimigis, H. J. McAndrews, S. J. Kanani, N. Krupp, and A. J. Coates (2010), Cassini observations of a Kelvin-Helmholtz vortex in Saturn's outer magnetosphere, *Journal of Geophysical Research: Space Physics*, *115*(7), doi:10.1029/2010JA015351.

Masters, A., D. G. Mitchell, A. J. Coates, and M. K. Dougherty (2011), Saturn's low-latitude boundary layer: 1. Properties and variability, *Journal of Geophysical Research: Space Physics*, *116*(6), doi:10.1029/2010JA016421.

Masters, A., J. P. Eastwood, M. Swisdak, M. F. Thomsen, C. T. Russell, N. Sergis, F. J. Crary, M. K. Dougherty, A. J. Coates, and S. M. Krimigis (2012), The importance of plasma β conditions for magnetic reconnection at Saturn's magnetopause, *Geophysical Research Letters*, *39*(8), doi:10.1029/2012GL051372.

McAndrews, H. J., C. J. Owen, M. F. Thomsen, B. Lavraud, A. J. Coates, M. K. Dougherty, and D. T. Young (2008), Evidence for reconnection at Saturn's magnetopause, *Journal of Geophysical Research: Space Physics*, *113*(4), doi:10.1029/2007JA012581.

McAndrews, H. J., M. F. Thomsen, C. S. Arridge, C. M. Jackman, R. J. Wilson, M. G. Henderson, R. L. Tokar, K. K. Khurana, E. C. Sittler, A. J. Coates, and M. K. Dougherty (2009), Plasma in Saturn ' s nightside magnetosphere and the implications for global circulation, *Planetary and Space Science*, *57*(14-15), 1–9, doi:10.1016/j.pss.2009.03.003.

McAndrews, H. J., M. F. Thomsen, C. Arridge, C. Jackman, R. Wilson, M. Henderson, R. Tokar, K. Khurana, E. Sittler, A. Coates, and M. Dougherty (2014), Corrigendum to Plasma in Saturns nightside magnetosphere and the implications for global circulation [Planet. Space Sci. 57(1415) (2009) 17141722], *Planetary and Space Science*, *97*(0), 86–87, doi:10.1016/j.pss.2014.05.011.

McNutt, R. L., S. C. Solomon, P. D. Bedini, B. J. Anderson, D. T. Blewett, L. G. Evans, R. E. Gold, S. M. Krimigis, S. L. Murchie, L. R. Nittler, R. J. Phillips, L. M. Prockter, J. A. Slavin, M. T. Zuber, E. J. Finnegan, and D. G. Grant (2014), MESSENGER at Mercury: Early orbital operations, *Acta Astronautica*, *93*, 509–515, doi:10.1016/J.ACTAASTRO.2012.08.012.

McPherron, R. L., C. T. Russell, M. G. Kivelson, and P. J. Coleman (1973), Substorms in space: The correlation between ground and satellite observations of the magnetic field, *Radio Science*, *8*(11), 1059–1076, doi:10.1029/RS008i011p01059.

Milan, S. E., M. Lester, S. W. H. Cowley, and M. Brittnacher (2000), Dayside convection and auroral morphology during an interval of northward interplanetary magnetic field, *Annales Geophysicae*, *18*(4), 436–444, doi:10.1007/s00585-000-0436-9.

Milan, S. E., M. Lester, S. W. H. Cowley, K. Oksavik, M. Brittnacher, R. A. Greenwald, G. Sofko, and J.-P. Villain (2003), Variations in the polar cap area during two substorm cycles, *Annales Geophysicae*, *21*(5), 1121–1140, doi:10.5194/angeo-21-1121-2003.

Milan, S. E., S. W. H. Cowley, M. Lester, D. M. Wright, J. A. Slavin, M. Fillingim, C. W. Carlson, and H. J. Singer (2004), Response of the magnetotail to changes in the open flux content of the magnetosphere, *Journal of Geophysical Research*, *109*(A4), A04,220, doi:10.1029/2003JA010350.

Milan, S. E., G. Provan, and B. Hubert (2007), Magnetic flux transport in the Dungey cycle: A survey of dayside and nightside reconnection rates, *Journal of Geophysical Research: Space Physics*, *112*(1), doi:10.1029/2006JA011642.

Milan, S. E., J. Hutchinson, P. D. Boakes, and B. Hubert (2009), Influences on the radius of the auroral oval, *Annales Geophysicae*, *27*(7), 2913–2924, doi:10.5194/angeo-27-2913-2009.

Milan, S. E., J. S. Gosling, and B. Hubert (2012), Relationship between interplanetary parameters and the magnetopause reconnection rate quantified from observations of the expanding polar cap, *Journal of Geophysical Research: Space Physics*, *117*(3), doi:10.1029/2011JA017082.

Mitchell, D. G., P. C. Brandt, E. C. Roelof, J. Dandouras, S. M. Krimigis, B. H. Mauk, C. P. Paranicas, N. Krupp, D. C. Hamilton, W. S. Kurth, P. Zarka, M. K. Dougherty, E. J. Bunce, and D. E. Shemansky (2005), Energetic ion acceleration in Saturn's magnetotail: Substorms at Saturn?, *Geophysical Research Letters*, *32*(20), 1–4, doi:10.1029/2005GL022647.

Mitchell, D. G., W. S. Kurth, G. B. Hospodarsky, N. Krupp, J. Saur, B. H. Mauk, J. F. Carbary, S. M. Krimigis, M. K. Dougherty, and D. C. Hamilton (2009), Ion conics and electron beams associated with auroral processes on Saturn, *Journal of Geophysical Research: Space Physics*, *114*(A2), doi:10.1029/2008JA013621.

Moldwin, M. B., and W. J. Hughes (1991), Plasmoids as magnetic flux ropes, *Physics*, *96*(A8), 51–64, doi:10.1029/91JA01167.

Moldwin, M. B., and W. J. Hughes (1992), On the Formation and Evolution of Plasmoids: A Survey of ISEE 3 Geotail Data, *J. Geophys. Res.*, *97*(A12), 19,259–19,282, doi:10.1029/92ja01598.

Mukai, T., S. Machida, Y. Saito, T. Terasawa, N. Kaya, T. Obara, M. Ejiri, and A. Nishida (1994), The Low Energy Particle (LEP) experiment onboard the GEOTAIL satellite, *J. Geomagn. Geoelectr.*, *46*(8), 669–692, doi:10.5636/jgg.46.669.

Mutel, R. L., J. D. Menietti, D. A. Gurnett, W. Kurth, P. Schippers, C. Lynch, L. Lamy, C. Arridge, and B. Cecconi (2010), CMI growth rates for Saturnian kilometric radiation, *Geophysical Research Letters*, *37*(19), doi:10.1029/2010GL044940.

Nagai, T., K. Takahashi, H. Kawano, T. Yamamoto, S. Kokubun, and A. Nishida (1994), Initial GEOTAIL survey of magnetic substorm signatures in the magnetotail, *Geophysical Research Letters*, *21*(25), 2991–2994, doi:10.1029/94GL01420.

Nakagawa, T., and A. Nishida (1989), Southward magnetic field in the neutral sheet produced by wavy motions propagating in the dawn-dusk direction, *Geophysical Research Letters*, *16*(11), 1265–1268, doi:10.1029/GL016i011p01265.

Nakamura, R., W. Baumjohann, B. Klecker, Y. Bogdanova, A. Balogh, H. Rème, J. M. Bosqued, I. Dandouras, J. A. Sauvaud, K.-H. Glassmeier, L. Kistler, C. Mouikis, T. L. Zhang, H. Eichelberger, and A. Runov (2002), Motion of the dipolarization front during a flow burst event observed by Cluster, *Geophysical Research Letters*, *29*(20), 3–1–3–4, doi:10.1029/2002GL015763.

Nakamura, R., A. Retinò, W. Baumjohann, M. Volwerk, N. Erkaev, B. Klecker, E. A. Lucek, I. Dandouras, M. André, and Y. Khotyaintsev (2009), Evolution of dipolarization in the near-Earth current sheet induced by Earthward rapid flux transport, *Annales Geophysicae*, *27*(4), 1743–1754, doi:10.5194/angeo-27-1743-2009.

Ness, N. F. (1965), The Earth's magnetic tail, *Journal of Geophysical Research*, *70*(13), 2989–3005, doi:10.1029/JZ070i013p02989.

Ness, N. F., K. W. Behannon, R. P. Lepping, Y. C. Whang, and K. H. Schatten (1974), Magnetic field observations near Mercury: Preliminary results from Mariner 10, *Science*, *185*(4146), 151–160, doi:10.1126/science.185.4146.151.

Ness, N. F., K. W. Behannon, R. P. Lepping, and Y. C. Whang (1976), Observations of Mercury's magnetic field, *Icarus*, *28*(4), 479–488, doi:10.1016/0019-1035(76)90121-4.

Ness, N. F., M. H. Acuña, R. P. Lepping, J. E. P. Connerney, K. W. Behannon, L. F. Burlaga, and F. M. Neubauer (1981), Magnetic Field Studies by Voyager 1: Preliminary Results at Saturn, *Science*, *212*(4491), 211–217, doi:10.1126/science.212.4491.211.

Newell, P. T., and K. Liou (2011), Solar wind driving and substorm triggering, *Journal of Geophysical Research: Space Physics*, *116*(A3), doi:10.1029/2010JA016139.

Newell, P. T., T. Sotirelis, K. Liou, C.-I. Meng, and F. J. Rich (2007), A nearly universal solar wind-magnetosphere coupling function inferred from 10 magnetospheric state variables, *Journal of Geophysical Research: Space Physics*, *112*(A1), doi:10.1029/2006JA012015.

Nichols, J. D., S. W. H. Cowley, and D. J. Mccomas (2006), Magnetopause reconnection rate estimates for Jupiter's magnetosphere based on interplanetary measurements at 5AU Magnetopause reconnection rate estimates for Jupiter's magnetosphere based on interplanetary measurements at 5 AU, *Annales Geophysicae*, *24*(24), 393–406.

Nichols, J. D., S. V.badman, K. H. Baines, R. H. Brown, E. J. Bunce, J. T. Clarke, S. W. H. Cowley, F. J. Crary, M. K. Dougherty, J. C. Gérard, A. Grocott, D. Grodent, W. S. Kurth, H. Melin, D. G. Mitchell, W. R. Pryor, and T. S. Stallard (2014), Dynamic auroral storms on Saturn as observed by the hubble space telescope, *Geophysical Research Letters*, *41*(10), 3323–3330, doi:10.1002/2014GL060186.

Nykyri, K., A. Otto, B. Lavraud, C. Mouikis, L. M. Kistler, A. Balogh, and H. Eme (2006), Cluster observations of reconnection due to the Kelvin-Helmholtz instability at the dawnside magnetospheric flank, *24*, 2619–2643.

Ohtani, S. I., M. A. Shay, and T. Mukai (2004), Temporal structure of the fast convective flow in the plasma sheet: Comparison between observations and two-fluid simulations, *Journal of Geophysical Research: Space Physics*, *109*(A3), 16, doi:10.1029/2003JA010002.

Øieroset, M., T. D. Phan, M. Fujimoto, R. P. Lin, and R. P. Lepping (2001), In situ detection of collisionless reconnection in the Earth's magnetotail, *Nature*, *412*(6845), 414–417, doi:10.1038/35086520.

Pan, D. X., X. Z. Zhou, Q. Q. Shi, J. Liu, V. Angelopoulos, A. Runov, Q. G. Zong, and S. Y. Fu (2015), On the generation of magnetic dips ahead of advancing dipolarization fronts, *Geophysical Research Letters*, *42*(11), 4256–4262, doi:10.1002/2015GL064369.

Pan, Q., M. Ashour-Abdalla, R. J. Walker, and M. El-Alaoui (2014a), Ion energization and transport associated with magnetic dipolarizations, *Geophysical Research Letters*, *41*(16), 5717–5726, doi:10.1002/2014GL061209.

Pan, Q., M. Ashour-Abdalla, R. J. Walker, and M. El-Alaoui (2014b), Electron energization and transport in the magnetotail during substorms, *Journal of Geophysical Research A: Space Physics*, *119*(2), 1060–1079, doi:10.1002/2013JA019508.

Parker, E. N. (1957), Sweet's mechanism for merging magnetic fields in conducting fluids, *Journal of Geophysical Research*, *62*(4), 509–520, doi:10.1029/JZ062i004p00509.

Parker, E. N. (1958), Dynamics of the Interplanetary Gas and Magnetic Fields., *The Astrophysical Journal*, *128*, 664, doi:10.1086/146579.

Paschmann, G., B. U. Ö. Sonnerup, I. Papamastorakis, N. Sckopke, G. Haerendel, S. J. Bame, J. R. Asbridge, J. T. Gosling, C. T. Russell, and R. C. Elphic (1979), Plasma acceleration at the Earth's magnetopause: evidence for reconnection, *Nature*, *282*(5736), 243–246, doi:10.1038/282243a0.

Paschmann, G., I. Papamastorakis, W. Baumjohann, N. Sckopke, C. W. Carlson, B. U. Ö. Sonnerup, and H. Lühr (1986), The magnetopause for large magnetic shear: AMPTE/IRM observations, *Journal of Geophysical Research*, *91*(A10), 11,099, doi:10.1029/JA091iA10p11099.

Perry, C., T. Eriksson, P. Escoubet, S. Esson, H. Laakso, S. McCaffrey, T. Sanderson, H. Bowen, A. Allen, and C. Harvey (2006), The ESA Cluster active archive, in *European Space Agency, (Special Publication) ESA SP*, edited by H. Laakso, M. Taylor, and P. Escoubet, C., 598, 1 ed., pp. 105–112, Springer Netherlands, doi:10.1007/978-90-481-3499-1.

Petrukovich, A. A. (2011), Origins of plasma sheet By, *Journal of Geophysical Research: Space Physics*, *116*(7), doi:10.1029/2010JA016386.

Petschek, H. E. (1964), Magnetic Field Annihilation, *The Physics of Solar Flares, Proceedings of the AAS-NASA Symposium*, *50*, 425, doi:10.1007/s13398-014-0173-7.2.

Phan, T. D., J. F. Drake, M. A. Shay, J. T. Gosling, G. Paschmann, J. P. Eastwood, M. Oieroset, M. Fujimoto, and V. Angelopoulos (2014), Ion bulk heating in magnetic reconnection exhausts at Earth's magnetopause: Dependence on the inflow Alfvén speed and magnetic shear angle, *Geophysical Research Letters*, *41*(20), 7002–7010, doi:10.1002/2014GL061547.

Pilkington, N. M., N. Achilleos, C. S. Arridge, P. Guio, A. Masters, L. C. Ray, N. Sergis, M. F. Thomsen, A. J. Coates, and M. K. Dougherty (2015), Internally driven large-scale changes in the size of Saturn's magnetosphere, *Journal of Geophysical Research A: Space Physics*, *120*(9), 7289–7306, doi:10.1002/2015JA021290.

Poh, G., J. A. Slavin, X. Jia, G. A. DiBraccio, J. M. Raines, S. M. Imber, D. J. Gershman, W. J. Sun, B. J. Anderson, H. Korth, T. H. Zurbuchen, R. L. McNutt, and S. C. Solomon (2016), MESSENGER observations of cusp plasma filaments at Mercury, *Journal of Geophysical Research A: Space Physics*, *121*(9), 8260–8285, doi:10.1002/2016JA022552.

Poh, G., J. A. Slavin, X. Jia, J. M. Raines, S. M. Imber, W. J. Sun, D. J. Gershman, G. A. DiBraccio, K. J. Genestreti, and A. W. Smith (2017a), Mercury's cross-tail

current sheet: Structure, X-line location and stress balance, *Geophysical Research Letters*, *44*(2), 678–686, doi:10.1002/2016GL071612.

Poh, G., J. A. Slavin, X. Jia, J. M. Raines, S. M. Imber, W.-J. Sun, D. J. Gershman, G. A. DiBraccio, K. J. Genestreti, and A. W. Smith (2017b), Coupling Between Mercury And Its Night-Side Magnetosphere: Cross-Tail Current Sheet Asymmetry And Substorm Current Wedge Formation, *Journal of Geophysical Research: Space Physics*, doi:10.1002/2017JA024266.

Pontius, D. H., and T. W. Hill (2009), Plasma mass loading from the extended neutral gas torus of Enceladus as inferred from the observed plasma corotation lag, *Geophysical Research Letters*, *36*(23), L23,103, doi:10.1029/2009GL041030.

Porco, C. C., P. Helfenstein, P. C. Thomas, A. P. Ingersoll, J. Wisdom, R. West, G. Neukum, T. Denk, R. Wagner, T. Roatsch, S. Kieffer, E. Turtle, A. McEwen, T. V. Johnson, J. Rathbun, J. Veverka, D. Wilson, J. Perry, J. Spitale, A. Brahic, J. A. Burns, A. D. DelGenio, L. Dones, C. D. Murray, and S. Squyres (2006), Cassini observes the active south pole of enceladus, *Science*, *311*(5766), 1393–1401, doi:10.1126/science.1123013.

Priest, E. R. (1990), The Equilibrium of Magnetic Flux Ropes, *Geophys. Monogr.*, *58*, 1–22.

Provan, G., D. J. Andrews, C. S. Arridge, A. J. Coates, S. W. H. Cowley, G. Cox, M. K. Dougherty, and C. M. Jackman (2012), Dual periodicities in planetary-period magnetic field oscillations in Saturn's tail, *Journal of Geophysical Research: Space Physics*, *117*(A1), doi:10.1029/2011JA017104.

Pulkkinen, A., L. Rastätter, M. Kuznetsova, H. Singer, C. Balch, D. Weimer, G. Toth, A. Ridley, T. Gombosi, M. Wiltberger, J. Raeder, and R. Weigel (2013), Community-wide validation of geospace model ground magnetic field perturbation predictions to support model transition to operations, *Space Weather*, *11*(6), 369–385, doi:10.1002/swe.20056.

Raines, J. M., J. A. Slavin, T. H. Zurbuchen, G. Gloeckler, B. J. Anderson, D. N. Baker, H. Korth, S. M. Krimigis, and R. L. McNutt (2011), MESSENGER observations of the plasma environment near Mercury, *Planetary and Space Science*, *59*(15), 2004–2015, doi:10.1016/j.pss.2011.02.004.

Raines, J. M., D. J. Gershman, T. H. Zurbuchen, M. Sarantos, J. A. Slavin, J. A. Gilbert, H. Korth, B. J. Anderson, G. Gloeckler, S. M. Krimigis, D. N. Baker, R. L. McNutt, and S. C. Solomon (2013), Distribution and compositional variations of plasma ions in Mercury's space environment: The first three Mercury years of MESSENGER

observations, *Journal of Geophysical Research: Space Physics*, *118*(4), 1604–1619, doi:10.1029/2012JA018073.

Reed, J. J., C. M. Jackman, L. Lamy, W. S. Kurth, and D. K. Whiter (2018), Low Frequency Extensions of the Saturn Kilometric Radiation as a proxy for magnetospheric dynamics, *Journal of Geophysical Research: Space Physics*, doi:10.1002/2017JA024499.

Richardson, I. G., S. W. H. Cowley, E. W. Hones, and S. J. Bame (1987), Plasmoid-associated energetic ion bursts in the deep geomagnetic tail: Properties of plasmoids and the postplasmoid plasma sheet, *Journal of Geophysical Research*, *92*(A9), 9997, doi:10.1029/JA092iA09p09997.

Rong, Z. J., W. X. Wan, C. Shen, T. L. Zhang, A. T. Y. Lui, Y. Wang, M. W. Dunlop, Y. C. Zhang, and Q. G. Zong (2013), Method for inferring the axis orientation of cylindrical magnetic flux rope based on single-point measurement, *Journal of Geophysical Research: Space Physics*, *118*(1), 271–283, doi:10.1029/2012JA018079.

Rong, Z. J., A. T. Y. Lui, W. X. Wan, Y. Y. Yang, C. Shen, A. A. Petrukovich, Y. C. Zhang, T. L. Zhang, and Y. Wei (2015), Time delay of interplanetary magnetic field penetration into Earth's magnetotail, *Journal of Geophysical Research A: Space Physics*, *120*(5), 3406–3414, doi:10.1002/2014JA020452.

Runov, A., V. A. Sergeev, R. Nakamura, W. Baumjohann, S. Apatenkov, Y. Asano, T. Takada, M. Volwerk, Z. Vörös, and T. L. Zhang (2006), Local structure of the magnetotail current sheet: 2001 Cluster observations, *Annales Geophysicae*, *24*(1), 247–262, doi:10.5194/angeo-24-247-2006.

Runov, A., V. Angelopoulos, M. I. Sitnov, V. A. Sergeev, J. Bonnell, J. P. McFadden, D. Larson, K. H. Glassmeier, and U. Auster (2009), THEMIS observations of an earthward-propagating dipolarization front, *Geophysical Research Letters*, *36*(14), L14,106, doi:10.1029/2009GL038980.

Runov, A., V. Angelopoulos, X. Z. Zhou, X. J. Zhang, S. Li, F. Plaschke, and J. Bonnell (2011), A THEMIS multicase study of dipolarization fronts in the magnetotail plasma sheet, *Journal of Geophysical Research: Space Physics*, *116*(5), doi:10.1029/2010JA016316.

Runov, A., V. Angelopoulos, C. Gabrielse, X. Z. Zhou, D. Turner, and F. Plaschke (2013), Electron fluxes and pitch-angle distributions at dipolarization fronts: THEMIS multipoint observations, *Journal of Geophysical Research: Space Physics*, *118*(2), 744–755, doi:10.1002/jgra.50121.

Runov, A., V. Angelopoulos, C. Gabrielse, J. Liu, D. L. Turner, and X. Z. Zhou (2015), Average thermodynamic and spectral properties of plasma in and around dipolarizing flux bundles, *Journal of Geophysical Research A: Space Physics*, *120*(6), 4369–4383, doi:10.1002/2015JA021166.

Runov, A., V. Angelopoulos, A. Artemyev, J. Birn, P. L. Pritchett, and X. Z. Zhou (2017), Characteristics of ion distribution functions in dipolarizing flux bundles: Event studies, *Journal of Geophysical Research: Space Physics*, *122*(6), 5965–5978, doi:10.1002/2017JA024010.

Russell, C., and R. Elphic (1978), Initial ISEE magnetometer results: magnetopause observations, *Space Science Reviews*, *22*(6), 681–715, doi:10.1007/BF00212619.

Russell, C. T. (1972), Configuration of the magnetosphere, in *Critical Problems of Magnetospheric Physics, Proceedings of the Symposium held 11-13 May, 1972 in Madrid, Spain*, vol. 1, edited by E. Dyer, p. 1.

Russell, C. T., C. M. Jackman, H. Y. Wei, C. Bertucci, and M. K. Dougherty (2008), Titan's influence on Saturnian substorm occurrence, *Geophysical Research Letters*, *35*(12), doi:10.1029/2008GL034080.

Schindler, K. (1974), A theory of the substorm mechanism, *Journal of Geophysical Research*, *79*(19), 2803, doi:10.1029/JA079i019p02803.

Scholer, M. (1988), Magnetic flux transfer at the magnetopause based on single X line bursty reconnection, *Geophysical Research Letters*, *15*(4), 291–294, doi:10.1029/GL015i004p00291.

Scholer, M., G. Gloeckler, D. Hovestadt, B. Klecker, and F. M. Ipavich (1984), Characteristics of plasmoidlike structures in the distant magnetotail, *Journal of Geophysical Research*, *89*(A10), 8872, doi:10.1029/JA089iA10p08872.

Scurry, L., C. T. Russell, and J. T. Gosling (1994), Geomagnetic activity and the beta dependence of the dayside reconnection rate, *Journal of Geophysical Research*, *99*(A8), 14,811, doi:10.1029/94JA00794.

Sergeev, V. A., D. G. Mitchell, C. T. Russell, and D. J. Williams (1993), Structure of the Tail Plasma/Current Sheet at -11 RE and Its Changes in the Course of a Substorm, *JOURNAL OF GEOPHYSICAL RESEARCH,*, *98*(A10), 345–365, doi:10.1029/93JA01151.

Sergis, N., S. M. Krimigis, D. G. Mitchell, D. C. Hamilton, N. Krupp, B. M. Mauk, E. C. Roelof, and M. Dougherty (2007), Ring current at Saturn: Energetic particle pressure in Saturn's equatorial magnetosphere measured with Cassini/MIMI, *Geophysical Research Letters*, *34*(9), doi:10.1029/2006GL029223.

Sergis, N., S. M. Krimigis, D. G. Mitchell, D. C. Hamilton, N. Krupp, B. H. Mauk, E. C. Roelof, and M. K. Dougherty (2009), Energetic particle pressure in Saturn's magnetosphere measured with the Magnetospheric Imaging Instrument on Cassini, *Journal of Geophysical Research: Space Physics*, *114*(A2), doi:10.1029/2008JA013774.

Sergis, N., S. M. Krimigis, E. C. Roelof, C. S. Arridge, A. M. Rymer, D. G. Mitchell, D. C. Hamilton, N. Krupp, M. F. Thomsen, M. K. Dougherty, A. J. Coates, and D. T. Young (2010), Particle pressure, inertial force, and ring current density profiles in the magnetosphere of Saturn, based on Cassini measurements, *Geophysical Research Letters*, *37*(2), doi:10.1029/2009GL041920.

Sergis, N., C. S. Arridge, S. M. Krimigis, D. G. Mitchell, A. M. Rymer, D. C. Hamilton, N. Krupp, M. K. Dougherty, and A. J. Coates (2011), Dynamics and seasonal variations in Saturn's magnetospheric plasma sheet, as measured by Cassini, *Journal of Geophysical Research: Space Physics*, *116*(4), 11, doi:10.1029/2010JA016180.

Sergis, N., C. M. Jackman, A. Masters, S. M. Krimigis, M. F. Thomsen, D. C. Hamilton, D. G. Mitchell, M. K. Dougherty, and A. J. Coates (2013), Particle and magnetic field properties of the Saturnian magnetosheath: Presence and upstream escape of hot magnetospheric plasma, *Journal of Geophysical Research: Space Physics*, *118*(4), 1620–1634, doi:10.1002/jgra.50164.

Shay, M. A., and M. Swisdak (2004), Three species collisionless reconnection: Effect of O + on magnetotail reconnection.

Shiokawa, K., Y. Miyashita, I. Shinohara, and A. Matsuoka (2005), Decrease in Bz prior to the dipolarization in the near-Earth plasma sheet, *Journal of Geophysical Research: Space Physics*, *110*(A9), doi:10.1029/2005JA011144.

Sibeck, D. G., G. L. Siscoe, J. A. Slavin, E. J. Smith, S. J. Bame, and F. L. Scarf (1984), Magnetotail flux ropes, *Geophysical Research Letters*, *11*(10), 1090–1093, doi:10.1029/GL011i010p01090.

Simon, S., A. Wennmacher, F. M. Neubauer, C. L. Bertucci, H. Kriegel, J. Saur, C. T. Russell, and M. K. Dougherty (2010), Titan's highly dynamic magnetic environment: A systematic survey of Cassini magnetometer observations from flybys TAT62, *Planetary and Space Science*, *58*(10), 1230–1251, doi:10.1016/j.pss.2010.04.021.

Siscoe, G. L., and T. S. Huang (1985), Polar cap inflation and deflation, *Journal of Geophysical Research: Space Physics*, *90*(A1), 543–547, doi:10.1029/JA090iA01p00543.

Siscoe, G. L., N. F. Ness, and C. M. Yeates (1975), Substorms on Mercury?, *Journal of Geophysical Research*, *80*(31), 4359–4363, doi:10.1029/JA080i031p04359.

Sittler, E. C., N. Andre, M. Blanc, M. Burger, R. E. Johnson, A. Coates, A. Rymer, D. Reisenfeld, M. F. Thomsen, A. Persoon, M. Dougherty, H. T. Smith, R. A. Baragiola, R. E. Hartle, D. Chornay, M. D. Shappirio, D. Simpson, D. J. McComas, and D. T. Young (2008), Ion and neutral sources and sinks within Saturn's inner magnetosphere: Cassini results, *Planetary and Space Science*, *56*(1), 3–18, doi: 10.1016/j.pss.2007.06.006.

Slavin, J. A., E. J. Smith, B. T. Tsurutani, D. G. Sibeck, H. J. Singer, D. N. Baker, J. T. Gosling, E. W. Hones, and F. L. Scarf (1984), Substorm associated traveling compression regions in the distant tail: ISEE-3 Geotail observations, *Geophysical Research Letters*, *11*(7), 657–660, doi:10.1029/GL011i007p00657.

Slavin, J. A., E. J. Smith, D. G. Sibeck, D. N. Baker, R. D. Zwickl, and S.-I. Akasofu (1985), An ISEE 3 study of average and substorm conditions in the distant magnetotail, *Journal of Geophysical Research*, *90*(A11), 10,875, doi:10.1029/JA090iA11p10875.

Slavin, J. A., D. N. Baker, J. D. Craven, R. C. Elphic, D. H. Fairfield, L. A. Frank, A. B. Galvin, W. J. Hughes, R. H. Manka, D. G. Mitchell, I. G. Richardson, T. R. Sanderson, D. J. Sibeck, E. J. Smith, and R. D. Zwickl (1989), CDAW 8 observations of plasmoid signatures in the geomagnetic tail: An assessment, *Journal of Geophysical Research*, *94*(A11), 15,153, doi:10.1029/JA094iA11p15153.

Slavin, J. A., M. F. Smith, E. L. Mazur, D. N. Baker, E. W. Hones, T. Iyemori, and E. W. Greenstadt (1993), ISEE 3 observations of traveling compression regions in the Earth's magnetotail, *Journal of Geophysical Research*, *98*(A9), 15,425, doi:10.1029/93JA01467.

Slavin, J. A., R. P. Lepping, J. Gjerloev, D. H. Fairfield, M. Hesse, C. J. Owen, M. B. Moldwin, T. Nagai, A. Ieda, and T. Mukai (2003a), Geotail observations of magnetic flux ropes in the plasma sheet, *Journal of Geophysical Research: Space Physics*, *108*(A1), 18, doi:10.1029/2002JA009557.

Slavin, J. A., R. P. Lepping, J. Gjerloev, M. L. Goldstein, D. H. Fairfield, M. H. Acuna, A. Balogh, M. Dunlop, M. G. Kivelson, K. Khurana, A. Fazakerley, C. J. Owen, H. Reme, and J. M. Bosqued (2003b), Cluster electric current density measurements within a magnetic flux rope in the plasma sheet, *Geophysical Research Letters*, *30*(7), 4, doi:10.1029/2002GL016411.

Slavin, J. A., E. I. Tanskanen, M. Hesse, C. J. Owen, M. W. Dunlop, S. Imber, E. A. Lucek, A. Balogh, and K. H. Glassmeier (2005), Cluster observations of traveling compression regions in the near-tail, *Journal of Geophysical Research: Space Physics*, *110*(A6), 19, doi:10.1029/2004JA010878.

Slavin, J. A., M. H. Acuna, B. J. Anderson, D. N. Baker, M. Benna, S. A. Boardsen, G. Gloeckler, R. E. Gold, G. C. Ho, H. Korth, S. M. Krimigis, R. L. McNutt, J. M. Raines, M. Sarantos, D. Schriver, S. C. Solomon, P. Travnicek, and T. H. Zurbuchen (2009), MESSENGER Observations of Magnetic Reconnection in Mercury's Magnetosphere, *Science*, *324*(5927), 606–610, doi:10.1126/science.1172011.

Slavin, J. A., B. J. Anderson, D. N. Baker, M. Benna, S. A. Boardsen, G. Gloeckler, R. E. Gold, G. C. Ho, H. Korth, S. M. Krimigis, R. L. McNutt, L. R. Nittler, J. M. Raines, M. Sarantos, D. Schriver, S. C. Solomon, R. D. Starr, P. M. Travnicek, and T. H. Zurbuchen (2010), MESSENGER Observations of Extreme Loading and Unloading of Mercury's Magnetic Tail, *Science*, *329*(5992), 665–668, doi:10.1126/science.1188067.

Slavin, J. A., B. J. Anderson, D. N. Baker, M. Benna, S. A. Boardsen, R. E. Gold, G. C. Ho, S. M. Imber, H. Korth, S. M. Krimigis, R. L. McNutt, J. M. Raines, M. Sarantos, D. Schriver, S. C. Solomon, P. Trávníček, and T. H. Zurbuchen (2012a), MESSENGER and Mariner 10 flyby observations of magnetotail structure and dynamics at Mercury, *Journal of Geophysical Research: Space Physics*, *117*(1), doi:10.1029/2011JA016900.

Slavin, J. A., S. M. Imber, S. A. Boardsen, G. A. Di Braccio, T. Sundberg, M. Sarantos, T. Nieves-Chinchilla, A. Szabo, B. J. Anderson, H. Korth, T. H. Zurbuchen, J. M. Raines, C. L. Johnson, R. M. Winslow, R. M. Killen, R. L. McNutt, and S. C. Solomon (2012b), MESSENGER observations of a flux-transfer-event shower at Mercury, *Journal of Geophysical Research: Space Physics*, *117*(10), doi:10.1029/2012JA017926.

Slavin, J. A., G. A. Dibraccio, D. J. Gershman, S. M. Imber, G. K. Poh, J. M. Raines, T. H. Zurbuchen, X. Jia, D. N. Baker, K. H. Glassmeier, S. A. Livi, S. A. Boardsen, T. A. Cassidy, M. Sarantos, T. Sundberg, A. Masters, C. L. Johnson, R. M. Winslow, B. J. Anderson, H. Korth, R. L. McNutt, and S. C. Solomon (2014), MESSENGER observations of Mercury's dayside magnetosphere under extreme solar wind conditions, *Journal of Geophysical Research: Space Physics*, *119*(10), 8087–8116, doi:10.1002/2014JA020319.

Smith, A. W., C. M. Jackman, and M. F. Thomsen (2016), Magnetic reconnection in Saturn's magnetotail: A comprehensive magnetic field survey, *Journal of Geophysical Research A: Space Physics*, *121*(4), 2984–3005, doi:10.1002/2015JA022005.

Smith, A. W., J. A. Slavin, C. M. Jackman, R. C. Fear, G. K. Poh, G. A. DiBraccio, J. M. Jasinski, and L. Trenchi (2017a), Automated force-free flux rope identification, *Journal of Geophysical Research: Space Physics*, *122*(1), 780–791, doi:10.1002/2016JA022994.

Smith, A. W., J. A. Slavin, C. M. Jackman, G. K. Poh, and R. C. Fear (2017b), Flux ropes in the Hermean magnetotail: Distribution, properties, and formation, *Journal of Geophysical Research: Space Physics*, *122*(8), 8136–8153, doi:10.1002/2017JA024295.

Smith, A. W., C. M. Jackman, M. F. Thomsen, L. Lamy, and N. Sergis (2018), Multi-instrument investigation of the location of Saturn's magnetotail x-line, *Journal of Geophysical Research: Space Physics*, doi:10.1029/2018JA025532.

Smith, E. J., L. Davis, D. E. Jones, P. J. Coleman, D. S. Colburn, P. Dyal, C. P. Sonett, and A. M. A. Frandsen (1974), The planetary magnetic field and magnetosphere of Jupiter: Pioneer 10, *Journal of Geophysical Research*, *79*(25), 3501–3513, doi:10.1029/JA079i025p03501.

Smith, E. J., L. Davis, D. E. Jones, P. J. Coleman, D. S. Colburn, P. Dyal, and C. P. Sonett (1975), Jupiter's Magnetic Field. Magnetosphere, and Interaction with the Solar Wind: Pioneer 11, *Science*, *188*(4187), 451–455, doi:10.1126/science.188.4187.451.

Smith, E. J., L. Davis, D. E. Jones, P. J. Coleman, D. S. Colburn, P. Dyal, and C. P. Sonett (1980), Saturn's magnetic field and magnetosphere, *Science*, *207*(4429), 407–410, doi:10.1126/science.207.4429.407.

Smith, H. T., R. E. Johnson, E. C. Sittler, M. Shappirio, D. Reisenfeld, O. J. Tucker, M. Burger, F. J. Crary, D. J. McComas, and D. T. Young (2007), Enceladus: The likely dominant nitrogen source in Saturn's magnetosphere, *Icarus*, *188*(2), 356–366, doi:10.1016/j.icarus.2006.12.007.

Smith, H. T., M. Shappirio, R. E. Johnson, D. Reisenfeld, E. C. Sittler, F. J. Crary, D. J. McComas, and D. T. Young (2008), Encelad us: A potential source of ammonia products and molecular nitrogen for Saturn's magnetosphere, *Journal of Geophysical Research: Space Physics*, *113*(11), 1–11, doi:10.1029/2008JA013352.

Snekvik, K., E. Tanskanen, N. Østgaard, L. Juusola, K. Laundal, E. I. Gordeev, and A. L. Borg (2012), Changes in the magnetotail configuration before near-Earth reconnection, *Journal of Geophysical Research: Space Physics*, *117*(A2), doi:10.1029/2011JA017040.

Solomon, S. C., R. L. McNutt, R. E. Gold, and D. L. Domingue (2007), MESSENGER mission overview, *Space Science Reviews*, *131*(1-4), 3–39, doi:10.1007/s11214-007-9247-6.

Sonnerup, B., and M. Scheible (1998), Minimum and maximum variance analysis, in *Analysis methods for multi-spacecraft data*, vol. 001, edited by G. Paschmann and P. W. Daly, pp. 185–220, ISSI Scientific Report SR-001, ISSI/ESA.

Sonnerup, B. U. Ö. (1974), Magnetopause reconnection rate, *Journal of Geophysical Research*, *79*(10), 1546–1549, doi:10.1029/JA079i010p01546.

Sonnerup, B. U. Ö., and L. J. Cahill (1967), Magnetopause structure and attitude from Explorer 12 observations, *Journal of Geophysical Research*, *72*(1), 171, doi:10.1029/JZ072i001p00171.

Southwood, D., C. Farrugia, and M. Saunders (1988), What are flux transfer events?, *Planetary and Space Science*, *36*(5), 503–508, doi:10.1016/0032-0633(88)90109-2.

Spencer, J. R., A. C. Barr, L. W. Esposito, P. Helfenstein, A. P. Ingersoll, R. Jaumann, C. P. McKay, F. Nimmo, and J. H. Waite (2009), Enceladus: An active cryovolcanic satellite, in *Saturn from Cassini-Huygens*, pp. 683–724, doi:10.1007/978-1-4020-9217-6_21.

Stephenson, D. B., and D. B. Stephenson (2000), Use of the Odds Ratio for Diagnosing Forecast Skill, *Weather and Forecasting*, *15*(2), 221–232, doi:10.1175/1520-0434(2000)015⟨0221:UOTORF⟩2.0.CO;2.

Sun, W. J., J. A. Slavin, S. Fu, J. M. Raines, Q. G. Zong, S. M. Imber, Q. Shi, Z. Yao, G. Poh, D. J. Gershman, Z. Pu, T. Sundberg, B. J. Anderson, H. Korth, and D. N. Baker (2015), MESSENGER observations of magnetospheric substorm activity in Mercury's near magnetotail, *Geophysical Research Letters*, *42*(10), 3692–3699, doi:10.1002/2015GL064052.

Sun, W. J., S. Y. Fu, J. A. Slavin, J. M. Raines, Q. G. Zong, G. K. Poh, and T. H. Zurbuchen (2016), Spatial distribution of Mercury's flux ropes and reconnection fronts: MESSENGER observations, *Journal of Geophysical Research A: Space Physics*, *121*(8), 7590–7607, doi:10.1002/2016JA022787.

Sundberg, T., J. A. Slavin, S. A. Boardsen, B. J. Anderson, H. Korth, G. C. Ho, D. Schriver, V. M. Uritsky, T. H. Zurbuchen, J. M. Raines, D. N. Baker, S. M. Krimigis, R. L. McNutt, and S. C. Solomon (2012a), Messenger observations of dipolarization events in Mercury's magnetotail, *Journal of Geophysical Research: Space Physics*, *117*(9), doi:10.1029/2012JA017756.

Sundberg, T., S. A. Boardsen, J. A. Slavin, B. J. Anderson, H. Korth, T. H. Zurbuchen, J. M. Raines, and S. C. Solomon (2012b), MESSENGER orbital observations of large-amplitude Kelvin-Helmholtz waves at Mercury's magnetopause, *Journal of Geophysical Research: Space Physics*, *117*(A4), doi:10.1029/2011JA017268.

Sweet, P. A. (1958), 14. The neutral point theory of solar flares, *Symposium - International Astronomical Union*, *6*, 123–134, doi:10.1017/S0074180900237704.

Swisdak, M., B. N. Rogers, J. F. Drake, and M. A. Shay (2003), Diamagnetic suppression of component magnetic reconnection at the magnetopause, *Journal of Geophysical Research: Space Physics*, *108*(A5), doi:10.1029/2002JA009726.

Szego, K., Z. Nemeth, G. Erdos, L. Foldy, Z. Bebesi, M. Thomsen, and D. Delapp (2012), Location of the magnetodisk in the nightside outer magnetosphere of Saturn near equinox based on ion densities, *Journal of Geophysical Research: Space Physics*, *117*(9), doi:10.1029/2012JA017817.

Tao, C., L. Lamy, and R. Prangé (2014), The brightness ratio of H Lyman-α/H2 bands in FUV auroral emissions: A diagnosis for the energy of precipitating electrons and associated magnetospheric acceleration processes applied to Saturn, *Geophysical Research Letters*, *41*(19), 6644–6651, doi:10.1002/2014GL061329.

Teh, W. L., R. Nakamura, H. Karimabadi, W. Baumjohann, and T. L. Zhang (2014), Correlation of core field polarity of magnetotail flux ropes with the IMF By: Reconnection guide field dependency, *Journal of Geophysical Research: Space Physics*, *119*(4), 2933–2944, doi:10.1002/2013JA019454.

Tenfjord, P., N. Østgaard, K. Snekvik, K. M. Laundal, J. P. Reistad, S. Haaland, and S. E. Milan (2015), How the IMF Byinduces a Bycomponent in the closed magnetosphere and how it leads to asymmetric currents and convection patterns in the two hemispheres, *Journal of Geophysical Research A: Space Physics*, *120*(11), 9368–9384, doi:10.1002/2015JA021579.

Thomas, P., R. Tajeddine, M. Tiscareno, J. Burns, J. Joseph, T. Loredo, P. Helfenstein, and C. Porco (2016), Enceladus's measured physical libration requires a global subsurface ocean, *Icarus*, *264*, 37–47, doi:10.1016/J.ICARUS.2015.08.037.

Thomsen, M. F. (2013), Saturn's magnetospheric dynamics, *Geophysical Research Letters*, *40*(20), 5337–5344, doi:10.1002/2013GL057967.

Thomsen, M. F., D. B. Reisenfeld, D. M. Delapp, R. L. Tokar, D. T. Young, F. J. Crary, E. C. Sittler, M. A. McGraw, and J. D. Williams (2010), Survey of ion plasma parameters in Saturn's magnetosphere, *Journal of Geophysical Research: Space Physics*, *115*(10), 1–22, doi:10.1029/2010JA015267.

Thomsen, M. F., R. J. Wilson, R. L. Tokar, D. B. Reisenfeld, and C. M. Jackman (2013), Cassini/CAPS observations of duskside tail dynamics at Saturn, *Journal of Geophysical Research: Space Physics*, *118*(9), 5767–5781, doi:10.1002/jgra.50552.

Thomsen, M. F., C. M. Jackman, R. L. Tokar, and R. J. Wilson (2014a), Plasma flows in Saturn's nightside magnetosphere, *Journal of Geophysical Research: Space Physics*, *119*(6), 4521–4535, doi:10.1002/2014JA019912.

Thomsen, M. F., D. B. Reisenfeld, R. J. Wilson, M. Andriopoulou, F. J. Crary, G. B. Hospodarsky, C. M. Jackman, X. Jia, K. K. Khurana, C. Paranicas, E. Roussos, N. Sergis, and R. L. Tokar (2014b), Ion composition in interchange injection events in Saturn's magnetosphere, *Journal of Geophysical Research: Space Physics*, *119*(12), 9761–9772, doi:10.1002/2014JA020489.

Thomsen, M. F., C. M. Jackman, D. G. Mitchell, G. Hospodarsky, W. S. Kurth, and K. C. Hansen (2015), Sustained lobe reconnection in Saturn's magnetotail, *Journal of Geophysical Research A: Space Physics*, *120*(12), 10,257–10,274, doi:10.1002/2015JA021768.

Thomsen, M. F., A. J. Coates, E. Roussos, R. J. Wilson, K. C. Hansen, and G. R. Lewis (2016), Suprathermal electron penetration into the inner magnetosphere of Saturn, *Journal of Geophysical Research A: Space Physics*, *121*(6), 5436–5448, doi:10.1002/2016JA022692.

Tindale, E., and S. C. Chapman (2016), Solar cycle variation of the statistical distribution of the solar wind ϵ parameter and its constituent variables, *Geophysical Research Letters*, *43*(11), 5563–5570, doi:10.1002/2016GL068920.

Tseng, W.-L., R. E. Johnson, M. F. Thomsen, T. A. Cassidy, and M. K. Elrod (2011), Neutral H 2 and H 2 + ions in the Saturnian magnetosphere, *Journal of Geophysical Research: Space Physics*, *116*(A3), doi:10.1029/2010JA016145.

Vandas, M., and E. P. Romashets (2003), A force-free field with constant alpha in an oblate\ncylinder: Ageneralization of the Lundquist solution, *Astronomy and Astrophysics*, *398*(3), 801–807, doi:10.1051/0004-6361:20021691.

Vasquez, B. J., V. I. Abramenko, D. K. Haggerty, and C. W. Smith (2007), Numerous small magnetic field discontinuities of Bartels rotation 2286 and the potential role of Alfvénic turbulence, *Journal of Geophysical Research: Space Physics*, *112*(11), doi:10.1029/2007JA012504.

Vasyliunas, V. M. (1983), *Plasma Distribution and Flow*, Physics of the {Jovian} Magnetosphere, 395–453 pp., Cambridge University Press, New York, doi:10.1029/2003JD004173.Aires.

Vogt, M. F., M. G. Kivelson, K. K. Khurana, S. P. Joy, and R. J. Walker (2010), Reconnection and flows in the Jovian magnetotail as inferred from magnetometer observations, *Journal of Geophysical Research: Space Physics*, *115*(6), 19, doi:10.1029/2009JA015098.

Vogt, M. F., C. M. Jackman, J. A. Slavin, E. J. Bunce, S. W. Cowley, M. G. Kivelson, and K. K. Khurana (2014), Structure and statistical properties of plasmoids in Jupiter's

magnetotail, *Journal of Geophysical Research A: Space Physics*, *119*(2), 821–843, doi: 10.1002/2013JA019393.

Waite, J., and J. Furman (2013), Cassini Orbiter Sat/Sw Caps Derived Electron Moments V1.0,Co-S/Sw-Caps-5-Ddr-Ele-Moments-V1.0.

Walsh, A. P., C. J. Owen, A. N. Fazakerley, C. Forsyth, and I. Dandouras (2011), Average magnetotail electron and proton pitch angle distributions from Cluster PEACE and CIS observations, *Geophysical Research Letters*, *38*(6), doi:10.1029/ 2011GL046770.

Walsh, A. P., S. Haaland, C. Forsyth, A. M. Keesee, J. Kissinger, K. Li, A. Runov, J. Soucek, B. M. Walsh, S. Wing, and M. G. G. T. Taylor (2014), Dawn-dusk asymmetries in the coupled solar wind-magnetosphere-ionosphere system: A review, *Annales Geophysicae*, *32*(7), 705–737, doi:10.5194/angeo-32-705-2014.

Winslow, R. M., B. J. Anderson, C. L. Johnson, J. A. Slavin, H. Korth, M. E. Purucker, D. N. Baker, and S. C. Solomon (2013), Mercury's magnetopause and bow shock from MESSENGER Magnetometer observations, *Journal of Geophysical Research: Space Physics*, *118*(5), 2213–2227, doi:10.1002/jgra.50237.

Wolfe, J. H., R. W. Silva, D. D. McKibbin, and R. H. Mason (1967), Preliminary observations of a geomagnetospheric wake at 1000 Earth radii, *Journal of Geophysical Research*, *72*(17), 4577–4581, doi:10.1029/JZ072i017p04577.

Xiao, C. J., Z. Y. Pu, Z. W. Ma, S. Y. Fu, Z. Y. Huang, and Q. G. Zong (2004), Inferring of flux rope orientation with the minimum variance analysis technique, *Journal of Geophysical Research: Space Physics*, *109*(A11), doi:10.1029/2004JA010594.

Yao, Z. H., D. Grodent, L. C. Ray, I. J. Rae, A. J. Coates, Z. Y. Pu, A. T. Lui, A. Radioti, J. H. Waite, G. H. Jones, R. L. Guo, and W. R. Dunn (2017a), Two fundamentally different drivers of dipolarizations at Saturn, *Journal of Geophysical Research: Space Physics*, doi:10.1002/2017JA024060.

Yao, Z. H., A. J. Coates, L. C. Ray, I. J. Rae, D. Grodent, G. H. Jones, M. K. Dougherty, C. J. Owen, R. L. Guo, W. R. Dunn, A. Radioti, Z. Y. Pu, G. R. Lewis, J. H. Waite, and J.-C. Gérard (2017b), Corotating Magnetic Reconnection Site in Saturn's Magnetosphere, *The Astrophysical Journal*, *846*(2), L25, doi:10.3847/2041-8213/aa88af.

Young, D. T., B. L. Barraclough, J. J. Berthelier, M. Blanc, J. L. Burch, A. J. Coates, R. Goldstein, M. Grande, T. W. Hill, J. M. Illiano, M. A. Johnson, R. E. Johnson, R. A. Baragiola, V. Kelha, D. Linder, D. J. McComas, B. T. Narheim, J. E. Nordholt,

A. Preece, E. C. Sittler, K. R. Svenes, S. Szalai, K. Szegö, P. Tanskanen, and K. Viherkanto (1998), Cassini plasma spectrometer investigation, *Geophysical Monograph Series*, *102*(1-4), 237–242, doi:10.1029/GM102p0237.

Zhao, S. Q., A. M. Tian, Q. Q. Shi, C. J. Xiao, S. Y. Fu, Q. G. Zong, H. Z. Wang, S. Zhang, S. J. Zhao, D. X. Pan, S. C. Teng, Y. X. Liu, and K. Tan (2016), Statistical study of magnetotail flux ropes near the lunar orbit, *Science China Technological Sciences*, *59*(10), 1591–1596, doi:10.1007/s11431-015-0962-3.

Zhong, J., W. X. Wan, Y. Wei, J. A. Slavin, J. M. Raines, Z. J. Rong, L. H. Chai, and X. H. Han (2015), Compressibility of Mercury's dayside magnetosphere, *Geophysical Research Letters*, *42*(23), 10,135–10,139, doi:10.1002/2015GL067063.

Zieger, B., K. C. Hansen, T. I. Gombosi, and D. L. De Zeeuw (2010), Periodic plasma escape from the mass-loaded Kronian magnetosphere, *Journal of Geophysical Research: Space Physics*, *115*(8), 8, doi:10.1029/2009JA014951.

Zurbuchen, T. H., J. M. Raines, G. Gloeckler, S. M. Krimigis, J. A. Slavin, P. L. Koehn, R. M. Killen, A. L. Sprague, R. L. McNutt, and S. C. Solomon (2008), MESSENGER observations of the composition of mercury's ionized exosphere and plasma environment, *Science*, *321*(5885), 90–92, doi:10.1126/science.1159314.

Zurbuchen, T. H., J. M. Raines, J. A. Slavin, D. J. Gershman, J. A. Gilbert, G. Gloeckler, B. J. Anderson, D. N. Baker, H. Korth, S. M. Krimigis, M. Sarantos, D. Schriver, R. L. McNutt, and S. C. Solomon (2011), MESSENGER Observations of the Spatial Distribution of Planetary Ions Near Mercury, *Science*, *333*(6051), 1862–1865, doi:10.1126/science.1211302.